

Electron transport and coherence in semiconductor quantum dots and rings

voor mijn ouders

Electron transport and coherence in semiconductor quantum dots and rings

Proefschrift

ter verkrijging van de graad van doctor
aan de Technische Universiteit Delft,
op gezag van de Rector Magnificus prof.dr.ir. J.T. Fokkema,
voorzitter van het College voor Promoties,
in het openbaar te verdedigen op maandag 28 januari 2002 om 16.00 uur

door

Wilfred Gerard VAN DER WIEL

natuurkundig ingenieur
geboren te Gouda.

Dit proefschrift is goedgekeurd door de promotoren:

Prof.dr.ir. L.P. Kouwenhoven

Prof.dr.ir. J.E. Mooij

Samenstelling van de promotiecommissie:

Rector Magnificus, voorzitter

Prof.dr.ir. L.P. Kouwenhoven, Technische Universiteit Delft, promotor

Prof.dr.ir. J.E. Mooij, Technische Universiteit Delft, promotor

Prof.dr. D. Loss, Universität Basel, Zwitserland

Prof.dr. C. Marcus, Harvard University, Verenigde Staten

Prof.dr. Yu.V. Nazarov, Technische Universiteit Delft

Prof.dr. S. Tarucha, Tokyo University, Japan

Prof.dr. R.M. Westervelt, Harvard University, Verenigde Staten



Published and distributed by: DUP Science

DUP Science is an imprint of

Delft University Press

P.O. Box 98

Telephone: +31 15 27 85678

2600 MG Delft

Telefax: +31 15 27 85706

The Netherlands

E-mail: DUP@Library.TUdelft.NL

ISBN 90-407-2270-6

Keywords: quantum dots, Kondo effect, Aharonov-Bohm effect

Cover design: Wilfred G. van der Wiel

Copyright © 2001 by Wilfred G. van der Wiel

All rights reserved. No part of the material protected by this copyright notice may be reproduced or utilized in any form or by any means, electronic or mechanical, including photocopying, recording or by any information storage and retrieval system, without permission from the publisher: Delft University Press.

Printed in the Netherlands

Preface

学問に近道なし

Gakumon ni chikamichi nashi

There is no royal road to learning

When I entered Delft University of Technology eight years ago, I did not have the slightest idea about quantum dots, Aharonov-Bohm rings or the Kondo effect. My first acquaintance with the field of mesoscopic physics was through the series of lectures on this topic in my third year. I decided to join QT, the Quantum Transport Group of Hans Mooij, in 1997 and I have been a group member ever since. First as an undergraduate student with Luuk Mur and Kees Harmans, later as a graduate student in the quantum dot section of Leo Kouwenhoven. In this period, little by little, I have become a young citizen of Mesoscopopolis. Although I have been learning a lot in this time, many of the phenomena occurring in our experiments do still astonish me as much as they did when I first heard about them. I cherish this astonishment as my traveling-companion on my continuing road to learning.

This thesis forms a result of four years of experimental research on semiconductor quantum dots and rings. The experiments have mainly been performed in our laboratory in Delft, whereas most of the devices have been fabricated at NTT Basic Research Laboratories in Atsugi, Japan. I feel privileged to have had the chance to work in a stimulating and dynamic environment both in Delft and Japan. The way research is organized and performed in QT and the Butsuden Group of Dr. Hirayama at NTT clearly shows that the commonplace of the lonely scientist behind a computer screen in a dark, dusty room is far from true. If anything, the work described in this thesis is a group effort and the result of intense collaboration. Let me therefore express my sincere thanks to everyone at Delft University of Technology, NTT Basic Research Laboratories, Tokyo University and Hokkaido University who have contributed to the realization of this thesis.

Although thanking people (read: ‘forgetting to thank people’) is a risky enterprise, there are some persons I would like to mention in particular.

First of all, I thank my Ph.D. advisor Leo Kouwenhoven for not only being a great guide into the realm of quantum dots, but also for being a chief advisor on Japanese nightlife. Leo’s ‘Fingerspitzengefühl’ has often given momentum to the successful completion of experiments. I also thank Tjerk Oosterkamp for introducing me thoroughly into quantum dot experiments. Of course, I have to mention the other members of the quantum dot team with whom I worked closely: Silvano De Franceschi, Jeroen Elzerman (also known as ‘Jero de la Ramblas’), Ronald Hanson and Joris Wijkema, and more recently, Laurens Willems van Beveren, Jacob Greidanus and Lieven Vandersypen. Silvano, grazie per tutto! You are a wonderful and sparkling colleague. Our visit to ‘la Mamma’ in Milan was certainly one of the highlights we experienced together. The way your mother welcomed me as ‘William, il principe d’Inghilterra’ still gives me a warm feeling. Jero, your dedication and imitation of people’s silly walks are admirable. Ronnie and Laurens, I am sure I will meet you in Japan. Lieven, ’t amusement! I am thankful for the nice time I have spent with my students Michael Janus, Jero, Frank Mallens, Elvira Huizeling and Joris, and for the hard work they did. Michael has made data analysis a lot more enjoyable thanks to his ‘Mick’s Advanced Peakfinder’. Joris’ work on Labview measurement software has marked the beginning of the end for our DOS-driven measurement system.

Besides my close collaborators in the quantum dot section, there are certainly some other people in QT who deserve some words. Hans Mooij has managed to build up a community where high-quality research has become the standard. It has been a pleasure working in his flourishing group. The technical support of Raymond Schouten, Bram van der Enden, Leo Dam, Bram Huis, Leo Lander, Mascha van Oossanen, Willem den Braver, Wim Schot and Etienne Swinkels has been of great value. Raymond, you are a real ‘electronics guru’, which is illustrated by the fact that even the Japanese import your products. Thanks to Bram van der Enden, I know how to bond a sample and how to deal with ‘langharig werkschuw tuig’. I would like to thank Peter Hadley for his valuable advice on the issue of electrochemical potential and energy diagrams. I wish him good luck in his continuing war against the confusion between them. Although not directly involved in my work anymore, Kees Harmans kept on following me in the group and I like to thank him for interesting discussions. Herre van der Zant I thank for the goals he scored in the ‘Wallast League’, that is when I joined his team. I need to thank Ria van Heeren for all the work she did, especially for convincing me it is better not to book my own flight tickets. It has also been a real pleasure to work with Yuki French. Yuki, doumo arigatou gozaimashita! I know you are very

happy that I decided to go and work in Japan and I am looking forward to seeing you there every now and then. I am very thankful to Yasunobu Nakamura, who invested a lot of time in translating the summary of this thesis into Japanese.

Of course, I also like to pay homage to Jorg Janssen and Henk Postma, my comrades of the ‘OiO Liberation Army’ (OLA). We fought a tough battle, but the victory was sweet. Besides Jorg, I shared my room through the last four years with Liesbeth Venema (‘Fryslân boppe’), Luca Canali (‘l’italiano di Bali’), Alexander ter Haar and Adrian Lupascu. I thank them for providing a pleasant base camp. Hannes Majer, ‘der schwyizerische Alpengeier’, was an enjoyable discussion partner on topics like female suffrage and gold reserves in Switzerland. In addition, he encouraged me to start writing a series of ‘The not-so-lonely Planet’ travel guides, which I see as my main task after finishing this thesis. Pablo Jarillo-Herrero, gracias por las clases de español. I would further like to thank Cees Dekker (‘Carbo Cees’), Alberto ‘Stromboli’ Morpurgo, Leonid Gurevich, Pieter Heij, Caspar van der Wal, Yann Kervennic (‘héros de la République’), Eugen Onac, Nathan Kemeling, Ewout Eijkelenboom, Hon Tin Man and Dionne Klein for the enjoyable time spent together.

Concerning the ‘theorists above’, I would like to express my special thanks to Yuli Nazarov, who has always been very much interested in what we, experimentalists from ‘down below’, showed him. Working with him has been most enjoyable and fruitful. I would also like to thank Maarten Wegewijs, Miriam Blaauboer, Daniel Huertas Hernando and Siggi Erlingsson for their theoretical input. Walter Hofstetter from the Universität Augsburg, now at Harvard University, I thank for his great contribution to the work on the two-stage Kondo effect. I am also grateful to Markus Büttiker who gave me the chance to join his group in Geneva for a short time.

An important part of my time as a Ph.D. student, I spent at NTT Basic Research Laboratories in Atsugi, Japan. I have not only been given the opportunity to learn how to fabricate devices, but also to learn the Japanese society from inside. I am very thankful to Toshimasa Fujisawa, who has invested a lot of time in teaching me the art of fabrication. He was also the one who taught me my first Japanese word: ‘komattana’, which means as much as ‘I am puzzled’ and which turned out to be a very useful phrase. I would like to thank Yoshiro Hirayama for his great hospitality and giving me a lot of freedom while working in his group. Kotaro Tsubaki, Guy Austing, Katsushi Hashimoto, Satoshi Sasaki, Toshiaki Hayashi, Hiroshi Yamaguchi, Yasuhiro Tokura, Tadashi Saku, Akihito Taguchi, Kiyoshi Kanisawa, Kyoichi Suzuki, Koji Muraki, Sen Miyashita, Sachiko Yoshida and Atsushi Kawaharazuka, doumo arigatou for all your help and making me feel at home in the Butsuden Group. In particular I like to thank Hashi for the many

enjoyable activities he organized and Hayashi-kun for teaching me the subtleties of Osaka dialect. I am very grateful to Seigo Tarucha, who played an important role in much of the work presented in this thesis. I am looking forward to joining his group at Tokyo University. Junichi Motohisa and Fumito Nakajima I thank for the very nice collaboration and the enjoyable time spent in both Delft and Hokkaido.

Finally, I would like to thank my family and friends, who closely followed and supported me. My parents, Arie and Joke, have always provided me with a warm ‘home port’ where I could drop my anchor. Yuko, thank you for everything. Although there may not be such a thing as a ‘royal’ road to learning, the constant support from all of you has made it at least a passable one. Let me finish with these three lines I found nearly ten years ago on the playground of the Störck Gymnasium in Saulgau, southern Germany:

Wissen ist Macht

Wir wissen nichts

Macht nichts.

Wilfred van der Wiel
Delft, November 2001



Contents

1	Introduction	1
1.1	Quantum dots	3
1.2	Kondo effect	6
1.3	Aharonov-Bohm effect	10
1.4	Fabrication process	12
1.5	Measurement technique	14
	References	15
2	Singlet-triplet transitions in a few-electron quantum dot	17
	References	23
3	Direct Coulomb and exchange interaction in artificial atoms	25
	References	34
4	The Kondo effect in the unitary limit	37
	References	45
5	Kondo effect in an integer-spin quantum dot	49
	References	57
6	Two-stage Kondo effect in a quantum dot at high magnetic field	61
	References	70
7	Double Quantum Dots in Series	73
7.1	Introduction	74
7.2	Stability diagram	76
7.2.1	Linear transport regime	76
7.2.2	Non-linear transport regime	87
7.3	Resonant tunneling	92
7.4	Magnetic field spectroscopy	99
7.5	Microwave spectroscopy	101

7.5.1	Two-level systems	102
7.5.2	Photon assisted tunneling in weakly coupled dots	105
7.5.3	Photon assisted tunneling in strongly coupled dots	110
7.6	Conclusions	118
	References	119
8	Spontaneous emission spectrum in double quantum dots	123
	References	131
9	Electro-magnetic Aharonov-Bohm effect in a 2D electron gas ring	133
	References	142
A	Electrostatic energy of quantum dots	145
A.1	Electrostatics of a system of N conductors	145
A.2	Single quantum dot	146
A.3	Double quantum dot	147
	References	148
	Summary	149
	Samenvatting	153
	Japanese summary	157
	Curriculum Vitae	161
	List of publications	163

Chapter 1

Introduction

‘Le macchine, diceva, sono effetto dell’arte, che è scimmia della natura, e di essa riproducono non le forme ma la stessa operazione.’¹

A bit more than one century ago, the young German Max Planck was strongly discouraged to study physics. Except for a few unsolved problems, physical knowledge was believed to be complete. Why should he waste his capabilities in a field that was going to be dead soon? Ironically, Planck became one of the pioneering contributors to a revolutionary new theory that has become known as quantum mechanics.

The optimism at the end of the nineteenth century was caused by the great success of Newton’s laws governing classical mechanics and Maxwell’s equations describing electromagnetism. Virtually all physical processes in our everyday macroscopic world can be described by these classical laws. It was in this period that one started to realize that classical theory was not applicable at the atomic scale. Whereas macroscopic phenomena are governed by the laws of classical mechanics, the microscopic world of electrons, nuclei, atoms and molecules can only be understood in terms of quantum mechanics.

To describe the behavior of electrons, for instance, quantum mechanics makes use of wave functions. A direct consequence of this approach is that there exists a fundamental uncertainty as to where to find an electron and with what velocity at a certain moment. Also it is possible that an electron interferes with itself when it can travel between two points in space along different trajectories. In some respects an electron thus behaves like a wave, whereas in other situations

¹ *‘Machines, zei hij, zijn een voortbrengsel van de kunst, welke de natuur nabootst, en zij nemen van haar niet de vormen over, maar de werking zelve.’* (*‘Machines, he said, are a product of art, which imitates nature, from which they borrow not the shapes, but its very functioning.’*) [1]

it exhibits particle-like behavior. This ambivalent nature is referred to as the particle-wave duality. Quantum mechanics has turned out to be one of the most successful physical theories in history and its predictions – how exotic they may be – are experimentally reproduced with high accuracy.

In the relatively young field of mesoscopic physics, the spheres of influence of the macroscopic world and microscopic world meet. Mesoscopic physics forms a part of solid state physics that explores semiconducting, metallic and superconducting systems with typical dimensions in the range 0.01 - 10 μm . Thanks to the great advances in lithographic technology – driven by the computer industry – fabrication of such structures has come within reach.

This thesis describes a series of experiments in mesoscopic semiconductor structures. For the greater part (chapters 2 to 8), electron transport through quantum dots is explored. Quantum dots are man-made sub-micron structures in a solid, typically consisting of 10^3 - 10^9 atoms and a comparable number of electrons [2]. In semiconductor quantum dots all electrons are tightly bound, except for a small number of free electrons, which can range from zero to several thousands. The free electrons are confined in all three dimensions leading to quantum effects that strongly influence electronic transport at low temperatures. In particular, confinement leads to the formation of a discrete energy spectrum, resembling that of atoms. This and other similarities have therefore led to the name ‘artificial atoms’ for quantum dots [3]. In section 1.1 quantum dots are discussed in more detail. Chapters 2 and 3 discuss the behavior of spin-singlet and spin-triplet states in vertical quantum dots and the analogy to Hund’s rule from atomic physics. The experiments in chapters 4 to 6 focus on the Kondo effect in quantum dots. The Kondo effect is a widely studied phenomenon in condensed matter physics arising from the coherent interaction between a localized impurity spin and surrounding electrons. As explained in section 1.2, quantum dots offer unprecedented opportunities for studying and tuning the Kondo effect. Double lateral quantum dots coupled in series form the subject of chapters 7 and 8. By coupling two quantum dots in series, a system is obtained with fundamentally different behavior and possibilities in comparison to a single dot. The experiment described in chapter 9 deals with the quantum interference of electron waves in a semiconductor Aharonov-Bohm ring interrupted by tunnel barriers. This geometry allows for studying the electron interference not only as function of magnetic field, but also as function of an electrostatic voltage. An introduction to the Aharonov-Bohm effect is given in section 1.3. In the last two sections of this introductory chapter, a brief overview is given of the fabrication process and measurement technique, respectively.

1.1 Quantum dots

Quantum dots are suitable devices to study the interplay of classical charging effects and quantum confinement. The quantum dots discussed in this thesis are defined in a 2-dimensional electron gas (2DEG) formed within a heterostructure of semiconductor materials. The 2DEG has a high electron mobility and low electron density (typically $10^5 - 10^6 \text{ cm}^2/\text{Vs}$ and $\sim 10^{15} \text{ m}^{-2}$, respectively). The low electron density results in a large Fermi wave length, and a large screening length, enabling to vary the 2DEG density with an electric field. Lithographically defined semiconductor quantum dots have the shape of a disk with a diameter as small as 50-100 nm, becoming of the same order of magnitude as the Fermi wavelength.

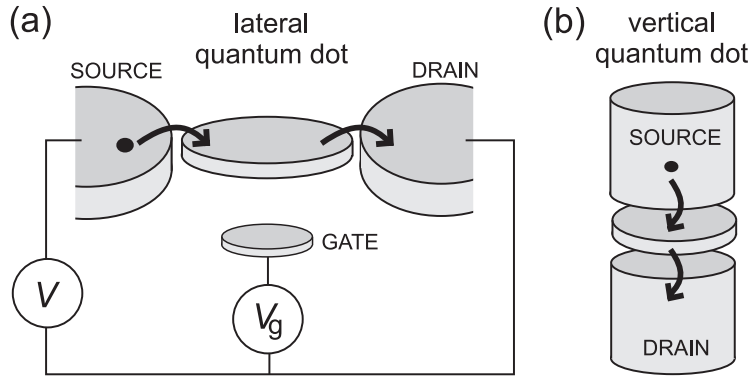


Figure 1.1: Schematic diagram of a quantum dot in a lateral geometry (a) and a vertical geometry (b). The quantum dot is represented by a disk, connected to source and drain contacts by tunnel junctions. For the lateral geometry the gate electrode is indicated, as well as the external voltage sources supplying the source drain voltage, V , and the gate voltage, V_g .

By attaching current and voltage probes to a quantum dot, it is possible to measure its electronic properties. In Fig. 1.1 two quantum dot geometries are shown schematically. The lateral dot in Fig. 1.1a is coupled to three terminals. Particle exchange can only occur with two of the terminals, as indicated by the arrows. These source and drain contacts connect the dot to the macroscopic world. The third terminal serves as a gate electrode and is used to change the dot's electrostatic energy. Whereas in the lateral geometry transport takes place in the plane of the 2DEG, in the vertical geometry of Fig. 1.1b transport occurs perpendicularly to that plane.

In the following discussion, two important assumptions are made. First, the Coulomb interactions among electrons in the dot, and between electrons in the

dot and those in the environment, are parameterized by a single, constant capacitance, C . This capacitance can be thought of as the sum of the capacitances between the dot and the left lead (source), C_L , the right lead (drain), C_R , and the gate, C_g : $C = C_L + C_R + C_g$. Second, the discrete energy spectrum can be described independently of the number of electrons on the dot.

Using these assumptions, known as the constant interaction (CI) model, the total energy of an N -electron dot with the source-drain voltage, V , applied to the left lead (and the right lead grounded), is given by (see Appendix A)

$$U(N) = \frac{[-|e|(N - N_0) + C_L V + C_g V_g]^2}{2C} + \sum_{n=1}^N E_n(B) \quad (1.1)$$

where $-|e|$ is the electron charge and N_0 the number of electrons in the dot at zero gate voltage, which compensates the positive background charge originating from the donors in the heterostructure. The terms $C_L V$ and $C_g V_g$ can change continuously and represent the charge on the dot that is induced by the bias voltage through the capacitance C_L and by the gate voltage, V_g , through the capacitance C_g . The last term of Eq. 1.1 is a sum over the occupied single-particle energy levels $E_n(B)$, which are separated by an energy $\Delta E_n = E_n - E_{n-1}$. The energy levels $E_n(B)$ are measured from the bottom of the conduction band and depend on the characteristics of the confinement potential. Note that, within the CI model, only these single-particle states depend on magnetic field, B .

The minimum energy for adding the N th electron to the dot is by definition the electrochemical potential of the dot:

$$\begin{aligned} \mu_{dot}(N) &\equiv U(N) - U(N-1) = \\ &= (N - N_0 - \frac{1}{2})E_C - \frac{E_C}{|e|}(C_L V_L + C_g V_g) + E_N \end{aligned} \quad (1.2)$$

where $E_C = e^2/C$ is the charging energy. The first two terms describe the electrostatic contribution $-|e|\varphi_N$ with φ_N the electrostatic potential of the N -electron dot. The last term, E_N , represents the chemical contribution $\mu_{ch}(N)$. Hence, $\mu_{dot}(N) = -|e|\varphi_N + \mu_{ch}(N)$. Electron transport through the dot is possible when μ_{dot} lies between μ_L and μ_R of the leads, i.e. $\mu_L \geq \mu_{dot} \geq \mu_R$ with $-|e|V = \mu_L - \mu_R$ (see Fig. 1.2). In the linear transport regime ($V \approx 0$), the N th Coulomb

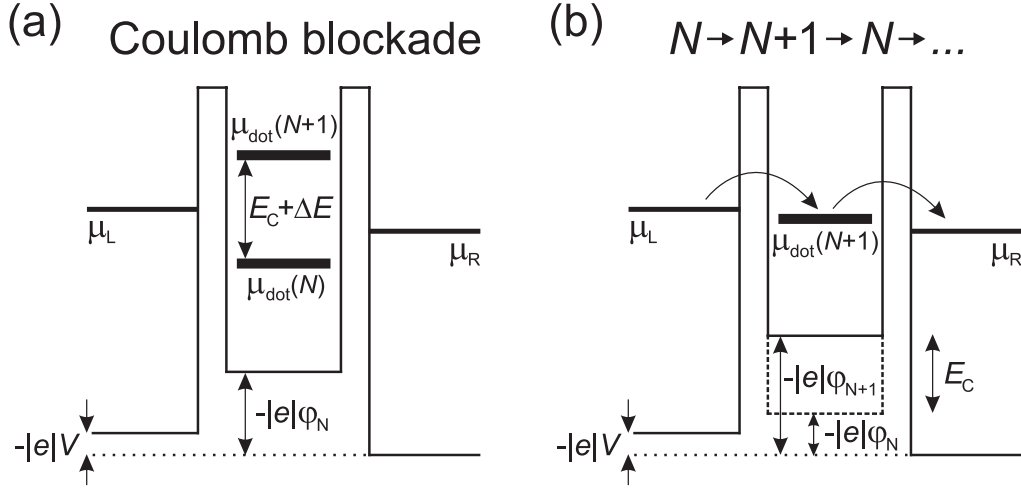


Figure 1.2: Schematic diagrams of the potential landscape of a quantum dot. The minimum energy needed to add an electron to the left (right) lead equals the electrochemical potential $\mu_{L(R)}$. The electrochemical potentials of the leads are related to the bias voltage, V , by $-|e|V = \mu_L - \mu_R$. (a) The electrochemical potential for adding the N th electron to the dot, $\mu_{dot}(N)$, lies below the lowest electrochemical potential of the leads (i.e. μ_R). The electrochemical potential for adding the next electron, $\mu_{dot}(N+1)$, is separated from $\mu_{dot}(N)$ by the addition energy, $E_C + \Delta E$, which is higher than μ_L so that the $(N+1)$ th electron cannot enter the dot. In this configuration the number of electrons on the dot, N , is fixed and transport through the dot is blocked (Coulomb blockade). The electrostatic potential of the dot is $-|e|\varphi_N$. (b) The addition of the $(N+1)$ th electron is allowed, since $\mu_{dot}(N+1)$ lies within the applied bias window. In this configuration the number of electrons on the dot alternates between N and $N+1$, resulting in electron transport through the dot.

peak is a direct measure of the lowest possible energy state of the N -electron dot, i.e. the ground state electrochemical potential. The change in electrochemical potential when at fixed voltages an electron is added to the dot, is called the addition energy and is given by

$$\begin{aligned} \Delta\mu_{dot}(N) &= \mu_{dot}(N+1) - \mu_{dot}(N) = U(N+1) - 2U(N) + U(N-1) \\ &= E_C + \Delta E. \end{aligned} \quad (1.3)$$

The addition energy consists of a purely electrostatic part, the charging energy E_C , and the energy spacing between two discrete quantum levels, ΔE . Note that in the case that two electrons are added to the same (spin-)degenerate level,

ΔE can be zero. Atomic energies related to the addition energy are defined by $A = U(N) - U(N + 1)$ for the electron affinity and $I = U(N - 1) - U(N)$ for ionization energy [4], so that $\Delta\mu(N) = I - A$.

An electron tunneling onto the dot leads to an increase of the electrostatic energy by the charging energy $E_C = e^2/C$. The charging energy becomes important when it exceeds the thermal energy, $k_B T$, and when the barriers are sufficiently opaque such that the electrons are located either in the reservoirs or in the dot. The latter condition implies that quantum fluctuations in the number of electrons on the dot must be sufficiently small. A lower bound for the tunnel resistances R_t of the barriers can be found from the Heisenberg uncertainty principle. The typical time Δt to charge or discharge the dot is given by the RC -time. This yields $\Delta E \Delta t = (e^2/C) R_t C > h$. Hence, R_t should be much larger than the quantum resistance h/e^2 to sufficiently reduce the uncertainty in the energy. In the next section the Kondo effect in quantum dots is discussed, a phenomenon that occurs when the tunnel barriers are made rather transparent.

1.2 Kondo effect

Normally, the electrical resistance of a pure metal decreases as its temperature is lowered (Fig. 1.3). The electrons can travel through a metallic crystal more easily when the vibrations of the atoms are small. The resistance typically saturates around 10 K, due to static effects in the metal. The value of the low-temperature resistance depends on the number of defects in the material. However, the temperature dependence changes considerably when a small concentration of magnetic atoms, such as cobalt, is added to the metal. Rather than saturating at low temperature, the resistance increases as the temperature is lowered further (see dashed curve in Fig. 1.3). Since the early 1930s there have been many observations of this anomalous temperature dependence of the resistance of metals [5]. This behavior, however, was not explained earlier than in 1964, when the Japanese theorist Jun Kondo provided an explanation [6, 7]. Since then, the phenomenon has been referred to as the Kondo effect.

The Kondo effect in metals occurs because below a certain temperature, which is called the Kondo temperature, T_K , the mobile electrons in the host metal tend to screen the non-zero total spin of the electrons in the magnetic impurity atom. In the simplest model of a magnetic impurity, introduced by Anderson in 1961 [8], there is only one electron level with energy ε_0 and the impurity spin is $1/2$. The z -component is fixed as either ‘spin up’ or ‘spin down’. However, so-called exchange processes can effectively flip the impurity spin, while simultaneously

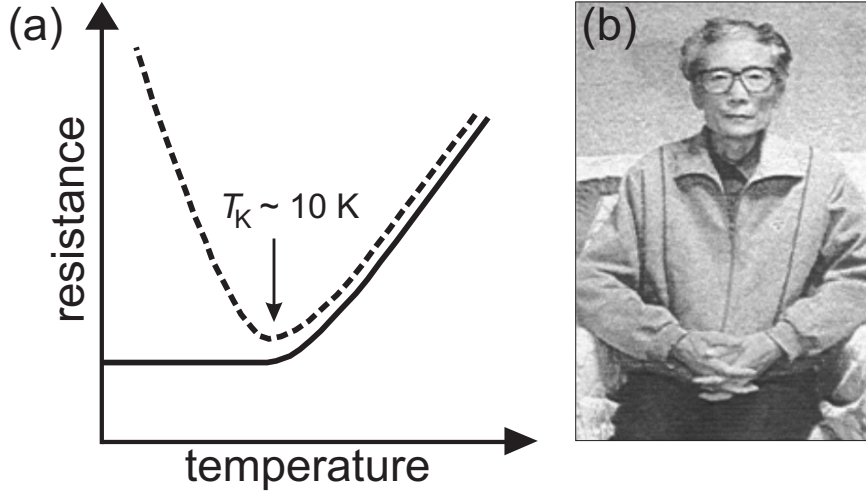


Figure 1.3: (a) Schematic temperature dependence of the resistance of pure metals (solid curve) and metals with a small concentration of magnetic impurity atoms (dashed curve). The latter curve shows a minimum around the Kondo temperature, T_K . (b) Jun Kondo, picture Asahi Shimbun.

creating a spin excitation in the Fermi sea. This spin exchange changes the energy spectrum of the system. When many such processes are added coherently, a new state – the Kondo resonance – is generated with the same energy as the Fermi level. Such a resonance is very effective at scattering electrons with energies close to the Fermi level. Since the same electrons are responsible for the low-temperature conductivity of a metal, the strong scattering contributes greatly to the resistance. As many electrons need to be involved, the Kondo effect is a many-body phenomenon. The whole system – that is, the magnetic impurity atom plus its surrounding electrons – forms a spin singlet. The energy scale for this singlet state is the Kondo temperature.

A quantum dot connected to source and drain leads, can nicely mimic the above situation of a localized spin impurity in a Fermi sea. Therefore, the Kondo effect was expected to occur in quantum dot systems as well [9, 10]. However, there is an important difference between metal and quantum dot systems. In a metal, electrons are described by plane wave functions. Scattering from impurities mixes electron waves with different momenta. This momentum transfer increases the resistance. In a quantum dot, on the contrary, all the electrons have to travel through the device, as there is no electrical path around it. In this case, the Kondo resonance makes it easier for states belonging to the two opposite leads to mix. This mixing process increases the conductance, that is the

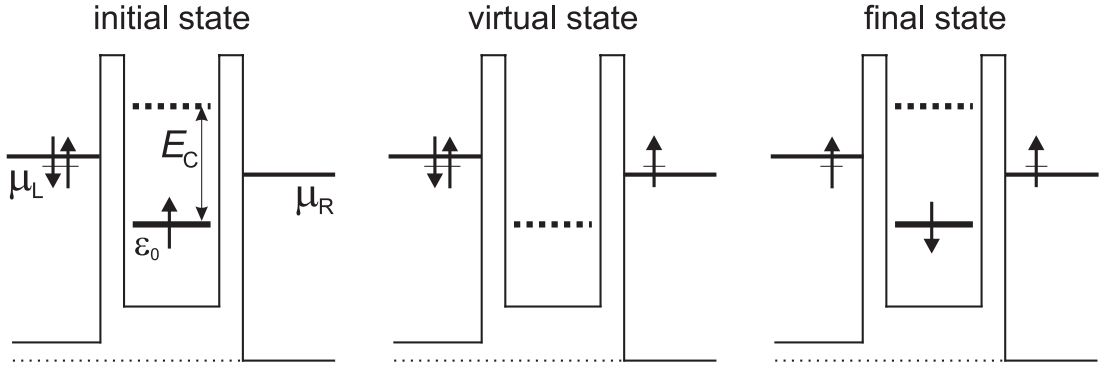


Figure 1.4: The Anderson model of a magnetic impurity applied to a single level quantum dot connected to source and drain leads. The level has an energy $-\epsilon_0$ ($\mu_L - \mu_R \approx 0$). By going through the different states, the dot spin can effectively be flipped, as explained in the text.

Kondo effect produces the *opposite* behavior in a quantum dot to that of a bulk metal. Figure 1.4 shows the Anderson model of a magnetic impurity, applied to a single level quantum dot connected to source and drain leads. The level has an energy ϵ_0 below the Fermi energy of the leads and is initially occupied by one spin-up electron (see leftmost diagram of Fig. 1.4). Adding another electron is prohibited by the charging energy, E_C , while it would at least cost $|\epsilon_0|$ to remove the electron. By virtue of quantum uncertainty, the spin-up electron can momentarily tunnel out of the dot, leaving the dot-lead system in a classically forbidden virtual state (see middle diagram of Fig. 1.4). If the spin-up electron is replaced by a spin-down electron from the leads, as in the rightmost diagram of Fig. 1.4, the dot spin has effectively been flipped. Many such events combine to produce the Kondo effect in quantum dots, which leads to the formation of an extra resonance at the Fermi level of the leads. The above spin-flip processes, and hence the Kondo effect, are favored by a strong coupling between the dot and the leads. The Kondo temperature is related to the parameters of the Anderson model by

$$T_K = \frac{\sqrt{\Gamma E_C}}{2} e^{\pi \epsilon_0 (\epsilon_0 + E_C) / \Gamma E_C} \quad (1.4)$$

where Γ is the width of the dot level, which is broadened by electrons tunneling to and from it. So the parameters that characterize the single-level dot system – E_C , ϵ_0 and Γ – can be replaced by a single energy scale, T_K . The advantage of quantum dots in studying the Kondo effect is that the parameters that determine the Kondo temperature, can be easily changed by adjusting the voltages on the

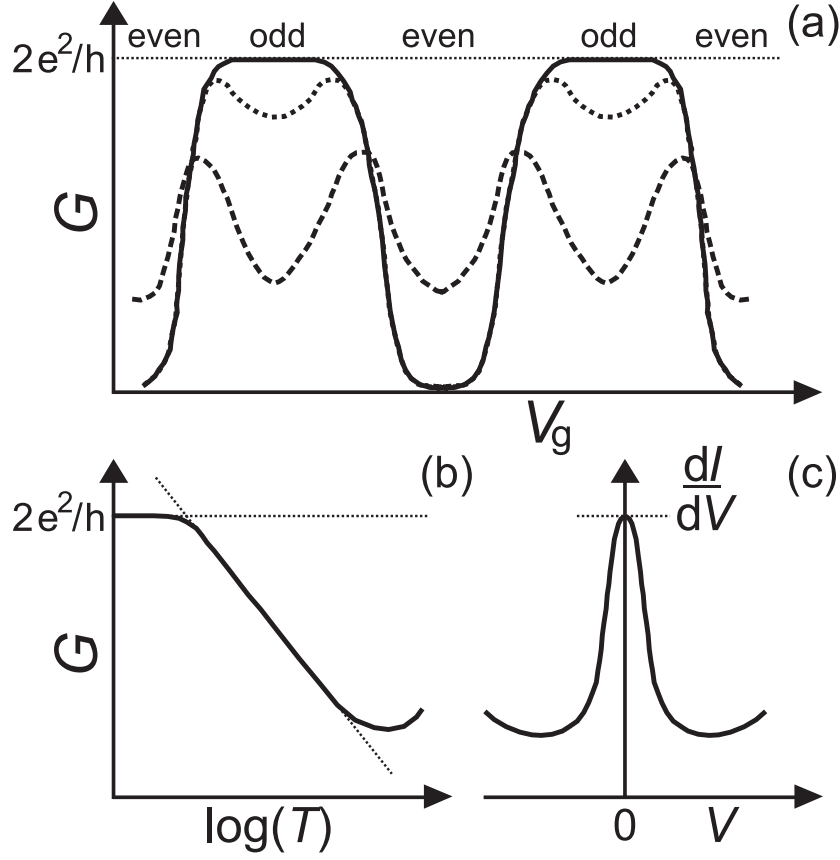


Figure 1.5: Schematic representation of the main characteristics of electron transport through a quantum dot strongly coupled to the leads, showing the Kondo effect. (a) Linear conductance, G , versus gate voltage, V_g . The solid curve is for $T \ll T_K$, the dotted curve for $T \lesssim T_K$ and the dashed curve for $T \gg T_K$. The Kondo effect only occurs for odd electron number, resulting in the odd-even asymmetry between the different Coulomb valleys. (b) In the Kondo valleys the conductance increases logarithmically with lowering temperature, saturating at $2e^2/h$. (c) The Kondo resonance leads to a zero-bias resonance in the differential conductance, dI/dV , versus bias voltage, V .

gates.

The main characteristics of electron transport through a quantum dot with spin-degenerate levels, coupled strongly to the leads, are schematically depicted in Fig. 1.5. For an odd number of electrons on the dot, the total spin of the dot, S , is necessarily non-zero and in the simplest case $S = 1/2$, like in Fig. 1.4. However, for an even electron number on the dot – again in the simplest scenario – the upper level is occupied by one spin-up electron and one spin-down electron. A dot with an even number of electrons therefore has $S = 0$ and the Kondo effect

is not expected to occur. This ‘even-odd-asymmetry’ results in the temperature dependence of the linear conductance, G , as shown in Fig. 1.5a. In the ‘odd’ or ‘Kondo’ Coulomb valleys the conductance increases as the temperature is lowered, due to the Kondo effect. In the ‘even’ valleys, on the contrary, the conductance decreases, due to a decrease of thermally excited transport through the dot. The temperature dependence of the conductance in the Kondo valleys is shown in Fig. 1.5b. The conductance increases logarithmically with decreasing temperature [9], and saturates at a value $2e^2/h$ at the lowest temperatures [10, 11]. Although the dot has two tunnel barriers and the charging energy tends to block electrons from tunneling into or out of it, the Kondo effect makes that electrons are transmitted perfectly through the dot. This complete transparency of the dot has led to the name ‘unitary limit’ of conductance. The first experimental observation of this limit in quantum dots is reported in chapter 4. The Kondo resonance at the Fermi level of the leads manifests itself as a zero-bias resonance in the differential conductance, dI/dV , versus V , as shown in Fig. 1.5c. The full width at half maximum of this resonance gives an estimate for the Kondo temperature.

Chapter 4 shows that a quantum dot having an odd number of electrons and a spin $S = 1/2$, can be well described in terms of the Anderson impurity model. However, in chapters 5 and 6 it is found that quantum dots can also push research into the Kondo effect in new directions, where artificial structures can be exploited in regimes that are inaccessible with magnetic impurities in metals.

1.3 Aharonov-Bohm effect

In their paper ‘*Significance of Electromagnetic Potentials in the Quantum Theory*’, Aharonov and Bohm predicted in 1959 that if a quantum-mechanical wave, such as a single-electron wave, is split into two partial waves enclosing a region of magnetic field, there will be a phase shift between the two waves [13]. Hence, if they later recombine, the interference between them depends on the amount of enclosed magnetic flux. Precisely speaking, it is not the magnetic field, B , that is important, but the magnetic vector potential, \mathbf{A} . The effect also occurs if the particle wave travels in a region of zero magnetic field, as long as within the path there is a region containing magnetic flux. Similarly, an electrostatic potential, V , contributes to the phase even in absence of an electric field, \mathbf{E} . The Aharonov-Bohm effect can be measured in electron transport through a mesoscopic metal or semiconducting ring (see Fig. 1.6a). The phase, ϕ , accumulated

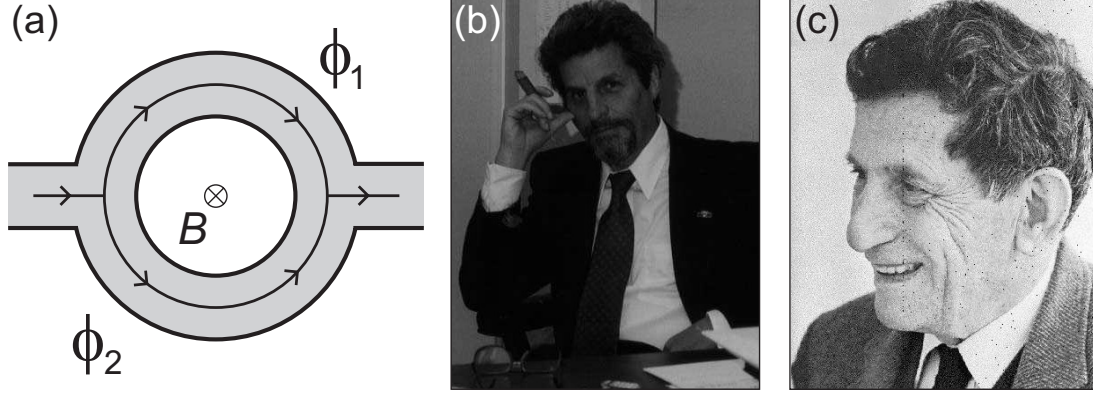


Figure 1.6: (a) Schematic picture of an Aharonov-Bohm ring. A single-electron wave splits and recombines, enclosing a magnetic flux. The accumulated phase along the upper (lower) arm, ϕ_1 (ϕ_2), is affected by the electrostatic potential, V , and the vector potential, \mathbf{A} . (b) Yakir Aharonov (1932), picture University of South Carolina. (c) David Joseph Bohm (1917-1992), picture MUC.DE-Verein München.

by the the electron wave, is given by

$$\begin{aligned}\phi &= \frac{2\pi}{h} \int (m\mathbf{v} + |e|\mathbf{A}) \cdot d\mathbf{s} = 2\pi \frac{|e|}{h} \int \left(\int \nabla V dt + \mathbf{A} \right) \cdot d\mathbf{s} \\ &= 2\pi \frac{|e|}{h} \left[\int V dt + \int \mathbf{A} \cdot d\mathbf{s} \right]\end{aligned}\quad (1.5)$$

with $\mathbf{E} = -\nabla V$, $\mathbf{B} = \nabla \times \mathbf{A}$, and m and \mathbf{v} the electron mass and velocity, respectively. The phase difference between the trajectories through the two arms of the ring is (see Fig. 1.6a)

$$\begin{aligned}\Delta\phi = \phi_1 - \phi_2 &= 2\pi \frac{|e|}{h} \left[\int_0^{t_0} \Delta V dt + \oint \mathbf{A} \cdot d\mathbf{l} \right] \\ &= 2\pi \frac{|e|}{h} \Delta V t_0 + 2\pi \frac{|e|}{h} BS\end{aligned}\quad (1.6)$$

where ΔV is the difference in electrostatic potential between the upper and lower arm, t_0 the time between splitting and recombination of the single-electron wave, and S the enclosed area of the ring. The first experimental observation of the Aharonov-Bohm effect in a single diffusive metal ring was made by Webb *et al.* in 1985 [14]. In this and later experiments, oscillations of the conductance as a function of B were observed with a period $h/(eS)$. The Aharonov-Bohm

experiments prove that electron waves preserve their phase coherence in these mesoscopic rings. In chapter 9, an experiment is presented in which both the magnetic and electrostatic contribution to the Aharonov-Bohm effect are controlled. In particular, electron dephasing at finite voltage and magnetic field is discussed.

1.4 Fabrication process

For the devices discussed in this thesis use is made of GaAs/AlGaAs heterostructures. A typical example of such a heterostructure is shown in Fig. 1.7. The 2-dimensional electron gas is situated at the interface of GaAs and AlGaAs, typically 100 nm below the surface. The electron density of the 2DEG is determined by the n-type doping (Si) in the n-AlGaAs layer. In order to confine electrons laterally, the 2DEG can be locally depleted, using metal gate electrodes on top of the heterostructure or using etched trenches.

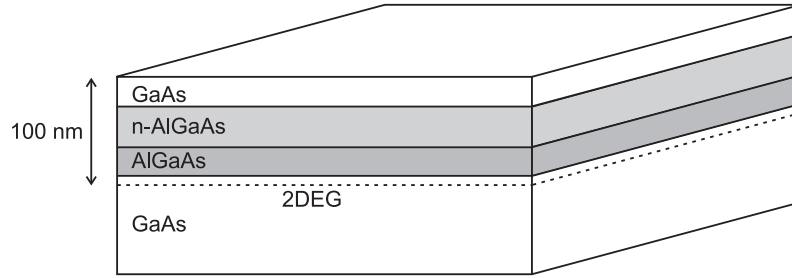


Figure 1.7: Schematic picture of a GaAs/AlGaAs heterostructure (not on scale). The position of the 2-dimensional electron gas (2DEG) is indicated by the dashed line.

The fabrication procedure for evaporating metal gates is schematically depicted in Fig. 1.8a-d. First, a layer of organic resist (poly-methyl-methacrylate, PMMA) is spun on top of the heterostructure. The gate pattern is defined by electron beam writing in the electron-sensitive resist (Fig. 1.8a). At the places where the resist is exposed, the polymers are broken. The exposed parts are removed by a developer (solution of methyl isobutyl ketone, MIBK, and iso-propyl alcohol, IPA), as shown in Fig. 1.8b. Note that there is some undercut of the PMMA layer. This undercut is caused by the significant electron scattering at the interface between GaAs and PMMA during the electron beam exposure. In the next step, metal is evaporated, which only makes contact to the heterostructure at the places where the resist has been exposed and removed (Fig. 1.8c). In our devices, the metal gates are fabricated by evaporating a layer of Ti and a

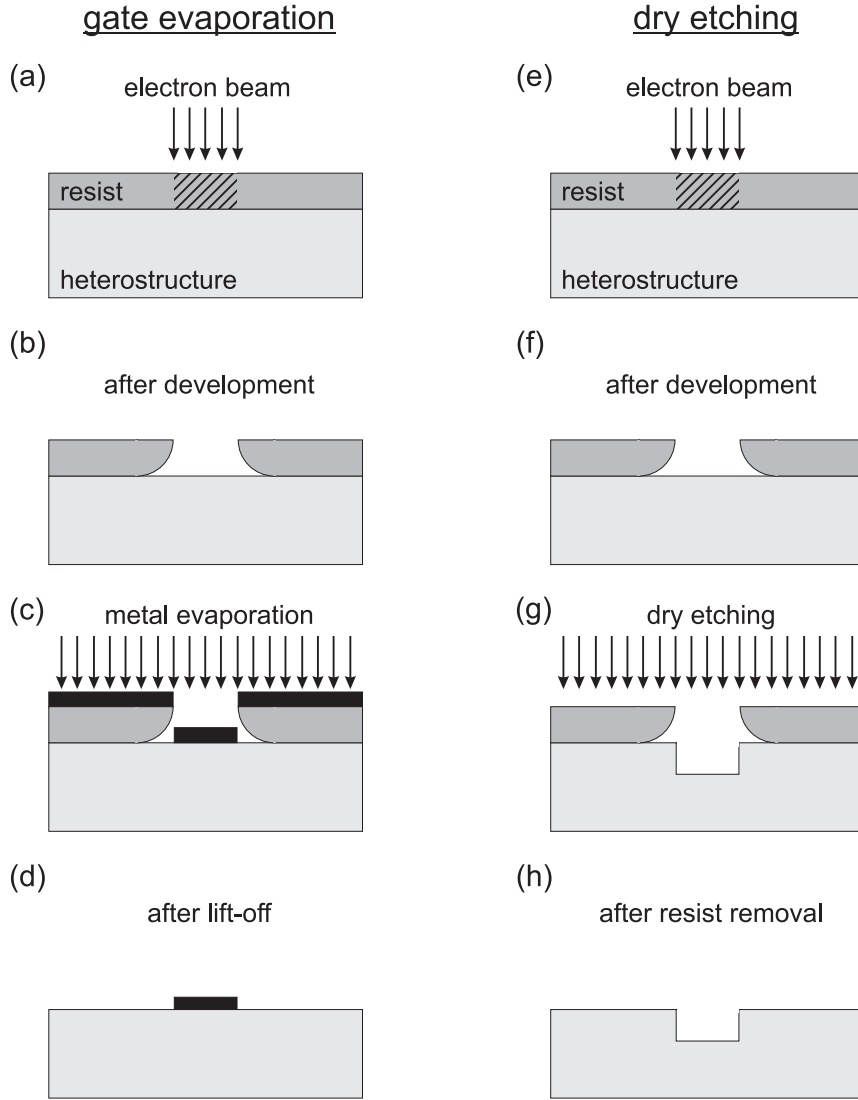


Figure 1.8: Schematic pictures showing the fabrication procedure for evaporating metal gate electrodes (a-d) and dry etching (e-h).

layer of Au consecutively. The Ti layer serves as a ‘sticking’ layer. The last step is the removal of the remaining resist by acetone. Thus the metal on top of the resist is removed as well, the so-called ‘lift-off’ (Fig. 1.8d). The lift-off process is facilitated by the undercut in the resist layer.

The first two fabrication steps for defining an etched pattern are identical to the first two steps of the metal evaporation (Fig. 1.8e,f). In Fig. 1.8g dry etching is illustrated. The dry etching of the devices discussed in this thesis, is done by focused ion beam (FIB) and electron cyclotron resonance (ECR) etching. The

last step is again the removal of the remaining resist by acetone (Fig. 1.8h).

For measuring electron transport through the 2DEG, ohmic contacts are connected to it by evaporating AuGeNi and annealing at ~ 400 degrees Celsius for 60 seconds.

1.5 Measurement technique

In order to observe quantum-mechanical phenomena like discrete level spectra, the Kondo effect and the Aharonov-Bohm effect, and to observe the effect of the charging energy on electron transport, it is necessary to perform our experiments at low temperature. We make use of a dilution refrigerator with a base temperature of 10 mK. However, the effective electron temperature in our devices is higher, but typically below 50 mK, because of various heating mechanisms, as briefly discussed below.

The noise introduced by the measurement electronics forms one source of heating. Copper powder filters are an important means to attenuate the noise. They consist of a long, thin resistive metal wound within a tube with copper powder. The filters are installed at low temperature to minimize the thermal noise of the resistors contained in them. The filters are integrated with the sample holder such that all sample wires are shielded once they are filtered.

Another source of heating is the interference picked up by the wires connecting the measurement electronics to the device. In order to reduce sources of interference, loops in the wiring are avoided to minimize magnetic pick-up, and the wires are shielded and well fastened to prevent them from acting as antennas and from vibrating, respectively. In addition, it is important that the circuit is grounded at only one place and that all shields are connected to this reference point by a low impedance.

For the microwave experiments we make use of a coaxial cable to transport power from a microwave source, outside the fridge, to the sample. From room temperature to the 1K-pot, a 0.085 inch semi-rigid Be-Cu (inner and outer conductor) coaxial cable is used. From the 1K-pot to the mixing chamber, we use a 0.085 inch semi-rigid stainless steel (inner and outer conductor) coax. From the mixing chamber to the sample, various types of low attenuation semi-rigid or flexible coaxial cable can be used, since here the thermal conductivity is no longer a constraint. Finally, the coaxial cable is capacitively coupled (typically through a 10 pF capacitor) to one of the gate electrodes of the device.

References

- [1] U. Eco, *Il nome della rosa*, Gruppo Editoriale Fabbri, Bompiani, Sonzogno, Etas S.p.A. 1980.
- [2] L.P. Kouwenhoven, C.M. Marcus, P.L. McEuen, S. Tarucha, R.M. Westervelt and N.S. Wingreen, *Electron transport in quantum dots*, in Mesoscopic Electron Transport, edited by L.L. Sohn, L.P. Kouwenhoven and G. Schön, (Kluwer, Series E **345**, 1997), p.105-214.
- [3] M. Kastner, Physics Today **46**, 24 (1993).
- [4] G.J. Iafrate, K. Hess, J.B. Krieger and M. Macucci, Phys. Rev. B **52**, 10737 (1995).
- [5] W.J. de Haas, J.H. de Boer and G.J. van den Berg, Physica **1**, 1115 (1934).
- [6] J. Kondo, Prog. Theor. Phys. **32**, 37 (1964).
- [7] L.P. Kouwenhoven and L.I. Glazman, Physics World **14**, 33 (2001).
- [8] P.W. Anderson, Phys. Rev. **124**, 41 (1961).
- [9] L.I. Glazman and M.E. Raikh, JETP Lett. **47**, 452 (1988).
- [10] T.K. Ng and P.A. Lee, Phys. Rev. Lett. **61**, 1768 (1988).
- [11] A. Kawabata, J. Phys. Soc. Jpn. **60**, 3222 (1991).
- [12] F.D.M. Haldane, Phys. Rev. Lett. **40**, 416 (1978).
- [13] Y. Aharonov and D. Bohm, Phys. Rev. **115**, 485 (1959).
- [14] R.A. Webb, S. Washburn, C.P. Umbach and R.B. Laibowitz, Phys. Rev. Lett. **54**, 2696 (1985).

Chapter 2

Singlet-triplet transitions in a few-electron quantum dot

W.G. van der Wiel, T.H. Oosterkamp, J.W. Janssen,
L.P. Kouwenhoven, D.G. Austing, T. Honda and S. Tarucha

We have measured spin-singlet – spin-triplet (ST) transitions in a vertical quantum dot containing up to four electrons. Current through the dot is measured as a function of gate voltage and magnetic field (0-9 Tesla) at both small and large source drain voltages. The ST transitions cannot be explained within the framework of single-particle states in combination with a constant Coulomb interaction. Taking into account exchange interaction and a magnetic field dependent direct Coulomb interaction is essential for describing the observed ST transitions.

This chapter has been published in *Physica B* **256-258**, 173 (1998).

Quantum dots are often referred to as artificial atoms, because of the many similarities with real atoms [1]. The relatively large dimensions of quantum dots (~ 100 nm) make that experimentally accessible magnetic field regimes (up to ~ 20 Tesla) correspond to regimes of the order 10^6 Tesla for real atoms. The constant interaction (CI) model has been successful in describing transport through quantum dots [2, 3]. The CI model assumes that the Coulomb interactions between electrons are independent of, for instance, the magnetic field, B , so that changes in the observed ground state energies are fully ascribed to changes in the single-particle energies. While the CI model is very useful at small magnetic fields ($B \lesssim 1$ T) [2], at larger B it is essential to include a varying Coulomb interaction [4]. Here, we discuss this non-constant interaction regime for dots with one to four electrons and B between 0 and 9 T. In particular, we describe the singlet-triplet (ST) transition induced by a magnetic field for a dot with two electrons.

Our vertical quantum dot consists of a sub-micrometer pillar fabricated in an In/Al/GaAs double barrier heterostructure and is described in Refs. [5, 6]. Source and drain wires are connected to the doped top and substrate contacts. Previous measurements have shown that the lateral confinement potential has the form of a circular-symmetric, harmonic potential [4, 5]. The diameter of the dot can be reduced by a gate voltage, V_g , from a few hundred nanometers to zero, thereby decreasing the electron number, N , from ~ 70 to zero. The measurements have been performed in a dilution refrigerator at 100 mK.

We first discuss the energy spectrum of a few-electron quantum dot. The Darwin-Fock (DF) energy spectrum for non-interacting electrons in a quantum dot with a parabolic confinement potential $V(r) = \frac{1}{2}m^*\omega_0^2r^2$ is given by [7]

$$E_{n,l} = (2n + |l| + 1)\hbar\sqrt{\frac{1}{4}\omega_c^2 + \omega_0^2} - \frac{1}{2}l\hbar\omega_c \quad (2.1)$$

with $m^* = 0.06m_0$ is the effective mass in GaAs, ω_0 the harmonic oscillator frequency, $\omega_c = eB/m^*$ the cyclotron frequency, n the radial quantum number, and l the angular momentum number. For a two-electron dot, we only consider the two lowest single-electron states, $E_{0,0}$ and $E_{0,1}$, which are relevant to the discussion here. For any value of B , $E_{0,0} < E_{0,1}$ and hence the two electrons both occupy the state $E_{0,0}$ with opposite spin; i.e. a singlet, $S = 0$ state. Including the Zeeman energy, we obtain

$$\begin{aligned} E_{0,0} &= \hbar\sqrt{\frac{1}{4}\omega_c^2 + \omega_0^2} \pm \frac{1}{2}g^*\mu_B B \\ E_{0,1} &= 2\hbar\sqrt{\frac{1}{4}\omega_c^2 + \omega_0^2} - \frac{1}{2}\hbar\omega_c \pm \frac{1}{2}g^*\mu_B B \end{aligned} \quad (2.2)$$

with $g^* = -0.44$ the effective Landé factor in GaAs and μ_B the Bohr magneton. Due to the Zeeman terms, we expect a crossing between $E_{0,0,\uparrow}$ and $E_{0,1,\downarrow}$ beyond which the two electrons are spin-polarized, i.e. an ST transition. Note that we use the symbol ‘ \uparrow ’ (‘ \downarrow ’) for the spin state in which the z -component of the spin is aligned with (opposite to) the direction of B . For $\hbar\omega_0 = 5.6$ meV, we predict an ST transition driven by the Zeeman energy at $B = 25$ T. Note that for this

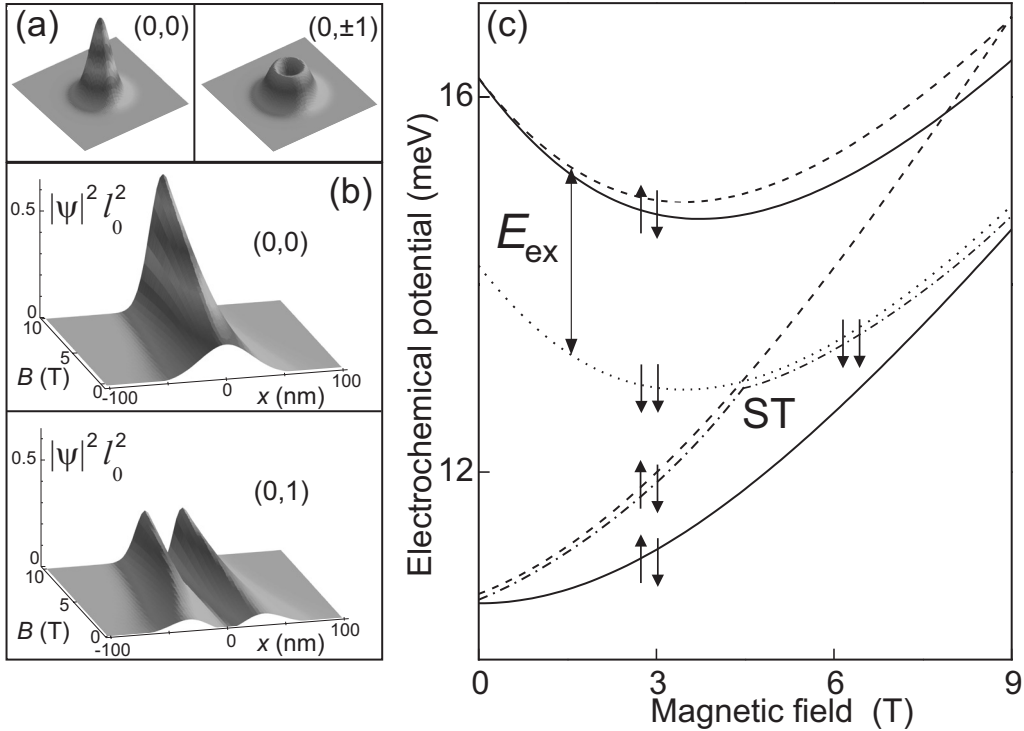


Figure 2.1: (a) Calculated spatial distribution functions $|\psi_{n,l}(r, \varphi)|^2$ for $(n, l) = (0, 0)$ and $(0, \pm 1)$. (b) Magnetic field (B) dependence of the distribution functions of (a) ($\hbar\omega_0 = 3$ meV). The vertical axes are normalized by $l_0^2 = \hbar/m^* \sqrt{\omega_0^2 + \omega_c^2/4}$. (c) Electrochemical potential $\mu(2)$ of a two-electron dot versus B ($\hbar\omega_0 = 5.6$ meV, charging energy, $E_C(B = 0) = 5$ meV). The lower solid curve represents the CI ground-state electrochemical potential $\mu^{\uparrow\downarrow}(2) = E_{0,0} + E_C$ (spins indicated by arrows), whereas the upper solid curve corresponds to the excited state, $\mu^{\uparrow\downarrow, ES}(2) = E_{0,1} + E_C$. The dashed lines schematically represent the situation of B -dependent Coulomb interaction. The dashed lines grow faster than the solid ones. The rise of the lower dashed line is faster, due to the larger overlap of states when both electrons are in the ground-state. The upper dashed curve with subtraction of a constant exchange energy, E_{ex} , results in the dotted curve $\mu^{\uparrow\downarrow}(2) = E_{0,1} + E_C(B) - E_{ex}$. $\mu^{\uparrow\downarrow}(2)$ and $\mu^{\uparrow\downarrow}(2)$ cross at $B \simeq 4.5$ T. The ground state before and after the singlet-triplet (ST) transition is indicated by a dashed-dotted line.

estimate electron-electron interactions are not taken into account. As we will argue below, the Coulomb interactions between the two electrons drive the ST transition to much lower B .

The interdependence of electron-electron interactions and single-particle states becomes important when a magnetic field changes the size of the electron states. For instance, the size of the DF-states shrinks in the radial direction at larger B . To illustrate this, we first show the probability functions $|\psi_{n,l}(r, \varphi)|^2$ for the $E_{0,0}$ and $E_{0,\pm 1}$ states at $B = 0$ in Fig. 2.1a [3]. Figure 2.1b shows cross sections of $|\psi_{n,l}(r, \varphi)|^2$ versus B . Increasing B , the distribution function shrinks in the radial direction. When two electrons both occupy the $E_{0,0}$ state, the average distance between them decreases with B and hence the Coulomb interaction increases. At some magnetic field it is energetically favorable if one of the two electrons makes a transition to a state with a larger radius (i.e. from $l = 0$ to $l = 1$), thereby increasing the average distance between the two electrons. This transition occurs when the gain in Coulomb energy exceeds the costs in single-particle energy. So, beside the Zeeman energy, the shrinking of wavefunctions favors a transition in angular momentum.

Numerical calculations by Wagner *et al.* [8] have predicted these ST transitions. In our discussion here, we generalize the CI model in order to keep track of the physics that gives rise to the ST transition. The electrochemical potential of a dot containing N electrons is defined as $\mu(N) \equiv U(N) - U(N - 1)$ where $U(N)$ is the total energy of the dot. For an $N = 1$ dot, $U^\uparrow(1) = E_{0,0}$ is the exact ground state energy. In the CI model, $U^{\uparrow\downarrow}(2) = 2E_{0,0} + E_C$, so that the ground-state electrochemical potential is $\mu^{\uparrow\downarrow}(2) = E_{0,0} + E_C$. Note that the Coulomb interactions are assumed to be described by a constant charging energy, E_C . The first excited state is $U^{\uparrow\downarrow, ES}(2) = E_{0,0} + E_{0,1} + E_C$ and $\mu^{\uparrow\downarrow, ES}(2) = E_{0,1} + E_C$. The solid lines in Fig. 2.1c show $\mu^{\uparrow\downarrow}(2)$ and $\mu^{\uparrow\downarrow, ES}(2)$, where we neglect the small contribution of the Zeeman energy.

The next level of approximation is to include the magnetic field dependence of the charging energy to account for the shrinking wavefunctions. The dashed curves in Fig. 2.1c rise somewhat faster than the solid curves, reflecting the B -dependence of the charging energy, $E_C(B)$. These dashed lines are schematic curves and do not result from calculations.

When both electrons occupy the $E_{0,0}$ state their spins must be anti-parallel. However, if one electron occupies $E_{0,0}$ and the other $E_{0,1}$, the two electrons can also take on parallel spins; i.e. total spin $S = 1$. In this case, the Coulomb interaction is reduced by an exchange energy, E_{ex} , and the corresponding electrochemical potential becomes $\mu^{\uparrow\downarrow}(2) = E_{0,1} + E_C(B) - E_{ex}$; see the dotted line in Fig. 2.1c. The exchange energy is due to a deformation of the distribution

functions of Fig. 2.1a for electrons with parallel spin, which yields a reduction of the Coulomb repulsion. Importantly, $\mu^{\uparrow\downarrow}(2)$ and $\mu^{\downarrow\downarrow}(2)$ cross at $B \simeq 4.5$ T for the parameters chosen in Fig. 2.1c. So, while for $B < 4.5$ T the ground state energy corresponds to two electrons with anti-parallel spins in the lowest single-particle state, for $B > 4.5$ T the ground state has contributions from two single-particle states and has total spin $S = 1$ (the two-electron ground state is indicated by a dashed-dotted line in Fig. 2.1c). Thus, while the Zeeman-driven transition would occur at 25 T, the electron-electron interactions push the ST transition to 4.5 T [9].

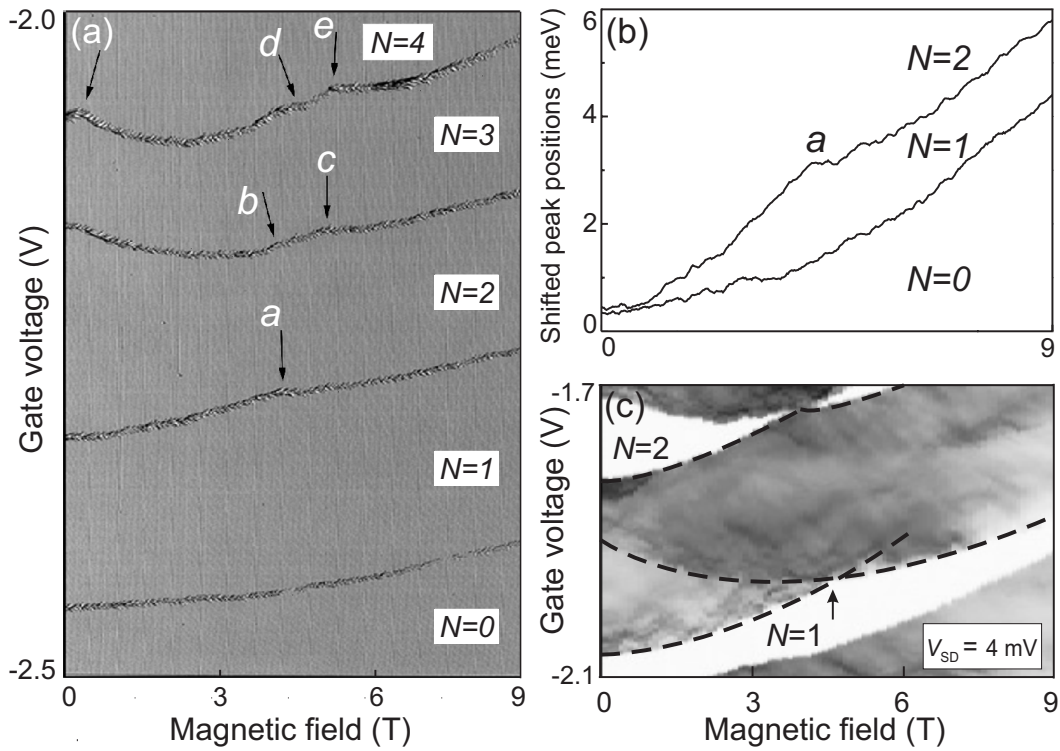


Figure 2.2: (a) Current measurement as function of gate voltage and magnetic field (0 - 9 T in steps of 25 mT) for $N = 1$ to 4 and $V_{sd} = 30 \mu\text{V}$. The indicated transitions are discussed in the text. (b) Peak positions extracted from the data in (a) and shifted towards each other. Gate voltage is converted to electrochemical potential. (c) Gray-scale plot of $I(V_g, B)$ for $V_{sd} = 4 \text{ mV}$. The stripe for the second electron entering the dot is shown. The ground state and first excited state are accentuated by dashed curves. The crossing indicated by an arrow, corresponds to the ST transition.

Capacitance [10] and tunneling [11, 12] spectroscopy have provided evidence for ST transitions in the two-electron ground state energy. Here, we report the evolution of the ground state as well as the first excited state versus B . Figure

2.2a shows the linear response Coulomb blockade peaks for $N = 0$ to 4. The four curves reflect how the ground-state electrochemical potentials $\mu(N)$ for $N = 1$ to 4 evolve with B . We emphasize that, based on the DF-spectrum for non-interacting electrons, one does not expect transitions or kinks in the B -dependence of $\mu(N)$ for $N = 1$ to 4. The peak for $N = 1$ indeed has a smooth B -dependence. For $N = 2, 3$, and 4, however, we observe kinks, which are indicated by arrows. These kinks must arise from interactions not included in the CI model. The left arrow in the $N = 4$ trace is due to the destruction of a Hund's rule state, which has been discussed previously [4, 5]. To blow up the different kinks, we extracted the peak positions and converted their values from gate voltage to energy [3]. The plotted curves in Fig. 2.2b are shifted towards each other and represent the variation of the electrochemical potential with B . The lowest curve for $N = 1$ shows a smooth [13] increase in energy in accordance with the expected solid curve for $E_{0,0}$ in Fig. 2.1c. The next curve for $N = 2$ rises faster with B than the $N = 1$ curve, which reflects the magnetic field dependent interaction $E_C(B)$ (see lower dashed curve in Fig. 2.1c). At 4.5 T, indicated by 'a', we observe a kink in the $N = 2$ curve, which is the expected ST transition. Our choice of shifting the peak position curves for $N = 1$ and 2 to zero at $B = 0$ in Fig. 2.2b, allows a direct comparison, and shows a good agreement with the lower solid curve and the dashed-dotted curve in Fig. 2.1c.

For larger source-drain voltage, V_{sd} , the current peaks become stripes with a width equal to V_{sd} [4]. In Fig. 2.2c an $I(V_g, B)$ gray-scale plot is given of the $N = 2$ stripe measured for $V_{sd} = 4$ mV. The edges of the stripe represent the ground-state electrochemical potential $\mu(2)$, which clearly contain the ST transition at ~ 4.5 T. Within the stripe, we clearly observe the first excited state. The down-going B -dependence of the first excited state is similar to $\mu^{\uparrow\downarrow}(2)$ (dotted curve in Fig. 2.1c). The crossing of the dashed curves in Fig. 2.2c is a direct observation of a crossing between the first excited state and ground state, which is in close agreement with Fig. 2.1c.

We briefly discuss the $N = 3$ and 4 curves in Fig. 2.2a, which both contain two kinks. The left kink (labeled 'b') in $\mu(3) = U(3) - U(2)$ is not due to a transition in the energy $U(3)$ of the three electron system, but is a remnant of the two-electron ST transition in $U(2)$. The right kink (labeled 'c') corresponds to the transition from $U(3) = E_{0,0}(\uparrow) + E_{0,0}(\downarrow) + E_{0,1}(\downarrow) + 2E_C$ to the spin-polarized case $U(3) = E_{0,0}(\downarrow) + E_{0,1}(\downarrow) + E_{0,2}(\downarrow) + 2E_C$. Detailed analysis shows that also this transition to increasing total angular momentum and total spin is driven largely by interactions. Similar transitions occur for the $N = 4$ system where on the right of the last kink (labeled 'e') the system is again in a polarized state with sequential filling of the angular momentum states: $U(4) = E_{0,0}(\downarrow) + E_{0,1}(\downarrow) +$

$$E_{0,2}(\downarrow) + E_{0,3}(\downarrow) + 3E_C.$$

We thank M. Wegewijs for useful discussions and R. Schouten for experimental help. The work was supported by the Dutch Foundation for Fundamental Research on Matter (FOM). L.P.K. was supported by the Royal Netherlands Academy of Arts and Sciences (KNAW).

References

- [1] R.C. Ashoori, *Nature* **379**, 413 (1996).
- [2] L.P. Kouwenhoven, C.M. Marcus, P.L. McEuen, S. Tarucha, R.M. Westervelt and N.S. Wingreen, *Electron transport in quantum dots*, in *Mesoscopic Electron Transport*, edited by L.L. Sohn, L.P. Kouwenhoven and G. Schön, (Kluwer, Series E **345**, 1997), p.105-214.
- [3] T.H. Oosterkamp, W.G. van der Wiel, L.P. Kouwenhoven, D.G. Austing, T. Honda and S. Tarucha, *Festkörper Probleme/Advances in Solid State Physics* **38**, 139-152 (1999).
- [4] L.P. Kouwenhoven, T.H. Oosterkamp, M.W.S. Danoesastro, M. Eto, D.G. Austing, T. Honda and S. Tarucha, *Science* **278**, 1788 (1997).
- [5] S. Tarucha, D.G. Austing, T. Honda, R.J. van der Hage and L.P. Kouwenhoven, *Phys. Rev. Lett.* **77**, 3613 (1996).
- [6] D.G. Austing, T. Honda and S. Tarucha, *Semicond. Sci. Technol.* **11**, 212 (1996).
- [7] V. Fock, *Z. Phys.* **47**, 446 (1928); C.G. Darwin, *Proc. Cambridge Philos. Soc.* **27**, 86 (1930).
- [8] M. Wagner, U. Merkt and A.V. Chaplik, *Phys. Rev. B* **45**, 1951 (1992).
- [9] An analogous singlet-triplet transition is predicted to occur in He atoms in the vicinity of white dwarfs and pulsars at $B = 4 \times 10^5$ T, see G. Thurner, H. Herold, H. Ruder, G. Schlicht and G. Wunner, *Phys. Lett.* **89A**, 133 (1982). Due to the larger dimensions, the transition is expected to occur around 4.5 T in our dots.
- [10] R.C. Ashoori, H.L. Stormer, J.S. Weiner, L.N. Pfeiffer, K.W. Baldwin and K.W. West, *Phys. Rev. Lett.* **71**, 613 (1993).
- [11] B. Su, V.J. Goldman and J.E. Cunningham, *Phys. Rev. B* **46**, 7644 (1992).
- [12] T. Schmidt, M. Tewordt, R.H. Blick, R.J. Haug, D. Pfannkuche, K. von Klitzing, A. Förster and H.L. Lüth, *Phys. Rev. B* **51**, 5570 (1995).

- [13] A small irregularity is visible around 3 T. This feature cannot be ascribed to a crossing of states in the dot, which is verified at finite source-drain voltages where both ground and excited states can be distinguished.

Chapter 3

Direct Coulomb and exchange interaction in artificial atoms

S. Tarucha, D.G. Austing, Y. Tokura,
W.G. van der Wiel and L.P. Kouwenhoven

We determine the contributions from the direct Coulomb and exchange interactions to the total interaction in semiconductor artificial atoms. We tune the relative strengths of the two interactions and measure them as a function of the number of confined electrons. We find that electrons tend to have parallel spins when they occupy nearly degenerate single-particle states. We use a magnetic field to adjust the single-particle state degeneracy, and find that the spin configurations in an arbitrary magnetic field are well explained in terms of two-electron singlet and triplet states.

This chapter has been published in Physical Review Letters **84**, 2485 (2000).

The addition of a single electron charge to a quantum box costs a certain energy, which is responsible for Coulomb blockade in electron transport [1]. Also a change in spin is associated with a certain change in energy, e.g. exchange energy is gained when electrons are added with parallel spins as compared to anti-parallel spins. Depending on the system, a large total spin (ferromagnetic filling) or a minimum total spin value (anti-ferromagnetic filling) is favored. In semiconductor quantum dots alternate spin filling [2] as well as spin-polarized filling [3] have been reported. Here, we study vertical quantum dots which have well-defined single-particle states. When these states are separated by a large energy, ΔE , an anti-ferromagnetic filling is favored. For small ΔE , a ferromagnetic filling is observed, which is in line with Hund's first rule from atomic physics. We use a magnetic field, B , to tune $\Delta E(B)$ allowing us to alter the spin filling.

We first discuss a simple model that describes filling of two single-particle states with two interacting electrons. Figure 3.1b shows two, spin-degenerate single-particle states with energies E_a and E_b crossing each other at $B = B_0$. The ground-state (GS) energy, $U(1)$, for one electron occupying these states, equals E_a for $B < B_0$ and E_b for $B > B_0$ (thick line in Fig. 3.1b). For two electrons we can distinguish four possible configurations with either total spin $S = 0$ (spin-singlet) or $S = 1$ (spin-triplet). (We neglect the Zeeman energy difference between $S_z = -1, 0$ and 1 .) The corresponding energies, $U_i(2, S)$ for $i = 1$ to 4 , are given by: $U_1(2, 0) = 2E_a + C_{aa}$, $U_2(2, 0) = 2E_b + C_{bb}$, $U_3(2, 1) = E_a + E_b + C_{ab} - |K_{ab}|$, $U_4(2, 0) = E_a + E_b + C_{ab}$. Here, C_{ij} ($i, j = a, b$) is the direct Coulomb (DC) energy between two electrons occupying states with energies E_i and E_j , and K_{ab} is the exchange (EX) energy ($K_{ab} < 0$) between two electrons occupying E_a and E_b with parallel spins [4].

The experiments below measure the electrochemical potential defined for a two-electron system as $\mu(2) \equiv U(2) - U(1)$. For each $U_i(2)$ we obtain the potentials: $\mu_i(2) = U_i(2) - E_a$ for $B < B_0$ and $\mu_i(2) = U_i(2) - E_b$ for $B > B_0$ (see Fig. 3.1c). The GS has $S = 0$ away from B_0 . Near B_0 , the lowest energy is $\mu_3(2)$, such that here $S = 1$. The downward cusp in the thick line identifies this spin-triplet region. The transition in the GS from $S = 0$ to 1 and $S = 1$ to 0 , respectively, occurs when $\mu_1 = \mu_3$ for $B < B_0$ and when $\mu_2 = \mu_3$ for $B > B_0$. We define two energies, Δ_1 and Δ_2 , to characterize the size of the downward cusp in the GS at $B = B_0$: $\Delta_1 = \mu_1 - \mu_3 = C_{aa} - C_{ab} + |K_{ab}|$, $\Delta_2 = \mu_2 - \mu_3 = C_{bb} - C_{ab} + |K_{ab}|$, $\Delta_1 - \Delta_2 = C_{aa} - C_{bb}$.

Our semiconductor quantum dot (see Fig. 3.1a) has the shape of a two-dimensional disk [5]. For detecting the GSs, we set the source-drain voltage, V , to a small value. The GSs and excited states (ESs) are both measured when V is set to a value sufficiently greater than the excitation energy [6]. For small V ,

a series of current peaks results from changing the number of electrons in the dot, N , one-by-one [1]. The position of a current peak for the transition from $N - 1$ to N measures the GS electrochemical potential $\mu(N)$. The sample is cooled down to about 100 mK.

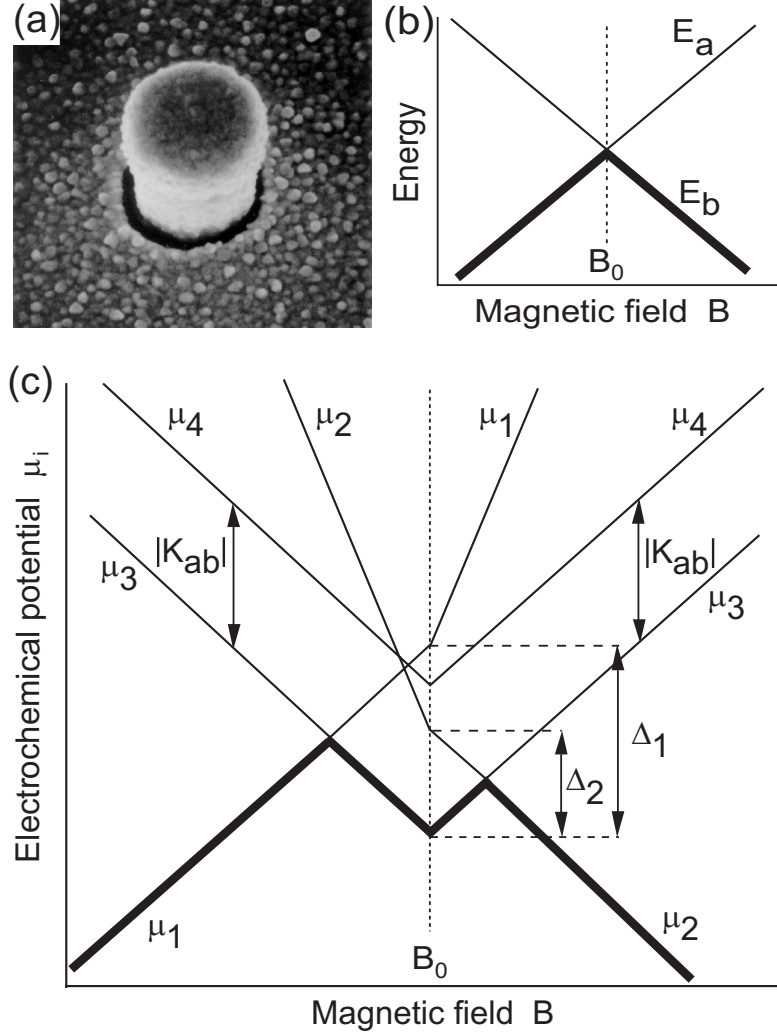


Figure 3.1: (a) Scanning electron micrograph of the semiconductor quantum dot device. The quantum dot is located inside the $0.5 \mu\text{m}$ -diameter pillar. The top and bottom contacts serve as source and drain electrodes. A Schottky gate is wrapped around the pillar. The current, I , flowing through the dot is measured as a function of gate voltage, V_g , in response to a dc voltage, V , applied between the source and drain. (b) Schematic diagram of two single-particle states with energies E_a and E_b crossing each other at a magnetic field $B = B_0$. (c) Electrochemical potential, $\mu_i(2) = U_i(2) - U(1)$, for two interacting electrons. The thick line depicts the ground-state energy, whereas the thin lines show the excited states.

Figure 3.2a shows the evolution of current peaks with magnetic field for $N = 7$ to 16. Features associated with a parabolic confining potential are all observed such as a shell structure [2]. The large spacing for $N = 12$ at $B = 0$ T can be seen in Fig. 3.2a (see double arrow) and marks the complete filling of the first three shells. The pairing between neighboring peaks indicates anti-parallel spin filling of a single orbital state by two electrons. Modifications to this pairing are observed for the peaks labeled by ‘■’ at 0 T, and in each of the dashed ovals connecting pairs of peaks at non-zero field. These are all signatures of Hund’s first rule; i.e. spin-polarized filling. Note that the Zeeman effect is negligible in this experiment [7]. We show expansions of the evolution of the $N = 8$ and $N = 24$ peaks in Fig. 2b. The downward cusps are clearly seen. The dashed lines form a parallelogram, from which we obtain parameters Δ_1 and Δ_2 .

To compare the two-electron model with larger electron numbers, we assume that other states are far away in energy so that they can be neglected. Then, the downward cusps should occur for higher *even* electron numbers, whereas they should be absent for *odd* electron numbers. This is clearly observed in the ovals in Fig. 3.2a. For instance, the B -field dependence of the 9th peak compares well to the thick line in Fig. 3.1b and the B -field dependence of the 10th peak compares well to the thick line in Fig. 3.1c. Other pairs of even and odd numbered peaks show the same behavior. This justifies our assumption so that we can simplify the many-electron system to just one or two electrons.

More detailed agreement is obtained by measuring the excitation spectrum [6]. Figure 3.3 shows a dI/dV_g plot, taken for $V = 2$ mV. This larger voltage opens a sufficiently wide transport window between the Fermi levels of the source and drain, that both the GS and first few ESs can be detected. The GS and ESs for $N = 7$ to 9 can be assigned from the magnetic field dependence of the dark gray lines. Solid white lines highlight the GSs whereas the ESs are indicated by dashed white lines. The set of GS and ES lines for $N = 7$ shows a single crossing similar to that in Fig. 3.1b. The spectrum for $N = 8$ compares well to Fig. 3.1c and we can clearly distinguish the parallelogram formed by the GS and first ES. The downward cusp in the GS for $N = 8$ (labeled ‘▲’) is at a slightly higher B -field than the upward cusp in the first ES (labeled ‘▼’). This asymmetry implies that $\Delta_1 > \Delta_2$, i.e. $C_{aa} > C_{bb}$. The same type of asymmetry is always observed along the dashed line in Fig. 3.2a, implying that $C_{aa} > C_{bb}$ for all N . Note that the GS for $N = 9$ shows an upward cusp (labeled by ‘▽’) quite similar in form to the first ES in the spectrum for $N = 8$. This implies that the filling of the ninth electron is closely linked to the configuration of the $N = 8$ first ES [3].

As illustrated in Fig. 3.2b, we can derive the experimental values for Δ_1 and Δ_2 for different N . These values are plotted in Fig. 3.4. We find that Δ_1 is larger

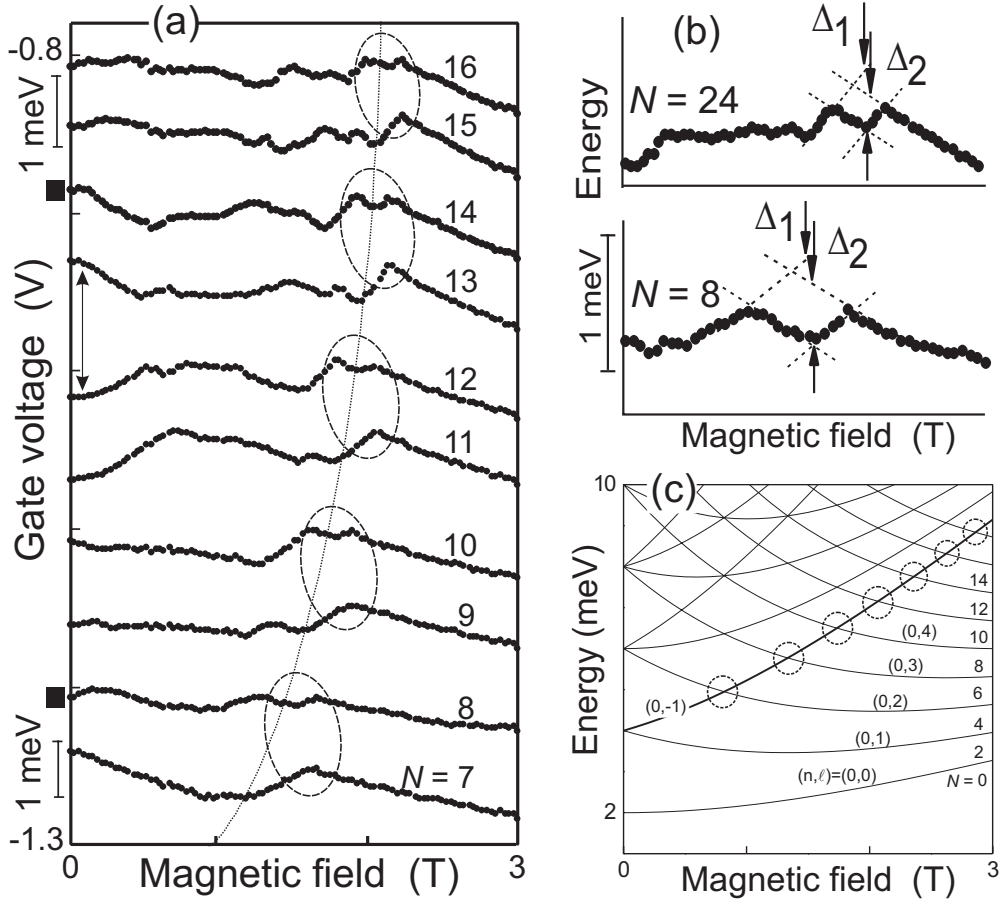


Figure 3.2: (a) Evolution of the ground state energies from $N = 7$ to 16 as measured from the current peaks versus magnetic field at $V = 120 \mu\text{V}$. The bars along the gate voltage axis show 1 meV energy scales calibrated at -1.26 and -0.85 V . The dotted curve indicates the last crossing between single-particle states. Dashed ovals correlate pairs of ground states for odd and even electron numbers. Spin transitions in the ground states are indicated by '■' at $B = 0 \text{ T}$ and occur in the ovals for $B \neq 0 \text{ T}$. (b) Magnified plots of the $N = 8$ and 24 current peaks vs. magnetic field. The dashed lines illustrate how the interaction-energy parameters, Δ_1 and Δ_2 are determined. (c) Fock-Darwin single-particle states calculated for $\omega_0 = 2 \text{ meV}$.

than Δ_2 for all N , again implying that $C_{aa} > C_{bb}$. As N increases from 6 to 12 , Δ_1 first increases and then slowly decreases, whilst Δ_2 slightly decreases.

To calculate DC and EX energies [4] we now need to specify the confining potential of the disk. In earlier work it was shown that the lateral confinement is well described by a parabolic potential with cylindrical symmetry [2]. The eigenfunctions with eigenenergies, $E_{n,l}$, in this potential are known as Fock-Darwin

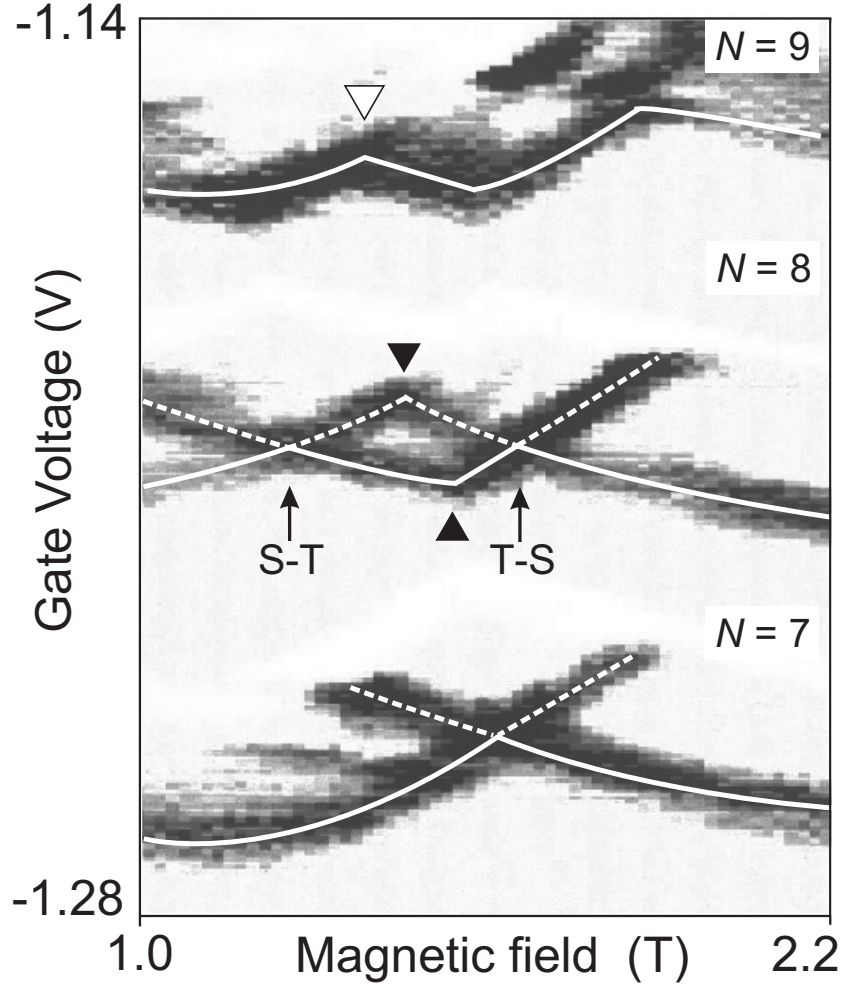


Figure 3.3: dI/dV_g in the plane of V_g and B for $N = 7$ to 9 measured for $V = 2$ mV. $dI/dV_g > 0$ for dark gray, $dI/dV_g < 0$ for white and $dI/dV_g \approx 0$ for light gray. The solid white lines indicate the evolution of the GSs with magnetic field whereas the dashed white lines show the ESs. The two arrows indicate singlet-triplet (S-T) and triplet-singlet (T-S) transitions in the GS for $N = 8$.

(FD) states [8]:

$$E_{n,l} = -\frac{l}{2}\hbar\omega_c + \left(n + \frac{1}{2} + \frac{1}{2}|l|\right)\hbar\sqrt{4\omega_0^2 + \omega_c^2} \quad (3.1)$$

where $n = 0, 1, 2, \dots$ is the radial quantum number and $l = 0, \pm 1, \pm 2, \dots$ is the quantum number for angular momentum. $\hbar\omega_0$ is the lateral confining energy and $\hbar\omega_c = eB/m^*$ is the cyclotron energy. Each FD-state is spin degenerate. At $B = 0$ T the FD-spectrum has sets of states with increasing degeneracy (see Fig. 3.2c). This degeneracy is lifted on increasing B , but as B is increased further new crossings can occur. The last crossing is always a crossing between just two

FD-states. The up-going state is always $(n, l) = (0, -1)$, whereas the down-going state, $(0, l > 1)$, has an increasing angular momentum for states with increasing energy. (The relation with Fig. 3.1 is: $E_a = E_{0,-1}$ and $E_b = E_{0,l>1}$.) Note that the last crossings also correspond to the dashed line in Fig. 3.2a.

From the electron distributions of the FD-states we calculate the DC and EX energies for two electrons occupying two degenerate states. We take $\hbar\omega_0 = 2$ meV as deduced from earlier experiments [2,6] and obtain Δ_1 and Δ_2 . The dashed

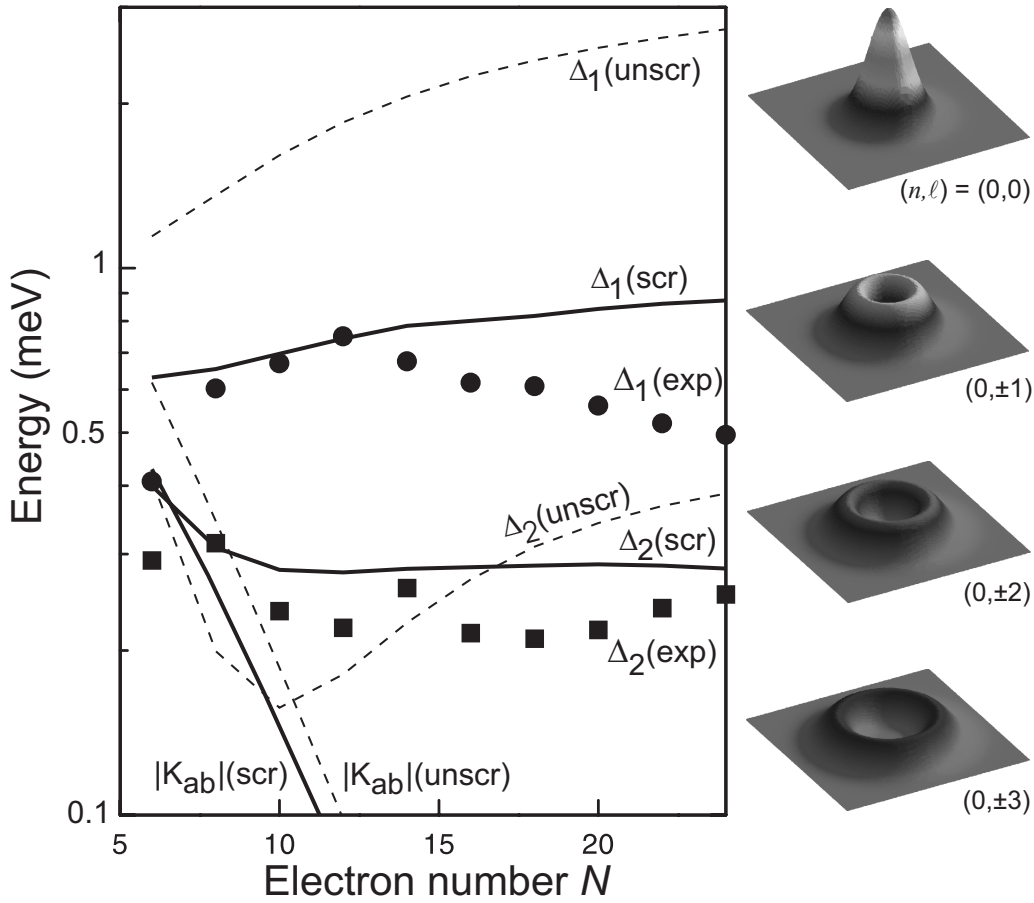


Figure 3.4: Experimental values for the energy parameters Δ_1 (●) and Δ_2 (■), on a log scale, versus electron number derived from data as shown in Fig. 3.2a. The uncertainty in the determination of the experimental values is $\pm 10\%$ or less. The dashed and solid curves are calculated from the FD wave functions at 2 T, for an unscreened (unscr) and screened (scr) Coulomb interaction. The calculated exchange energy $|K_{ab}|$ between states with energies $E_a = E_{0,-1}$ and $E_b = E_{0,N/2-1}$ decreases quickly with N . Next to the main figure the absolute squares of the wave functions are shown for the relevant quantum numbers $n = 0$ and $l = 0, \pm 1, \pm 2, \pm 3$. As the angular momentum quantum number l increases, the average radius increases.

curves in Fig. 3.4 show Δ_1 and Δ_2 when we neglect screening of the interactions within the dot by electrons in the leads and in the gate. In this case the Coulomb potential falls off as $1/r$, where r is the distance between the electrons [4]. For the solid curves we have approximated the screening effects by replacing the Coulomb potential by $\exp(-r/d)/r$. We have taken $d = 10$ nm which is roughly the thickness of the tunnel barriers. Figure 3.4 shows that screening considerably reduces

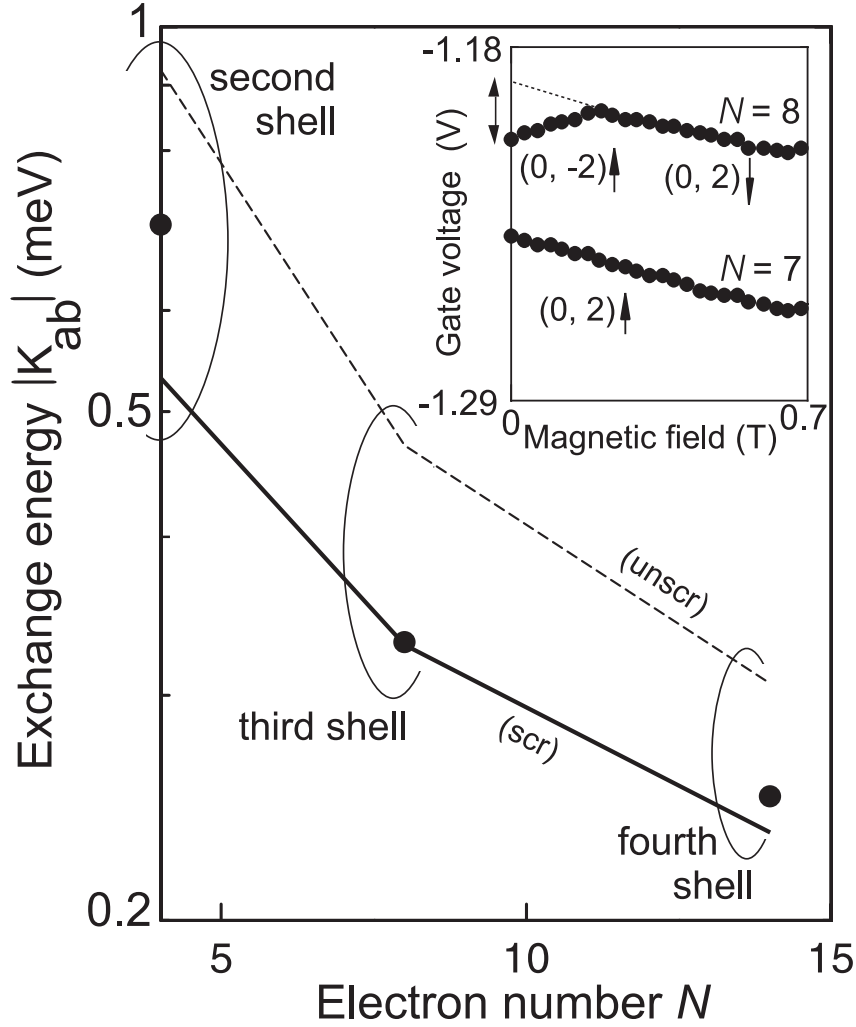


Figure 3.5: Exchange energy $|K_{ab}|$, on a log scale, associated with spin-triplets formed when each new shell is filled by just two electrons at $B = 0$ T. The solid circles are the experimental values whose uncertainty in the determination is $\pm 10\%$ or less. The inset shows an expansion for the filling of the first two electrons into the third shell (i.e. $N = 7$ and 8). The vertical double-arrow represents $|K_{ab}|$ in units of gate voltage which is then converted to energy. The calculated curves in the main figure are for the unscreened (dashed) and screened (solid) cases.

Δ_1 to values much closer to the experimental values. Screening also removes the minimum in Δ_2 , which is also in better agreement with the experiment. Since the average radius of the wave functions increases with angular momentum, two electrons are closer together when they both occupy (0,-1) compared to when they both occupy (0, $l = N/2 - 1$) for even $N > 4$ (or $l > 1$), so the DC interaction is stronger in the former. This explains our observation ($\Delta_1 > \Delta_2$) $C_{aa} > C_{bb}$ for all N . The overlap between *different* wave functions, (0,-1) and (0, $l = N/2 - 1$), decreases for even $N > 4$ (or $l > 1$). This results in a decrease in both C_{ab} and $|K_{ab}|$ with N . It then follows that Δ_1 increases until it saturates at a value equal to C_{aa} . The gradual decrease of experimental Δ_1 for $N > 12$ is probably related to the decrease in the lateral confinement with N [2] and thus the decrease in C_{aa} .

We finally discuss the interaction effects for the $N = 4, 8$ and 14 peaks near $B = 0$ T (the $N = 8$ and 14 peaks are labeled ‘■’ in Fig. 3.2a). These correspond to the GS electrochemical potentials for adding the second electron to the second, third and fourth shells, respectively. The inset to Fig. 3.5 demonstrates the resemblance to the model of Fig. 3.1c for $N = 8$ near $B = 0$ T. Comparing these data to the FD-spectrum, we assign the states such that: $E_a = E_{0,-2}$ and $E_b = E_{0,2}$. Likewise, for $N = 4$ we have $E_a = E_{0,-1}$ and $E_b = E_{0,1}$ [2] and for $N = 14$ we have $E_a = E_{0,-3}$ and $E_b = E_{0,3}$ [9]. Note that these states correspond to wave functions with a complete overlap. Also, for $B = B_0 = 0$ T the two crossing states have the same orbital symmetry implying $\Delta_1 = \Delta_2 = |K_{ab}|$, i.e. only EX effects contribute to the downward cusp [10].

We derive $|K_{ab}|$ as illustrated in the inset to Fig. 3.5. The obtained EX energy quickly becomes smaller for higher lying shells. For comparison, we also show the calculated screened and unscreened values. The screened case provides the best quantitative agreement for our realistic choices of the confining energy and the screening distance.

Our general model provides a clear identification of effects due to EX and DC interactions. More advanced calculations support our analysis [11]. An important simplification is the reduction of a many-electron system to just two interacting electrons. The type of spin filling in many nearly degenerate levels near $B = 0$ T in larger electron boxes remains an interesting open issue.

We thank G. Bauer, M. Danoesastro, M. Eto, R. van der Hage, T. Honda, J. Janssen, T. Oosterkamp, H. Tamura and T. Uesugi for their help and useful discussions. S.T. and L.P.K. acknowledge financial support from the Specially Promoted Research, Grant-in-Aid for Scientific Research, from the Ministry of Education, Science and Culture in Japan, from the Dutch Organization FOM, from the NEDO program NTDP-98, and from the EU via a TMR network.

References

- [1] L.P. Kouwenhoven, C.M. Marcus, P.L. McEuen, S. Tarucha, R.M. Westervelt and N.S. Wingreen, *Electron transport in quantum dots*, in Mesoscopic Electron Transport, edited by L.L. Sohn, L.P. Kouwenhoven and G. Schön, (Kluwer, Series E **345**, 1997), p.105-214.
- [2] S. Tarucha, D.G. Austing, T. Honda, R.J. van der Hage and L.P. Kouwenhoven, Phys. Rev. Lett. **77**, 3613 (1996); S. Tarucha, T. Honda, D.G. Austing, Y. Tokura, K. Muraki, T.H. Oosterkamp, J.W. Janssen and L.P. Kouwenhoven, Physica E **3**, 112 (1998).
- [3] D.R. Stewart, D. Sprinzak, C.M. Marcus, C.I. Duruöz and J.S. Harris Jr., Science **278**, 1784 (1997).
- [4] C_{ij} and K_{ij} are the usual wavefunction overlap integrals for an unscreened Coulomb potential:

$$C_{ij} = \iint |\psi_i(\vec{r}_1)|^2 \frac{e^2}{4\pi\epsilon_0 |\vec{r}_1 - \vec{r}_2|} |\psi_j(\vec{r}_2)|^2 d\vec{r}_1 d\vec{r}_2$$

$$K_{ij} = - \iint \psi_i^*(\vec{r}_1) \psi_j(\vec{r}_1) \frac{e^2}{4\pi\epsilon_0 |\vec{r}_1 - \vec{r}_2|} \psi_j^*(\vec{r}_2) \psi_i(\vec{r}_2) d\vec{r}_1 d\vec{r}_2$$

E_i and E_j are eigenvalues for the eigenfunctions ψ_i and ψ_j , respectively, and \vec{r}_1 and \vec{r}_2 represent the positions of the two electrons.

- [5] D.G. Austing, T. Honda and S. Tarucha, Semicond. Sci. Technol. **11**, 388 (1996).
- [6] L.P. Kouwenhoven, T.H. Oosterkamp, M.W.S. Danoesastro, M. Eto, D.G. Austing, T. Honda and S. Tarucha, Science **278**, 1788 (1997).
- [7] S. Sasaki, D.G. Austing and S. Tarucha, Physica B, **256**, 157 (1998).
- [8] V. Fock, Z. Phys. **47**, 446 (1928); C.G. Darwin, Proc. Cambridge Philos. Soc. **27**, 86 (1930).
- [9] For $N=14$ it is difficult to identify the corresponding state since the B -dependence is not clear enough to distinguish between $E_{0,-3}$ and $E_{1,-1}$. We assume it is $E_{0,-3}$, and continue to evaluate $|K_{ab}|$.
- [10] Note that the asymmetry ($\Delta_1 \neq \Delta_2$) can only occur for $B_0 \neq 0$. Symmetry is required if $B_0 = 0$, implying that $\Delta_1 = \Delta_2$. Then, the eigenfunctions for the states with energy E_a and E_b must have the same spatial form, from which we conclude that: $C_{aa} = C_{bb} = C_{ab}$ and thus $\Delta_1 = \Delta_2 = |K_{ab}|$.

- [11] There are various calculations consistent with our experiment; exact calculation for $N < 7$ by M. Eto, Jpn. J. Appl. Phys. **36**, 3924 (1997), Hartree-Fock calculations for $N > 8$ by A. Natori *et al.*, Jpn. J. Appl. Phys. **36**, 3960 (1997), H. Tamura, Physica B **249-251**, 210 (1998) and M. Rontani *et al.*, Phys. Rev. B **59**, 10165 (1999), and spin density-functional theory at $B = 0$ T by In-Ho Lee *et al.*, Phys. Rev. B **57**, 9035 (1998) and M. Koskinen, M. Manninen and S.M. Reimann, Phys. Rev. Lett. **79**, 1817 (1997), and also at non-zero B by O. Steffen, U. Rossler and M. Suhrke, Europhys. Lett. **42**, 529 (1998).

Chapter 4

The Kondo effect in the unitary limit

W.G. van der Wiel, S. De Franceschi, T. Fujisawa,
J.M. Elzerman, S. Tarucha and L.P. Kouwenhoven

We observe a strong Kondo effect in a semiconductor quantum dot when a small magnetic field is applied. The Coulomb blockade for electron tunneling is overcome completely by the Kondo effect and the conductance reaches the unitary-limit value. We compare the experimental Kondo temperature with the theoretical predictions for the spin-1/2 Anderson impurity model. Excellent agreement is found throughout the Kondo regime. Phase coherence is preserved when a Kondo quantum dot is included in one of the arms of an Aharonov-Bohm ring structure and the phase behavior differs from previous results on a non-Kondo dot.

This chapter has been published in Science **289**, 2105 (2000).

The Kondo theory explains the increased resistivity of a metal with magnetic impurities at low temperatures [1]. Predictions from 1988 indicate that quantum dots could also exhibit the Kondo effect [2-7], but now as an increased conductance, G , which can reach the unitary limit ($G = 2e^2/h$) at low temperature. Recent experiments have confirmed the presence of the Kondo effect in quantum dots, however not reaching the unitary limit [8-12]. We demonstrate the unitary limit Kondo effect in a semiconductor quantum dot. Our quantum dot is embedded in one of the arms of an Aharonov-Bohm (AB) ring, which enables us to show that electron transport through the many-body Kondo state is at least partly phase-coherent. The Kondo effect arises from the coupling between a localized electron spin to a sea of conduction electrons. The strength is characterized by the Kondo temperature, T_K [13]

$$T_K = \frac{\sqrt{\Gamma U}}{2} e^{\pi \varepsilon_0 (\varepsilon_0 + U) / \Gamma U} \quad (4.1)$$

U is the on-site electron repulsion energy, or charging energy, ε_0 the energy of the single-particle state, and Γ reflects its width, due to a finite lifetime from tunneling to the leads (see left inset to Fig. 4.2a). In quantum dots these parameters can be controlled experimentally, resulting in a ‘tunable Kondo effect’ [8-12].

Our device (Fig. 4.1a) consists of an AB ring defined in a 2-dimensional electron gas (2DEG) [14]. The conductance of the ring without applying gate voltages is $\sim 10e^2/h$, implying that the current is carried by several modes in each arm. In our experiment, a quantum dot has only been formed in the lower arm. One gate in the upper arm is used to pinch off the upper arm. All measurements are performed in a dilution refrigerator with a base temperature of 15 mK, using a standard lock-in technique with an ac voltage excitation between source and drain contacts of 3 μ V.

The linear-response conductance, G , through the lower dot versus gate voltage, V_{gl} , and magnetic field, B , is shown in a color scale plot (Fig. 4.1b). Here, the left and right parts of the lower arm serve as leads to the dot. In Fig. 4.1c two $G(V_{gl})$ curves are extracted from Fig. 4.1b for $B = 0$ and 0.4 T. At $B = 0$, regular Coulomb oscillations are observed with low valley conductance. In some magnetic field ranges, however, the valley conductance increases considerably and can even reach $2e^2/h$, for instance for $B = 0.4$ T. We will discuss Fig. 4.1b in more detail below, but first focus on the large conductance values observed at $B = 0.4$ T.

Figure 4.2a shows Coulomb oscillations for different temperatures. At base temperature, the valleys around $V_{gl} = -413$ mV and -372 mV reach the maximum

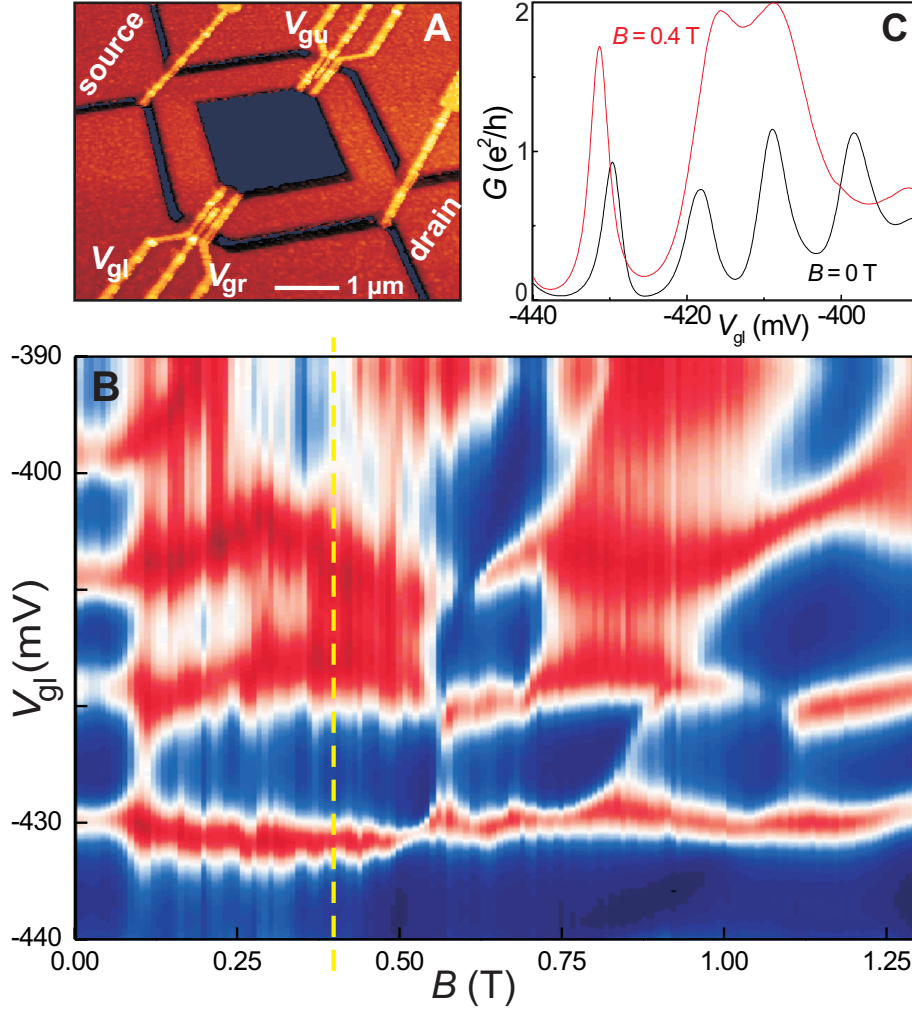


Figure 4.1: (a) Atomic force microscope image of the device. An Aharonov-Bohm (AB) ring is defined in a 2DEG by dry etching of the dark regions (depth is 75 nm). The 2DEG with electron density, $n_S = 2.6 \times 10^{15} \text{ m}^{-2}$, is situated 100 nm below the surface of an AlGaAs/GaAs heterostructure. In both arms of the ring (lithographic width $0.5 \mu\text{m}$, inner perimeter $6.6 \mu\text{m}$) a quantum dot can be defined by applying negative voltages to gate electrodes. The gates at the entry and exit of the ring are not used. A quantum dot of size $\sim 200 \text{ nm} \times 200 \text{ nm}$, containing ~ 100 electrons, is formed in the lower arm using gate voltages, V_{gl} and V_{gr} (the central plunger gate was not working). The average energy spacing between single-particle states is $100 \mu\text{eV}$. The conductance of the upper arm, set by V_{gu} , is kept zero except for AB measurements. (b) Color scale plot of the conductance, G , as function of V_{gl} and B for $V_{gr} = -448 \text{ mV}$ and $T = 15 \text{ mK}$. The upper arm of the AB ring is pinched off by $V_{gu} = -1.0 \text{ V}$. Red (blue) corresponds to high (low) conductance. (c) Two selected traces $G(V_{gl})$ for $B = 0$ and $B = 0.4 \text{ T}$. The Coulomb oscillations at $B = 0$ correspond to the oscillating color in (b). For some ranges of B , the valley conductance increases considerably, reaching values close to $2e^2/h$, i.e. the unitary limit, e.g. along the yellow dashed line at 0.4 T .

possible conductance value of $2e^2/h$. In fact, the valleys tend to disappear. When the temperature is increased, two separate Coulomb peaks develop with growing peak spacing. The conductance in the center of the valley has a logarithmic T -dependence with a saturation at $2e^2/h$ for low T , which is not due to electronic noise (right inset to Fig. 4.2a). The adjacent Coulomb valleys show an opposite T -dependence. This even-odd asymmetry indicates an unpaired spin in a valley with an odd electron number, where we observe the Kondo anomaly, and a spin singlet for an even electron number [8, 9]. Figure 4.2b shows the differential conductance for different T in the middle of the Kondo plateau at $2e^2/h$. The pronounced peak around $V_{SD} = 0$ reflects the Kondo resonance at the Fermi energy. The peak height has the same T -dependence as shown in the right inset to Fig. 4.2a. The width of the peak increases linear with temperature (inset to Fig. 4.2b).

These measurements are taken after optimizing the two barrier gate voltages, V_{gl} and V_{gr} , in order to obtain nearly equal tunnel barriers. However, sweeping V_{gl} , as in Fig. 4.2a, changes the left barrier much more effectively than the right tunnel barrier and hence the barriers cannot be symmetric over the whole V_{gl} -range. For a quantitative comparison to theory, we therefore optimize V_{gr} by fixing it at a value chosen such that, upon sweeping V_{gl} , we obtain a flat plateau close to $2e^2/h$ (Fig. 4.3a) [15]. The two discernable Coulomb oscillations at higher temperatures have completely merged together at low temperature. This unitary limit was predicted [3, 4], but not observed before. The unitary limit implies that the transmission probability through the quantum dot is equal to one. This is a remarkable phenomenon since the quantum dot contains two tunnel barriers, each with a transmission probability much less than one. In addition, the on-site Coulomb energy, U , tends to block the state with an extra electron on the dot. Despite U being an order of magnitude larger than the characteristic energy scale, $k_B T_K$, the Kondo effect completely determines electron tunneling at low energies (i.e. low T and V_{SD}). Note that in the absence of the Kondo effect (e.g. for electron number $N = \text{even}$), the system consists of two separated Fermi seas. In contrast, for $N = \text{odd}$ the screening of the local spin creates a single, extended many-body system with a single, well-defined Fermi surface extending throughout the whole system. The quasi-particles at this Fermi surface no longer experience the repulsive barrier potentials, nor the on-site Coulomb repulsion. Also note that since the local spin for $N = \text{odd}$ is completely screened and since the dot has zero spin for $N = \text{even}$, the whole system of leads and dot is in a singlet state over a wide gate voltage range (between -430 mV and -350 mV in Fig. 4.2a), although the nature of the ground state in the even and odd valleys is very different.

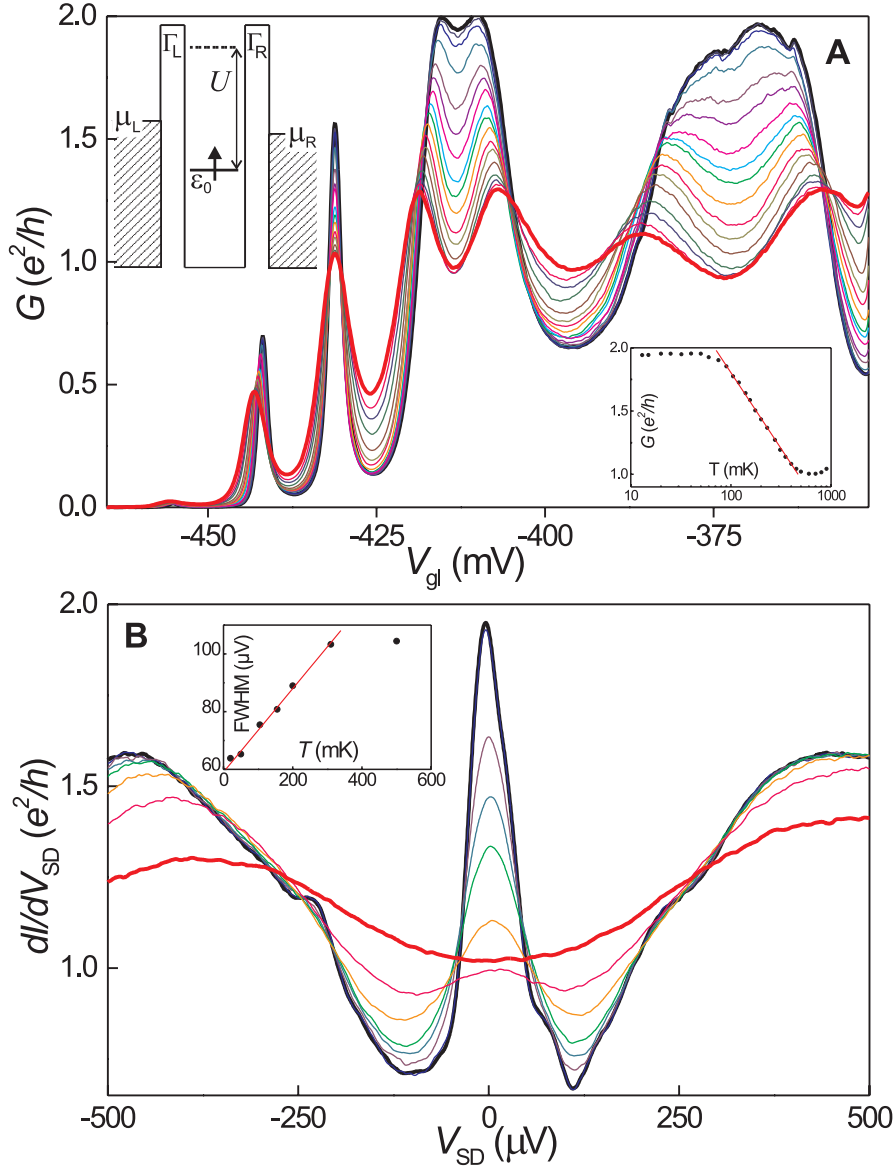


Figure 4.2: (a) Coulomb oscillations in G versus V_{gl} at $B = 0.4$ T for different temperatures. $T = 15$ mK (thick black trace) up to 800 mK (thick red trace). V_{gr} is fixed at -448 mV. The lower-right inset highlights the logarithmic T -dependence between 90 and 500 mK for $V_{gl} = -413$ mV. The upper-left inset explains the symbols used in the text with $\Gamma = \Gamma_L + \Gamma_R$. Note that ε_0 is negative and measured from the Fermi level in the leads at equilibrium. (b) Differential conductance, dI/dV_{SD} , versus dc bias voltage between source and drain contacts, V_{SD} , for $T = 15$ mK (thick black trace) up to 900 mK (thick red trace), also at $V_{gl} = -413$ mV and $B = 0.4$ T. The left inset shows that the width of the zero-bias peak, measured from the full-width-at-half-maximum (FWHM) increases linearly with T . The red line indicates a slope of $1.7 k_B/e$, where k_B is the Boltzmann constant. At 15 mK the FWHM = 64 μV and it starts to saturate around 300 mK.

For a quantitative analysis we rewrite Eq. 4.1 as $\ln(T_K) = \pi\varepsilon_0(\varepsilon_0 + U)/\Gamma U + \text{constant}$, indicating a quadratic dependence for $\ln(T_K)$ on gate voltage, V_{gl} [16]. Following the work in [17], we fit G versus T for different gate voltages (see Fig. 4.3c) to the empirical function

$$G(T) = G_0 \left(\frac{T_K'^2}{T^2 + T_K'^2} \right)^s \quad (4.2)$$

with $T_K' = T_K/\sqrt{2^{1/s} - 1}$ where the fit parameter $s \approx 0.2$ for a spin-1/2 system [17, 18]. Figure 4.3b shows the obtained Kondo temperatures, T_K versus V_{gl} . The red parabola demonstrates that the obtained values for T_K are in excellent agreement with Eq. 4.1 [19].

The Kondo temperature as derived above, is obtained from the linear response conductance. In earlier works [8-12] estimates for T_K were obtained from measurements of dI/dV_{SD} versus V_{SD} (I is the current between source and drain). In that case, the full width at half maximum (FWHM) was set equal to $k_B T_K/e$. However, applying a finite V_{SD} introduces dephasing even at $T = 0$ [6,20]. To compare these two methods, we also plot in Fig. 4.3b (FWHM/ k_B) measured for different gate voltages at base temperature. Also now we find a parabolic dependence, but the values are larger than T_K obtained from linear-response measurements. The difference may indicate the amount of dephasing due to a non-zero V_{SD} .

The normalized conductance, $G/(2e^2/h)$, is expected to be a universal function of the normalized temperature, T/T_K , independent of the other energy scales, U , ε_0 and Γ . Over a range of $\Delta\varepsilon_0 = 225 \mu\text{eV}$ corresponding to 2.6 Kelvin, which is several times larger than T_K , this expected one-parameter scaling is indeed observed in the inset to Fig. 4.3c.

We now return to the significance of the applied magnetic field. Near $B = 0$ we observe in Fig. 4.1c regular Coulomb oscillations. Here, we find that the Kondo effect typically changes the valley conductance by only 20% [9]. In Fig. 4.1b a big change occurs at $B \sim 0.1$ T, reflecting the onset of a different transport regime, an observation that seems common for half-open quantum dots [21,22]. The magnetic field scale corresponds to adding a flux quantum to the area of the dot, implying, for instance, that time-reversal symmetry is broken. At $B = 0.4$ T, where we observe the unitary limit, the Zeeman spin splitting is much smaller than $k_B T_K$ and so it can safely be ignored. This magnetic field scale is also too small for the formation of Landau levels, which can introduce additional spin physics [22,23].

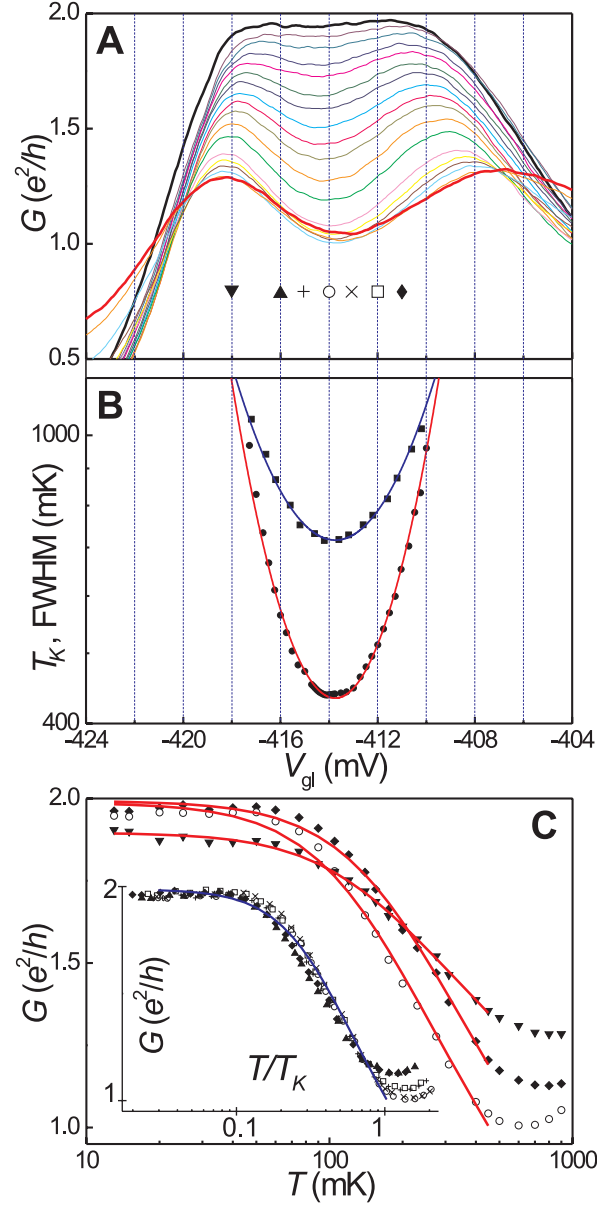


Figure 4.3: Quantitative analysis in the case of optimized symmetric tunnel barriers. (a) $G(V_{gl})$ for $T = 15$ mK (thick black trace) up to 900 mK (thick red trace) and $V_{gr} = -448$ mV, $B = 0.4$ T. (b) T_K versus V_{gl} (\bullet) as obtained from many fits as in (c). In addition, we plot the peak width (FWHM/ k_B) versus V_{gl} (\blacksquare) as deduced from $dI/dV_{SD}(V_{SD})$ measurements at base temperature (see, e.g., black trace in Fig. 4.2b). Both data sets are fitted to Eq. 4.1, resulting in the red and blue parabolas, respectively. (c) $G(T)$ at fixed gate voltage as extracted from (a) for $V_{gl} = -411$ (\blacklozenge), -414 (\circ) and -418 (\blacktriangledown) mV (labels are also indicated in (a)). The red curves are fits to Eq. 4.2. The inset shows that G versus normalized temperature T/T_K scales to a single curve for different gate voltages, $V_{gl} = -411$ (\blacklozenge), -412 (\square), -413 (\times), -414 (\circ), -415 ($+$), -416 (\blacktriangle) mV. The blue curve is a fit to Eq. 4.2 with fixed $T_K = 1$ and $G_0 = 2e^2/h$; $s = 0.29$ is the only fit parameter.

Recent calculations [24] indicate a spin polarization near $B = 0$ to enhanced values in line with earlier observations [25,26]. A small magnetic field reduces the spin values to $\frac{1}{2}$ for $N = \text{odd}$ and 0 for $N = \text{even}$. Since higher spin states

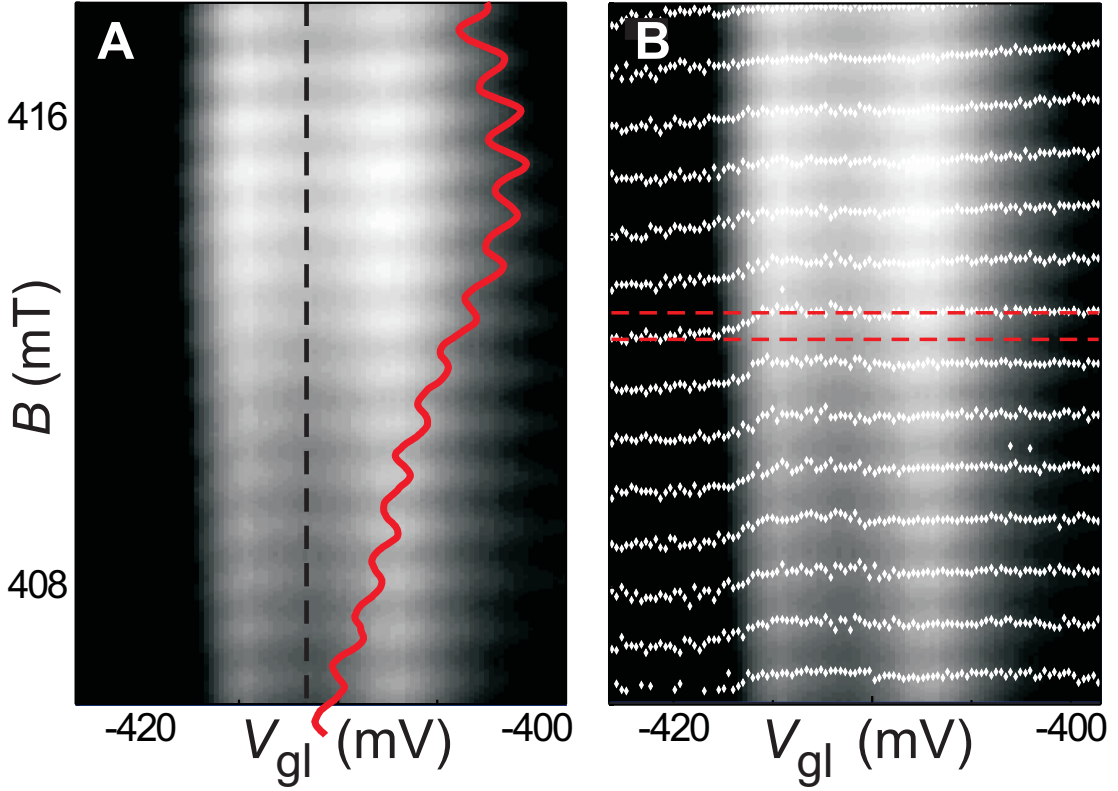


Figure 4.4: AB oscillations in the conductance through the ring containing the unitary Kondo quantum dot. In this measurement the conductance through the upper arm is set close to $2e^2/h$ in order to have approximately equal transmissions through both arms. (a) Gray-scale plot of the conductance, G , as function of V_{gl} and magnetic field B at 15 mK. Light (dark) corresponds to high (low) conductance. AB oscillations are observed over the whole gate voltage range. The red curve highlights the AB oscillations in the middle of the Kondo plateau ($V_{gl} = -412$ mV). The period of 0.87 mT corresponds well to a flux quantum, h/e , through the area enclosed by the ring. The modulation is 2-3% of the total conductance through the ring. (b) Same gray-scale plot with the AB conductance maxima indicated by white diamond symbols. A π phase flip is observed when stepping through the left Coulomb peak (e.g. along the red dashed lines). No phase change is observed in the Kondo valley or at the right Coulomb peak.

generally lead to a lower Kondo temperature, the Kondo effect can become much stronger by applying a magnetic field [27]. We believe this to be the origin for the

transition in transport regimes near $B = 0.1$ T in Fig. 4.1b, although a thorough theoretical analysis would be desirable.

So far, the upper arm of the ring was pinched off. To study how electron interference is affected by a Kondo quantum dot in the lower arm, we adjust the upper arm conductance to $\sim 2e^2/h$. In the gray-scale plot of Fig. 4.4a clear AB oscillations around $B = 0.4$ T are visible in the Kondo valley and the neighboring valleys. The period agrees well with a flux quantum, h/e , applied through the area enclosed by the ring. The AB oscillations demonstrate that at least part of the tunnel processes through the Kondo quantum dot is phase coherent. Our 2-terminal geometry only allows phase changes by multiples of π , due to symmetry reasons [28]. We observe a π phase flip at the left Coulomb peak, but no phase change is observed in the Kondo valley or at the right Coulomb peak (Fig. 4.4b). This behavior is different from the phase evolution described in [14]. A further study in a 4-terminal geometry should allow us to determine arbitrary phase shifts in the transmission through a Kondo dot, as proposed in [29].

We thank E. Huizeling, T. Hayashi, S. Sasaki, D. Goldhaber-Gordon, Y. Meir, M. Eto, L. Glazman, Yu. Nazarov, and R. Schouten for their help. We acknowledge financial support from the Specially Promoted Research, Grant-in-Aid for Scientific Research, from the Ministry of Education, Science and Culture in Japan, from the Dutch Organization for Fundamental Research on Matter (FOM), from the NEDO joint research program (NTDP-98), and from the EU via a TMR network.

References

- [1] J. Kondo, Prog. Theor. Phys. **32**, 37 (1964).
- [2] L.I. Glazman and M.E. Raikh, JETP Lett. **47**, 452 (1988).
- [3] T.K. Ng and P.A. Lee, Phys. Rev. Lett. **61**, 1768 (1988).
- [4] A. Kawabata, J. Phys. Soc. Jpn. **60**, 3222 (1991).
- [5] Y. Meir, N.S. Wingreen and P.A. Lee, Phys. Rev. Lett. **70**, 2601 (1993).
- [6] N.S. Wingreen and Y. Meir, Phys. Rev. B **49**, 11040 (1994).
- [7] W. Izumida, O. Sakai and Y. Shimizu, J. Phys. Soc. Jpn. **67**, 2444 (1998).
- [8] D. Goldhaber-Gordon, H. Shtrikman, D. Mahalu, D. Abusch-Magder, U. Meirav and M.A. Kastner, Nature **391**, 156 (1998).
- [9] S.M. Cronenwett, T.H. Oosterkamp and L.P. Kouwenhoven, Science **281**, 540 (1998).

- [10] J. Schmid, J. Weis, K. Eberl and K. von Klitzing, *Physica B* **256-258**, 182 (1998).
- [11] F. Simmel, R.H. Blick, J.P. Kotthaus, W. Wegscheider and M. Bichler, *Phys. Rev. Lett.* **83**, 804 (1999).
- [12] S. Sasaki, S. De Franceschi, J.M. Elzerman, W.G. van der Wiel, M. Eto, S. Tarucha and L.P. Kouwenhoven, *Nature* **405**, 764 (2000).
- [13] F.D.M. Haldane, *Phys. Rev. Lett.* **40**, 416 (1978).
- [14] A. Yacoby, M. Heiblum, D. Mahalu and H. Shtrikman, *Phys. Rev. Lett.* **74**, 4047 (1995).
- [15] The Kondo region around -372 mV does not develop a plateau at $2e^2/h$. In this gate voltage regime the tunnel coupling can be rather large so that charge fluctuations become important. This regime has been described by: L.I. Glazman, F.W.J. Hekking and A.I. Larkin, *Phys. Rev. Lett.* **83**, 1830 (1999), who predict a similar rounded-off Kondo region.
- [16] $\varepsilon_0 = \alpha V_{gl} + \text{constant}$, with $\alpha = C_{gl}/C_\Sigma = 45 \mu\text{eV}/\text{mV}$. Here, C_{gl} is the capacitance of the left gate electrode and C_Σ is the total capacitance of the dot. Using this α -factor and the T -dependence of G , we obtain $U = 500 \mu\text{eV}$ and $\Gamma = 240 \mu\text{eV}$.
- [17] D. Goldhaber-Gordon, J. Göres, M.A. Kastner, H. Shtrikman, D. Mahalu and U. Meirav, *Phys. Rev. Lett.* **81**, 5225 (1998).
- [18] Eq. 4.2 is an empirical fitting function to numerical renormalization group calculations reported in T.A. Costi, A.C. Hewson and V. Zlatić, *J. Phys.: Condens. Matter* **6**, 2519 (1994).
- [19] From these fits we obtain $\Gamma = 231 \pm 12 \mu\text{eV}$ taking $U = 500 \mu\text{eV}$. Since $\Gamma \gg k_B T_K$, we conclude that the low-energy properties are set by T_K , which is required for using Eq. 4.1, and that the dot is in the Kondo regime and not in the mixed-valence regime.
- [20] A. Kaminski, Yu.V. Nazarov and L.I. Glazman, *Phys. Rev. B* **62**, 8154 (2000).
- [21] S.M. Maurer, S.R. Patel, C.M. Marcus, C.I. Duruöz and J.S. Harris Jr., *Phys. Rev. Lett.* **83**, 1403 (1999).
- [22] J. Schmid, J. Weis, K. Eberl and K. von Klitzing, *Phys. Rev. Lett.* **84**, 5824 (2000).
- [23] C. Tejedor and L. Martin-Moreno, *Phys. Rev. B* **63**, 035319 (2001). The theory developed in this paper to describe the experimental results in [22],

requires the formation of Landau levels, so it cannot describe our present results.

- [24] M. Stopa, unpublished. The enhanced values for the spin polarization can sometimes reoccur at higher magnetic fields.
- [25] S. Tarucha, D.G. Austing, T. Honda, R.J. van der Hage and L.P. Kouwenhoven, Phys. Rev. Lett. **77**, 3613 (1996).
- [26] D.R. Stewart, D. Sprinzak, C.M. Marcus, C.I. Duruöz and J.S. Harris Jr., Science **278**, 1784 (1997).
- [27] M. Stopa, W. Izumida and M. Eto, private communication.
- [28] M. Büttiker, Phys. Rev. Lett. **57**, 176 (1986).
- [29] U. Gerland, J. von Delft, T. Costi and Y. Oreg, Phys. Rev. Lett. **84**, 3710 (2000).

Chapter 5

Kondo effect in an integer-spin quantum dot

S. Sasaki, S. De Franceschi, J.M. Elzerman,
W.G. van der Wiel, M. Eto, S. Tarucha and L.P. Kouwenhoven

The Kondo effect is a key many-body phenomenon in condensed matter physics. It concerns the interaction between a localized spin and free electrons. Discovered in metals containing small amounts of magnetic impurities, it is now a fundamental mechanism in a wide class of correlated electron systems [1,2]. Control over single, localized spins has become relevant also in fabricated structures due to the rapid developments in nano-electronics [3,4]. Experiments have already demonstrated artificial realizations of isolated magnetic impurities at metallic surfaces [5,6], nanometer-scale magnets [7], controlled transitions between two-electron singlet and triplet states [8], and a tunable Kondo effect in semiconductor quantum dots [9-12]. Here, we report an unexpected Kondo effect realized in a few-electron quantum dot containing singlet and triplet spin states whose energy difference can be tuned with a magnetic field. This effect occurs for an even number of electrons at the degeneracy between singlet and triplet states. The characteristic energy scale is found to be much larger than for the ordinary spin-1/2 case.

This chapter has been published in Nature **405**, 764 (2000).

Quantum dots are small electronic devices [13], which confine a well-defined number of electrons, N . The total spin is zero or an integer for $N = \text{even}$ and half-integer for $N = \text{odd}$. The latter case constitutes the canonical example for the Kondo effect [14,15] when all electrons can be ignored, except for the one with the highest energy; i.e. the case of a single, isolated spin, $S = 1/2$ (see Fig. 5.1a). Although the energy level ε_0 is well below the Fermi energies of the two leads, Heisenberg uncertainty allows the electron on the dot to tunnel to one of the leads when it is replaced quickly by another electron. The time scale for such a co-tunneling process [16] is $\sim \hbar/U$, where $\hbar = 2\pi\hbar$ is Planck's constant and U is the on-site Coulomb energy. Figure 5.1a illustrates that particle exchange by co-tunneling can effectively flip the spin on the dot. At low temperature, the coherent superposition of all possible co-tunneling processes involving spin flip can result in a time-averaged spin equal to zero. The whole system, i.e. quantum dot plus electrodes, forms a spin singlet. The energy scale for this singlet state is the Kondo temperature, T_K . In terms of density of states, a narrow peak with a width $\sim k_B T_K$ develops at the Fermi energy (k_B is Boltzmann's constant). Note that for $N = \text{even}$ and $S = 0$, co-tunneling gives rise to a lifetime broadening of the confined state, without producing any Kondo resonance. Such even/odd behavior corresponding to no-Kondo/Kondo has been observed in recent experiments [9,10].

It is also possible that a quantum dot with $N = \text{even}$ has a total spin $S = 1$; e.g. when the last two electrons have parallel spins. If the remaining $N - 2$ electrons can be ignored, this corresponds to a triplet state. Parallel spin filling is a consequence of Hund's rule occurring when the gain in exchange energy exceeds the spacing between single-particle states [8]. The spin of the triplet state can also be screened by co-tunneling events. These are illustrated in the center-left side of Fig. 5.1b. In contrast to single-particle states that are considered in the spin-1/2 Kondo problem, the spin triplet consists of three degenerate two-particle states. Co-tunneling exchanges only one of the two electrons with an electron from the leads. The total spin of the many-body Kondo state depends on how many modes in the leads couple effectively to the dot [17,18]. If there is only one mode, the screening is not complete and the whole system does not reach a singlet state. In this case the Kondo effect is called 'underscreened'. Calculations show that also for $S = 1$ a narrow Kondo resonance arises at the Fermi energy, however, the corresponding T_K is typically lower than in the case of $S = 1/2$ [19,20]. Some experiments have reported the absence of even/odd behavior [21,22], which may be related to the formation of higher spin states.

Here, we investigate a quantum dot with $N = \text{even}$ where the last two electrons occupy a degenerate state of a spin singlet and a spin triplet. Figure 5.1b

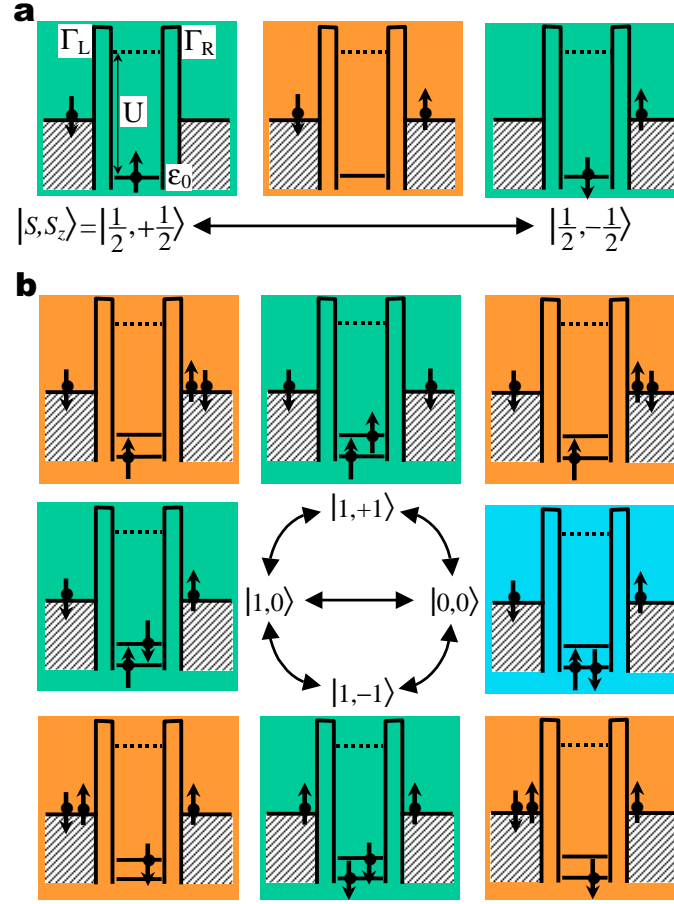


Figure 5.1: Spin-flip processes leading to ordinary and singlet-triplet Kondo effect in a quantum dot. (a) Co-tunneling event in a spin-1/2 quantum dot for $N = \text{odd}$. Only the highest-energy electron is shown, occupying a single spin-degenerate level, ε_0 . (The case of two, or more, closely spaced levels has also been considered theoretically within the context of the spin-1/2 Kondo effect [30].) The green panels refer to $S_z = 1/2$ and $-1/2$ ground states, which are coupled by a co-tunneling event. The two tunnel barriers have tunneling rates Γ_R and Γ_L . In the Coulomb blockade regime ($|\varepsilon_0| \sim U$) adding or subtracting an electron from the dot implies an energy cost $\sim U$. Hence the intermediate step (orange panel) is a high-energy, virtual state. The spin-flip event depicted here is representative of a large number of higher-order processes which add up coherently such that the local spin is screened. This Kondo effect leads to an enhanced linear-response conductance at temperatures $T \lesssim T_K$. (b) Co-tunneling in an integer-spin quantum dot for $N = \text{even}$ at a singlet-triplet degeneracy. Two electrons can share the same orbital with opposite spins (singlet state in the blue panel) or occupy two distinct orbitals in one of the three spin-triplet configurations (green panels). The different spin states are coupled by virtual states (orange panels). Similar to the spin-1/2 case, spin-flip events can screen the local magnetic moment. Note that an $S = 1$ Kondo effect only involves $|1, +1\rangle$, $|1, 0\rangle$ and $|1, -1\rangle$.

illustrates the different co-tunneling processes occurring in this special circumstance. Starting from $|S = 1, S_z = 1\rangle$, where S_z is the z -component of the total spin on the dot, co-tunneling via a virtual state $|1/2, 1/2\rangle$, can lead either to the triplet state $|1, 0\rangle$, or to the singlet state $|0, 0\rangle$. Via a second co-tunneling event the state $|1, -1\rangle$ can be reached. As for the $S = 1$ case, the local spin can fluctuate by co-tunneling events. By coupling to all triplet states, the singlet state enhances the spin exchange interaction between the dot and the leads, resulting in a higher rate for spin fluctuations. This particular situation yields a strong Kondo effect, which is characterized by an enhanced T_K . This type of Kondo effect has not been considered before, probably because a singlet-triplet degeneracy does not occur in magnetic elements. Recent scaling calculations indeed indicate a strong enhancement of T_K at the singlet-triplet degeneracy [23]. These workers also argue that the total spin of the many-body Kondo state behaves as in the case of $S = 1$.

Our quantum dot has the external shape of a rectangular pillar (see Fig. 5.2a,b) and an internal confinement potential close to a two-dimensional ellipse [24]. The tunnel barriers between the quantum dot and the source and drain electrodes are thinner than in our previous devices [8,24] such that co-tunneling processes are enhanced. Figure 2d shows the linear response conductance (dc bias voltage $V_{sd} = 0$) versus gate voltage, V_g , and magnetic field, B . Dark blue regions have low conductance and correspond to the regimes of Coulomb blockade for $N = 3$ to 10. In contrast to previous experiments [9-12] on the Kondo effect, all performed on lateral quantum dots with unknown electron number, here the number of confined electrons is precisely known. Red stripes represent Coulomb peaks as high as $\sim e^2/h$. The B -dependence of the first two lower stripes reflects the ground-state evolution for $N = 3$ and 4. Their similar B -evolution indicates that the 3rd and 4th electron occupy the same orbital state with opposite spin, which is observed also for $N = 1$ and 2 (not shown). This is not the case for $N = 5$ and 6. The $N = 5$ state has $S = 1/2$, and the corresponding stripe shows a smooth evolution with B . Instead, the stripe for $N = 6$ has a kink at $B \approx 0.22$ T. From earlier analyses [24] and from measurements of the excitation spectrum at finite V_{sd} (discussed below) we can identify this kink with a transition in the ground state from a spin triplet to a spin singlet. Strikingly, at the triplet-singlet transition (at $B = B_0$ in Fig. 5.2c) we observe a strong enhancement of the conductance. In fact, over a narrow range around 0.22 T, the Coulomb gap for $N = 6$ has disappeared completely.

To explore this conductance anomaly, we show in Fig. 5.3a differential conductance measurements, dI/dV_{sd} vs V_{sd} , taken at $B = B_0$ and V_g corresponding to the dotted line in Fig. 5.2d. At $T = 14$ mK the narrow resonance around

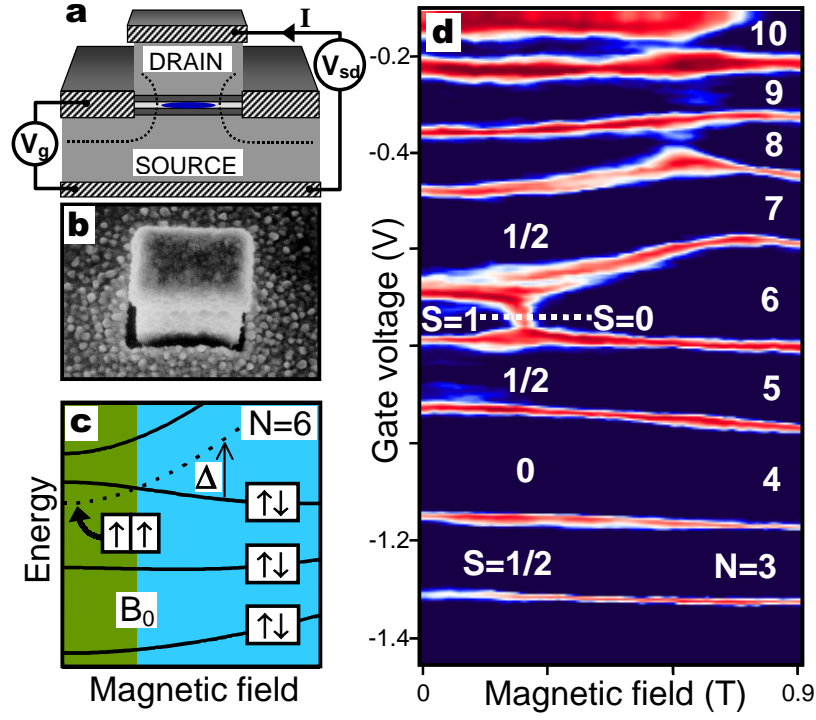


Figure 5.2: Sample description, energy spectrum and magnetic-field evolution of the ground state. (a) Cross-section of our rectangular quantum dot. The semiconductor material consists of an undoped AlGaAs(7nm)/InGaAs(12nm)/AlGaAs(7nm) double barrier structure sandwiched between n-doped GaAs source and drain electrodes. A gate electrode surrounds the pillar and is used to control the electrostatic confinement in the quantum dot. A dc bias voltage, V_{sd} , is applied between source and drain and current, I , flows vertically through the pillar. In addition to V_{sd} , we apply a modulation with rms amplitude $V_{ac} = 3 \mu\text{V}$ at 17.7 Hz for lock-in detection. The gate voltage, V_g , can change the number of confined electrons, N , one-by-one from ~ 10 at $V_g = 0$ to 0 at $V_g = -1.8 \text{ V}$. A magnetic field, B , is applied along the vertical axis. Temperature, T , is varied between 14 mK and 1 K. Our lowest effective electron temperature is $25 \pm 5 \text{ mK}$. (b) Scanning electron micrograph of a quantum dot with dimensions $0.45 \times 0.6 \mu\text{m}^2$ and height of $\sim 0.5 \mu\text{m}$. (c) Schematic energy spectrum. Solid lines represent the B -evolution of the first four orbital levels in a single-particle model. The dashed line is obtained by subtracting the two-electron exchange coupling from the fourth level. At the crossing between this dashed line and the third orbital level at $B = B_0$ the ground state for $N = 6$ undergoes a triplet-to-singlet transition. $B_0 \approx 0.22 \text{ T}$ with a slight dependence on V_g . We define Δ as the energy difference between the triplet and the singlet states. (d) Color-scale representation of the linear conductance versus V_g and B . Red stripes denote conductance peaks of height $\sim e^2/h$. Blue regions of low conductance indicate Coulomb blockade. The V_g -position of the stripes reflects the ground state evolution with B , for $N = 3$ to 10. The $N = 6$ ground state undergoes a triplet-to-singlet transition at $B_0 \approx 0.22 \text{ T}$, which results in a conductance anomaly inside the corresponding Coulomb gap.

zero bias has a full-width-at-half-maximum, $\text{FWHM} \approx 30 \mu\text{V}$. This is several times smaller than the lifetime broadening, $\Gamma = \Gamma_R + \Gamma_L \approx 150 \mu\text{V}$, as estimated from the FWHM of the Coulomb peaks. The height of the zero-bias resonance decreases logarithmically with T (see Fig. 5.3b). These are typical fingerprints of the Kondo effect. From $\text{FWHM} \approx k_B T_K$, we estimate $T_K \approx 350 \text{ mK}$. We

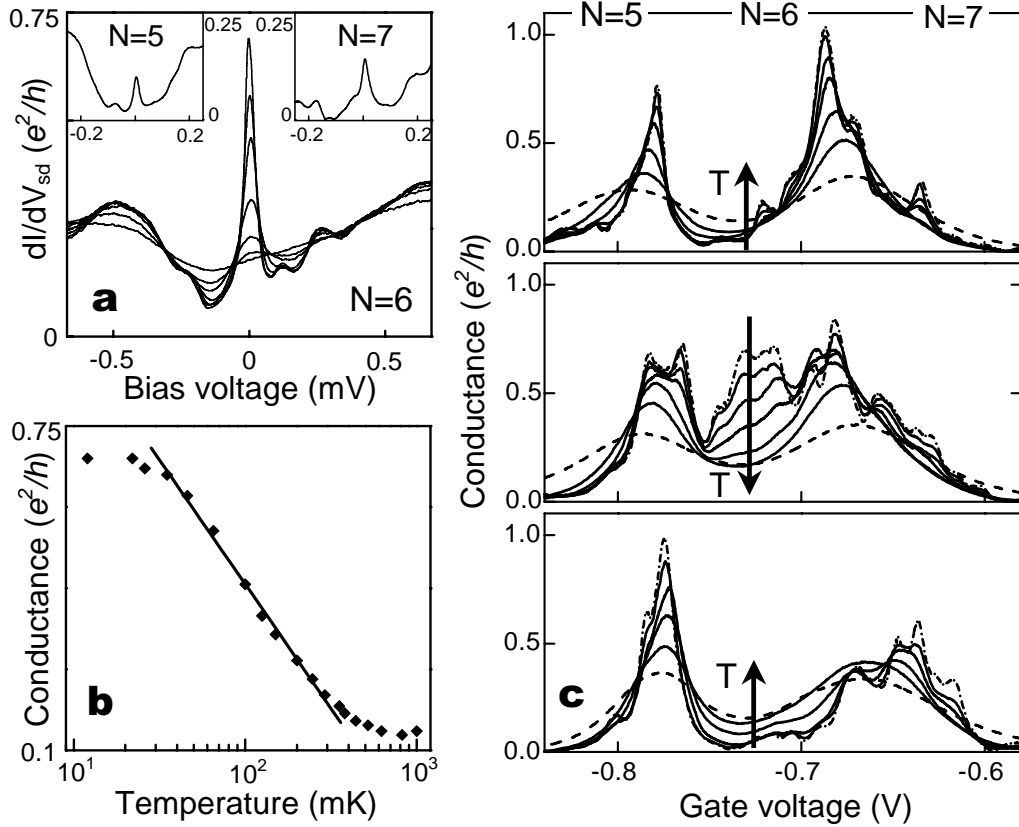


Figure 5.3: Zero-bias resonance and T -dependence of the conductance at the singlet-triplet degeneracy. (a) Kondo resonance at the singlet-triplet transition. The dI/dV_{sd} vs V_{sd} curves are taken at $V_g = -0.72 \text{ V}$, $B = 0.21 \text{ T}$ and for $T = 14, 65, 100, 200, 350, 520$, and 810 mK . Insets to (a): Kondo resonances for $N = 5$ (left inset) and $N = 7$ (right inset), measured at $V_g = -0.835 \text{ V}$ and $V_g = -0.625 \text{ V}$, respectively, and for $B = 0.11 \text{ T}$ and $T = 14 \text{ mK}$. (b) Peak height of zero-bias Kondo resonance vs T as obtained from a (solid diamonds). The line demonstrates a logarithmic T -dependence, which is characteristic for the Kondo effect. The saturation at low T is probably due to electronic noise. (c) T -dependence of the linear conductance versus V_g for $B = 0.12 \text{ T}$ (spin-triplet ground state), $B = 0.22 \text{ T}$ (singlet-triplet degeneracy), and $B = 0.32 \text{ T}$ (spin-singlet ground state). Each panel shows 7 traces at $T = 20$ (dot-dashed line), 35, 70, 120, 260, 490 (solid lines), 1050 (dashed line) mK. The arrows emphasize the temperature dependence in the valley for $N = 6$.

note that we can safely neglect the Zeeman spin splitting since $g\mu_B B_0 \approx 5 \mu\text{V} \ll k_B T_K$, implying that the spin triplet is in fact three-fold degenerate at $B = B_0$. This condition is essential to the Kondo effect illustrated in Fig. 5.1b. Alternative schemes have recently been proposed for a Kondo effect where the degeneracy of the triplet state is lifted by a large magnetic field [25,26].

For $N = 6$ we find markedly anomalous T -dependence only at the singlet-triplet degeneracy. Figure 5.3c shows the conductance versus V_g for different T . The upper panel is at $B = 0.12$ T. The two Coulomb peaks correspond to the transition from $N = 5$ to 6 and from $N = 6$ to 7. The small, short-period modulations superimposed on the Coulomb peaks are due to a weak charging effect in the upper part of GaAs pillar above the dot [27]. We will ignore this fine structure and focus on the general T -dependence. Upon increasing T , the valley conductance for $N = 6$ goes up due to thermally activated transport. A similar behavior is seen in the lower graph for $B = 0.32$ T. In contrast, at the singlet-triplet transition for $B = 0.22$ T we find an opposite T -dependence, again indicating the formation of a Kondo resonance. At the lowest T , the valley conductance is as high as $0.7 e^2/h$, which is close to the height of the Coulomb peaks.

The T -dependence for $N = 5$ and 7 is visibly different than in the non-Kondo valley for $N = 6$ (lower panel). Such a difference is a manifestation of the ordinary spin-1/2 Kondo effect expected for $N = \text{odd}$. Indeed the corresponding zero-bias resonances are clearly observed (see insets to Fig. 5.3a). Their height, however, is much smaller than for the singlet-triplet Kondo effect. There is also some indication for a triplet Kondo effect in the T -dependence for $N = 6$ at $B = 0.12$ T, although the associated zero-bias anomaly is not as apparent.

We now investigate the effect of lifting the singlet-triplet degeneracy by changing B at a fixed V_g corresponding to the dotted line in Fig. 5.2d. Near the edges of this line, i.e. away from B_0 , the Coulomb gap is well developed as denoted by the dark colors. The dI/dV_{sd} vs V_{sd} traces still exhibit anomalies, however, now at finite V_{sd} (see Fig. 5.4a). For $B = 0.21$ T we observe the singlet-triplet Kondo resonance at $V_{sd} = 0$. At higher B this resonance splits apart showing two peaks at finite V_{sd} . It is important to note that these peaks occur inside the Coulomb gap. They result from ‘inelastic’ co-tunneling events [16,28] where ‘inelastic’ refers to exchanging energy between quantum dot and electrodes (see right drawing in Fig. 5.4d). The upper traces in Fig. 5.4a, for $B < 0.21$ T, also show peak structures, although less pronounced.

In Fig. 5.4b we plot the positions of the dI/dV_{sd} peaks in the plane of V_{sd} and B . The symbols refer to different gate voltages indicating that these positions do not depend on V_g . The solid lines are obtained from the excitation spectrum measured (see Fig. 5.4c) in direct tunneling (explained on the left in Fig. 5.4d).

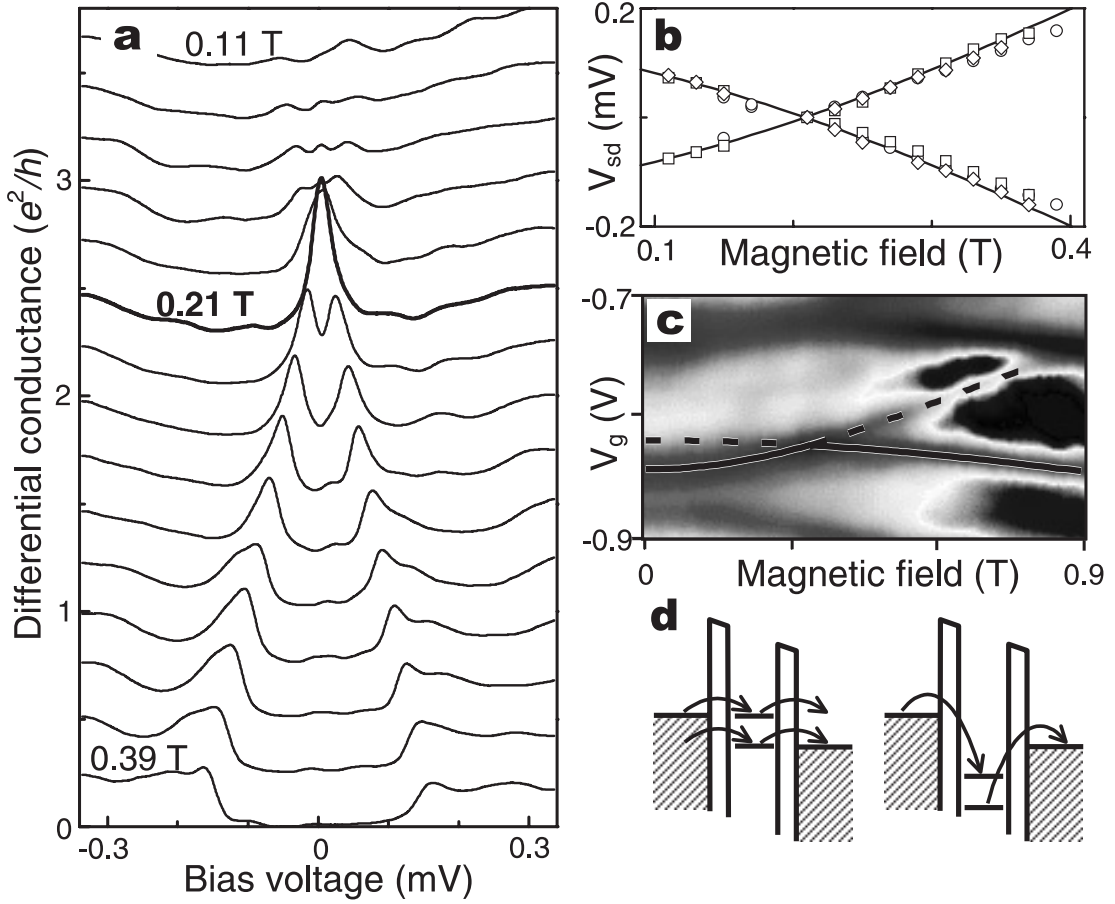


Figure 5.4: Singlet-triplet energy separation tuned by a magnetic field. (a) dI/dV_{sd} vs V_{sd} characteristics taken along the dotted line in Fig. 5.2d ($V_g = -0.72$ V) at equally spaced magnetic fields $B = 0.11, 0.13, \dots, 0.39$ T. Curves are offset by $0.25 e^2/h$. (b) Extracted peak positions from dI/dV_{sd} curves in (a) versus B . Each symbol refers to a gate voltage taken between -0.72 and -0.70 V. (c) Gray-scale plot of dI/dV_{sd} measured at $V_{sd} = 0.67$ mV as a function of B and V_g . The solid line identifies the ground state, whereas the dashed line indicates the first excited state [8] for $N = 6$. From their difference we extract the singlet-triplet energy splitting, $\Delta(B)$, using a proportionality factor $\alpha = 6.7$ meV/V to convert gate voltage into energy. The two solid lines in (b) represent $\pm\Delta(B)$ with a horizontal shift of 0.08 T to compensate for the shift of the singlet-triplet transition to a higher magnetic field in a high-bias measurement. (d) Energy diagrams for two different transport regimes, both with $eV_{sd} = \Delta$. Left: both ground and excited state lie between the two Fermi energies, so two channels are available for direct tunneling. The excitation spectrum in (c) is measured in this regime. Right: both ground and excited state lie below the Fermi levels of the leads (Coulomb blockade regime). Inelastic co-tunneling is illustrated, where one electron tunnels out of the lower energy state and another tunnels into the higher energy state.

They represent the measured B -dependence of the singlet-triplet energy difference, Δ . The fact that these independent measurements coincide implies that inelastic co-tunneling occurs when $eV_{sd} = \pm\Delta$. Note that this condition is independent of V_g , consistently with our observation. We believe that for small Δ ($\lesssim k_B T_K$) the split resonance reflects the singlet-triplet Kondo anomaly shifted to finite bias. This resembles the splitting of the Kondo resonance by the Zeeman effect [9,10,29], although on a very different B -scale. In the present case, the splitting occurs between two different multi-particle states and originates from the B -dependence of the orbital motion. For increasing Δ , the shift to larger V_{sd} induces spin-decoherence processes, which broaden and suppress the finite-bias peaks [29]. For $B \approx 0.39$ T the peaks have evolved into steps [28] which may indicate that the spin coherence associated with the Kondo effect has completely vanished.

We thank Yu.V. Nazarov, K. Maijala, S.M. Cronenwett, J.E. Mooij and Y. Tokura for discussions. We acknowledge financial support from the Specially Promoted Research, Grant-in-Aid for Scientific Research, from the Ministry of Education, Science and Culture in Japan, from the Dutch Organisation for Fundamental Research on Matter (FOM), from the NEDO joint research program (NTDP-98), and from the EU via a TMR network.

References

- [1] A.C. Hewson, *The Kondo Problem to Heavy Fermions* (Cambridge University Press, Cambridge, 1993).
- [2] D.L. Cox and M.B. Maple, Electronic pairing in exotic superconductors. *Physics Today* **48**, 32-40 (1995).
- [3] G.A. Prinz, Magnetoelectronics. *Science* **282**, 1660-1663 (1998).
- [4] D. Loss and D.P. DiVincenzo, Quantum computation with quantum dots. *Phys. Rev. A* **57**, 120-126 (1998).
- [5] V. Madhavan, W. Chen, T. Jamneala, M.F. Crommie and N.S. Wingreen, Tunneling into a Single Magnetic Atom: Spectroscopic Evidence of the Kondo Resonance. *Science* **280**, 567-569 (1998).
- [6] J. Li, W.-D. Schneider, R. Berndt and B. Delley, Kondo Scattering Observed at a Single Magnetic Impurity. *Phys. Rev. Lett.* **80**, 2893-2896 (1998).
- [7] D.D. Awschalom and D.P. DiVincenzo, Complex Dynamics of Mesoscopic Magnets. *Physics Today* **48**, 43-48 (1995).

- [8] S. Tarucha, D.G. Austing, Y. Tokura, W.G. van der Wiel and L.P. Kouwenhoven, Direct Coulomb and Exchange Interaction in Artificial Atoms. *Phys. Rev. Lett.* **84**, 2485-2488 (2000).
- [9] D. Goldhaber-Gordon, H. Shtrikman, D. Mahalu, D. Abusch-Magder, U. Meirav and M.A. Kastner, Kondo effect in a single-electron transistor. *Nature* **391**, 156-159 (1998).
- [10] S.M. Cronenwett, T.H. Oosterkamp and L.P. Kouwenhoven, A Tunable Kondo Effect in Quantum Dots. *Science* **281**, 540-544 (1998).
- [11] J. Schmid, J. Weis, K. Eberl and K. v. Klitzing, A quantum dot in the limit of strong coupling to reservoirs. *Physica B* **256-258**, 182-185 (1998).
- [12] F. Simmel, R.H. Blick, J.P. Kotthaus, W. Wegscheider and M. Bichler, Anomalous Kondo Effect in a Quantum Dot at Nonzero Bias. *Phys. Rev. Lett.* **83**, 804-807 (1999).
- [13] L.P. Kouwenhoven, C.M. Marcus, P.L. McEuen, S. Tarucha, R.M. Westervelt and N.S. Wingreen, *Electron transport in quantum dots*, in *Mesoscopic Electron Transport*, edited by L.L. Sohn, L.P. Kouwenhoven and G. Schön, (Kluwer, Series E **345**, 1997), p.105-214.
- [14] L.I. Glazman and M.E. Raikh, Resonant Kondo transparency of a barrier with quasilocal impurity states. *JETP Lett.* **47**, 452-455 (1988).
- [15] T.K. Ng and P.A. Lee, On-site Coulomb repulsion and resonant tunneling. *Phys. Rev. Lett.* **61**, 1768-1771 (1988).
- [16] D.V. Averin and Yu. V. Nazarov, Single Charge Tunneling, *Proceedings of a NATO Advanced Study Institute*, H. Grabert, M.H. Devoret, Eds., Les Houches, France, 5 March to 15 March, 1991 (Series B, **294**, 217, Plenum Press, New York, 1991).
- [17] D.C. Mattis, Symmetry of ground state in a dilute magnetic metal alloy. *Phys. Rev. Lett.* **19**, 1478-1481 (1967).
- [18] P. Nozières and A. Blandin, Kondo effect in real metals. *J. Physique* **41**, 193-211 (1980).
- [19] Y. Wan, P. Phillips and Q. Li, Suppression of the Kondo effect in quantum dots by even-odd asymmetry. *Phys. Rev. B* **51**, 14782-14785 (1995).
- [20] W. Izumida, O. Sakai and Y. Shimizu, Kondo Effect in Single Quantum Dot Systems - Study with NRG Method - *J. Phys. Soc. Jpn.* **67**, 2444-2454 (1998).

- [21] S.M. Maurer, S.R. Patel, C.M. Marcus, C.I. Duruöz and J.S. Harris Jr., Coulomb Blockade Fluctuations in Strongly Coupled Quantum Dots. *Phys. Rev. Lett.* **83**, 1403-1406 (1999).
- [22] J. Schmid, J. Weis, K. Eberl and K. von Klitzing, Absence of odd-even parity behaviour for Kondo resonances in quantum dots. *Phys. Rev. Lett.* **84**, 5824 (2000).
- [23] M. Eto and Yu.V. Nazarov, Enhancement of Kondo effect in quantum dots with even number of electrons. *Phys. Rev. Lett.* **85**, (2000).
- [24] D.G. Austing, S. Sasaki, S. Tarucha, S.M. Reimann, M. Koskinen and M. Manninen, Ellipsoidal deformation of vertical quantum dots. *Phys. Rev. B* **60**, 11514-11523 (1999).
- [25] M. Pustilnik, Y. Avishai and K. Kikoin, Quantum dots with even number of electrons: Kondo effect in a finite magnetic field. *Phys. Rev. Lett.* **84**, 1756-1759 (2000).
- [26] D. Giuliano and A. Tagliacozzo, Spin fractionalization of an even number of electrons in a quantum dot. *Phys. Rev. Lett.* **84**, 4677 (2000).
- [27] U. Sivan *et al.*, Spectroscopy, Electron-Electron Interaction, and Level Statistics in a Disordered Quantum Dot. *Europhys. Lett.* **25**, 605-611 (1994).
- [28] Y. Funabashi, K. Ohtsubo, M. Eto and K. Kawamura, Phase Relaxation and Non-Equilibrium Transport Properties through Multilevel Quantum Dot. *Jpn. J. Appl. Phys.* **38**, 388-391 (1999).
- [29] N.S. Wingreen and Y. Meir, Anderson model out of equilibrium: Noncrossing-approximation approach to transport through a quantum dot. *Phys. Rev. B* **49**, 11040-11052 (1994).
- [30] T. Inoshita, A. Shimizu, Y. Kuramoto and H. Sakaki, Correlated electron transport through a quantum dot: The multiple-level effect. *Phys. Rev. B* **48**, 14725-14728 (1993).

Chapter 6

Two-stage Kondo effect in a quantum dot at high magnetic field

W.G. van der Wiel, S. De Franceschi, J.M. Elzerman,
S. Tarucha and L.P. Kouwenhoven

J. Motohisa, F. Nakajima and T. Fukui

We report a strong Kondo effect (Kondo temperature $\sim 4\text{K}$) at high magnetic field in a selective area growth semiconductor quantum dot. The Kondo effect is ascribed to a singlet-triplet transition in the ground state of the dot. At the transition, the low-temperature conductance approaches the unitary limit. Away from the transition, for low bias voltages and temperatures, the conductance is sharply reduced. The observed behavior is compared to predictions for a two-stage Kondo effect in quantum dots coupled to single-channel leads.

This chapter has been submitted to Physical Review Letters.

The observation of the Kondo effect in quantum dots [1-3] has lead to an increased experimental and theoretical interest in this many-body phenomenon. Unlike the conventional case of bulk metals containing magnetic impurities [4], quantum dots [5] offer the possibility to study the Kondo effect at the level of a single artificial magnetic impurity [6], allowing to tune different parameters. Experiments on quantum dots have also revealed novel Kondo phenomena that have no analog in bulk-metal systems. In particular, multi-level Kondo effects have been studied both theoretically [7-12] and experimentally [13-15] that differ substantially from the ordinary case of a spin-1/2 Anderson impurity.

In this chapter, we present results on a strong Kondo effect in a lateral quantum dot at high magnetic field. We associate the Kondo effect with a magnetically induced crossing between a spin-singlet and a spin-triplet ground state [9-14]. In contrast to the results for a vertical semiconductor quantum dot [13] and for a carbon nanotube dot [14], we find a sharp reduction of the conductance at low bias voltage, V_{SD} , and temperature, T . We ascribe the different behavior to the number of channels in the leads which couple to the states in the dot. In lateral dots, tunnel barriers are obtained by successively pinching off the propagating channels. Coulomb blockade develops when the last channel is nearly pinched off. Therefore, only one channel in each lead is coupled to the dot [16]. In vertical dots however, the tunnel barrier characteristics are determined by the growth parameters, i.e. by the thickness of the different semiconductor materials forming the heterostructure and their relative conduction band offsets. In this case, more than one conducting channel can effectively couple to the dot states. The same is true for carbon nanotubes connected to metal leads. Our results, in combination with previous findings [13, 14], show that screening of higher spin states ($S \geq 1$) depends strongly on the number of channels coupled to the (artificial) magnetic impurity. Comparison is made to recent theoretical studies on quantum dots in Refs. [16, 17], which are partly inspired on the experimental work presented here.

Our device (Fig. 6.1a,b) consists of a lateral quantum dot [18] with a nominal diameter ~ 300 nm that is further decreased by application of a negative voltage to the top gate electrode (Fig. 6.1a). The top gate is also used to tune the tunnel barriers between the dot and the source and drain leads. A side gate electrode is used to change the electrostatic potential on the dot, although an effect on the dot shape and tunnel barrier characteristics is unavoidable. Basic characteristics of the device are reported in Refs. [19, 20]. All measurements have been performed in a dilution refrigerator with a base temperature of 15 mK, using a standard lock-in technique with an ac voltage between source and drain of $5 \mu\text{V}$.

Figure 6.1c shows the linear conductance, G , through the dot versus side gate voltage, V_{sg} , and perpendicular magnetic field, B . The B -dependence of the

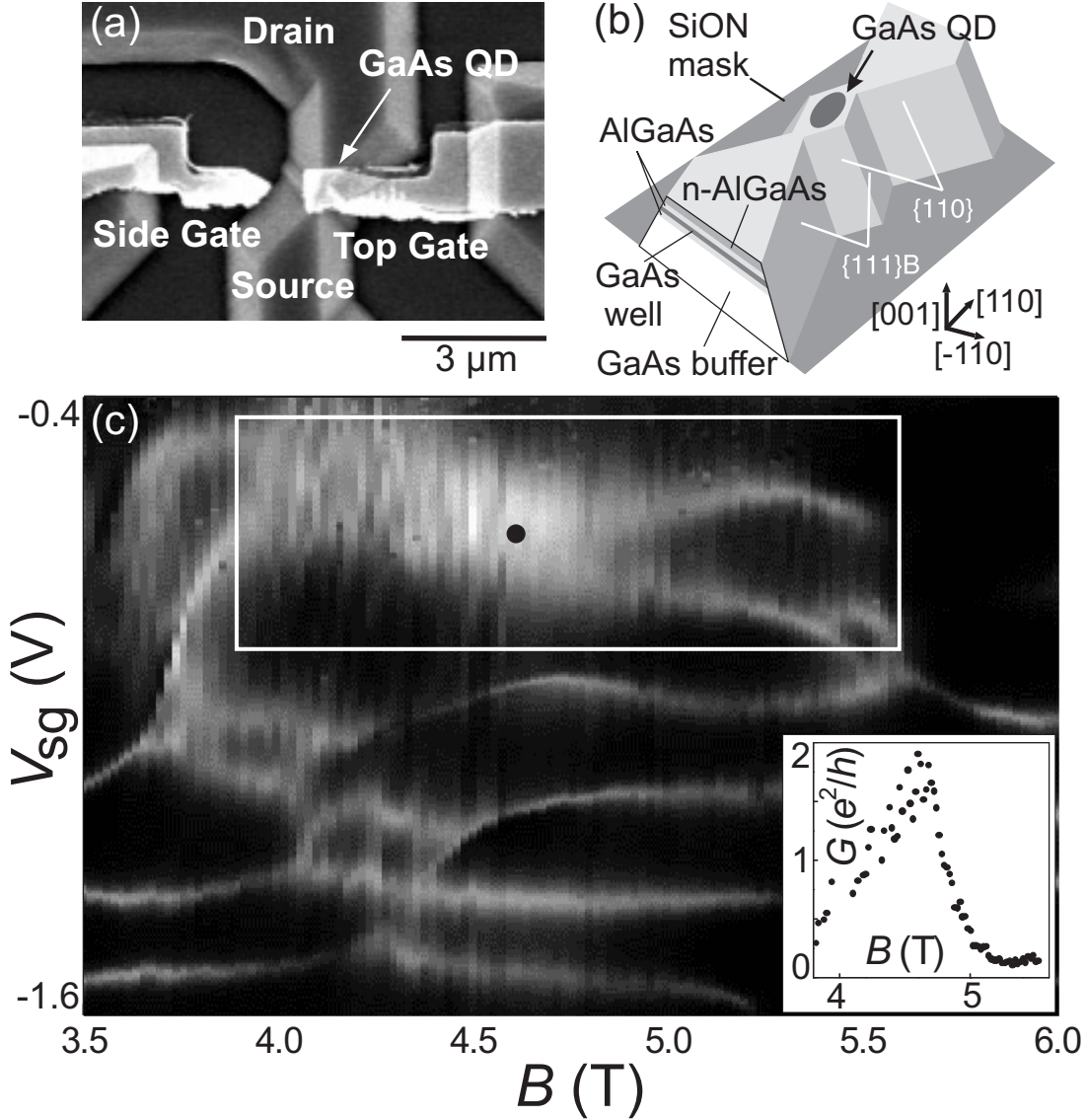


Figure 6.1: (a) Scanning electron micrograph. The device consists of a dual-gated single-electron transistor fabricated by selective area growth using metal-organic vapor phase epitaxy. (b) Schematic picture of the quantum dot (QD). An n-doped AlGaAs/GaAs heterostructure is selectively grown using a SiON mask, determining the dot shape. The crystal axes are indicated. The GaAs quantum well is 15 nm thick, lies 60 nm below the surface and has an electron density of $8.7 \times 10^{15} \text{ m}^{-2}$. (c) Gray-scale plot of the linear conductance, G , versus side gate voltage, V_{sg} , and magnetic field, B . The top gate voltage is fixed at -266 mV. Light gray lines indicate Coulomb peaks. The dark regions correspond to Coulomb blockade. The white window encloses a region of enhanced valley conductance, which is the focus of the present study. (inset) G versus B in the middle of the Coulomb valley within the white window.

Coulomb peaks (light gray lines) is rather complicated and non-monotonic. In some regions an enhanced valley conductance is observed. We will focus on the region within the white window. Moving from right to left in this window, two Coulomb peaks approach each other and the valley conductance increases. The inset to Fig. 6.1c shows G versus B in the middle of the Coulomb valley. The highest conductance is achieved around $B = 4.6$ T and $V_{sg} = -625$ mV (indicated by a ‘●’ in Fig. 6.1c). This local enhancement of the valley conductance is ascribed to a singlet-triplet (S-T) Kondo effect, as we substantiate below.

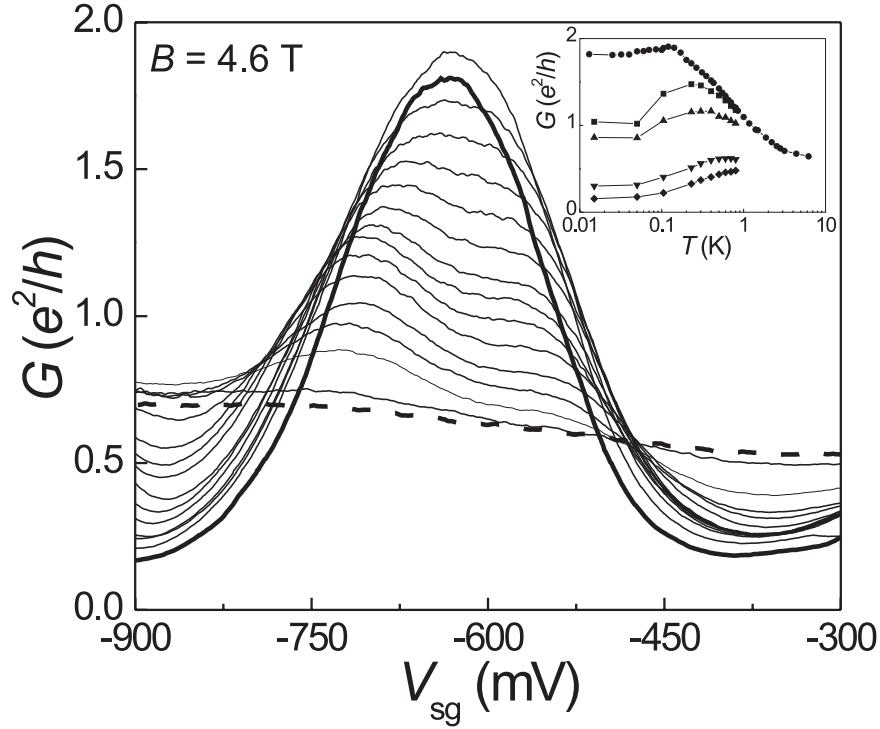


Figure 6.2: G - V_{sg} traces taken at $B = 4.6$ T and different temperatures, T , between 15 mK (thick solid line) and 6 K (thick dashed line). At the lowest T , G approaches the unitary limit at $2e^2/h$. (inset) G versus T in the middle of the Coulomb valley ($V_{sg} = -625$ mV) for different B (■ at 4.4 T, ● at 4.6 T, ▲ at 4.8 T, ▼ at 5.0 T, ◆ at 5.2 T). At the degeneracy field $B = B_0 = 4.6$ T, G decreases logarithmically between 0.1 and 2 K. The curves for other B show a clear bump that shifts to higher T with increasing distance to $B = B_0$.

To illustrate the Kondo character of the enhanced valley conductance, we show in Fig. 6.2 the T -dependence of G at $B = 4.6$ T (which we will call B_0). At low T , G at $V_{sg} = -625$ mV approaches the unitary limit at $2e^2/h$ [21-23]. Around this side gate voltage, G decreases with increasing T . The upper curve in the inset

to Fig. 6.2 shows the T -dependence of G in the middle of the Coulomb valley. The observed behavior is a typical signature of Kondo correlations. Up to our highest T of 6 K, the Kondo valley conductance keeps on decreasing, indicating an unusually strong Kondo effect. This is quite remarkable, considering the large magnetic field.

In Fig. 6.3a we show the T -dependence of the differential conductance, dI/dV_{SD} , versus source-drain voltage, V_{SD} measured at B_0 and $V_{sg} = -625$ mV. In the ordinary, spin-1/2 Kondo effect, the Kondo resonance in the dI/dV_{SD} - V_{SD} characteristics should split by $2|g|\mu_B B$ [24], where g is the Landé factor and μ_B the Bohr magneton. Assuming $g = -0.44$, as in bulk GaAs, this splitting is $230 \mu\text{eV}$ at B_0 . However, this is not observed in the dI/dV_{SD} - V_{SD} curve at B_0 (thick solid line in Fig. 6.3a). Instead, we measure a single zero-bias resonance with a full width at half maximum (FWHM) of about $300 \mu\text{eV}$, corresponding to a Kondo temperature $T_K \sim \text{FWHM}/k_B \approx 4$ K in the center of the Coulomb valley. This Kondo temperature is considerably larger than the values found in earlier experiments [1-3,13,14,23].

Based on the above considerations, we believe that the explanation for the enhanced G is an S-T transition around B_0 , assuming an even number of confined electrons. As a result of the generalized Hund's rule [25], the nature of the ground state near a level crossing can change from a singlet to a triplet, or vice versa. An S-T degeneracy leads to an enhanced low-temperature conductance as shown experimentally in Ref. [13, 14] and theoretically in Refs. [9, 10]. The local conductance enhancement at B_0 in the present study suggests a similar S-T Kondo effect. In the vertical quantum dot studied in Ref. [13], it is possible to determine the number of electrons in the dot and to identify the singlet and triplet states. The present data do not allow us to unambiguously identify the spin character of the states on both sides of B_0 .

An interesting and unexpected feature is observed when moving away from B_0 . A sharp dip develops around $V_{SD} = 0$ within a broader Kondo resonance. The dip vanishes upon increasing T , restoring the broad Kondo resonance. This is shown in Figs. 3b-d for the representative fields $B = 4.4$ T, 4.8 T and 5.0 T. The broad Kondo resonance disappears at a much slower rate with T than the sharp dip, leading to the non-monotonic behavior in the corresponding G - T curves in the inset to Fig. 6.2. Moving away from B_0 , the position of the maximum in G shifts to higher T and the low- T conductance decreases.

Increasing B from B_0 , we find that the dip width grows up to $\sim 250 \mu\text{V}$ (see Figs. 6.4a,b). In Fig. 6.4c we compare the position of the Coulomb peaks (converted from V_{sg} to energy [26]) to the positions of the dip edges. We expect the on-site Coulomb interaction energy to be essentially constant within the window

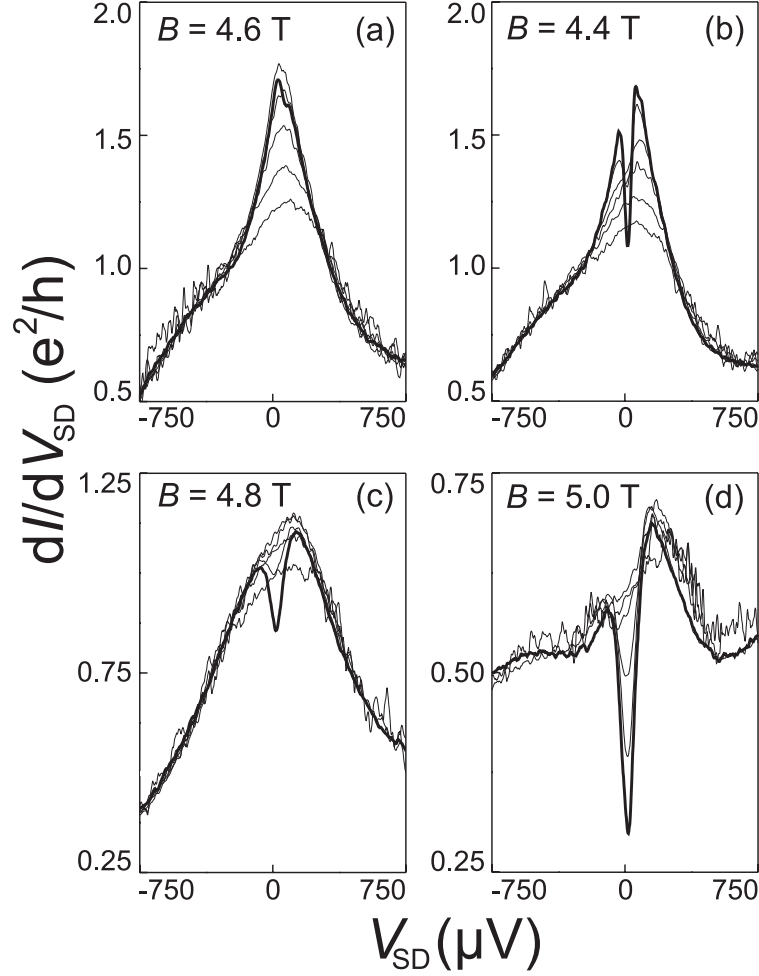


Figure 6.3: (a)-(d) T -dependence (between 15 mK, solid line, and 800 mK) of the differential conductance, dI/dV_{SD} , versus source drain voltage, V_{SD} , in the middle of the Coulomb valley for different B .

in Fig. 6.1c. Hence, we believe that the B -evolution of the Coulomb peak spacing reflects the B -dependence of the energy difference between two consecutive levels of the dot, i.e. the S-T energy spacing. The dip width shows qualitatively the same B -dependence as the spacing between the Coulomb peaks, and thus the same as that of the S-T energy spacing. The dip width at fixed B is independent of V_{sg} within the Coulomb valley where the dI/dV_{SD} - V_{SD} characteristics are measured (see Fig. 6.4c). This observation is in line with a relation between the dip width and the level spacing, irrespective of the absolute level energies.

For $3.8 < B < B_0$ we find a dip whose width does not vary significantly with B (see Figs. 6.4a,b). From Fig. 6.1c we note that, in the same B -range, the

Coulomb peaks are closely and constantly spaced, denoting a virtually constant Δ . This may explain why there is no clear B -dependence of the dip width for $B < B_0$.

In summary, on both sides of B_0 we observe a non-monotonic T -dependence of G and a narrow anti-resonance superimposed on a broader Kondo resonance. The widths of these resonances correspond to two clearly distinct energy scales. Our observations are in qualitative agreement with recent theoretical predictions

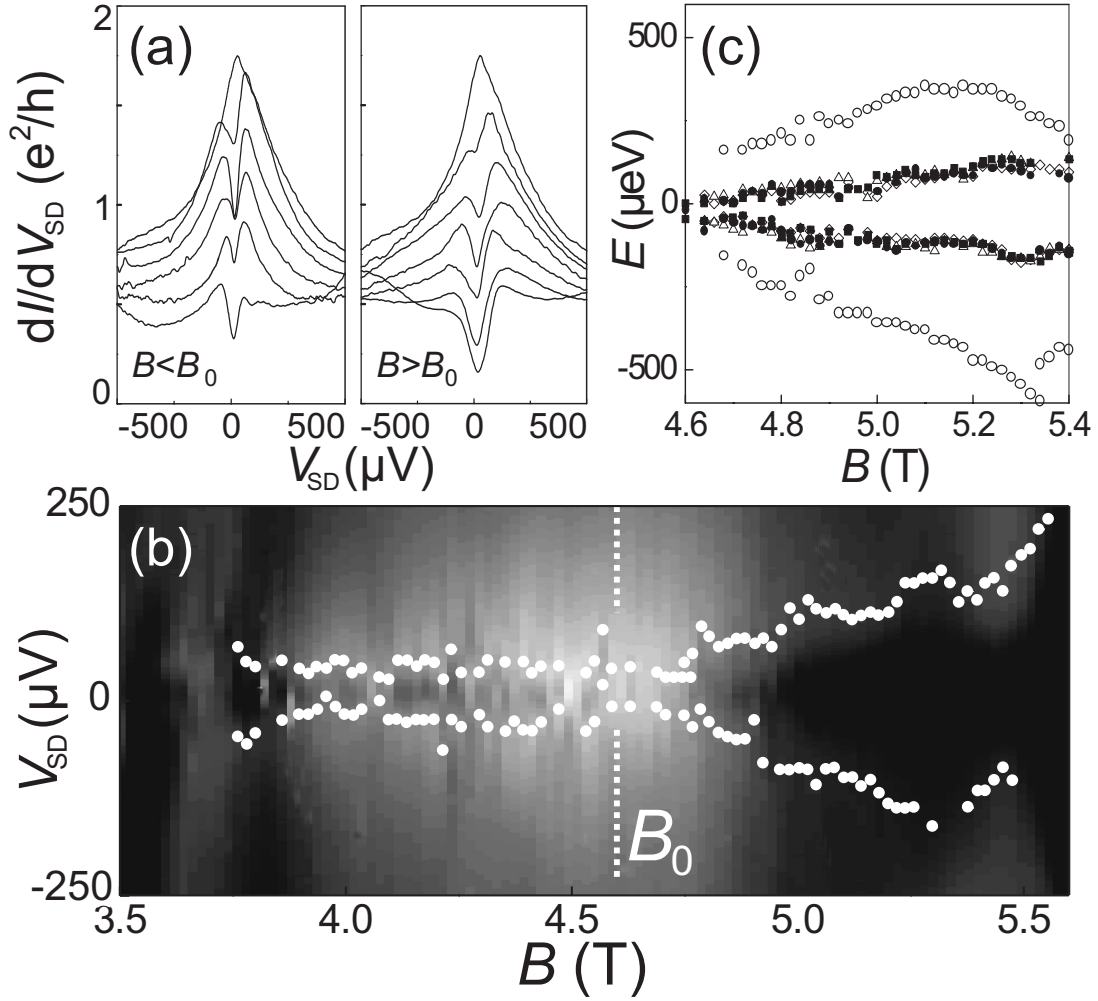


Figure 6.4: (a) dI/dV_{SD} versus V_{SD} between 3.8 and 4.6 T (bottom to top, left), and between 4.6 and 5.2 T (top to bottom, right). (b) Gray-scale plot of dI/dV_{SD} versus B and V_{SD} . The edges of the zero bias dip are indicated by white dots. (c) Comparison between the B -evolution of the dip edges (different symbols correspond to different V_{sg} -values within the Coulomb valley) and that of the Coulomb peaks (\circ). Note that the distance between the Coulomb peaks includes a (constant) charging energy.

for quantum dots coupled to single-channel leads [16, 17]. The single-channel character of the leads results in both studies, but under different conditions, to a *two-stage* Kondo effect. Two-stage Kondo phenomena have been theoretically studied also in other systems, such as coupled magnetic impurities in metals [27]. However, no experimental observation has been reported so far.

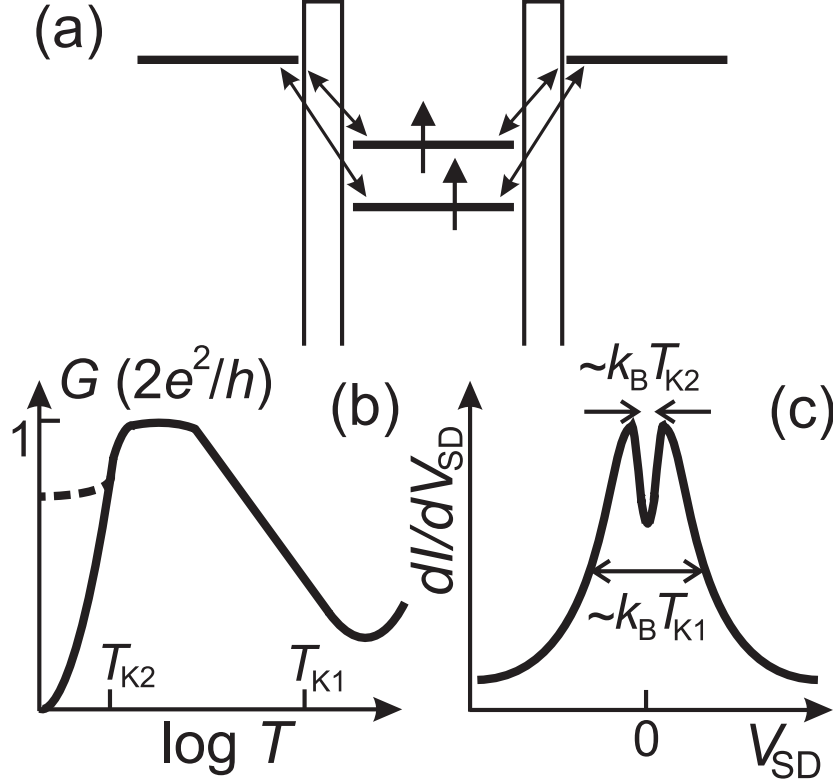


Figure 6.5: Schematics of a two-stage Kondo effect. (a) Two single-particle states with total spin $S = 1$ coupled to single channel leads. (b) T -dependence of G showing the different regimes characterized by the energy scales T_{K1} and T_{K2} . The dashed line corresponds to the case of a finite electron temperature and/or Zeeman energy. (c) dI/dV_{SD} - V_{SD} showing a dip with a width $\sim k_B T_{K2}$ within a Kondo resonance with width $\sim k_B T_{K1}$.

For a two-stage Kondo effect to occur in quantum dots, it is necessary that the dot has a spin state $S \geq 1$ coupled to single-channel leads, as illustrated in Fig. 6.5a for $S = 1$. Instead of one low-energy scale, T_K , a two-stage Kondo effect is characterized by two separate energy scales T_{K1} and T_{K2} ($T_{K2} < T_{K1}$). The first-stage screening process with characteristic energy scale T_{K1} is an *underscreened* Kondo effect, reducing the net spin from $S = 1$ to $S = 1/2$. The second stage of the Kondo effect, with a smaller energy scale T_{K2} , reduces the spin to $S = 0$,

forming a spin singlet. For $T_{K2} < (T, V_{SD}) < T_{K1}$, the first-stage Kondo screening overcomes the Coulomb blockade and G is expected to reach the unitary limit. For $(T, V_{SD}) < T_{K2}$, the second stage of the Kondo effect quenches the first one, resulting in a suppression of G , ideally to zero. A finite electron temperature or Zeeman energy may reduce the effect of the second screening process. The signatures of a two-stage Kondo effect are a non-monotonic T -dependence of G and a sharp dip superimposed on the usual zero-bias resonance in the dI/dV_{SD} , as schematically depicted in Figs. 6.5b and 6.5c, respectively.

Our results are very similar to the schematic graphs in Fig. 6.5b,c, supporting an interpretation in terms of a two-stage Kondo effect. As the character of the ground state on both sides of B_0 may differ, the mechanism underlying the two-stage Kondo effect need not be the same though. Hofstetter and Schoeller find a two-stage Kondo effect for a singlet ground state with a nearby triplet excited state [17]. Pustilnik and Glazman predict a two-stage Kondo effect for an $S \geq 1$ ground state when there is significant asymmetry in the dot-lead coupling [16]. The latter model, however, does not include dot excitations, which can be important in proximity of an S-T transition.

For $B > B_0$, we can tune the S-T spacing, Δ , between ~ 0 and a few hundred μeV (see open white circles in Fig. 6.4c). Due to the high Kondo temperature ($k_B T_{K1} \sim 300 \mu\text{eV}$), we cover the range from $\Delta \ll k_B T_{K1}$ to $\Delta \approx k_B T_{K1}$. Over a B -range of about 0.5 T we observe that the dip width scales linearly with Δ . From the observed dip width (Fig. 6.4c) we can estimate $T_{K2} \lesssim 1$ K. The observed behavior for $B > B_0$ is in line with the results of Ref. [17] for the case of a singlet ground state with a nearby triplet. There the energy scale T_{K2} increases linearly with Δ for $\Delta \sim k_B T_{K1}$. We also note that the absence of a triplet Kondo resonance for $B > B_0$ favors the interpretation of a singlet ground state here.

For $B < B_0$ there is no clear B -dependence of the conductance dip. Possibly, a singlet ground state is close to a triplet excited state over a relatively wide B -range. In this case an explanation as for $B > B_0$ applies. This interpretation requires a transition from a singlet ground state ($B < B_0$) to a region of S-T degeneracy ($B \sim B_0$) to again a singlet ground state ($B > B_0$). Alternatively, the ground state for $B < B_0$ could also be a triplet, in which case the mechanism proposed in Ref. [16] may be responsible for the dip.

We conclude that, irrespective of the precise model, our results can be interpreted in terms of a two-stage Kondo effect, characterized by two well-separated energy scales.

We thank W. Hofstetter, H. Schoeller, M. Pustilnik, L. Glazman, T. Costi, W. Izumida, M. Eto and R. Schouten for their help. We acknowledge financial support from the Specially Promoted Research Grant-in-Aid for Scientific Research;

Ministry of Education, Culture, Sports, Science and Technology in Japan; the Dutch Organization for Fundamental Research on Matter; the Core Research for Evolutional Science and Technology (CREST-JST); and the European Union through a Training and Mobility of Researchers Program network.

References

- [1] D. Goldhaber-Gordon, H. Shtrikman, D. Mahalu, D. Abusch-Magder, U. Meirav and M.A. Kastner, *Nature* **391**, 156 (1998).
- [2] S.M. Cronenwett, T.H. Oosterkamp and L.P. Kouwenhoven, *Science* **281**, 540 (1998).
- [3] J. Schmid, J. Weis, K. Eberl and K. von Klitzing, *Physica B* **256-258**, 182 (1998).
- [4] J. Kondo, *Prog. Theor. Phys.* **32**, 37 (1964).
- [5] L.P. Kouwenhoven, C.M. Marcus, P.L. McEuen, S. Tarucha, R.M. Westervelt and N.S. Wingreen, *Electron transport in quantum dots*, in *Mesoscopic Electron Transport*, edited by L.L. Sohn, L.P. Kouwenhoven and G. Schön, (Kluwer, Series E **345**, 1997), p.105-214.
- [6] L.I. Glazman and M.E. Raikh, *JETP Lett.* **47**, 452 (1988).
- [7] T. Inoshita, A. Shimizu, Y. Kuramoto and H. Sakaki, *Phys. Rev. B* **48**, 14725 (1993).
- [8] M. Pustilnik, Y. Avishai and K. Kikoin, *Phys. Rev. Lett.* **84**, 1756 (2000).
- [9] M. Eto and Yu.V. Nazarov, *Phys. Rev. Lett.* **85**, 1306 (2000).
- [10] M. Pustilnik and L.I. Glazman, *Phys. Rev. Lett.* **85**, 2993 (2000).
- [11] M. Pustilnik and L.I. Glazman, *Phys. Rev. B* **64**, 045328 (2001).
- [12] M. Pustilnik, L.I. Glazman, D.H. Cobden and L.P. Kouwenhoven, *cond-mat/0010336* (2001).
- [13] S. Sasaki, S. De Franceschi, J.M. Elzerman, W.G. van der Wiel, M. Eto, S. Tarucha and L.P. Kouwenhoven, *Nature* **405**, 764 (2000).
- [14] J. Nyg ård, D.H. Cobden and P.E. Lindelof, *Nature* **408**, 342 (2000).
- [15] J. Schmid *et al.*, *Phys. Rev. Lett.* **84**, 5824 (2000).
- [16] M. Pustilnik and L.I. Glazman, *cond-mat/0105155*.
- [17] W. Hofstetter and H. Schoeller, *cond-mat/0108359*.

- [18] F. Nakajima, Y. Ogasawara, J. Motohisa and T. Fukui, to be published in J. Appl. Phys.
- [19] J. Motohisa, W.G. van der Wiel, J.M. Elzerman, S. De Franceschi, F. Nakajima, Y. Ogasawara, T. Fukui and L.P. Kouwenhoven, to be published in Physica E.
- [20] J. Motohisa, W.G. van der Wiel, J.M. Elzerman, S. De Franceschi, F. Nakajima, T. Fukui and L.P. Kouwenhoven, unpublished.
- [21] T.K. Ng and P.A. Lee, Phys. Rev. Lett. **61**, 1768 (1988).
- [22] A. Kawabata, J. Phys. Soc. Jpn. **60**, 3222 (1991).
- [23] W.G. van der Wiel, S. De Franceschi, T. Fujisawa, J.M. Elzerman, S. Tarucha and L.P. Kouwenhoven, Science **289**, 2105 (2000).
- [24] Y. Meir, N.S. Wingreen and P.A. Lee, Phys. Rev. Lett. **70** 2601 (1993); N.S. Wingreen and Y. Meir, Phys. Rev. B **49**, 11040 (1994).
- [25] S. Tarucha, D.G. Austing, Y. Tokura, W.G. van der Wiel and L.P. Kouwenhoven, Phys. Rev. Lett. **84**, 2485 (2000).
- [26] We use $\varepsilon = \alpha V_{sg} + \text{constant}$, with $\alpha = C_{sg}/C_{\Sigma} = 3.4 \mu\text{eV/mV}$. Here, ε is the level energy, C_{sg} the capacitance of the side gate and C_{Σ} the total capacitance of the dot.
- [27] C. Jayaprakash *et al.*, Phys. Rev. Lett. **47**, 737 (1981); L.C. Andreani and H. Beck, Phys. Rev. B **48**, 7322 (1993); N. Andrei and A. Jerez, Phys. Rev. Lett. **74**, 4507 (1995); J.B. Silva *et al.*, Phys. Rev. Lett. **76**, 275 (1996).

Chapter 7

Double Quantum Dots in Series

W.G. van der Wiel, S. De Franceschi, J.M. Elzerman
T. Fujisawa, S. Tarucha and L.P. Kouwenhoven

We review electron transport experiments on two lateral quantum dots coupled in series. We give an introduction to the charge stability diagram in terms of the electrochemical potentials of both dots. Resonant tunneling experiments show that the double dot geometry allows for an accurate determination of the intrinsic lifetime of discrete energy states in quantum dots. The evolution of discrete energy levels in magnetic field is studied. The resolution allows to resolve avoided crossings in the spectrum of a quantum dot. With microwave spectroscopy it is possible to probe the transition from ionic bonding (for weak inter-dot tunnel coupling) to covalent bonding (for strong inter-dot tunnel coupling) in a double dot artificial molecule. This review on the present experimental status of double quantum dot studies is motivated by their relevance for realizing solid state quantum bits.

7.1 Introduction

Quantum dots are man-made sub-micron structures in a solid, typically consisting of 10^3 - 10^9 atoms and a comparable number of electrons [1]. In semiconductor quantum dots all electrons are tightly bound, except for a small number of free electrons, which can range from zero to several thousands. For the quantum dot devices considered in this review, the starting point for fabrication is formed by a heterostructure consisting of different semiconductor materials (GaAs/AlGaAs). The free electrons are strongly confined to the interface between GaAs and AlGaAs, forming a 2-dimensional electron gas (2DEG). Confinement in the other two dimensions is accomplished by locally depleting the 2DEG, via etching techniques or metal gate electrodes. The resulting structure is weakly coupled to source and drain electrical contacts by tunnel barriers, connecting it to the outside world.

An important element of electronic transport through quantum dots is Coulomb blockade [1-3]. An extra electron can only be added to the dot, if enough energy is provided to overcome the Coulomb repulsion between the electrons. Next to this purely classical effect, the confinement in all three directions leads to quantum effects that strongly influence electronic transport at low temperature. In particular it leads to the formation of a discrete (0D) energy spectrum, resembling that of an atom. This and other similarities have therefore lead to the name artificial atoms for quantum dots [4].

The next logical step after studying individual quantum dots is to study systems of more than one dot. Where single quantum dots are regarded as ‘artificial atoms’, two quantum dots can be coupled to form an ‘artificial molecule’. Depending on the strength of the inter-dot coupling, the two dots can form ionic-like (weak tunnel coupling) or covalent-like bonds (strong tunnel coupling). In the case of ionic bonding the electrons are localized on the individual dots. The binding occurs, because a static redistribution of electrons leads to an attractive Coulomb interaction. Weakly, electrostatically coupled quantum dots with negligible inter-dot tunnel conductance are covered by orthodox Coulomb blockade theory [3]. In the case of covalent bonding, two electron states are quantum-mechanically coupled. The main requirement for covalent binding is that an electron can tunnel many times between the two dots in a phase-coherent way. Here the electron cannot be regarded as a particle that resides in one particular dot, but it must be thought of as a coherent wave that is delocalized over the two dots. The bonding state of a strongly coupled artificial molecule has a lower energy than the energies of the original states of the individual dots. This energy gain forms the binding force between the two dots.

The theoretical possibility to perform certain tasks in a much more efficient way using a ‘quantum computer’ instead of a ‘classical computer’, has stimulated the search for physical realizations of the basic building block of such a computer: the quantum bit. In principle, any quantum two-level system can be used as such a qubit. In particular, recent studies have put forward double quantum dots as interesting candidates for realizing qubits [5]. The possible application of double quantum dot devices in quantum logic forms an important motivation for this work.

In this review we concentrate on electron transport through lateral double quantum dots coupled in series. All devices have been fabricated and all experiments have been performed at Delft University of Technology and NTT Basic Research Laboratories. Experimental studies of electron transport through double lateral quantum dots coupled in series, are described in Refs. [6-23] and in lateral double dots coupled in parallel in Refs. [22,24-26]. Vertical double quantum dot structures [27-34] fall outside the focus of this review. In vertical structures, the characteristics of the tunnel barriers are set by the growth parameters of the heterostructure, limiting the experimental tunability. Besides that, the gate geometry used in these devices, makes it difficult to address dots independently.

As a first step to understanding double dot systems we introduce the stability diagram [35], or honeycomb diagram, in section 7.2. It is a convenient tool in the analysis of double dot transport properties. Resonant tunneling experiments discussed in section 7.3, show that the resonant widths are only determined by the lifetime of the discrete energy states, independent of the electron temperature. In section 7.4 we discuss level spectroscopy in a magnetic field. The double dot geometry offers sufficient energy resolution to probe intra-dot level repulsion. In section 7.5 we present microwave spectroscopy measurements on a quantum dot molecule. We illustrate the transition from a weakly coupled double dot to a strongly coupled double dot, by discussing a two-level system in section 7.5.1. Although being a clear simplification, the mapping of the double dot on a two-level system grasps much of the physics of the experiments presented in section 7.5. Irradiation with microwaves leads to photon assisted tunneling (PAT) (sections 7.5.2 and 7.5.3), which turns out to be a powerful tool not only to reveal the character of the inter-dot coupling, but also to quantitatively determine the bonding strength.

7.2 Stability diagram

In this section we introduce the stability – or honeycomb – diagram that visualizes the equilibrium charge states of two serially coupled dots.

7.2.1 Linear transport regime

Classical theory

We start with a purely classical description in which the influence of discrete quantum states is not taken into account yet [22, 35, 36]. The double dot is modeled as a network of resistors and capacitors (Fig. 7.1). The number of electrons on dot 1(2) is $N_{1(2)}$. Each dot is capacitively coupled to a gate voltage

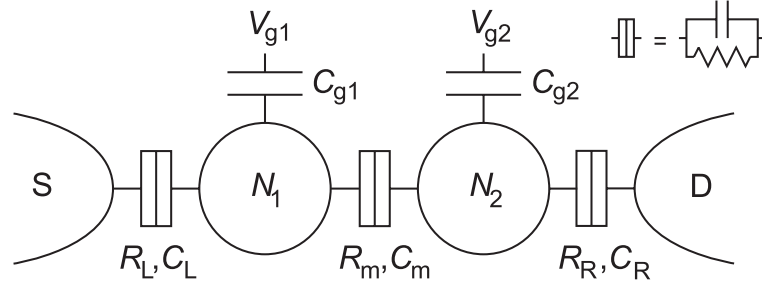


Figure 7.1: Network of resistors and capacitors representing two quantum dots coupled in series. The different elements are explained in the text. Note that tunnel barriers are characterized by a resistor and a capacitor, as indicated in the inset.

$V_{g1(2)}$ through a capacitor $C_{g1(2)}$ and to the source (S) or drain (D) contact through a tunnel barrier represented by a resistor $R_{L(R)}$ and a capacitor $C_{L(R)}$ connected in parallel. The dots are coupled to each other by a tunnel barrier represented by a resistor R_m and a capacitor C_m in parallel. The bias voltage, V , is applied to the source contact with the drain contact grounded (asymmetric bias). In this section we consider the linear transport regime, i.e. $V \approx 0$. If cross-capacitances (such as between V_{g1} and dot 2), other voltage sources and stray capacitances are negligible, the double dot electrostatic energy reads (a full derivation is given in Appendix A)

$$\begin{aligned}
U(N_1, N_2) &= \frac{1}{2}N_1^2 E_{C1} + \frac{1}{2}N_2^2 E_{C2} + N_1 N_2 E_{Cm} + f(V_{g1}, V_{g2}) \quad (7.1) \\
f(V_{g1}, V_{g2}) &= \frac{1}{-|e|} \{ C_{g1} V_{g1} (N_1 E_{C1} + N_2 E_{Cm}) + C_{g2} V_{g2} (N_1 E_{Cm} + N_2 E_{C2}) \} \\
&\quad + \frac{1}{e^2} \{ \frac{1}{2} C_{g1}^2 V_{g1}^2 E_{C1} + \frac{1}{2} C_{g2}^2 V_{g2}^2 E_{C2} + C_{g1} V_{g1} C_{g2} V_{g2} E_{Cm} \}
\end{aligned}$$

where $E_{C1(2)}$ is the charging energy of the individual dot 1(2) and E_{Cm} is the electrostatic coupling energy. The coupling energy E_{Cm} is the change in the energy of one dot when an electron is added to the other dot. These energies can be expressed in terms of the capacitances as follows

$$E_{C1} = \frac{e^2}{C_1} \left(\frac{1}{1 - \frac{C_m^2}{C_1 C_2}} \right); \quad E_{C2} = \frac{e^2}{C_2} \left(\frac{1}{1 - \frac{C_m^2}{C_1 C_2}} \right); \quad E_{Cm} = \frac{e^2}{C_m} \left(\frac{1}{\frac{C_1 C_2}{C_m^2} - 1} \right) \quad (7.2)$$

Here $C_{1(2)}$ is the sum of all capacitances attached to dot 1(2) including C_m : $C_{1(2)} = C_{L(R)} + C_{g1(2)} + C_m$. Note that $E_{C1(2)}$ can be interpreted as the charging energy of the single, uncoupled dot 1(2) multiplied by a correction factor that accounts for the coupling. When $C_m = 0$, and hence $E_{Cm} = 0$, Eq. 7.1 reduces to

$$U(N_1, N_2) = \frac{(-N_1|e| + C_{g1}V_{g1})^2}{2C_1} + \frac{(-N_2|e| + C_{g2}V_{g2})^2}{2C_2} \quad (7.3)$$

This is the sum of the energies of two independent dots. In the case when C_m becomes the dominant capacitance ($C_m/C_{1(2)} \rightarrow 1$), the electrostatic energy is given by

$$U(N_1, N_2) = \frac{[-(N_1 + N_2)|e| + C_{g1}V_{g1} + C_{g2}V_{g2}]^2}{2(\tilde{C}_1 + \tilde{C}_2)} \quad (7.4)$$

This is the energy of a single dot with a charge $N_1 + N_2$ and a capacitance of $\tilde{C}_1 + \tilde{C}_2$, where $\tilde{C}_{1(2)} = C_{1(2)} - C_m$ is the capacitance of dot 1(2) to the outside

world. Thus, a large inter-dot capacitance C_m effectively leads to one big dot.

The electrochemical potential $\mu_{1(2)}(N_1, N_2)$ of dot 1(2) is defined as the energy needed to add the $N_{1(2)}$ th electron to dot 1(2), while having $N_{2(1)}$ electrons on dot 2(1). Using the expression for the total energy Eq. 7.1, the electrochemical potentials of the two dots are

$$\begin{aligned}\mu_1(N_1, N_2) &\equiv U(N_1, N_2) - U(N_1 - 1, N_2) \\ &= (N_1 - \frac{1}{2})E_{C1} + N_2E_{Cm} - \frac{1}{|e|} (C_{g1}V_{g1}E_{C1} + C_{g2}V_{g2}E_{Cm})\end{aligned}\quad (7.5)$$

$$\begin{aligned}\mu_2(N_1, N_2) &\equiv U(N_1, N_2) - U(N_1, N_2 - 1) \\ &= (N_2 - \frac{1}{2})E_{C2} + N_1E_{Cm} - \frac{1}{|e|} (C_{g1}V_{g1}E_{Cm} + C_{g2}V_{g2}E_{C2})\end{aligned}\quad (7.6)$$

The change in $\mu_1(N_1, N_2)$ if, at fixed gate voltages, N_1 is changed by one, $\mu_1(N_1 + 1, N_2) - \mu_1(N_1, N_2) = E_{C1}$, is called the *addition energy* of dot 1 and equals the charging energy of dot 1 in this classical regime. Similarly, the addition energy of dot 2 equals E_{C2} , and $\mu_1(N_1, N_2 + 1) - \mu_1(N_1, N_2) = \mu_2(N_1 + 1, N_2) - \mu_2(N_1, N_2) = E_{Cm}$. In the next section we will discuss the addition energy in the quantum regime, where also the spacing between discrete energy levels plays a role.

From the electrochemical potentials in Eqs. 7.5 and 7.6 we construct a charge stability diagram, giving the equilibrium electron numbers N_1 and N_2 as a function of V_{g1} and V_{g2} . We define the electrochemical potentials of the left and right leads to be zero if no bias voltage is applied, $\mu_L = \mu_R = 0$. Hence, the equilibrium charges on the dots are the largest values of N_1 and N_2 for which both $\mu_1(N_1, N_2)$ and $\mu_2(N_1, N_2)$ are less than zero. If either is larger than zero, electrons escape to the leads. This constraint, plus the fact that N_1 and N_2 must be integers, creates hexagonal domains in the (V_{g1}, V_{g2}) -phase space in which the charge configuration is stable.

For completely decoupled dots ($C_m = 0$) the diagram looks as in Fig. 7.2a. The gate voltage $V_{g1(2)}$ changes the charge on dot 1(2), without affecting the charge on the other. If the coupling is increased, the domains become hexagonal (Fig. 7.2b). The vertices of the square domains have separated into ‘triple-points’. When C_m becomes the dominant capacitance ($C_m/C_{1(2)} \rightarrow 1$), the triple-point separation reaches its maximum (see Fig. 7.2c). The double dot behaves like one

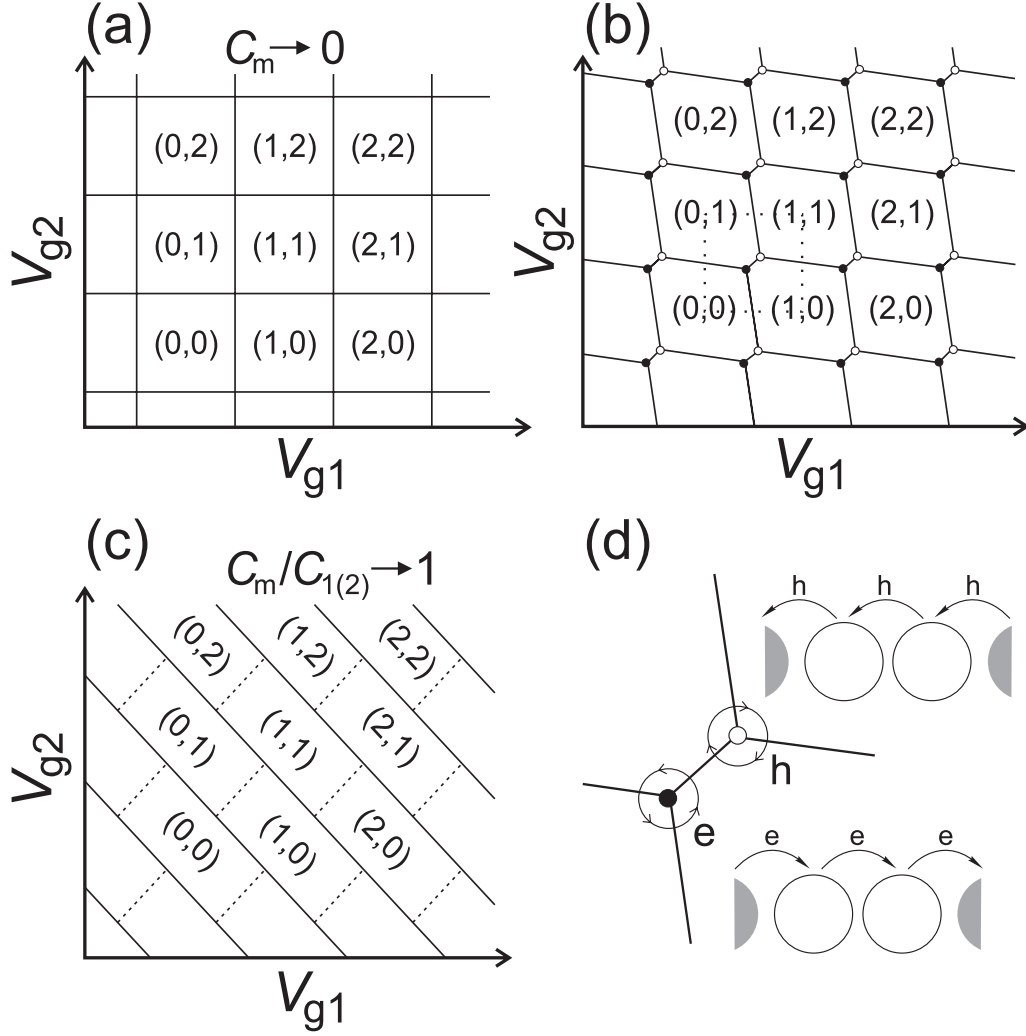


Figure 7.2: Schematic stability diagram of the double-dot system for (a) small, (b) intermediate, and (c) large inter-dot coupling. The equilibrium charge on each dot in each domain is denoted by (N_1, N_2) . The two kinds of triple-points corresponding with the electron transfer process (●) and the hole transfer process (○) are illustrated in (d). The region in the dotted square in (b) is depicted in more detail in Fig. 7.5.

dot with charge $N_1 + N_2$, as seen from Eq. 7.4.

We are considering the linear regime of conductance, implying $\mu_L - \mu_R = -|e|V \approx 0$. In order to obtain a measurable current, the tunnel barriers need to be sufficiently transparent. At the same time, however, the tunnel barriers need to be sufficiently opaque to ensure a well-defined electron number on each dot, as explained in chapter 1. For double dots coupled in series, a conductance resonance is found when electrons can tunnel through both dots. This condition is met

whenever three charge states become degenerate, i.e. whenever three boundaries in the honeycomb diagram meet in one point. In Fig. 7.2d two kinds of such triple-points are distinguished, (\bullet) and (\circ) , corresponding to different charge transfer processes. At the triple point (\bullet) , the dots cycle through the sequence $(N_1, N_2) \rightarrow (N_1 + 1, N_2) \rightarrow (N_1, N_2 + 1) \rightarrow (N_1, N_2)$, which shuttles one electron through the system. This process is illustrated by the counterclockwise path e and the diagram of an electron sequentially tunneling from the left lead to the right in Fig. 7.2d. At the other triple-point (\circ) , the sequence is $(N_1 + 1, N_2 + 1) \rightarrow (N_1 + 1, N_2) \rightarrow (N_1, N_2 + 1) \rightarrow (N_1 + 1, N_2 + 1)$, corresponding to the clockwise path h in Fig. 7.2d. This can be interpreted as the sequential tunneling of a hole in the direction opposite to the electron. The energy difference between both processes determines the separation between the triple-points (\bullet) and (\circ) , and is given by E_{Cm} , as defined in Eq. 7.2.

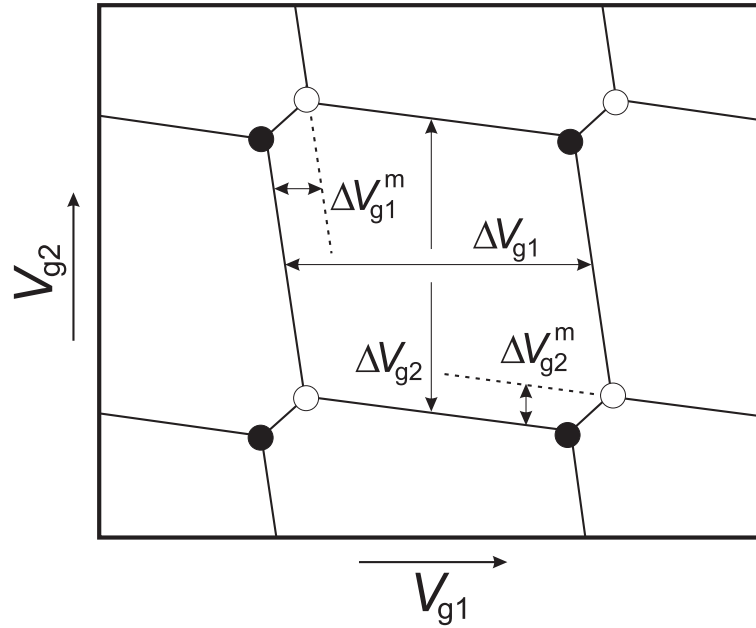


Figure 7.3: Schematic stability diagram showing the Coulomb peak spacings given in Eqs. 7.8 and 7.10. These spacings can be determined experimentally by connecting the triple-points.

The dimensions of the honeycomb cell (see Fig. 7.3) can be related to the capacitances using Eqs. 7.5 and 7.6. From

$$\mu_1(N_1, N_2; V_{g1}, V_{g2}) = \mu_1(N_1 + 1, N_2; V_{g1} + \Delta V_{g1}, V_{g2}) \quad (7.7)$$

we obtain

$$\Delta V_{g1} = \frac{|e|}{C_{g1}} \quad (7.8)$$

and similarly we can derive

$$\Delta V_{g2} = \frac{|e|}{C_{g2}} \quad (7.8')$$

From

$$\mu_1(N_1, N_2; V_{g1}, V_{g2}) = \mu_1(N_1, N_2 + 1; V_{g1} + \Delta V_{g1}^m, V_{g2}) \quad (7.9)$$

we obtain

$$\Delta V_{g1}^m = \frac{|e|C_m}{C_{g1}C_2} = \Delta V_{g1} \frac{C_m}{C_2} \quad (7.10)$$

and similarly we can derive

$$\Delta V_{g2}^m = \frac{|e|C_m}{C_{g2}C_1} = \Delta V_{g2} \frac{C_m}{C_1} \quad (7.10')$$

However, for a full characterization of all capacitances in the system an analysis in the non-linear transport regime is required, as is discussed in section 7.2.2.

Above we assumed that V_{g1} and V_{g2} only couple directly to the respective dots. In practice, however, there is a finite cross-capacitance from one gate to the other. The respective cross-capacitances result in a change of the slope of the charge domain boundaries in the honeycomb diagram. From Figs. 7.2b and 7.3 it is clear that both kinds of triple points (\bullet and \circ) form a square lattice. However, with finite cross-capacitances the positions of the triple points move to lower $V_{g1(2)}$ for increasing $V_{g2(1)}$ (at constant V).

Quantized states

The discussion of the stability diagram so far has been completely classical. However, the strong confinement of electrons in the dots can lead to the formation of a discrete energy spectrum. To account for the quantized energy states in the dot, we need to incorporate their energies in the electrochemical potential. The electrochemical potential for adding an electron into energy level n of dot i is denoted by $\mu_{i,n}$. Within the constant interaction model (see chapter 1), $\mu_{i,n}$ is the sum of the classical electrochemical potential μ_i^{class} and the single-particle

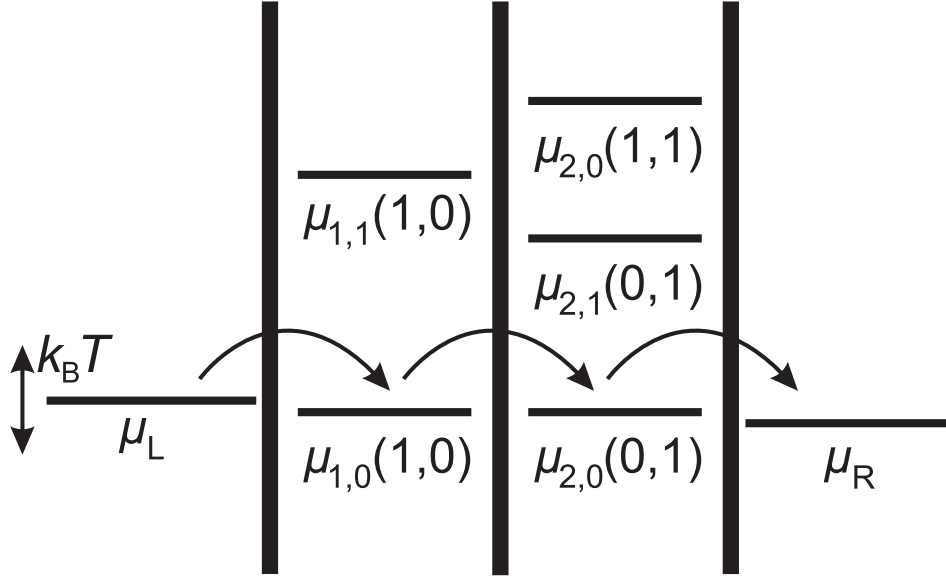


Figure 7.4: Schematic diagram of the electrochemical potentials $\mu_{i,n}(N_1, N_2)$ in dots and leads in the linear regime. The first subscript indicates either the lead (L,R) or the dot (1,2). The second subscript refers to the nature of the dot energy state (ground state, $n = 0$ or n th excited state).

energy E_n : $\mu_{i,n} = \mu_i^{class} + E_n$. In the classical regime we found that the addition energy (the change in electrochemical potential needed to add an extra electron) equals the charging energy E_{C1} (for dot 1) or E_{C2} (for dot 2). In the quantum regime, the addition energy for the $(N_1 + 1)$ th electron occupying discrete level m , with the N_1 th electron occupying discrete level n , becomes

$$\begin{aligned} \mu_{1,m}(N_1 + 1, N_2) - \mu_{1,n}(N_1, N_2) &= E_{C1} + (E_m - E_n) \\ &= E_{C1} + \Delta E. \end{aligned} \tag{7.11}$$

Similarly, we find $E_{C2} + \Delta E$ for the addition energy of dot 2. Note that for a (spin-)degenerate level ΔE can be zero. The dimensions of the honeycomb cell as given in Eqs. 7.8 and 7.10, and depicted in Fig. 7.3 for the classical regime, change as follows

$$\Delta V_{g1(2)} = \frac{|e|}{C_{g1(2)}} \left(1 + \frac{\Delta E}{E_{C1(2)}} \right) \quad (7.12)$$

$$\Delta V_{g1(2)}^m = \frac{|e|C_m}{C_{g1(2)}C_{2(1)}} \left(1 + \frac{\Delta E}{E_{Cm}} \right) \quad (7.13)$$

The electronic configuration that gives the lowest possible total energy in dot 1(2), is referred to as the dot 1(2) *ground state*. Any configuration with a higher total energy is referred to as an *excited state*. The electrochemical potential for adding the $N_{1(2)}$ th electron to the lowest unfilled energy level of the $(N_{1(2)} - 1)$ -electron ground state is labeled $\mu_{1,0}(N_1, N_2)$ $\{\mu_{2,0}(N_1, N_2)\}$. The electrochemical potential for adding the $N_{1(2)}$ th electron to a higher unfilled level of the $(N_{1(2)} - 1)$ -electron ground state – or to any unfilled level of an $(N_{1(2)} - 1)$ -electron excited state – is labeled $\mu_{1,1}(N_1, N_2)$, $\mu_{1,2}(N_1, N_2)$, ... $\{\mu_{2,1}(N_1, N_2)$, $\mu_{2,2}(N_1, N_2)$, ... $\}$.

In Fig. 7.4 a schematic diagram is given, showing the electrochemical potentials in the leads and dots in the linear regime ($\mu_L - \mu_R = -|e|V \approx 0$). The ground state electrochemical potentials $\mu_{1,0}(1, 0)$ and $\mu_{2,0}(0, 1)$ align within the small bias window, allowing an electron to tunnel from left to right. This is an example of an electron transfer process as depicted in Fig. 7.2d. Note that an alignment of an arbitrary combination of electrochemical potentials in dot 1 and dot 2 does not necessarily lead to a current. For example, the alignment of $\mu_{1,0}(1, 0)$ and $\mu_{2,0}(1, 1)$ does not result in current through the double dot. In the linear regime electron transport occurs via ground states, whereas the excited states start to play a role in non-linear transport, as will be discussed in section 7.2.2. In the following discussion of the linear regime the ground state of dot 1(2) is denoted by $\mu_{1(2)}(N_1, N_2)$ (without the discrete level index).

A more detailed picture of a honeycomb cell in the linear regime, marked by the dashed square in Fig. 7.2b, is given in Fig. 7.5. The configuration of the ground-state electrochemical potentials is given in schematic diagrams on some places in the stability diagram. The dashed lines, which are extensions of the solid lines forming the honeycomb cells, help to find the position of both electrochemical potentials on a certain place. A crossing of dashed lines (as in the charge domains (0,1) and (1,0)) indicates that two electrochemical potentials align, but does not result in a current through the double dot.

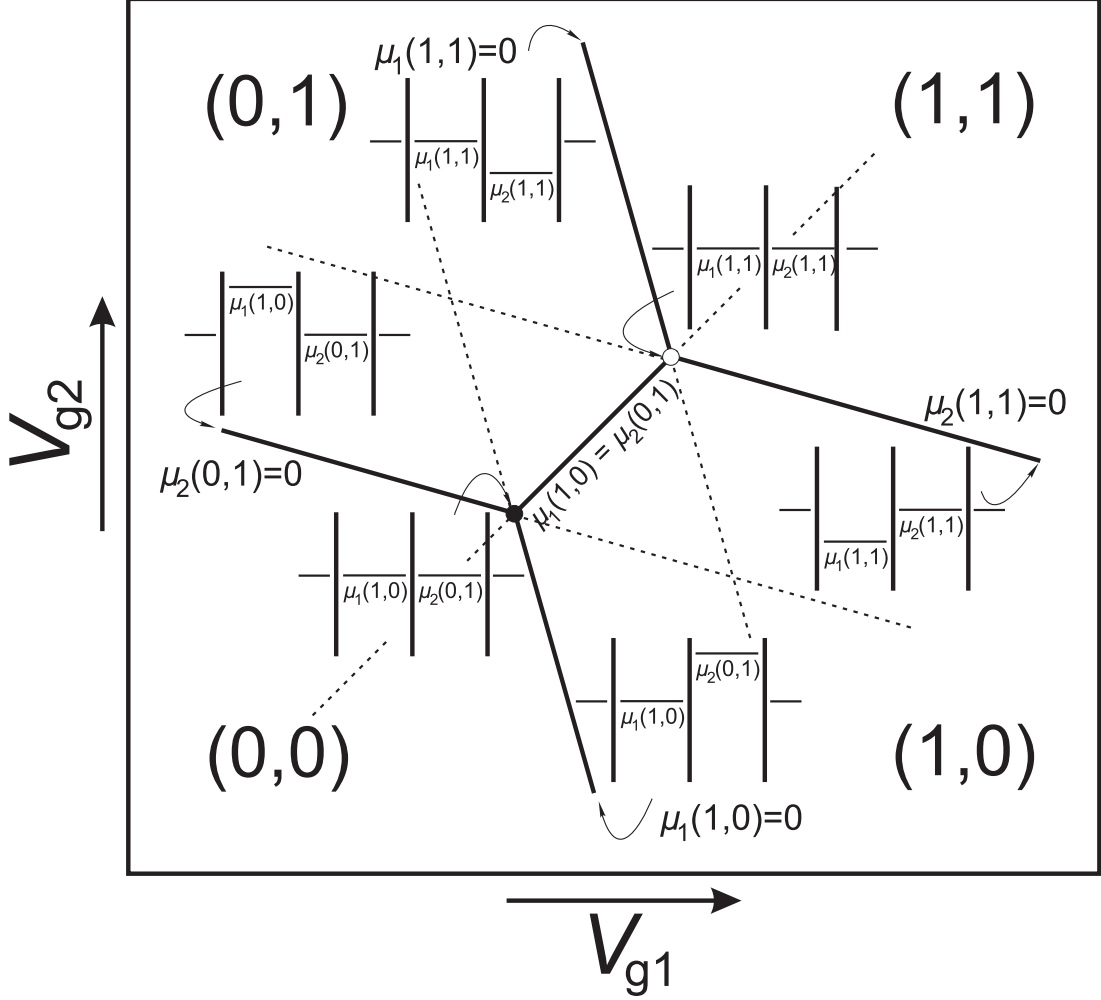


Figure 7.5: Region within the dotted square of Fig. 7.2b, corresponding with the ‘unit cell’ of the double-dot stability diagram. Four different charge states can be distinguished, separated by solid lines. At the solid line connecting the two triple points, the charge states $(0,1)$ and $(1,0)$ are degenerate. At the other solid lines the electrochemical potential of at least one dot is zero and thus equals the electrochemical potential of the leads. The dashed lines are the extensions of the solid lines within the honeycomb cells. The triple-points lie on the crossing points between the solid lines. The schematic diagrams show the configuration of the ground-state electrochemical potentials on the corresponding place in the honeycomb diagram.

Experimental stability diagrams

Before discussing some experimental stability diagrams, we introduce the two kinds of lateral double dot devices being studied in this review. For the first type, only metal gate electrodes are used to confine the electrons in the 2DEG beneath. For the second type we use a combination of metal gates and dry etching to realize confinement.

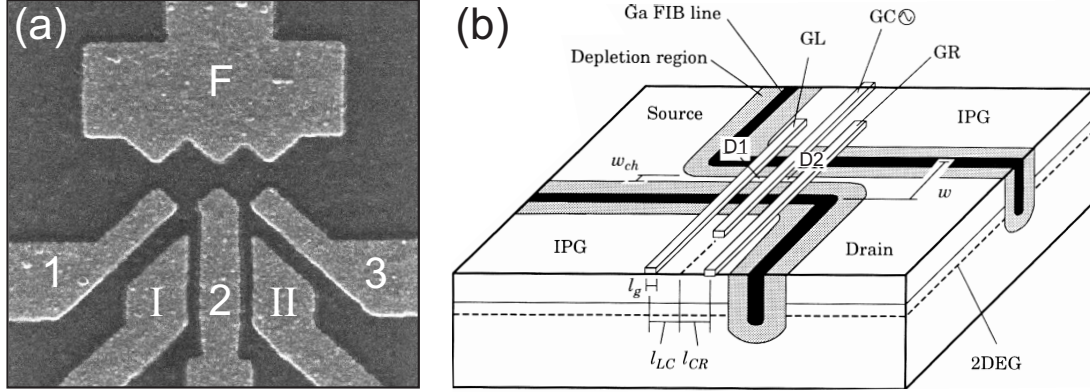


Figure 7.6: Double quantum dot devices. (a) SEM micrograph of a double dot defined by metallic gates (light gray areas). The ungated 2DEG (100 nm below the surface) has a mobility of $2.3 \times 10^6 \text{ cm}^2/(\text{Vs})$ and an electron density of $1.9 \times 10^{15} \text{ m}^{-2}$ at 4.2 K. The dimensions of the dots defined by the gate pattern are $320 \times 320 \text{ nm}^2$ (dot 1, left) and $280 \times 280 \text{ nm}^2$ (dot 2, right). (b) Schematic diagram of a double dot defined by a combination of dry etching and metallic gates. The carrier concentration and mobility of the ungated 2DEG (100 nm below the surface) at 1.6 K and in the dark are $3 \times 10^{11} \text{ cm}^{-2}$ and $8 \times 10^5 \text{ cm}^2/(\text{Vs})$, respectively. The lithographic distance between the etched trenches (black lines), w , is typically $0.5 \mu\text{m}$. The effective width of the channel, w_{ch} , can be tuned by voltages on the in-plane gates (IPGs). The gate electrodes are $\sim 40 \text{ nm}$ wide (l_g) and are separated by $l_{LC} = 160 \text{ nm}$ and $l_{CR} = 220 \text{ nm}$. A double quantum dot (dot 1, D1; dot 2, D2) can be formed by applying negative gate voltages to gates GL, GC and GR. A microwave field can be applied to the center gate GC.

A scanning electron microscope (SEM) image of the first device is shown in Fig. 7.6a. Metal gates are deposited on top of a GaAs/AlGaAs heterostructure with a 2DEG 100 nm below the surface [7]. Applying a negative voltage to all gates depletes the 2DEG underneath them and forms two quantum dots. Current can flow from the large electron reservoir on the left via the three tunnel barriers induced by the gate pairs 1-F, 2-F, and 3-F to the reservoir on the right. The transmission of each tunnel barrier can be controlled individually by the voltage

on gates 1, 2 or 3. A single quantum dot can be defined in the 2DEG by applying only a voltage to gates 1, 2, I and F (dot 1) or to gates 2, 3, II and F (dot 2). In this way, the individual dots can be characterized and their properties compared to those of the double dot.

The second device is schematically shown in Fig. 7.6b. First a channel is defined in the 2DEG by focused-ion-beam (FIB) or electron-cyclotron-resonance (ECR) etching of an $\text{Al}_{0.3}\text{Ga}_{0.7}\text{As}/\text{GaAs}$ modulation-doped heterostructure [10]. A double quantum dot can be formed by applying negative voltages to gates GL, GC and GR.

All experiments have been performed in a dilution refrigerator with a base temperature of 10 mK. The effective electron temperature in the leads is higher and can vary between ~ 40 and ~ 100 mK. A significant source of heating is the noise coming from the measurement electronics. The filters, used to attenuate the noise, have to be effective over a very large band width. They consist of a distributed RC network, usually a thin resistive wire going through a conducting medium such as copper powder or silver epoxy. The filters are installed at low temperature to minimize the thermal noise of the resistors inside. The filters are integrated with the sample holder in such a way that all sample wires are carefully shielded once they are filtered.

To effectively create a double quantum dot, all gate voltages need to be tuned properly. The cross capacitances between the various gate electrodes, make it difficult to vary just a single parameter without affecting the others. The stability diagram is of great value in setting up and characterizing a double quantum dot. Figure 7.7 illustrates the process of the creation of a double dot in a device similar to the one in Fig. 7.6b. Starting point is the creation of a single large dot formed by the outer tunnel barriers, GL and GR. The measured stability diagram (Fig. 7.7a) resembles Fig. 7.2c. The successive stability diagrams are measured for increasingly negative voltages on the middle gate electrode, GC, thus reducing the coupling between the dots. It is clearly seen that going from Fig. 7.7a to Fig. 7.7f, the stability diagram gradually evolves into the characteristic honeycomb structure. The edges of the honeycomb cells are visible due to off-resonance current. At the edges of a honeycomb cell, the electrochemical potential of one of the dots aligns with its neighboring lead (see Fig. 7.5). By a process called co-tunneling [37], transport can still take place via an intermediate virtual state. Co-tunneling processes are suppressed by increasing the tunnel barriers (i.e. making the gate voltages more negative), as can be seen from Fig. 7.7.

Figure 7.8a shows a detail of a stability diagram obtained in the device shown in Fig. 7.6a. The edges of the honeycomb cells are indicated by dashed lines. The triple points within the black square are well separated, whereas the other ones

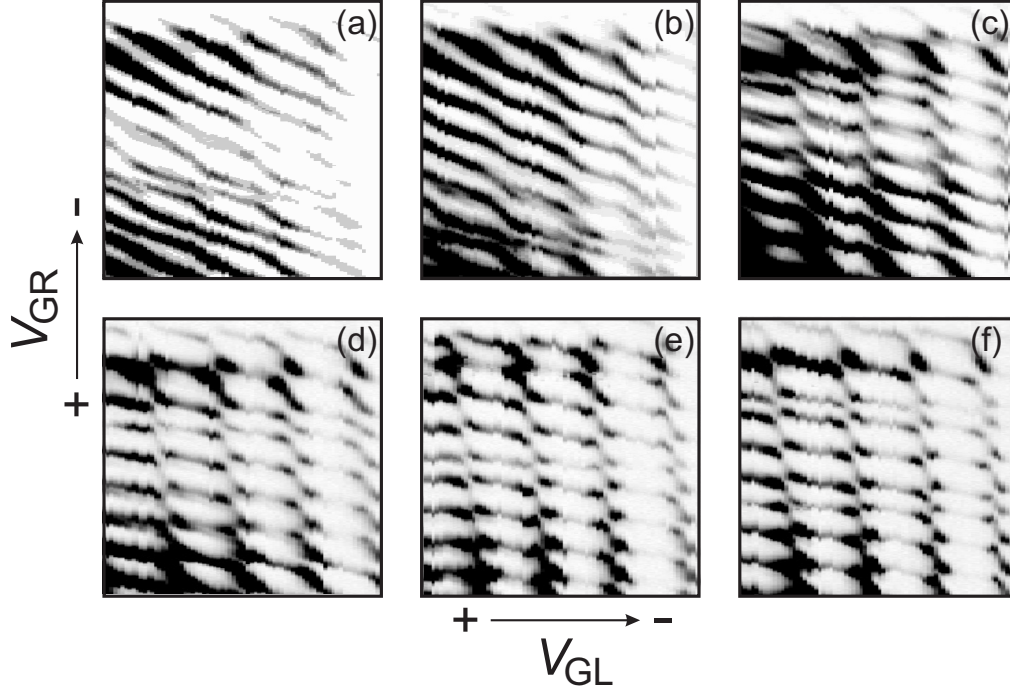


Figure 7.7: Experimental gray-scale plots of stability diagrams in a device similar to that shown in Fig. 7.6b for increasingly negative gate voltage on the middle gate electrode, GC. Dark (light) gray-scale corresponds to large (small) current through the double dot. GL is swept between -500 mV and -530 mV, GR between -840 mV and -900 mV, GC = -660 mV (a), -670 mV (b), -690 mV (c), -700 mV (d), -710 mV (e) and -720 mV (f).

are still grown together. To separate also those points outside, the gate voltage on the middle barrier has to be tuned towards more negative values.

7.2.2 Non-linear transport regime

Classical theory

We assume that the bias voltage is applied to the left lead ($\mu_L = -|e|V$) and that the right lead is grounded ($\mu_R = 0$). The bias voltage is coupled to the double dot through the capacitance of the left lead, C_L , and hence also affects the electrostatic energy of the system. The bias dependence can be accounted for by replacing $C_{g1(2)}V_{g1(2)}$ with $C_{g1(2)}V_{g1(2)} + C_{L1(2)}V$ in Eq. 7.1, where $C_{L1(2)}$ is the capacitance of the left lead to dot 1 (see Appendix A).

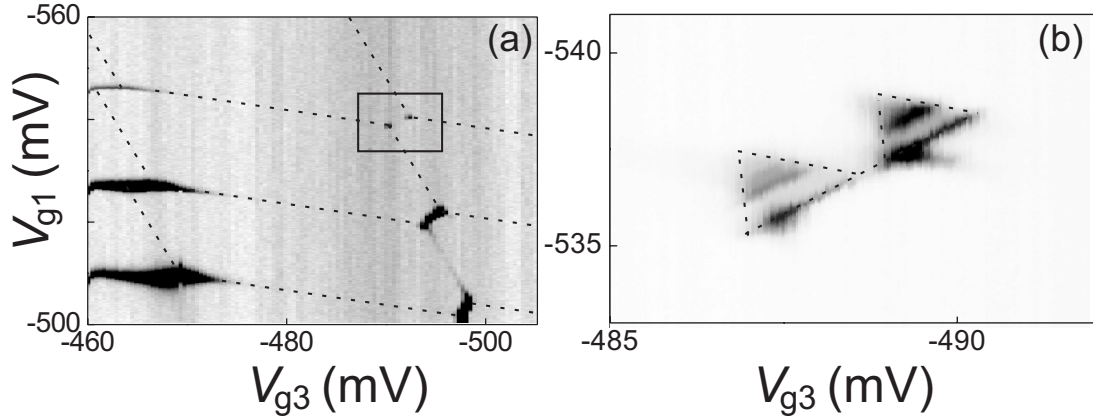


Figure 7.8: (a) Experimental gray-scale plot of a stability diagram in the device of Fig. 7.6a at small bias voltage, $V = 15 \mu\text{eV}$. Dark (light) gray-scale corresponds to large (small) current through the double dot. The dashed lines indicate the honeycomb cells. (b) Region within the black rectangle of (a) at large bias voltage, $V = 120 \mu\text{eV}$. The triple points have grown into triangles and show clear resonant tunneling lines (black stripes), as discussed in section 7.2.2. The shape of the triangles is accentuated by dashed lines.

The conductance regions at finite bias change from triple-points to triangularly shaped regions (Fig. 7.9). The conditions $-|e|V = \mu_L \geq \mu_1$, $\mu_1 \geq \mu_2$, and $\mu_2 \geq \mu_R = 0$ determine the boundaries of the triangular regions. The dimensions of the triangles δV_{g1} and δV_{g2} (see Fig. 7.9) are related to the applied bias voltage as follows

$$\begin{aligned}\alpha_1 \delta V_{g1} &= \frac{C_{g1}}{C_1} |e| \delta V_{g1} = |eV| \\ \alpha_2 \delta V_{g1} &= \frac{C_{g2}}{C_2} |e| \delta V_{g2} = |eV|\end{aligned}\tag{7.14}$$

where α_1 and α_2 are the conversion factors between gate voltage and energy. Combining Eqs. 7.8, 7.10 and 7.14, we can calculate the values of the total capacitances $C_{1,2}$ and mutual capacitance C_m .

Quantized states

For sufficiently large bias voltages, multiple discrete energy levels can enter the bias window. In this case, not only ground states, but also excited states con-

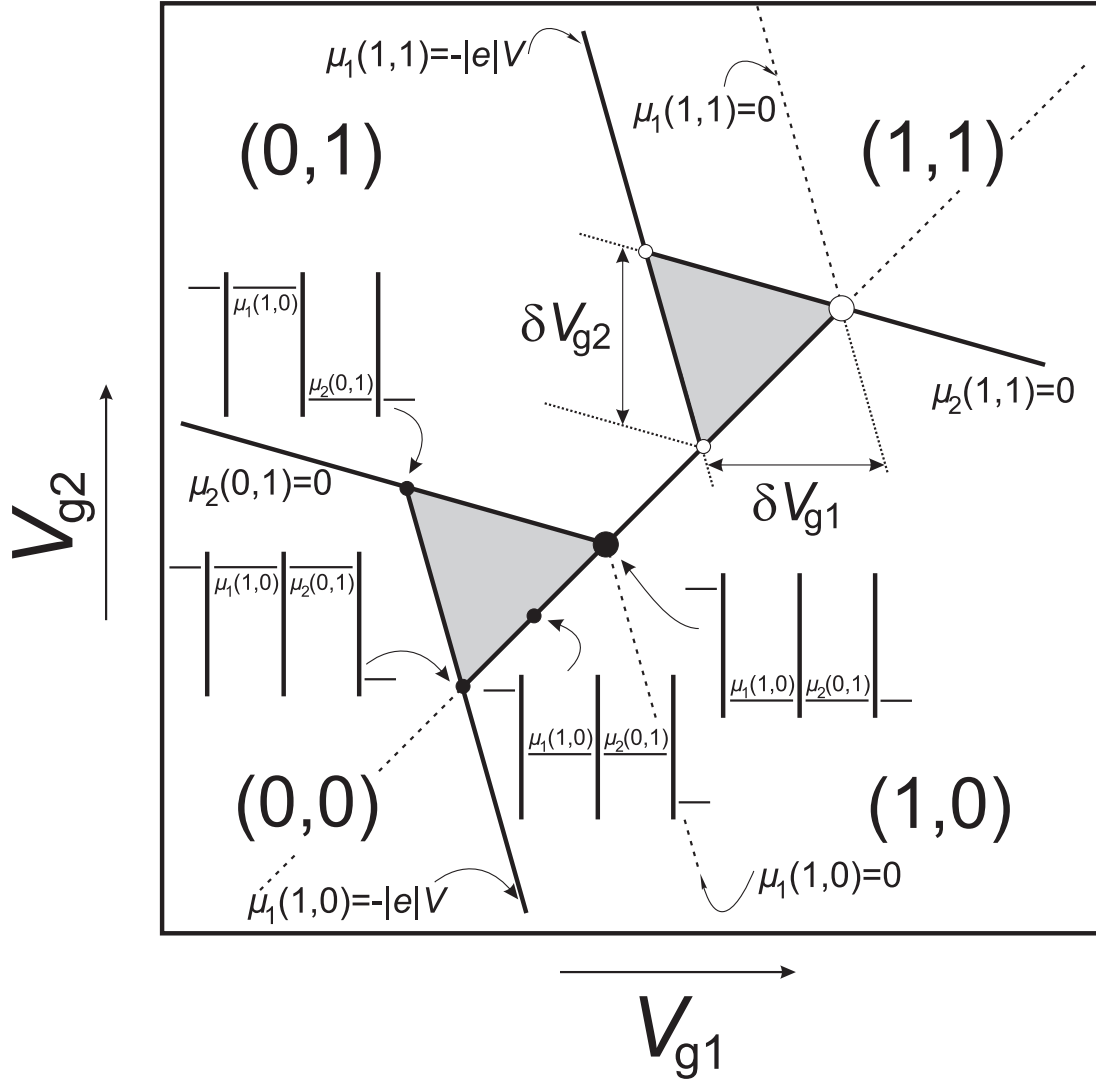


Figure 7.9: Region within the dotted square of Fig. 7.2a, corresponding to the ‘unit cell’ of the double-dot stability diagram, at finite bias voltage. The solid lines separate the charge domains. Classically, the regions of the stability diagram where current flows, are given by the gray triangles. In the case of one discrete level per dot, as in the schematic pictures, resonant tunneling is only possible along the side of the triangle that coincides with the dashed line connecting the original triple-points (● and ○). However, also in this case *inelastic tunneling* and *co-tunneling* still contribute to a finite current within the gray triangles.

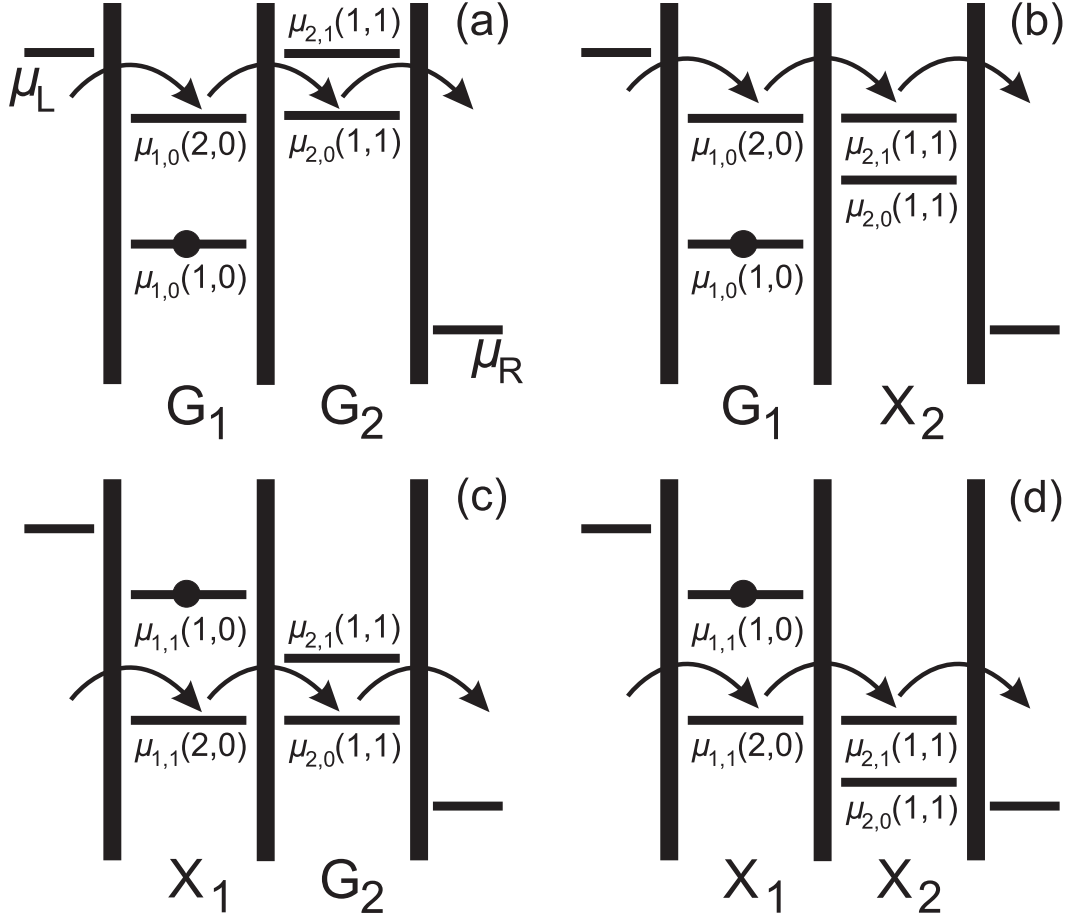


Figure 7.10: Schematic diagrams showing the possible alignments of the electrochemical potentials in the case of two levels per dot. (a) The first electrochemical potentials to align correspond to the ground states of both dots, G_1 and G_2 . (b) When moving down the levels in the right dot, the next states to align are the ground state of the left dot, G_1 , and the first excited state of the right dot, X_2 . (c) Shifting the levels of the right dot further down, results in transport through the first excited state of the left dot, X_1 and the right dot ground state, G_2 . (d) Finally, the excited states, X_1 and X_2 align.

tribute to the conductance. For the illustrative case of two levels per dot, the four possible alignments of the electrochemical potentials are shown in Fig. 7.10. Note that the electrochemical potentials are drawn for the situation where one electron is on the double dot and a second one is tunneling on to it. Due to Coulomb blockade, not less than one and not more than a total of two electrons is allowed on the double dot. The labeling of the electrochemical potentials, using the notation introduced in section 7.2.1 is straightforward, except for tunneling

through the excited state of dot 1 in Figs. 7.10c,d. Although the second electron is tunneling into the lowest level available in dot 1, this level is only accessible because dot 1 is in an excited state. For that reason, we choose the label $\mu_{1,1}(2,0)$ (instead of $\mu_{1,0}(2,0)$). The successive alignment of ground and excited states leads to resonances within the conductance triangles, as shown in Fig. 7.11. The off-resonance conductance in the grey triangles is due to inelastic processes [7, 20] and co-tunneling [37]. Note that V is so large that the two triangles partly overlap.

Figure 7.8b shows the triple points within the black rectangle of Fig. 7.8a at finite bias. The triangular regions are clearly visible as well as the resonances within the triangles. The growth of the triangular regions with increasing bias voltage is illustrated in Fig. 7.12. Whereas only the ground state resonance is observed in Fig. 7.12a, multiple resonances appear within the triangles of Fig. 7.12b.

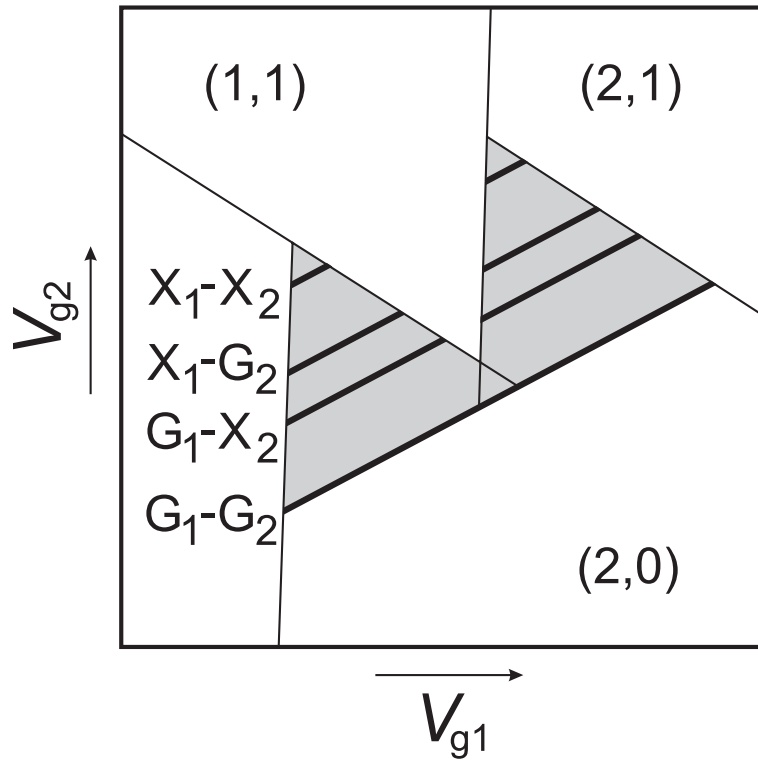


Figure 7.11: Schematic stability diagram corresponding to the finite-bias diagrams of Fig. 7.10. The black solid lines within the gray triangles correspond, from bottom to top, to the level alignments shown in Fig. 7.10(a)-(d), respectively.

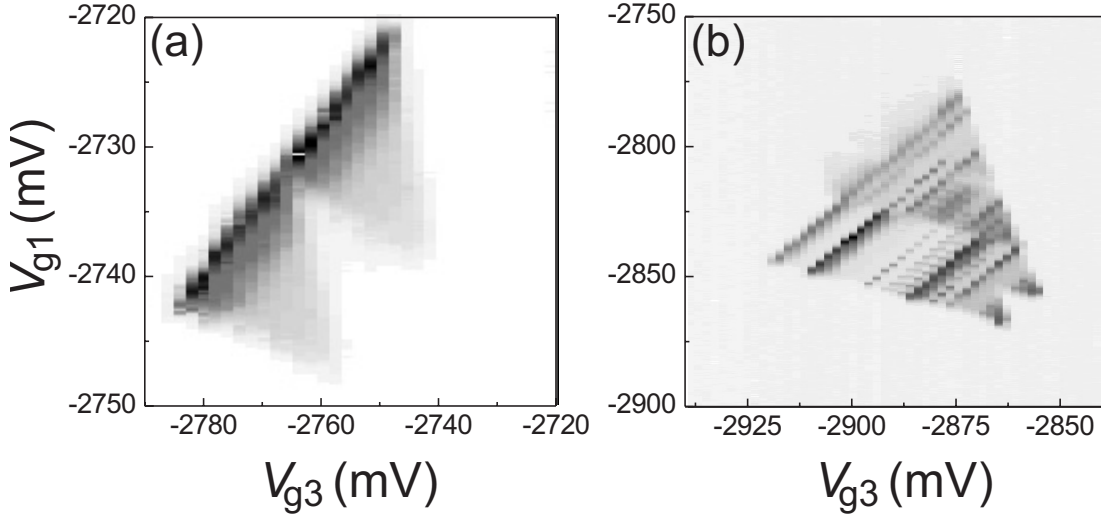


Figure 7.12: Experimental gray-scale plots of stability diagrams in the non-linear regime, obtained in the device of Fig. 7.6a. Dark (light) gray-scale corresponds to large (small) current through the double dot. The bias voltage between source and drain contacts is $200 \mu\text{V}$ (a) and 1 mV (b).

7.3 Resonant tunneling

In this section we discuss resonant tunneling experiments through the double dot of Fig. 7.6a with discrete energy levels [7]. We show that, under appropriate conditions, the resonance widths are only determined by the lifetime of the discrete energy states, independent of the electron temperature in the leads. A small asymmetric deviation from the Lorentzian resonance shape is attributed to inelastic tunnel processes.

The current-voltage (I - V) curves of the single quantum dots in Fig. 7.13 provide two clear signatures for the presence of both Coulomb blockade effects and discrete levels. At low bias voltages, the current through the dot is suppressed by the Coulomb blockade [1]. Increasing the bias voltage lifts the blockade. The current shows a stepwise increase: each time when an additional level enters the bias window $-|e|V$, an extra transport channel is opened and the current increases [38-40]. Hence, the voltage spacing of the current steps directly reflects the energy spacing of the levels. For the average level spacing, δ , we obtain $\delta_1 = 125 \mu\text{eV}$ for dot 1 (upper inset) and $\delta_2 = 225 \mu\text{eV}$ for dot 2 (lower inset). The difference in these two energies reflects the different lithographic sizes of the two dots (see Fig. 7.6a). Accounting for the depletion areas, we estimate that dot 1

has an effective diameter of 240 nm and contains about $N_1 = 90$ electrons, while dot 2 has an effective diameter of 200 nm and contains roughly $N_2 = 60$ electrons. Using the Fermi energy, E_F , at bulk density, we estimate $\delta_1 \approx 2E_F/N_1 = 150 \mu\text{eV}$ and $\delta_2 \approx 2E_F/N_2 = 230 \mu\text{eV}$. This is in good agreement with the estimates obtained from the I - V curves. From the dimensions of the Coulomb diamonds [1, 35] we obtain the charging energies E_C for adding an electron to the dot : $E_{C1} = 1.1 \text{ meV}$ (dot 1) and $E_{C2} = 1.8 \text{ meV}$ (dot 2).

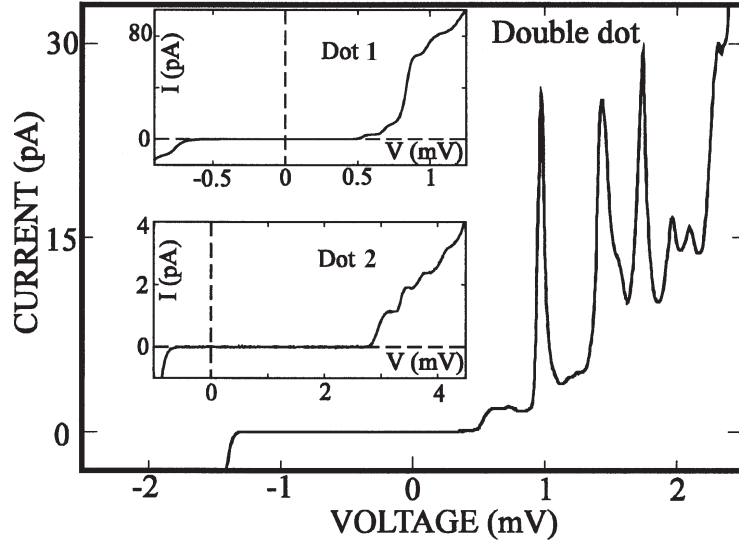


Figure 7.13: I - V curve of the double dot, showing sharp resonances in the current when two discrete levels align. Upper inset: I - V curve of dot 1. Lower inset: I - V curve of dot 2. Both insets show a suppression of the current at low voltages due to the Coulomb blockade and a stepwise increase of the current due to the discrete energy spectrum of the dot (from Ref. [7]).

We focus on the role of the discrete levels and consider the charging energies as constant offsets in the transport conditions. Figure 7.13 shows an I - V curve of the double dot with all three tunnel barriers set in the weak-tunneling regime. The Coulomb blockade suppresses the current through the double dot at low bias voltages. At larger bias the current shows sharp resonances. The spacing of the resonances is about $250 \mu\text{eV}$. This is of the same order as the level spacing in the single dots.

The same resonances are seen when we sweep the gate voltage. Figure 7.14 shows the current through the double dot versus the gate voltage on gate 1, V_{g1} , with $V = 280 \mu\text{eV}$. This corresponds to a vertical cut through a stability diagram as shown in Fig. 7.12. The current shows three groups of sharp resonances sepa-

rated by regions of zero current with a period $\Delta V_{g1} = 9$ mV in gate voltage V_{g1} . With only dot 1 formed, we observe Coulomb oscillations as a function of V_{g1} with the same period ΔV_{g1} ; each period thus corresponds to a change of one electron in dot 1, while keeping the number of electrons on dot 2, N_2 , constant. ΔV_{g1} corresponds to the horizontal dimension of the honeycomb unit cell, as indicated in Fig. 7.3 in section 7.2.1.

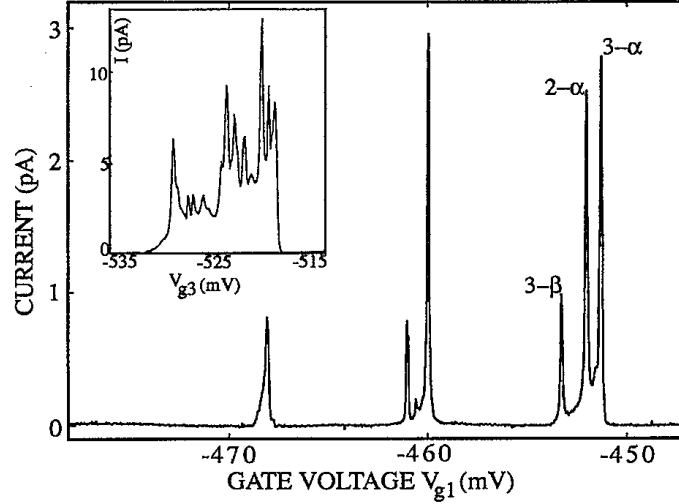


Figure 7.14: Current through the double dot versus gate voltage V_{g1} using a bias voltage $V = 280$ μ V. Inset: The current through the double dot as a function of V_{g3} with $V = 1$ mV, showing that the number of resonances increases with bias voltage (from Ref. [7]).

When elastic tunnel processes are the dominant transport mechanism, the current through the double dot is resonantly enhanced only when two levels in dot 1 and 2 align, as explained in section 7.2.2. Tuning the level alignment with V or V_{g1} gives rise to the sharp resonances in Figs. 7.13 and 7.14. Resonant tunneling through the double dot is illustrated in the schematic potential landscape of the double dot in Fig. 7.15. This figure shows a few of the levels in dot 1 (levels 1 to 5) and dot 2 (levels α and β). The electrostatic potentials φ_1 and φ_2 are tuned in such a way that transport through the double dot is possible only via the charge states $(N_1, N_2) \rightarrow (N_1 + 1, N_2) \rightarrow (N_1, N_2 + 1) \rightarrow (N_1, N_2)$. The finite bias voltage gives an electron from the left reservoir three choices to tunnel into dot 1: it can tunnel to one of the unoccupied levels 3, 4 or 5. This changes the electrostatic potential φ_1 by the charging energy E_{C1} (the levels are drawn at the positions applicable after an electron has occupied one of them). When dot 1 relaxes to the ground state (the incoming electron occupying level 3), the

electron can tunnel via level α to the right reservoir.

Note that if dot 1 does not immediately relax to the ground state, but remains in an excited state, with an electron occupying either level 4 or 5, electron transport through the double dot is temporarily blocked. The electron is ‘trapped’ within dot 1. Only after relaxation to the ground state a next tunnel event can occur. If the relaxation rate is small on the scale of the tunneling rates through the barriers, the inclusion of levels 4 and 5 within the bias window could therefore lead to a *decrease* of the current through the double dot. On the other hand, in case of fast relaxation, the enhanced tunnel probability when also the levels 4 and 5 lie within the bias window, could lead to an increase in the current. Note that next to intra-dot relaxation, also inelastic tunneling from level 4 or 5 to either level α or β can occur. This process is accompanied by emission of a boson (usually phonons [20]) and contributes to the off-resonance current in Fig. 7.14.

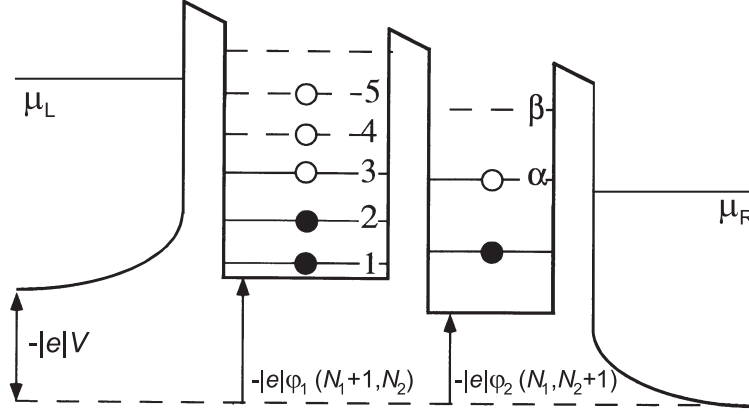


Figure 7.15: Schematic potential landscape of the double quantum dot, where μ_L and μ_R denote the electrochemical potentials of the left and right reservoirs and V the bias voltage across the double dot. The 0D states in dot 1 are denoted by levels 1 to 5 and in dot 2 by levels α and β (from Ref. [7]).

The resonances in a particular group in Fig. 7.14 can be identified with the energy diagram of Fig. 7.15. The first resonance occurs when level 3 aligns with level α (peak 3- α). This corresponds to the rightmost peak in Fig. 7.14. Increasing $-|e|\phi_1$ by making V_{g1} more negative, brings transport off-resonance until level 2 aligns with α (peak 2- α) followed by the third peak 3- β . Continuing to sweep V_{g1} increases the energy of level 3 above the electrochemical potential μ_L of the left reservoir. This blocks transport and removes an electron from dot 1 permanently. The next group of resonances is observed when V_{g1} is changed by one Coulomb oscillation period ΔV_{g1} (see Fig. 7.14). Note that the number of

resonances decreases in the next two groups. Sweeping V_{g1} also shifts the levels in dot 2, due to a small cross-capacitance between gate 1 and 2. Transport is possible until level α is shifted above μ_L ($V_{g1} < -470$ mV).

The level spacing is obtained by converting gate voltage to energy [2]. This yields an energy separation of resonances $2-\alpha$ and $3-\alpha$ by $70 \mu\text{eV}$, which is the energy separation of levels 2 and 3. In the same way we find for levels α and β a separation of $200 \mu\text{eV}$. Both values are in good agreement with the typical values we found above. On increasing V , we observe that the number of resonances in a particular group increases. The inset to Fig. 7.14 shows approximately 11 resonances as V_{g3} is swept. These observations are in agreement with the resonant tunneling picture of Fig. 7.15: when V is larger, more levels can align.

Generally, the relaxation rate to the ground state is not necessarily higher than the tunnel rate through the dot. In Fig. 7.16 the amplitude of the ground state resonance (see lower curve) clearly decreases with increasing bias voltage. At the same time new resonances appear, having a larger amplitude than the ground state resonance. This implies that in general transport through excited states can play a significant role.

When a discrete level in dot 1 is at a distance much larger than the thermal energy, $k_B T$, from the electrochemical potential of the left lead, dot 1 acts as low-temperature-pass filter for dot 2, such that only cold electrons contribute to the current [41]. If the energy levels in the dots are separated by more than $k_B T$, the occupation of excited states becomes suppressed. This effectively leaves the dot at zero temperature. Hence, the double dot geometry allows for an accurate measurement of the intrinsic line width of the discrete levels, which is not averaged by the Fermi-Dirac distribution of the electrons in the reservoirs. In other words, an energy resolution better than $k_B T$ can be obtained. The line shape of a resonance is lorentzian when only elastic tunneling is important [42, 43]. In our geometry (assuming a bias voltage sufficiently large such that electrons must tunnel from the left lead to the left dot to enter the system, and must tunnel from the right dot to the right lead to leave it again) the current is given by

$$I(\Delta E) = e \frac{\Gamma_3 |t_{12}|^2}{(\Delta E/h)^2 + \frac{\Gamma_3^2}{4} + |t_{12}|^2 \left(2 + \frac{\Gamma_3}{\Gamma_1}\right)} \quad (7.15)$$

where ΔE is the energy difference between two discrete energy levels in the two dots, Γ_1 is the tunnel rate from the left lead to dot 1, $|t_{12}|$ is the modulus of the tunnel coupling between the two dots and Γ_3 is the tunnel rate from dot 2 to the

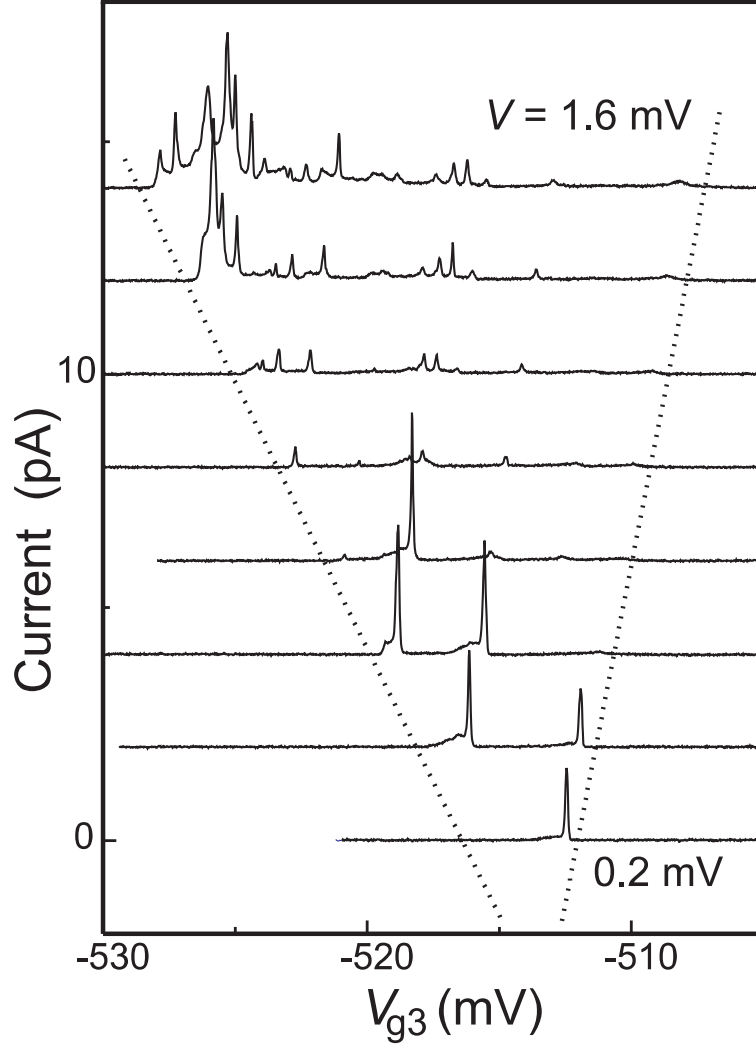


Figure 7.16: Current through the double dot of Fig. 7.6a versus the voltage on gate 3, V_{g3} for bias voltages, V , between 0.2 mV (lower trace) and 1.6 mV (upper trace). The traces have been given an offset proportional to their bias voltage for clarity.

right lead. Note that for elastic tunneling the resonance width is only determined by the lifetime of the 0D states and independent of temperature.

Figure 7.17 shows a single resonance (black dots). The right-hand side of the peak fits very well with the lorentzian line shape of Eq. 7.15 (solid line), while the left-hand side shows a deviation from the lorentzian fit. The only free fit parameter is the full width at half maximum, $\text{FWHM} = 5 \mu\text{eV}$. From the maximum current and the width of the resonance we find with Eq. 7.15 a tunnel coupling $|t_{12}| \approx 0.2 \mu\text{eV}$ and a tunneling rate between the right dot and

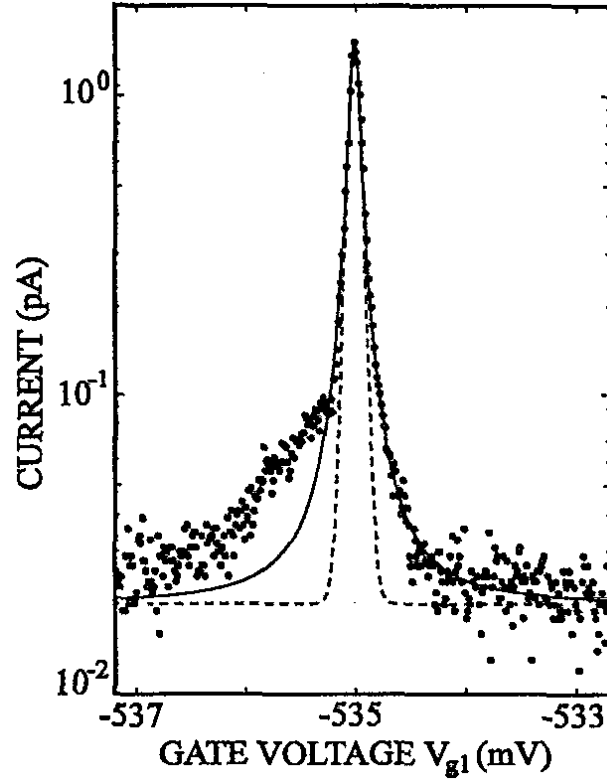


Figure 7.17: Enlarged resonance measured in a second device of identical design using a bias voltage of $400 \mu\text{eV}$. The data points (black dots) are fit to a Lorentzian line shape (solid line). For comparison we plot a thermally broadened resonance with a fitted temperature $T = 34 \text{ mK}$ (dashed line) (from Ref. [7]).

the right lead $\Gamma_3 \approx 10 \mu\text{eV}$. For comparison, we have fitted the resonance with a thermally broadened resonance $I(\Delta E) \sim \cosh(\Delta E/2kT)^{-2}$ (dashed line) [44]. The top is fit very well for $T = 34 \text{ mK}$, but there is a large deviation in both tails of the resonance. On the right-hand side, the deviation can be accounted for by the Lorentzian broadening. At the left-hand side, the deviation consists of two components. The first one is the same Lorentzian broadening as observed on the right-hand side. The second one, however, is an asymmetric contribution only occurring on this side of the resonance. The asymmetric contribution to the current appears at the side where an electron tunnels from a higher to a lower electrochemical potential. Upon reversing the sign of V , we find that the asymmetry appears at the other side of the resonance. As shown in Ref. [20], this is due to inelastic tunnel processes. In such a process, an electron can tunnel inelastically and spontaneously emit its energy as a photon or a phonon.

7.4 Magnetic field spectroscopy

In this section we measure the energy evolution versus magnetic field, B , of energy states near the Fermi energy, E_F , in the double quantum dot shown in Fig. 7.6a. As a function of B and the voltage on gate 3, V_{g3} , we observe crossings and anti-crossings between Coulomb peaks. The resolution is high enough that avoided crossings in the spectrum of a quantum dot can be resolved [18]. To our knowledge, these are the only existing data revealing intra-dot level repulsion in a quantum dot system.

The experiments are performed in the weak coupling limit, such that mixing between quantum states in one dot with states in the other dot or in the leads is negligible (see section 7.5). We sweep the gate voltages over small ranges and focus on a particular charging transition; i.e. transitions between (N_1+1, N_2) and (N_1, N_2+1) only. Since we discuss only one transition at a time, we can, for simplicity, leave out the Coulomb energies from the discussion and concentrate on the alignment of discrete energy levels.

Using the notation introduced in section 7.2.1, we label the accompanying electrochemical potentials $\mu_{1,n}(N_1, N_2)$ for dot 1 and $\mu_{2,n}(N_1, N_2)$ for dot 2 (or simply $\mu_{1(2),n}$). The condition for tunneling between the lowest possible states, i.e. from ground state to ground state, is $\mu_{1,0}(N_1 + 1, N_2) = \mu_{2,0}(N_1, N_2 + 1)$. To tunnel from the first excited state of dot 1 to the ground state of dot 2, the condition becomes $\mu_{1,1}(N_1 + 1, N_2) = \mu_{2,0}(N_1, N_2 + 1)$. The changes in the electrochemical potential $\mu_{1,n+1} - \mu_{1,n}$ and $\mu_{2,n+1} - \mu_{2,n}$ are typically $\sim 150\text{-}200 \mu\text{eV}$.

Figure 7.18a shows a typical set of current traces for different magnetic fields while sweeping V_{g3} . The bias voltage $V = 1.2 \text{ mV}$ is such that several discrete levels in each dot are between the electrochemical potentials of the two leads. This is similar as in the inset to Fig. 7.14, but now measured for different magnetic fields. The *change* in Coulomb peak position versus B , $\Delta V_{g3}^{peak}(\Delta B)$, is proportional to the difference in the B -evolution of the electrochemical potentials $\mu_{1,n}(B)$ and $\mu_{2,n}(B)$

$$\begin{aligned} \Delta\mu(\Delta B) &= [\mu_{1,n}(B + \Delta B) - \mu_{1,n}(B)] - [\mu_{2,n}(B + \Delta B) - \mu_{2,n}(B)] \\ &= \alpha \Delta V_{g3}^{peak}(\Delta B) \end{aligned} \quad (7.16)$$

where α is the conversion factor between V_{g3} and the electrostatic potential of dot 2. Note that if the states $\mu_{1,n}(B)$ and $\mu_{2,n}(B)$ have the same B -dependence, the Coulomb peak position does not change. The energy resolution of $\Delta\mu(\Delta B)$ is $\sim 5 \mu\text{eV}$, corresponding to $k_B T \sim 50 \text{ mK}$.

The data in Fig. 7.18a contain several interesting features. First, we observe crossings between different peaks as well as anti-crossings (two are indicated by

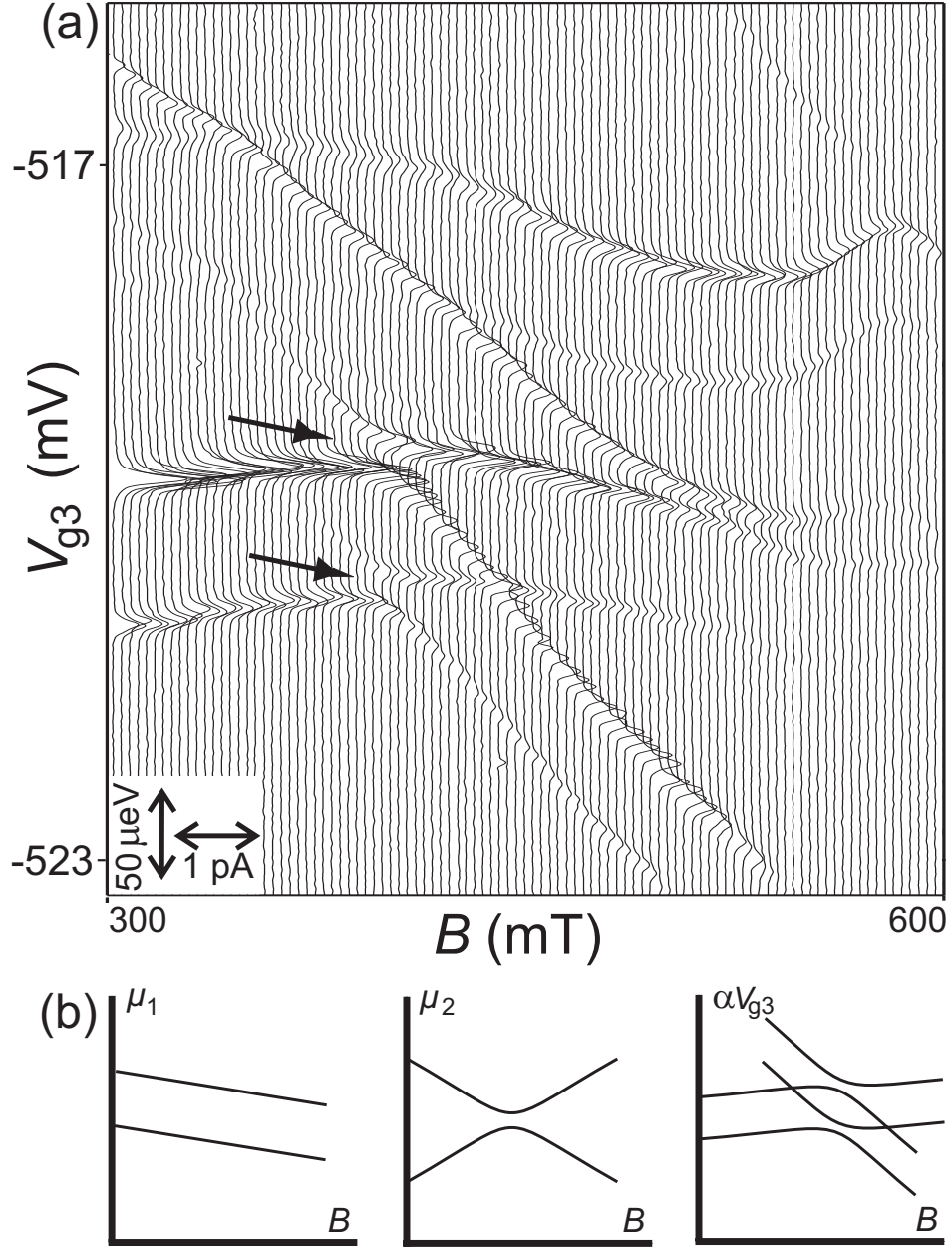


Figure 7.18: (a) Current through the double dot sweeping the voltage on gate 3, V_{g3} , at different magnetic fields, B . The curves have been given an offset for clarity. From the leftmost to the rightmost curve, B increases from 300 mT to 600 mT in 3 mT increments. The conversion factor α between V_{g3} and the electrostatic potential of dot 2, $\alpha = -63 \mu\text{eV/mV}$, is determined through independent measurements from which we deduced the energy scale, indicated by the vertical arrow in the lower left corner (α does not change in this magnetic field range). (b) The first two diagrams show how levels may evolve in each of the two dots as a function of B . When these four levels are scanned along each other by sweeping V_{g3} , this results in peak positions as sketched in the rightmost diagram.

arrows). Second, pairs of peaks exhibit the same B -dependence. These are general features that we observe at several charge transitions (that is for several choices of N_1, N_2). Independent measurements on *one* of the individual dots also show states evolving in pairs below $B \sim 0.5$ T. The observed pairing and (anti-)crossing of the Coulomb peaks in the double dot experiments can then be explained as shown schematically in Fig. 7.18b. Suppose two levels in one dot have an anti-crossing in their B -dependence. Then two paired levels in the other dot, having the same B -dependence, both probe this anti-crossing. At the points where two Coulomb peaks actually cross, two levels in dot 1 align with two levels in dot 2 simultaneously (though only one electron can tunnel at a time, due to Coulomb blockade).

For the interpretation of the data as schematically given in Fig. 7.18b, tunneling through the excited state of dot 1 is a key ingredient. If dot 1 would relax to its ground state much faster than the tunnel rate through the barriers after an electron has tunneled onto it via $\mu_{1,1}$, we would only observe the two lower traces in the rightmost diagram of Fig. 7.18b. However, our data suggest a relatively slow relaxation rate between the excited and ground state of dot 1. Recent experiments on (single) quantum dots have shown that indeed relaxation times can be of the order of μs or longer when relaxation to the ground state involves electron spin flips [45]. The condition for the relaxation rate from the excited state to the ground state in dot 2 is more subtle. The electron can tunnel onto dot 2 via $\mu_{2,1}$ and leave dot 2 either directly or after a relaxation process from $\mu_{2,1}$ to $\mu_{2,0}$ has occurred (this second possibility requires $\mu_{2,0} \geq \mu_R$). For transport through the double dot, the relaxation rate in dot 2 does not necessarily need to be slow as well. However, if the relaxation rate would be too high, the anti-crossing as shown in the middle diagram of Fig. 7.18b would smear out. The constant level spacing $\mu_{1,1} - \mu_{1,0}$ in dot 1 (see left diagram of Fig. 7.18b) could be explained by an exchange energy, e.g. when the upper level would correspond to a spin singlet state and the lower level to a spin triplet [46].

7.5 Microwave spectroscopy

In this section we present microwave (0-50 GHz) spectroscopy experiments [1, 15, 16, 47] on double quantum dots for different coupling and microwave power regimes [19, 48]. We use photon assisted tunneling (PAT) processes, as described in sections 7.5.2 and 7.5.3, to measure the energy differences between states in the two dots of the devices shown in Figs. 7.6a and 7.6b. Depending on the strength of the inter-dot coupling, the two dots can form ionic-like [7,12,14-16]

or covalent-like bonds [17, 19, 48]. In the first case, the electrons are localized on individual dots, while in the second case, the electrons are delocalized over both dots. The covalent binding leads to a symmetric and anti-symmetric state, whose energy difference is proportional to the tunneling strength between the dots.

For the microwave experiments we make use of a coaxial cable. From room temperature to the 1K-pot, a 0.085 inch semi-rigid Be-Cu (inner and outer conductor) coaxial cable is used. From the 1K-pot to the mixing chamber, we use a 0.085 inch semi-rigid stainless steel (inner and outer conductor) coax. From the mixing chamber to the sample, various types of low attenuation semi-rigid or flexible coaxial cable can be used, since here the thermal conductivity is no longer a constraint. Finally, the coaxial cable is capacitively coupled (typically through a 10 pF capacitor) to one of the gate electrodes of the sample, usually the center gate. This gate is capacitively coupled to both dots, and hence part of the incident power can generate a microwave oscillating potential across the center barrier.

7.5.1 Two-level systems

So far, we assumed a purely electrostatic coupling between both dots, whereas tunnel coupling was neglected. However, when electrons can tunnel coherently from one dot to the other at appreciable rates, the eigenstates become delocalized, extending over the entire double dot system. In principle, these are quantum-mechanical many-body states of the two coupled dots. It is very difficult to give a full description of such a many-body system. Therefore, we discuss here the elementary case of a quantum-mechanical two-level system, which is quite adequate in grasping the physics of a tunnel-coupled double dot. Basically, we only take into account the topmost occupied level in each dot and neglect the interaction with electrons in lower energy levels.

We consider a double dot consisting of two well-separated dots, described by a total Hamiltonian \mathbf{H}_0 [49], with eigenstates $|\phi_1\rangle$ and $|\phi_2\rangle$, and eigenenergies E_1 and E_2 (Fig. 7.19a)

$$\begin{aligned}\mathbf{H}_0 |\phi_1\rangle &= E_1 |\phi_1\rangle \\ \mathbf{H}_0 |\phi_2\rangle &= E_2 |\phi_2\rangle\end{aligned}\tag{7.17}$$

We introduce a finite tunnel coupling between the levels in both dots described by the Hermitian matrix \mathbf{T} , which for simplicity [49] we assume to be purely

non-diagonal

$$\mathbf{T} = \begin{pmatrix} 0 & t_{12} \\ t_{21} & 0 \end{pmatrix}, \quad t_{12} = t_{21}^*, \quad t_{21} = |t_{21}| e^{i\varphi} \quad (7.18)$$

One obtains a new Hamiltonian, $\mathbf{H} = \mathbf{H}_0 + \mathbf{T}$, with delocalized eigenstates $|\psi_S\rangle$ (symmetric state) and $|\psi_A\rangle$ (anti-symmetric state), and eigenvalues E_S and E_A

$$\begin{aligned} \mathbf{H} |\psi_S\rangle &= E_S |\psi_S\rangle \\ \mathbf{H} |\psi_A\rangle &= E_A |\psi_A\rangle. \end{aligned} \quad (7.19)$$

The new eigenvalues can be expressed in terms of the eigenvalues of the uncoupled double dot and the tunnel matrix elements as follows

$$\begin{aligned} E_S &= E_M - \sqrt{\frac{1}{4}(\Delta E)^2 + |t_{12}|^2} \\ E_A &= E_M + \sqrt{\frac{1}{4}(\Delta E)^2 + |t_{12}|^2} \end{aligned} \quad (7.20)$$

where $E_M = \frac{1}{2}(E_1 + E_2)$ and $\Delta E = E_1 - E_2$ and $|t_{12}| = |t_{21}|$. The eigenstates $|\psi_S\rangle$ and $|\psi_A\rangle$ in the basis of $|\phi_1\rangle$ and $|\phi_2\rangle$ are written

$$\begin{aligned} |\psi_S\rangle &= -\sin \frac{\theta}{2} e^{-i\varphi/2} |\phi_1\rangle + \cos \frac{\theta}{2} e^{i\varphi/2} |\phi_2\rangle \\ |\psi_A\rangle &= \cos \frac{\theta}{2} e^{-i\varphi/2} |\phi_1\rangle + \sin \frac{\theta}{2} e^{i\varphi/2} |\phi_2\rangle \end{aligned} \quad (7.21)$$

with $\tan \theta = 2|t_{12}|/\Delta E$. Figure 7.19b shows the eigenenergies of the coupled two-level system as function of ΔE . The renormalized energy difference, ΔE^* , is given by

$$\Delta E^* = E_A - E_S = \sqrt{(\Delta E)^2 + (2|t_{12}|)^2}. \quad (7.22)$$

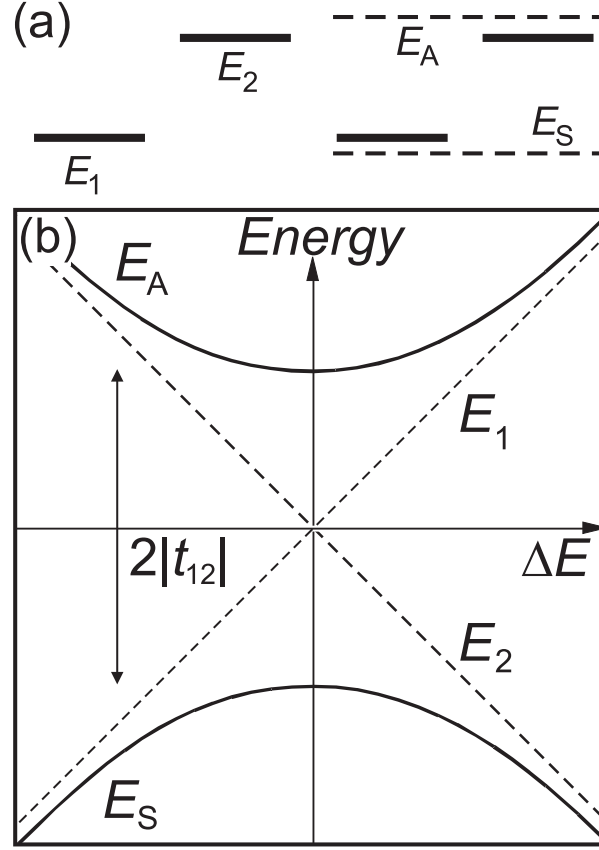


Figure 7.19: Schematic diagrams of a two-level system. (a) Unperturbed energy levels E_1 and E_2 (solid lines), and energy levels belonging to the symmetric state, E_S , and the anti-symmetric state, E_A . (b) Energies E_S and E_A versus the energy difference $\Delta E = E_1 - E_2$. For vanishing coupling ($|t_{12}| \approx 0$), the levels cross at the origin (dashed straight lines). For non-zero coupling, an ‘anti-crossing’ occurs: the curves belonging to E_S and E_A as function of ΔE are branches of a hyperbola (solid lines) whose asymptotes are the unperturbed levels (see also Ref. [49]).

Note that the effect of the coupling is stronger for small ΔE , i.e. close to the crossing of the unperturbed energies E_1 and E_2 . Where E_1 and E_2 cross ($\Delta E = 0$), we have an anti-crossing of E_A and E_S , with $E_A - E_S = 2|t_{12}|$, the minimum bonding–anti-bonding energy difference. For large ΔE , the eigenenergies of the coupled double dot approach the eigenenergies of the uncoupled dots, E_1 and E_2 . The general solution of the *time-dependent* Schrödinger equation can be written in the form

$$|\psi(t)\rangle = \lambda e^{-iE_A t/\hbar} |\psi_A\rangle + \mu e^{-iE_S t/\hbar} |\psi_S\rangle. \quad (7.23)$$

With Eq. 7.21, $|\psi(t)\rangle$ can be expressed in terms of $|\phi_1\rangle$ and $|\phi_2\rangle$. Since $|\phi_1\rangle$ and $|\phi_2\rangle$ are not eigenstates of the total Hamiltonian \mathbf{H} , they are no longer stationary states. If the system is in state $|\phi_1\rangle$ at time $t = 0$ ($|\psi(0)\rangle = |\phi_1\rangle$) the probability $P_{12}(t)$ of finding it in the state $|\phi_2\rangle$ at time t is

$$P_{12}(t) = |\langle\phi_2|\psi(t)\rangle|^2 \frac{4|t_{12}|^2}{4|t_{12}|^2 + (\Delta E)^2} \sin^2 \left[\sqrt{(\Delta E)^2 + (2|t_{12}|)^2} \frac{t}{2\hbar} \right]. \quad (7.24)$$

Equation 7.24 describes a coherent charge oscillation in the double dot system.

7.5.2 Photon assisted tunneling in weakly coupled dots

If the inter-dot coupling is weak, electrons are strongly localized on the individual dots. In section 7.2.1 we saw that we expect a resonant current through the double dot system if $\mu_L \geq \mu_1 = \mu_2 \geq \mu_R$. If we represent a weakly coupled double dot by a two-level system, we need the discrete energy levels E_1 and E_2 to align within the bias window. We will only consider the discrete, quantum contribution to the electrochemical potentials and therefore simply use the discrete level notation E_1 and E_2 instead of μ_1 and μ_2 .

An additional time-varying potential $V_{ac}\cos(2\pi ft)$ can induce *inelastic* tunnel events when electrons exchange photons of energy hf with the oscillating field (frequency, f , is typically 1-75 GHz in our experiments). This inelastic tunneling with discrete energy exchange is known as photon assisted tunneling (PAT) [50-52]. PAT through a single quantum dot with well resolved discrete 0D-states is reviewed in Ref. [53]. PAT is an invaluable spectroscopic tool for studying the energy spectra of quantum dots. A theoretical study of PAT in double dots is given in Refs. [54, 55]. A voltage drop $V_{ac}\cos(2\pi ft)$ across a tunnel barrier modifies the tunnel rate through the barrier as [56]

$$\tilde{\Gamma}(E) = \sum_{n=-\infty}^{\infty} J_n^2(\alpha) \Gamma(E + nhf) \quad (7.25)$$

Here $n = 0, \pm 1, \pm 2, \dots$, and $\tilde{\Gamma}(E)$ and $\Gamma(E)$ are the tunnel rates at energy E with and without an ac voltage, respectively. $J_n^2(\alpha)$ is the square of the n th order Bessel function of the first kind, evaluated at $\alpha = eV_{ac}/hf$, which describes the probability that an electron absorbs ($n > 0$) or emits ($n < 0$) n photons of

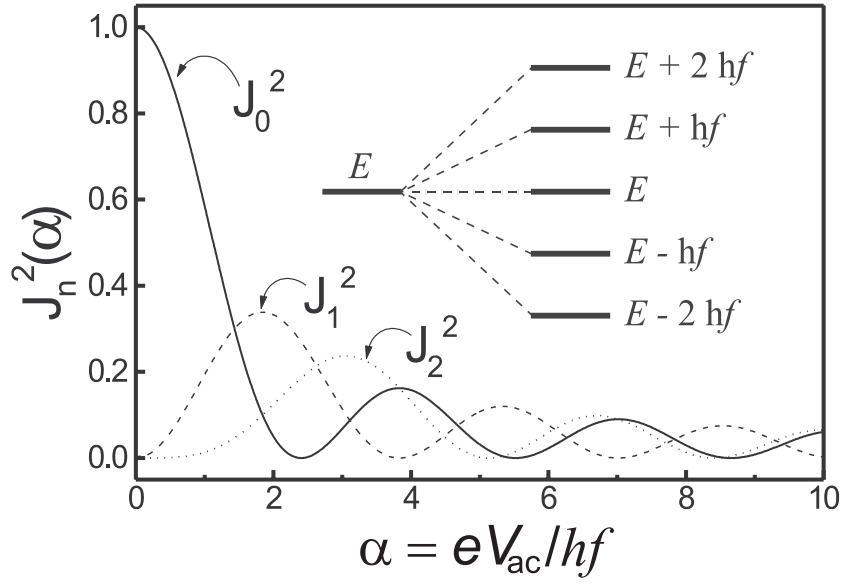


Figure 7.20: Squared Bessel functions of the first kind, $J_n^2(\alpha)$, for $n = 0, \pm 1, \pm 2$. The inset schematically shows the development of sidebands of the original energy as a consequence of the microwave field. A positive (negative) n corresponds to the absorption (emission) of n photons during the tunnel process. Elastic tunneling corresponds to $n = 0$.

energy hf . Thus, the effect of the interaction between a single-electron state with a classical, oscillating field is that the energy state E is split in a set of states $E + nhf$ (see inset to Fig. 7.20). The power of PAT as a spectroscopic tool lies in the fact that PAT can only take place if the energy difference ΔE equals an integer number times the photon energy hf : $\Delta E = nhf$, see Fig. 7.21. For the multiple photon processes ($|n| > 1$) to take place, the microwave power needs to be sufficiently large.

To use PAT as a spectroscopic tool, we can make use of the configurations shown in Fig. 7.21. In the pumping configuration [57, 58], the double dot is operated at zero bias voltage. Absorption of a photon with energy $hf = \Delta E$ leads to pumping of an electron from left to right (Fig. 7.21a) or vice versa (Fig. 7.21b). The advantage of this configuration is that relaxation due to spontaneous emission does not contribute to the current. Figure 7.22 schematically shows how the honeycomb unit cell of Fig. 7.5 changes in the presence of a microwave field.

Alternatively, the double dot can be operated in the large bias regime as depicted in Fig. 7.21c,d. In this regime, in the case of weak coupling with $|t_{12}| \ll \Delta E, hf, \hbar\Gamma_{L,R}$, the dc PAT current is given by [54]

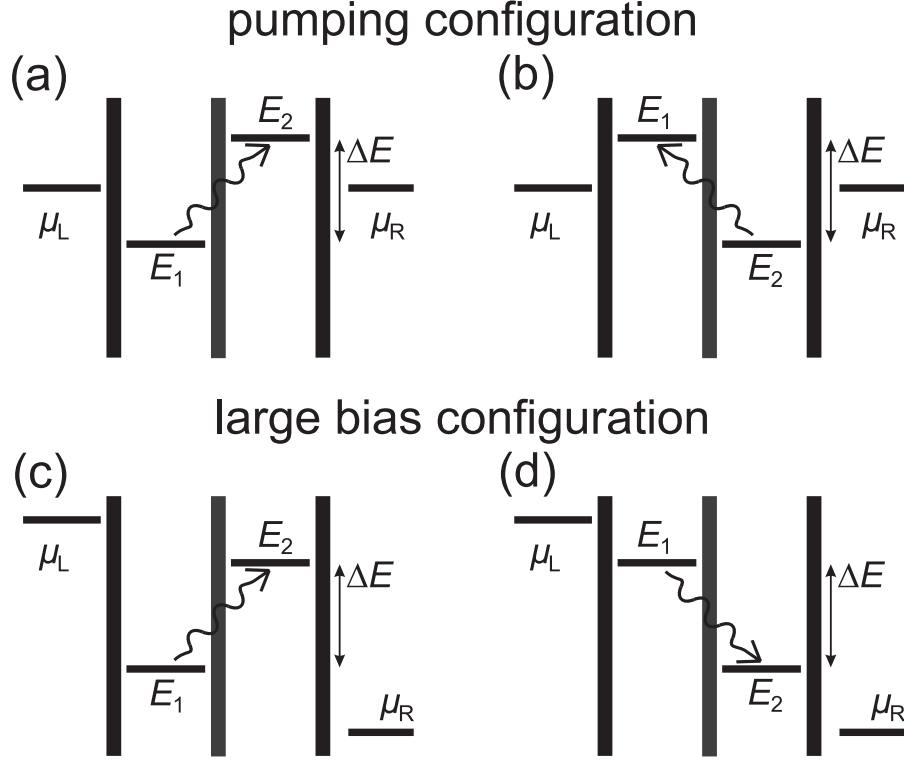


Figure 7.21: Schematic electrochemical potential diagrams of photon assisted tunneling (PAT) in a weakly coupled double quantum dot. The upper diagrams (a) and (b) show absorption of a photon with energy $hf = \Delta E$ in the so called pumping configuration. Although $V = 0$, an electron can tunnel from left to right through the dot (a), or vice versa (b). The lower diagrams show absorption (c) and (stimulated) emission (d) of a photon with energy $hf = \Delta E$ in the large bias configuration.

$$I_{PAT} = e|t_{12}|^2 \Gamma_R \sum_{n=-\infty}^{\infty} J_n^2(\alpha) / (\frac{1}{4}\Gamma_R^2 + (n2\pi f - \Delta E/h)^2) \quad (7.26)$$

The current is composed of a number of satellite peaks, separated by the photon energy hf and all with width Γ_R . Note that the satellite peaks can become of the same order of magnitude as the main resonance, but that they have a smaller width than the main resonance. The PAT experiment described below, is performed on a weakly coupled dot in the large bias regime.

The double dot, shown in Fig. 7.6a, is tuned such that only one level in each dot contributes to electron transport. The gate voltages are used to shift the level in dot 1 and in dot 2. The resonance in the lowest trace in Fig. 7.23a arises from the alignment of the two levels. The other traces are measured while applying

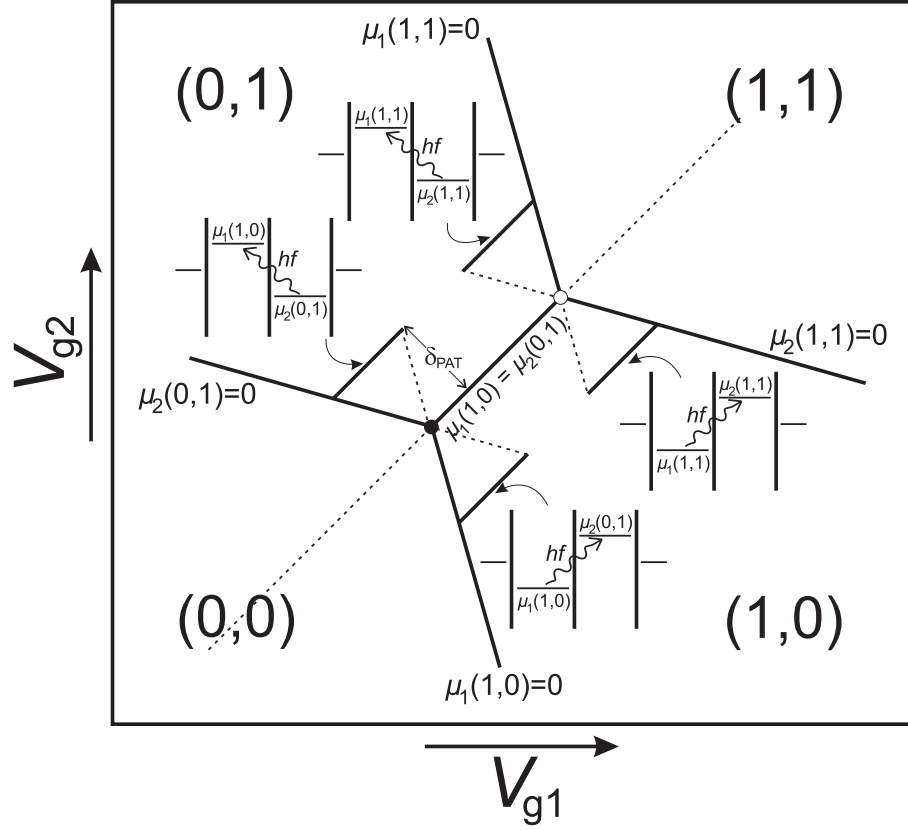


Figure 7.22: Schematic of a double quantum dot stability diagram in the weak coupling and linear transport regime irradiated by microwaves with frequency f . Next to the triple points, finite current is measured along the PAT lines at a distance δ_{PAT} from the line $\mu_1(1,0) = \mu_2(0,1)$, where $\Delta E = hf$. The various PAT processes are illustrated by the electrochemical potential diagrams.

a microwave signal. The satellite resonances are due to PAT processes which involve the emission (left satellite peak) or absorption (right satellite peak) of one photon. Figure 7.23b shows that the energy separation of the satellite peaks from the main peak, ΔE , depends linearly on frequency between 1 and 50 GHz. As we will discuss below, this linearity implies that the tunnel coupling is negligible. The electrons are localized on the individual dots and they have an ionic bonding. The line proportional to $2hf$ is taken from data at higher microwave powers where electrons absorb or emit two photons during tunneling.

As the microwave power is increased, more satellite peaks appear corresponding to the absorption of multiple photons, which are observed up to $n = 11$ (see Fig. 7.24). A high power microwave field strongly perturbs tunneling. This is reflected by the non-linear dependence of the peak heights on microwave power.

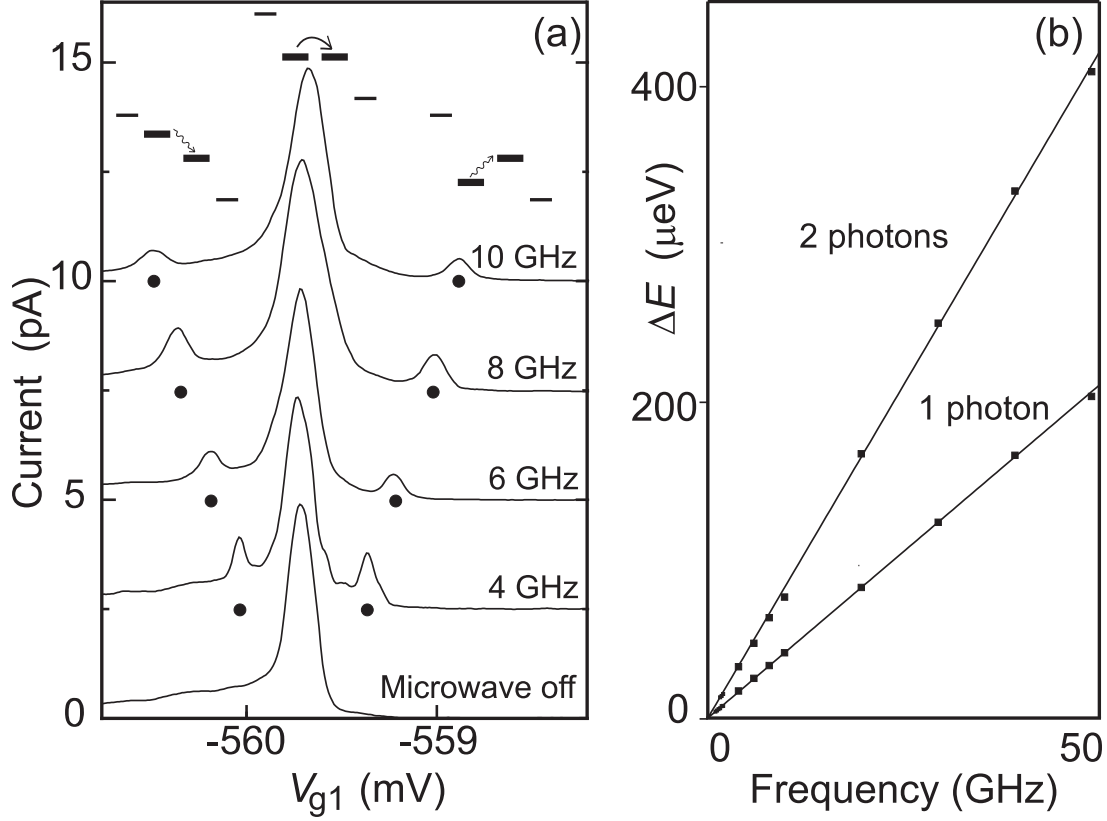


Figure 7.23: Weakly coupled double quantum dot in the low microwave power regime. (a) The upper schematic pictures illustrate three configurations of the discrete energy level in the left dot relative to the level in the right dot (thick solid lines). The electrochemical potentials of the leads are indicated by thinner solid lines. The bottom curve shows the current as a function of the voltage on gate 1, V_{g1} , (see Fig. 7.6b) for source-drain voltage, $V = 500 \mu\text{V}$ without applying microwaves. A single resonance occurs when two levels align. The other curves, which have been offset for clarity, show the current when microwaves with frequency f from 4 to 10 GHz are applied. Now, two additional satellite resonances occur when the two levels are exactly a photon energy apart. The corresponding photon-assisted tunneling processes are illustrated in the upper diagrams. (b) Distance between main resonance and first two satellites as a function of the applied frequency from 1 to 50 GHz. The distance is transferred to energy through $\Delta E = \kappa \Delta V_{g1}$ where κ is the appropriate capacitance ratio for our device that converts gate voltage to energy. The agreement between data points and the two solid lines, which have slopes of h and $2h$, demonstrates that we observe the expected linear frequency dependence of the one and two photon processes.

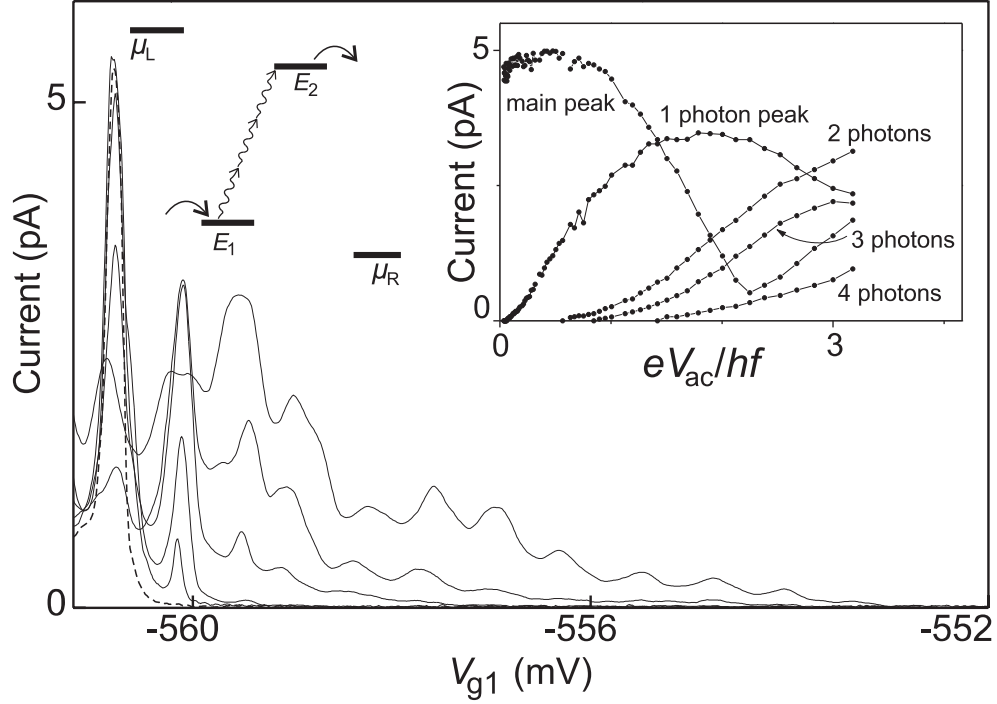


Figure 7.24: Weakly coupled double quantum dot in the high microwave power regime. The main graph shows current versus gate voltage. The dashed curve is without microwaves and contains only the main resonance. The solid curves are taken at 8 GHz for increasing microwave powers resulting in an increasing number of satellite peaks. At the right side of the main peak, these correspond to photon absorption. $V = 700 \mu\text{V}$ and the photon energy $hf = 32 \mu\text{eV}$ at 8 GHz. At the highest power we observe 11 satellite peaks, demonstrating multiple photon absorption. (left inset) Schematic diagram showing multi-photon absorption. (right inset) Height of the first four satellite peaks as a function of the microwave amplitude. The observed dependence shows the expected Bessel function behavior given in Fig. 7.20.

In the right inset to Fig. 7.24 the peak heights of the main peak and the first four photon satellite peaks are shown, which agree well with the expected squared Bessel function behavior shown in Fig. 7.20.

7.5.3 Photon assisted tunneling in strongly coupled dots

The large bias configuration of Figs. 7.21c,d was successfully employed to study PAT in a weakly coupled double dot system. For the microwave spectroscopy of a strongly coupled double dot we will make use of the pumping configuration shown in Fig. 7.25. With increasing the coupling between the dots, the sponta-

neous emission rate from the higher level to the lower one increases as well. The advantage of the pumping configuration is that these processes are ‘filtered out’ and do not contribute to the current.

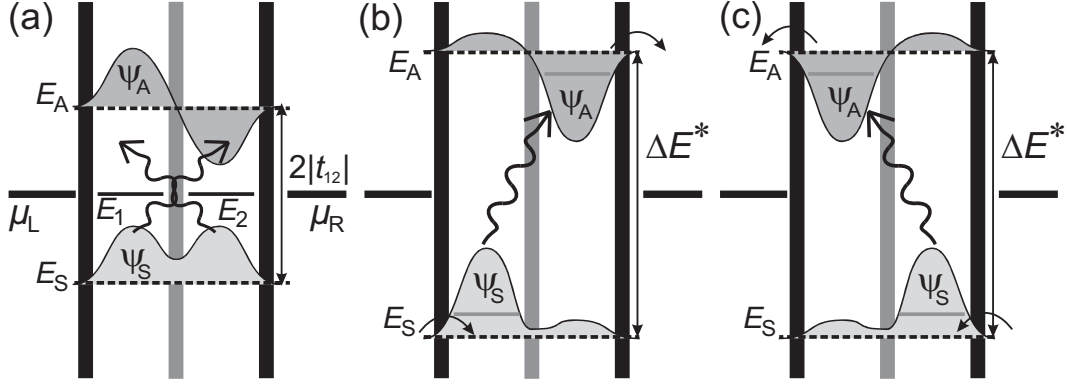


Figure 7.25: Schematic electrochemical potential diagrams of PAT in a strongly coupled double quantum dot in the pumping configuration. The diagrams show the symmetric state with wave function ψ_S and energy E_S (lower dashed line), and the anti-symmetric state with wave function ψ_A and energy E_A (upper dashed line) in combination with the eigenenergies E_1 and E_2 of the weakly coupled double dot (solid lines). (a) $E_1 = E_2 = 0$, $\Delta E^* = E_A - E_S = 2|t_{12}|$. Irradiation with photons with energy $hf = 2|t_{12}|$ leads to PAT, but the net current through the double dot remains zero. (b) By lowering $-|e|\varphi_1$ and increasing $-|e|\varphi_2$ the weight of the wave functions is redistributed such that net electron transport from left to right occurs. (c) By increasing $-|e|\varphi_1$ and lowering $-|e|\varphi_2$ the weight of the wave functions is redistributed such that net electron transport from right to left occurs.

Figure 7.25a schematically shows the symmetric and anti-symmetric states in the double dot for $\Delta E = 0$. When microwave radiation is applied with a frequency such that $hf = \Delta E^* = E_A - E_S = 2|t_{12}|$, electrons are pumped from the left lead to the right lead and vice versa. Since the weight of the symmetric and anti-symmetric wave function is distributed equally over both dots (see Fig. 7.25a), there is no net current. However, if we detune the levels ($|\Delta E| > 0$) the weight gets distributed asymmetrically as shown in Figs. 7.25b,c and a net current is generated by applying microwave radiation matching $hf = \Delta E^*$. Note that for frequencies $hf < 2|t_{12}|$ no PAT is possible.

Multi-photon processes occur if the condition $\Delta E^* = nhf$ ($|n| > 1$) is met. Besides allowing for these higher order photon processes, a high power microwave field also renormalizes the tunnel coupling to a smaller value. The energy splitting

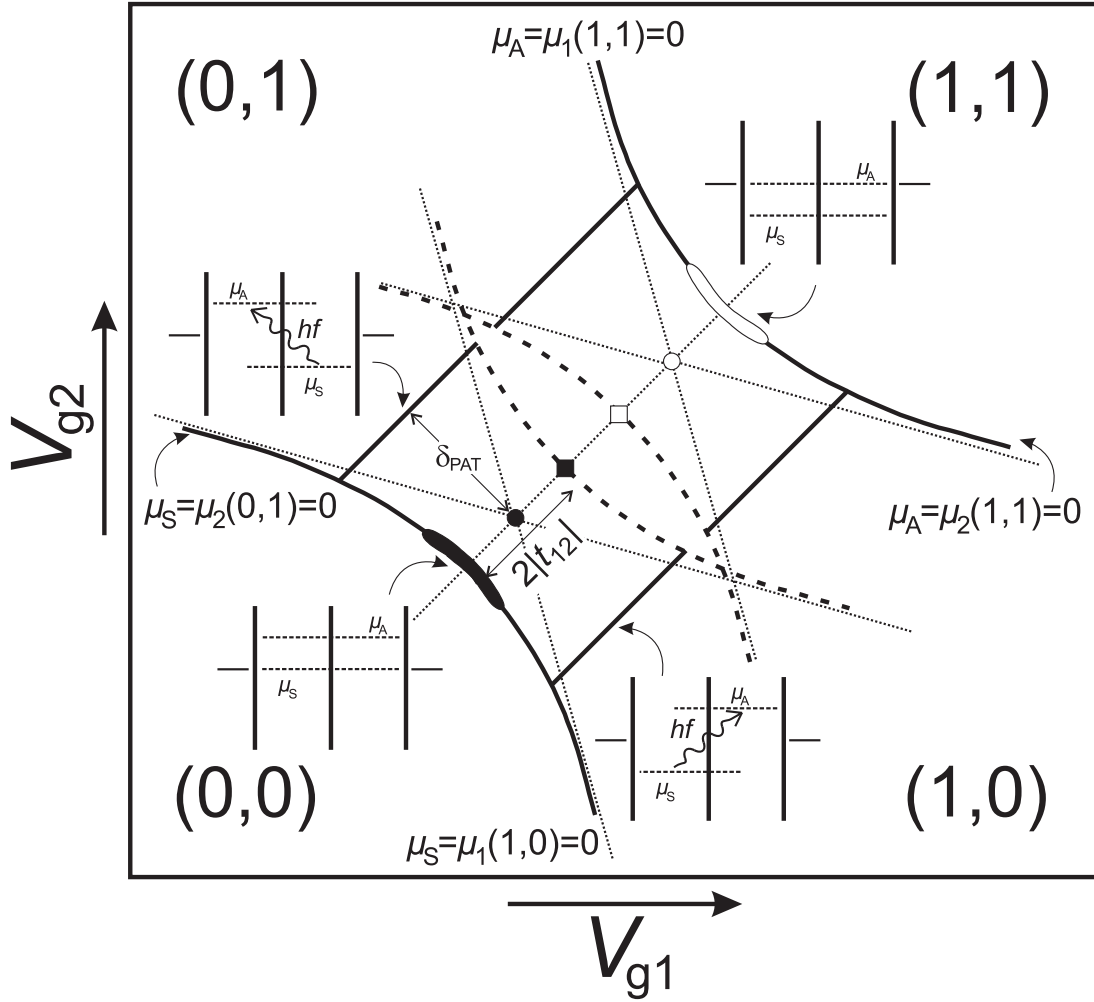


Figure 7.26: Schematic of a double quantum dot stability diagram in the strong coupling and linear transport regime irradiated by microwaves with frequency f . The symmetric and anti-symmetric states are assumed to be singly occupied. At the solid hyperbolic lines either μ_S or μ_A equals zero, marking the separation of charge domains. At the dashed hyperbolic lines either μ_S or μ_A equals zero as well, but electron transport is blocked. The triple points of the weakly coupled double dot (● and ○) develop into the black and white crescent, respectively. At the position of the black and white square no current occurs, as explained in the text. At a distance δ_{PAT} from the dotted line connecting the crescents, $\Delta E^* = hf$ and PAT occurs. The various configurations of the electrochemical potentials are also illustrated.

ΔE^* now becomes

$$\Delta E^* = \sqrt{(\Delta E)^2 + [2J_0(\alpha)|t_{12}|]^2}. \quad (7.27)$$

The experiments for strong inter-dot coupling are performed on the device shown in Fig. 7.6b. To single out the current only due to microwaves, we operate the device as an electron pump driven by photons [57, 58] (see the diagrams in Fig. 7.25). An electron is excited from the bonding to the anti-bonding state if the condition $hf = \Delta E^*$ is fulfilled, or conversely

$$\Delta E = \sqrt{(hf)^2 - (2J_0(\alpha)|t_{12}|)^2}. \quad (7.28)$$

Figure 7.26 schematically shows the stability diagram for a strongly coupled double dot in the presence of a microwave field. Here we assume that the symmetric and anti-symmetric states can only be occupied by a single electron. In other words, we assume spinless electrons. The triple points of the weakly coupled double dot, denoted by \bullet and \circ , develop into a black and a white crescent, respectively. The length of these crescents increases with $|t_{12}|$.

Moving along the dotted line connecting the crescents from lower left to upper right, first the symmetric state aligns with the electrochemical potentials of the leads (at the black crescent). Current through the double dot is possible via the electron transfer process of Fig. 7.2d. At the black square, the anti-symmetric state aligns with the leads. However, current is blocked, since an extra electron is already added to the double dot and the charging energy E_{Cm} is not available yet. At the white square, the electrochemical potential for adding the second electron to the symmetric state aligns with the leads. As we assumed single occupation of the delocalized states, current is blocked here as well. When arriving at the white crescent, the electrochemical potential for adding the second electron to the double dot in the (empty) anti-symmetric state becomes available. This enables the hole transfer process of Fig. 7.2d.

The black bars at a distance δ_{PAT} from the dotted line connecting the crescents, denote the places where $\Delta E^* = hf$ and PAT occurs. Note that PAT is only possible if the photon energy exceeds the coupling energy, $hf \geq 2|t_{12}|$. Depending on the level configuration, pumping results in a negative or positive contribution to the current, as shown in Fig. 7.27a (here we choose $I > 0$ for an electron moving from left to right). Figure 7.27b shows a part of the corresponding stability diagram between two triple points, clearly showing the energy regions of constant charge and extra transport lines due to PAT.

Figure 7.28 shows measured current traces as a function of the uncoupled energy splitting ΔE , where from top to bottom the applied microwave frequency

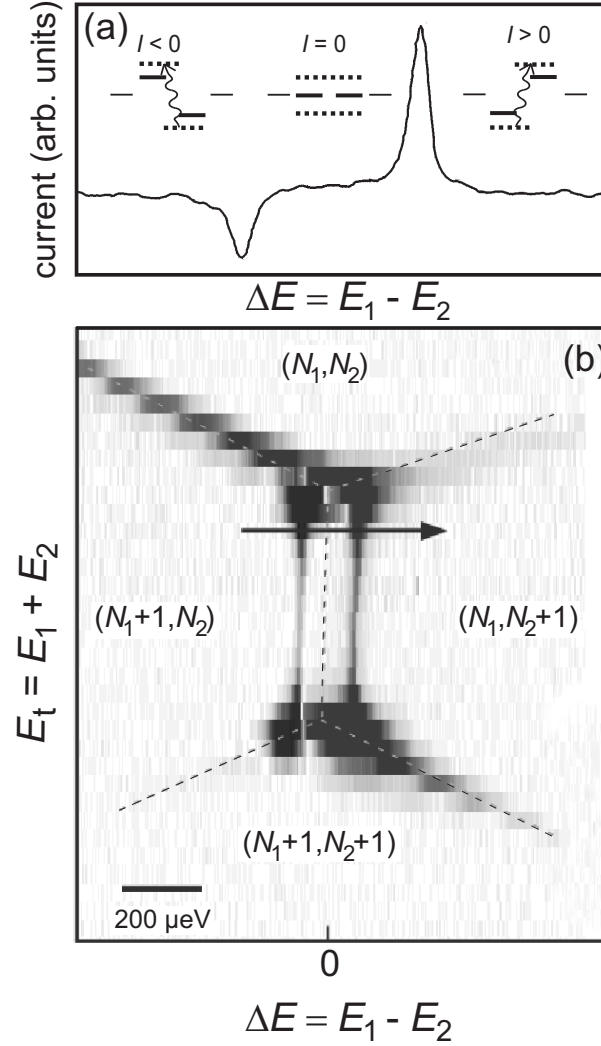


Figure 7.27: Strongly coupled double dot in the low-power regime. (a) Current through the double dot as function of the energy difference between the level in the left and the right dot. The current trace is taken from the stability diagram in (b) at the position indicated by the arrow. The diagrams depict the discrete levels E_1 and E_2 in the two dots for the case that the coupling is weak (solid lines) and the bonding and anti-bonding states in the case of strong coupling (dotted lines). The PAT processes leading to a negative (left diagram) and a positive current (right diagram) are indicated. (b) Gray-scale plot of the current through the double dot versus the energy level difference, ΔE , and the total energy, E_t . The bias voltage is $6 \mu\text{V}$ and the applied microwave frequency is 16 GHz such that $hf = 66 \mu\text{eV}$. The dashed lines divide the stability diagram in 4 regions of stable electron numbers. In between the two triple points clear features of photon-assisted tunneling are seen. The black arrow indicates the position of the trace shown in (a).

is decreased from 17 to 7.5 GHz in 0.5 GHz steps. At the highest frequencies, the distance between the pumping peaks is close to $2\Delta E$. However, the peak distance decreases faster than linearly as the frequency is lowered; in fact the peaks follow the dotted hyperbola rather than the dashed straight lines. The distance goes to zero when the frequency approaches the minimum energy gap between bonding and anti-bonding states, $hf = 2|t_{12}|$. The coupling between the

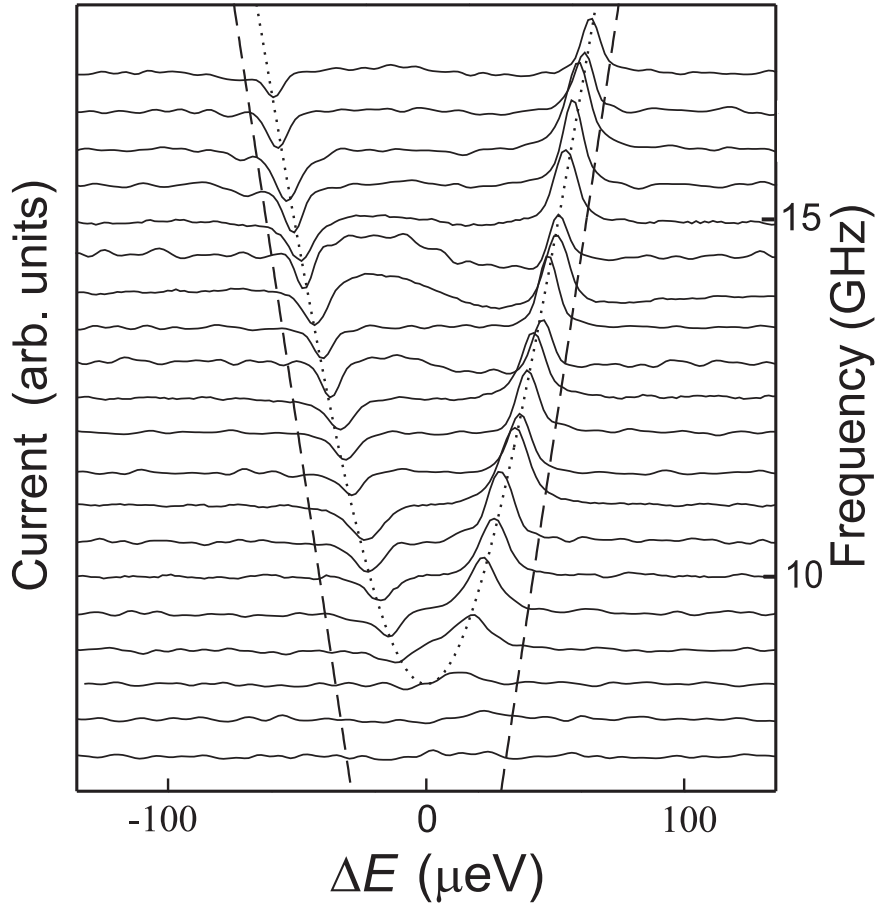


Figure 7.28: Measured pumped current through the strongly coupled double dot. Gates 1 and 3 are swept simultaneously in such a way that we vary the energy difference ΔE . The different traces are taken at different microwave frequencies, and are offset such that the right vertical axis gives the frequency. The main resonance is absent as we have set $V = 0$. The satellite peaks typically have an amplitude of 0.5 pA. For weakly coupled dots the satellite peaks are expected to move linearly with frequency, thereby following the straight dashed lines. In contrast, we observe that the satellite peaks follow the fitted dotted hyperbola $hf = [\Delta E^2 + (2|t_{12}|)^2]^{1/2}$ using the coupling $|t_{12}|$ as a fitting parameter.

dots can be decreased by changing the gate voltage on the center gate to more negative values, or by applying a magnetic field perpendicular to the sample. In Fig. 7.29a we plot half the spacing between the positive and negative satellite peaks as a function of frequency. The microwave power is kept as low as possible in order to meet the condition $eV_{ac} \ll hf$. In that case $J_0^2(\alpha) \approx 1$ and the general relation Eq. 7.28 reduces to

$$\Delta E = \sqrt{(hf)^2 - (2|t_{12}|)^2}. \quad (7.29)$$

Different symbols correspond to different center gate voltage settings and magnetic fields. The solid lines are fits to Eq. 7.29. The good agreement with Eq. 7.29 demonstrates the control over the formation of a covalent bonding between the two dots and that the condition $eV_{ac} \ll hf$ is satisfied.

We now discuss the case $eV_{ac} \gtrsim hf$. As can be seen in Fig. 7.20, $J_0^2(\alpha)$ deviates from 1 in this case and cannot be neglected as before [48]. In Fig. 7.29b we show the power dependence for the case of a coupling of 60 μeV and a microwave frequency of 16 GHz, as indicated by the circle in Fig. 7.29a (similar results have been obtained for other couplings and microwave frequencies). The inset to Fig. 7.29b shows the measured PAT current as a function of ΔE for different powers. The absolute value of the microwave power at the position of the double quantum dot is unknown. Therefore, we use a relative microwave power scale, which is expressed in terms of the attenuation of the microwave source signal. The positions of the PAT peaks at the lowest power are indicated with two dashed lines. Increasing the microwave power from the lowest value, the PAT peak separation becomes larger, which is in agreement with Eq. 7.28. For higher powers, multi-photon processes can also take place, which result in extra current peaks. Figure 7.29b shows half the PAT peak separation energy as function of the relative microwave power. The solid line is a fit with Eq. 7.28, $f = 16$ GHz, $2|t_{12}| = 60 \mu\text{eV}$. Because of the relative power scale, the fitting curve has been adjusted horizontally to give the best fit. We thus see that the microwave power effectively reduces the coupling between the dots. This is further illustrated by the vertical dotted line in Fig. 7.29a at $f = 16$ GHz. At -33 dB the energy separation equals hf , which implies that the higher microwave power has effectively reduced the coupling between the dots. We can obtain an estimate of the power by noting that $J_0^2(\alpha)$ has its first zero for $\alpha = eV_{ac}/hf = 2.4$ and hence $V_{ac} = 0.16$ mV.

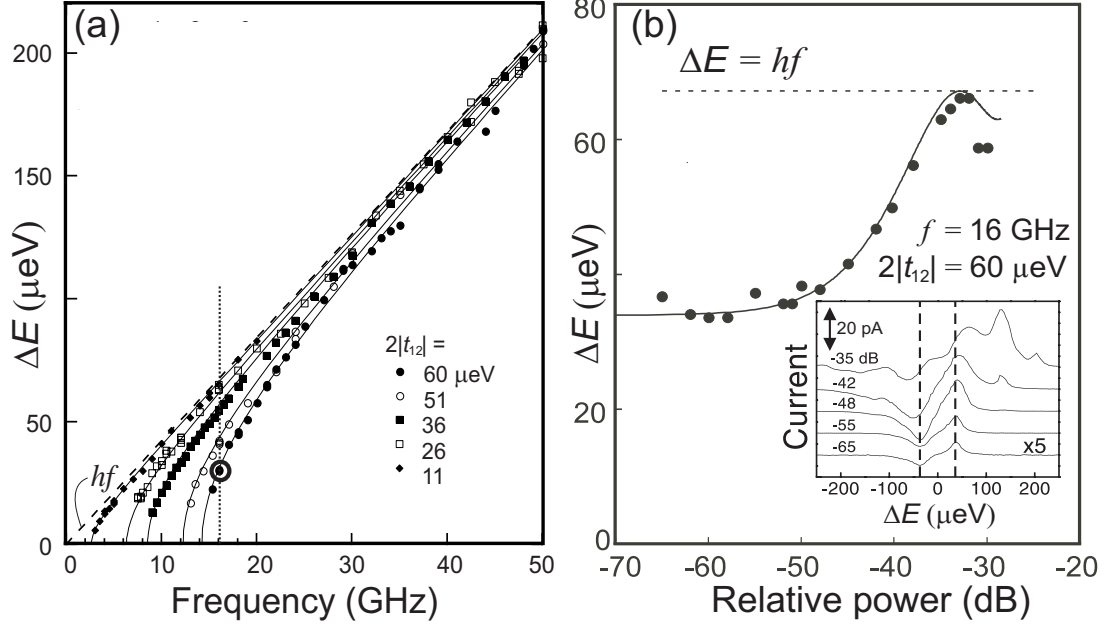


Figure 7.29: (a) Half the spacing in gate voltage between the positive and negative satellite peaks as a function of frequency for $eV_{ac} \ll hf$. Gate voltage spacing has been transferred to energy difference ΔE (see also figure caption Fig. 7.23b). Different curves correspond to different tunnel couplings $|t_{12}|$. Solid lines are theoretical fits to Eq. 7.29. In the limit of weak coupling, this reduces to $\Delta E = hf$, which is indicated by the dashed line. The resulting values for $2|t_{12}|$ are given in the figure. The coupling is varied by applying different voltages to the center gate or by changing the magnetic field (\blacklozenge $B = 3.3 \text{ T}$; \blacksquare $B = 2.2 \text{ T}$; other curves $B = 0 \text{ T}$). The circle marks a coupling of $60 \mu\text{eV}$ and frequency of 16 GHz (dotted line). (b) Strongly coupled double dot ($2|t_{12}| = 60 \mu\text{eV}$) in the high microwave power regime for $f = 16 \text{ GHz}$ (along dotted line in (a)). The inset shows the measured PAT current as a function of ΔE for different powers. The positions of the PAT peaks at the lowest power are indicated with two dashed lines. The PAT peak separation becomes larger for increasing microwave power. For higher powers, multi-photon processes can also take place, which result in extra current peaks. In the main part, half the PAT peak separation in energy as function of the relative microwave power is shown. The solid line is a fit to Eq. 7.28, $f = 16 \text{ GHz}$, $2|t_{12}| = 60 \mu\text{eV}$. Because of the relative power scale, the fitting curve has been adjusted horizontally to obtain the best fit.

7.6 Conclusions

By coupling two quantum dots in series, we obtain a system with fundamentally different behavior and possibilities in comparison to a single quantum dot. In this review we have discussed the superiority of a double quantum dot system in determining the intrinsic lifetime of quantum states and in probing intra-dot level repulsion. Next to the added value as a spectroscopic instrument, the double dot manifests itself as an artificial molecule. By changing the inter-dot coupling, we have been able to tune the double dot from an ionic-like bonded to a covalent-like bonded molecule.

Now that the ability to create and manipulate double quantum dots has been shown, the next challenge lies in the study and time-control of coherent phenomena in these systems. Double quantum dots have been suggested as possible candidates for building blocks of a quantum computer [5]. We have shown that it is indeed possible to coherently couple dots, and that one can induce transitions between the extended states. The next crucial step towards quantum logic gates is to show that the coherence of the superposition is preserved on time scales much longer than the time needed for manipulating the electron wave functions. The time-resolved measurement of coherent charge oscillations in double quantum dots using pulsed gate voltages, will be an essential step in determining the dephasing time in these systems.

In addition, the role of the electron spin and its relaxation and dephasing times (T_1 and T_2 , respectively) need to be characterized, as they are essential in the proposed quantum bit schemes based on coupled electron spins in double dots [5]. The relaxation time T_1 in quantum dots has been experimentally shown to exceed 10 - 100 μ s if the relaxation involves a spin-flip [59]. The determination of the spin dephasing time T_2 , which is the most relevant timescale for quantum computing purposes, will be an experimental challenge for the near future. We conclude that our work on double dots so far, in combination with the results on the spin relaxation times in this kind of systems, forms a promising point of departure for further study on the suitability of double quantum dots as quantum coherent devices.

Acknowledgements

We thank R. Aguado, S.M. Cronenwett, D.C. Dixon, S. Godijn, P. Hadley, C.J.P.M. Harmans, R.V. Hijman, Y. Hirayama, K. Ishibashi, M.P. Janus, K.K. Likharev, F. Mallens, J.E. Mooij, Yu.V. Nazarov, T.H. Oosterkamp, R.M. Schouten,

T.H. Stoof, M.J. Uilenreef, N.C. van der Vaart and L. Vandersypen for their help. We acknowledge financial support from the DARPA grant number DAAD19-01-1-0659 of the QuIST program, the Specially Promoted Research Grant-in-Aid for Scientific Research; the Ministry of Education, Culture, Sports, Science and Technology in Japan; the Dutch Organization for Fundamental Research on Matter (FOM); the Core Research for Evolutional Science and Technology (CREST-JST); and the European Union through a Training and Mobility of Researchers (TMR) Program network.

References

- [1] L.P. Kouwenhoven, C.M. Marcus, P.L. McEuen, S. Tarucha, R.M. Westervelt and N.S. Wingreen, *Electron transport in quantum dots*, in Mesoscopic Electron Transport, edited by L.L. Sohn, L.P. Kouwenhoven and G. Schön, (Kluwer, Series E **345**, 1997), p.105-214.
- [2] *Single Charge Tunneling*, edited by H. Grabert and M.H. Devoret (Plenum, New York, 1991).
- [3] D.V. Averin and K.K. Likharev, J. Low Temp. Phys. **62**, 345 (1986); in Mesoscopic Phenomena in Solids, edited by B.L. Altshuler, P.A. Lee and R.A. Webb (Elsevier, 1991).
- [4] M. Kastner, Physics Today **46**, 24 (1993).
- [5] D. Loss and D.P. DiVincenzo, Phys. Rev. A **57**, 120-126 (1998).
- [6] M. Kemerink and L.W. Molenkamp, Appl. Phys. Lett. **65**, 1012 (1994).
- [7] N.C. van der Vaart, S.F. Godijn, Yu.V. Nazarov, C.J.P.M. Harmans and J.E. Mooij, Phys. Rev. Lett. **74**, 4702 (1995).
- [8] F.R. Waugh, M.J. Berry, D.J. Mar, R.M. Westervelt, K.L. Campman and A.C. Gossard, Phys. Rev. Lett. **75**, 705 (1995).
- [9] L.W. Molenkamp, K. Flensberg, M. Kemerink, Phys. Rev. Lett. **75**, 4282 (1995).
- [10] T. Fujisawa and S. Tarucha, Appl. Phys. Lett. **68**, 526 (1996).
- [11] F.R. Waugh, M.J. Berry, C.H. Crouch, C. Livermore, D.J. Mar, R.M. Westervelt, K.L. Campman and A.C. Gossard, Phys. Rev. B **53**, 1413 (1996).
- [12] R.H. Blick, R.J. Haug, J. Weis, D. Pfannkuche, K. v. Klitzing and K. Eberl, Phys. Rev. B **53**, 7899 (1996).

- [13] D.C. Dixon, L.P. Kouwenhoven, P.L. McEuen, Y. Nagamune, J. Motohisa and H. Sakaki, *Phys. Rev. B* **53**, 12625 (1996).
- [14] C. Livermore, C.H. Crouch, R.M. Westervelt, K.L. Campman and A.C. Gossard, *Science* **274**, 1332 (1996).
- [15] T. Fujisawa and S. Tarucha, *Superlattices and Microstructures* **21**, 247 (1997).
- [16] T. Fujisawa and S. Tarucha, *Jpn. J. Appl. Phys.* **36**, 4000 (1997).
- [17] R.H. Blick, D. Pfannkuche, R.J. Haug, K. von Klitzing and K. Eberl, *Phys. Rev. Lett.* **80**, 4032 (1998).
- [18] T.H. Oosterkamp, S.F. Godijn, M.J. Uilenreef, Yu. V. Nazarov, N.C. van der Vaart and L.P. Kouwenhoven, *Phys. Rev. Lett.* **80**, 4951 (1998).
- [19] T.H. Oosterkamp, T. Fujisawa, W.G. van der Wiel, K. Ishibashi, R.V. Hijman, S. Tarucha and L.P. Kouwenhoven, *Nature* **395**, 873 (1998).
- [20] T. Fujisawa, T.H. Oosterkamp, W.G. van der Wiel, B.W. Broer, R. Aguado, S. Tarucha and L.P. Kouwenhoven, *Science* **282**, 932 (1998).
- [21] K. Ishibashi, T.H. Oosterkamp, R.V. Hijman and L.P. Kouwenhoven, *Jpn. J. Appl. Phys.* **37**, 7161 (1998).
- [22] D.C. Dixon, Ph.D. thesis, University of California, Berkeley (1998).
- [23] H. Jeong, A.M. Chang and M.R. Melloch, *Science* **293**, 2221 (2001).
- [24] F. Hofmann, T. Heinzl, D.A. Wharam, J.P. Kotthaus, G. Böhm, W. Klein, G. Tränkle and G. Weimann, *Phys. Rev. B* **51**, 13872 (1995).
- [25] A.S. Adourian, C. Livermore, R.M. Westervelt, K.L. Campman and A.C. Gossard, *Superlattices and Microstructures* **20**, 411 (1996).
- [26] A.S. Adourian, C. Livermore, R.M. Westervelt, K.L. Campman and A.C. Gossard, *Appl. Phys. Lett.* **75**, 424 (1999).
- [27] M.A. Reed, J.N. Randall, J.H. Luscombe, W.R. Frensley, R.J. Aggarwal, R.J. Matyi, T.M. Moore and A.E. Wetsel, *Adv. Solid State Phys* **29**, 267 (1989).
- [28] M. Tewordt, H. Asahi, V.J. Law, R.T. Syme, M.J. Kelly, D.A. Ritchie, A. Churchill, J.E.F. Frost, R.H. Hughes and G.A.C. Jones, *Appl. Phys. Lett.* **60**, 595 (1992).
- [29] T. Schmidt, R.J. Haug, K. von Klitzing, A. Förster and H. Lüth, *Phys. Rev. Lett.* **78**, 1544 (1997).
- [30] D.G. Austing, T. Honda and S. Tarucha, *Jpn. J. Appl. Phys.* **36**, 1667 (1997).

- [31] D.G. Austing, T. Honda, K. Muraki, Y. Tokura and S. Tarucha, *Physica B* **249-251**, 206 (1998).
- [32] S. Tarucha, T. Fujisawa, K. Ono, D.G. Austing, T.H. Oosterkamp, W.G. van der Wiel and L.P. Kouwenhoven, *Microelectronic Engineering* **47**, 101 (1999).
- [33] D.G. Austing, H. Tamura, Y. Tokura, K. Muraki, S. Amaha, K. Ono and S. Tarucha, to be published in *Physica E* (2001).
- [34] S. Amaha, D.G. Austing, Y. Tokura, K. Muraki, K. Ono and S. Tarucha, *Solid State Comm.* **119**, 183 (2001).
- [35] H. Pothier, P. Lafarge, C. Urbina, D. Estève and M.H. Devoret, *Europhys. Lett.* **17**, 249 (1992).
- [36] I.M. Ruzin, V. Chandrasekhar, E.I. Levin and L.I. Glazman, *Phys. Rev. B* **45**, 13469 (1992). Ruzin *et al.* have an error in their Eq. (9), namely the numerator, $(2C + C_i\delta_{ij})$. For $i = j$, this relation gives $(2C + C_1)$ when it should read $(2C + C_2)$, and vice-versa.
- [37] D.V. Averin and Yu.V. Nazarov, in *Single Charge Tunneling: Coulomb Blockade Phenomena in Nanostructures*, edited by H. Grabert and M.H. Devoret (Plenum Press and NATO Scientific Affairs Division, New York, 1992), p. 217.
- [38] B. Su, V.J. Goldman and J.E. Cunningham, *Science* **255**, 313 (1992); P. Gueret *et al.*, *Phys. Rev. Lett.* **68**, 1896 (1992).
- [39] A.T. Johnson, L.P. Kouwenhoven, W. de Jong, N.C. van der Vaart, C.J.P.M. Harmans and C.T. Foxon, *Phys. Rev. Lett.* **69**, 1592 (1992).
- [40] E.B. Foxman, P.L. McEuen, U. Meirav, Ned S. Wingreen, Y. Meir, P.A. Belk, N.R. Belk, M.A. Kastner and S.J. Wind, *Phys. Rev. B* **47**, 10020 (1993).
- [41] L.P. Kouwenhoven, *Science* **268**, 1440 (1995).
- [42] Yu.V. Nazarov, *Physica B* **189**, 57 (1993).
- [43] T.H. Stoof, Delft University of Technology, Ph.D. Thesis, 1997.
- [44] C.W.J. Beenakker, *Phys. Rev. B* **44**, 1646 (1991).
- [45] T. Fujisawa, Y. Tokura and Y. Hirayama, *Phys. Rev. B* **63**, 081304(R) (2001).
- [46] S. Tarucha, D.G. Austing, Y. Tokura, W.G. van der Wiel and L.P. Kouwenhoven, *Phys. Rev. Lett.* **84**, 2485 (2000).

- [47] T.H. Oosterkamp, L.P. Kouwenhoven, A.E.A. Koolen, N.C. van der Vaart and C.J.P.M. Harmans, Phys. Rev. Lett. **78**, 1536 (1997).
- [48] W.G. van der Wiel, T. Fujisawa, T.H. Oosterkamp and L.P. Kouwenhoven, Physica B **272**, 31 (1999).
- [49] C. Cohen-Tannoudji, B. Diu and F. Laloë, Quantum Mechanics Vol. 1, John Wiley & Sons, New York (1977).
- [50] L.P. Kouwenhoven, S. Jauhar, K. McCormick, D.C. Dixon and P.L. McEuen, Phys. Rev. B **50**, 2019 (1994).
- [51] L.P. Kouwenhoven, S. Jauhar, J. Orenstein, P.L. McEuen, Y. Nagamune, J. Motohisa and H. Sakaki, Phys. Rev. Lett. **73**, 3443 (1994).
- [52] R.H. Blick, R.J. Haug, D.W. van der Weide, K. von Klitzing and K. Eberl, Appl. Phys. Lett. **67**, 3924 (1995).
- [53] T.H. Oosterkamp, W.G. van der Wiel, S. De Franceschi, C.J.P.M. Harmans and L.P. Kouwenhoven, cond-mat/9904359.
- [54] T.H. Stoof and Yu.V. Nazarov, Phys. Rev. B **53**, 1050 (1996).
- [55] B.L. Hazelzet, M.R. Wegewijs, T.H. Stoof and Yu.V. Nazarov, Phys. Rev. B **63**, 165313 (2001).
- [56] P.K. Tien and J.R. Gordon, Phys. Rev. **129**, 647-651 (1963).
- [57] C.A. Stafford and N.S. Wingreen, Phys. Rev. Lett. **76**, 1916 (1996).
- [58] Ph. Brune, C. Bruder and H. Schoeller, Physica E **1**, 216 (1997).
- [59] T. Fujisawa *et al.*, to be published.

Chapter 8

Spontaneous emission spectrum in double quantum dots

T. Fujisawa, T.H. Oosterkamp, W.G. van der Wiel
B.W. Broer, R. Aguado, S. Tarucha and L.P. Kouwenhoven

A double quantum dot device is a tunable two-level system for electronic energy states. A dc electron current directly measures the rates for elastic and inelastic transitions between the two levels. For inelastic transition energy is exchanged with bosonic degrees of freedom in the environment. The inelastic transition rates are well described by the Einstein coefficients, relating absorption with stimulated and spontaneous emission. The most effectively coupled bosons in the specific environment of our semiconductor device are acoustic phonons. The experiments demonstrate the importance of vacuum fluctuations in the environment for little circuits of coherent quantum devices.

This chapter has been published in Science **282**, 932 (1998).

Electronic quantum devices explore quantum mechanical properties of electrons confined to small regions in a solid by means of modern fabrication techniques. Existing devices include semiconductor resonant tunneling diodes [1] (based on quantum mechanical confinement), superconducting Josephson junction circuits [2] (based on macroscopic phase coherence), metallic single electron transistors [3] (based on quantization of charge), and molecular electronic devices [4]. The principle of operation in circuits of these devices is based on controlling energy states, for instance, by means of an external (gate) voltage. One source for unwanted transitions and errors is always the thermal energy from a non-zero temperature. However, even at zero temperature vacuum fluctuations in the environment can give rise to transitions between states of non-equal energy by spontaneous emission of an energy quantum. Such inelastic transitions cause errors in many proposed schemes for quantum circuits. We have studied inelastic transitions in a fully-controllable, two-level quantum system realized in a double quantum dot device. We can relate the transition rates involving emission to absorption rates by the Einstein coefficients over our full energy and temperature range. At our lowest temperature we directly measure the energy-dependent rate for spontaneous emission. In our specific semiconductor device this energy is emitted into the environment formed by acoustic phonons.

Our double quantum dot (Fig. 8.1a) is fabricated in the two-dimensional electron gas (2DEG) of an AlGaAs/GaAs semiconductor heterostructure [5]. The source and drain are large 2DEG regions which serve as leads for contacting current and voltage wires. The two dots, L and R , are separated from each other and from the leads, by potential barriers induced by negative voltages applied to the three metallic gates. Tunneling between the different regions is sufficiently strong to detect current, but weak enough such that the number of electrons in each dot is a well-defined integer. The energy states in such fully confined regions are discrete, 0D-states; resembling discrete atomic states [6, 7]. The discrete energies include contributions from single-electron charging energies, arising from Coulomb interactions, and from quantum-mechanical confinement. The lowest energy state for one additional electron in the left dot is labelled in Fig. 8.1b-d as E_L and similarly E_R for the right dot. Fig. 8.1c illustrates the resonance condition, $E_L = E_R$, in which case an electron can tunnel elastically from an occupied state in the source via E_L and E_R to an empty state in the drain. Such tunneling sequences of single electrons are regulated by the Coulomb charging energies [3, 7]. When the two states are not aligned, $E_L \neq E_R$, only inelastic transitions are allowed for which some energy needs to be exchanged with the environment. A measured off-resonance current, therefore, directly provides information about the coupling between electrons on the dots to degrees of freedom in the envi-

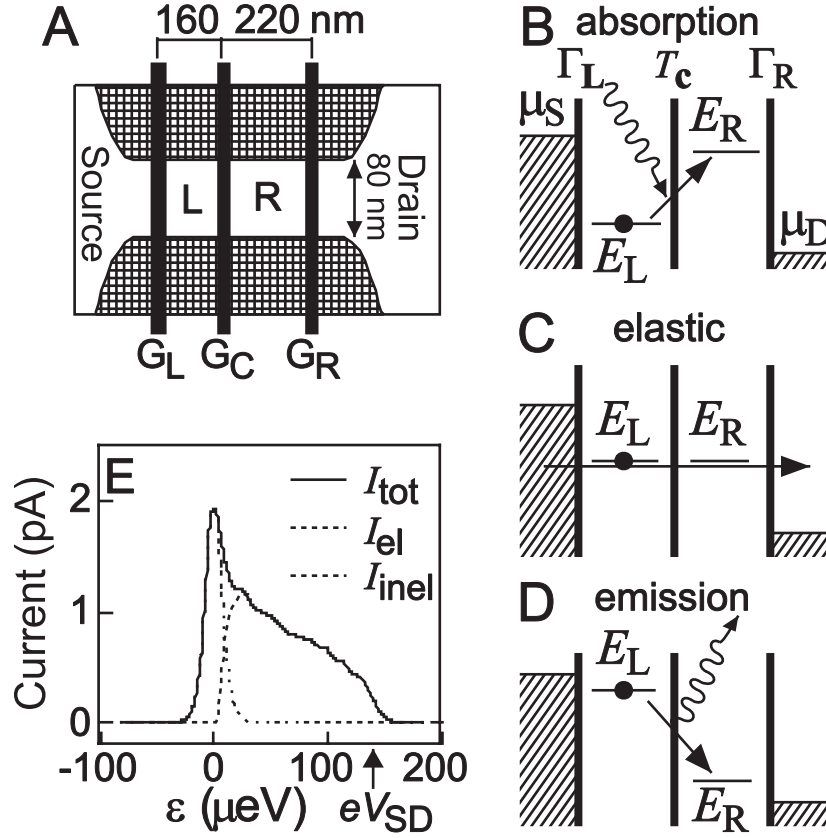


Figure 8.1: (a) Double quantum dot device defined in the 2DEG of a GaAs/AlGaAs heterostructure by focused ion beam implantation. The narrow channel connects the large 2D source and drain leads. Negative voltages (V_{GL} , V_{GC} , and V_{GR}) applied to the metal gates (G_L , G_C , and G_R ; widths are 40 nm) induce three tunable tunnel barriers in the wire. The two quantum dots, L and R, respectively, contain ~ 15 and ~ 25 electrons; charging energies are ~ 4 and ~ 1 meV; and the measured average spacing between single-particle states are ~ 0.5 and ~ 0.25 meV. (b, c, and d) Energy diagrams (vertical axis) along the spatial axis through the dots (horizontal axis) for the tunnel situations: absorption, elastic and emission. Thick vertical lines denote tunnel barriers. The continuous electron states in the leads are filled up to the Fermi energies μ_S and μ_D . The external voltage V_{SD} between leads opens a transport window of size: $eV_{SD} = \mu_S - \mu_D$. The energy, $\varepsilon \equiv E_L - E_R$, is defined as the difference between the topmost filled discrete-state of the left dot, E_L , and the lowest discrete-state for adding an extra electron to the right dot, E_R . (The inter-dot capacitance prevents that E_L and E_R are simultaneously occupied.) An elastic current can flow when $\varepsilon = 0$, otherwise a non-zero current requires absorption ($\varepsilon < 0$) or emission of energy ($\varepsilon > 0$). T_c is the tunnel coupling and Γ_i is the inelastic rate between the two dots. Γ_L and Γ_R are the tunnel rates across the left and the right barriers. (e) Typical measurement of the current (solid) versus ε at 23 mK. The measured current is decomposed in an elastic (dashed) and an inelastic (dotted-dashed) part.

ronment. The inelastic rates can be analyzed with well-developed methods in quantum optics [8, 9].

Figure 8.1e shows a typical current spectrum versus $\varepsilon \equiv E_L - E_R$ at our lowest lattice temperature $T = 23$ mK [10]. The gate voltages V_{GR} and V_{GL} are swept simultaneously such that the respective energies are like in Fig. 8.1b-d; that is, $\varepsilon = 0$ occurs in the middle between the Fermi energies of source and drain, μ_S and μ_D , and $|\varepsilon| = eV_{SD}$ is maximal corresponds to having the states E_L and E_R aligned to one of the Fermi energies. To analyze the large asymmetry, we decompose the total current $I_{tot}(\varepsilon) = I_{el}(\varepsilon) + I_{inel}(\varepsilon > 0)$ into a symmetric part $I_{el}(\varepsilon) = I_{el}(-\varepsilon)$ (dashed curve) and the remaining asymmetric part $I_{inel}(\varepsilon > 0)$ (dotted-dashed curve). At $T = 0$, $I_{el}(\varepsilon)$ is due to elastic tunneling and has a lorentzian line shape $I_{el}(\varepsilon) = I_{el,max} w^2 / (w^2 + \varepsilon^2)$ [11]. The full width at half maximum (FWHM), $2w$, can be tuned by the central gate voltage V_{GC} roughly from 4 to 20 μeV . From measurements of $I_{el}(\varepsilon)$ at positive and negative V_{SD} it is possible to extract values for the tunnel couplings Γ_L , Γ_R and T_c [11, 12].

The remaining current, $I_{inel}(\varepsilon > 0)$, which is non-zero only for $\varepsilon > 0$ (at $T=0$), is due to inelastic tunneling. In Fig. 8.1e, I_{inel} is non-zero over an energy range of ~ 100 μeV ; this despite that the thermal energy $k_B T$ (23 mK) = 2 μeV is much smaller. (The irregular fine structure is discussed below.) In general we find that I_{inel} vanishes when one of the levels, E_L or E_R , crosses one of the two Fermi energies. In the specific case of Fig. 8.1e, E_L and E_R cross the Fermi energies simultaneously, implying that I_{inel} is cut off at $\varepsilon = eV_{SD}$. Below this cut off, the value of I_{inel} was not influenced by the value of V_{SD} [13]. For $T = 0$, we can write the condition for a non-zero inelastic current as $\mu_S > E_L > E_R > \mu_D = \mu_S - eV_{SD}$. The amount of inelastic current depends on the transition rates as: $I_{inel}(\varepsilon) = e(\Gamma_L^{-1} + \Gamma_i^{-1}(\varepsilon) + \Gamma_R^{-1})^{-1}$. When the inelastic rate $\Gamma_i(\varepsilon)$ from E_L to E_R is much smaller than the rates through the outer barriers, this reduces to $I_{inel}(\varepsilon) = e\Gamma_i(\varepsilon)$.

The effect of a non-zero temperature on the current is shown in Fig. 8.2a. A higher temperature T , enhances I_{tot} on both the emission ($\varepsilon > 0$) and the absorption ($\varepsilon < 0$) side. The absorption spectrum shows an exponential temperature dependence, $e^{\varepsilon/kT}$ (dashed lines) for absolute energies larger than the elastic current measured at 23 mK, that is $|\varepsilon| > w$.

To analyze the temperature dependence, we assume boson statistics for the degrees of freedom in the environment. The average occupation number $\langle n \rangle$ of environmental modes at energy ε is given by the Bose-Einstein distribution function: $\langle n \rangle = 1/(e^{\varepsilon/kT} - 1)$. The rates for absorption, W_a , and emission, W_e , can be expressed very generally by $W_a = B_a \rho$ and $W_e = A + B_e \rho$, where the Einstein coefficients stand for spontaneous emission (A), stimulated emission

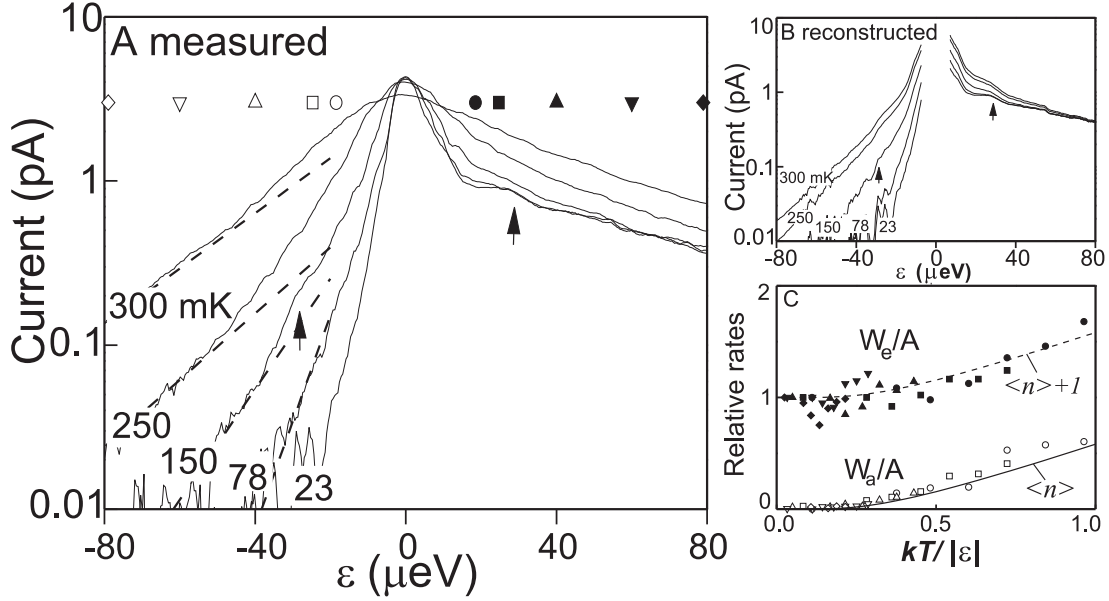


Figure 8.2: (a) Measured current versus ε for $T = 23$ to 300 mK. The current is measured for $eV_{SD} = 140$ μeV while sweeping V_{GR} and V_{GL} simultaneously in opposite directions such that we change the energy difference ε . Gate voltage is translated to energy ε by a calibration better than 10% with photon-assisted tunneling measurements [16]. Dashed lines indicate exponential dependence, $e^{\varepsilon/kT}$, for $|\varepsilon| \gg kT$. Arrows point at step-like structure on the emission side ($\varepsilon > 0$) and a shoulder on the absorption side ($\varepsilon < 0$). From fits [11] to the elastic current part at 23 mK, we obtain $\hbar\Gamma_R \approx \hbar T_c \approx 1$ μeV and $\hbar\Gamma_L \approx 0.1$ μeV for this data set. (b) Reconstructed current for different T . The spontaneous emission spectrum derived from the measured data at 23 mK and Eqs. 8.1 are used to reconstruct the full temperature and energy dependence. (c) The absorption rate W_a (open symbols) and emission rate W_e (closed symbols) normalized by the spontaneous emission rate A versus $kT/|\varepsilon|$. Circles, squares, upper and lower triangles, and diamonds are taken at $|\varepsilon| = 18, 24, 40, 60$, and 80 μeV , respectively (see also symbols in a). The solid line indicates the Bose-Einstein distribution, $\langle n \rangle$, whereas the dashed line shows $\langle n \rangle + 1$.

(B_e) and absorption (B_a), and ρ is the energy density [8]. From the Einstein relations, $B_a = B_e = A\langle n \rangle/\rho$ [8], we obtain:

$$\begin{aligned} \Gamma_i(\varepsilon < 0) &= W_a(\varepsilon) = \langle n \rangle A(-\varepsilon) \\ \Gamma_i(\varepsilon > 0) &= W_e(\varepsilon) = (\langle n \rangle + 1) A(\varepsilon) \end{aligned} \quad (8.1)$$

To test whether the inelastic current follows emission and absorption statistics, we calculate the full current spectrum from Eqs. 8.1. First, we obtain the spontaneous emission rate from $A(\varepsilon) = I_{inel}(\varepsilon > 0, T = 23 \text{ mK})/e$. The trace

at 23 mK is effectively at zero temperature for $\varepsilon \gg 2 \mu\text{eV}$ since then $\langle n \rangle \ll 1$. The emission current at higher temperatures follows from $I_{inel}(\varepsilon > 0, T) = e(\langle n \rangle + 1)A(\varepsilon)$, whereas the absorption current follows from $I_{inel}(\varepsilon < 0, T) = e\langle n \rangle A(-\varepsilon)$. The reconstructed current spectrum is shown in Fig. 8.2b. The central part of the curves ($|\varepsilon| < 10 \mu\text{eV}$) is kept blank since Eq. 8.1 does not include the T -dependence of I_{el} . The calculated current reproduces the measured current well up to 200 mK. Even the small step-like feature seen at $\varepsilon \sim 30 \mu\text{eV}$ is reflected by a shoulder-like feature at $\varepsilon \sim -30 \mu\text{eV}$ in the measured and in the calculated absorption spectra (indicated by arrows). For $T > 200$ mK the measured current significantly exceeds the calculated current, which is probably due to thermally excited electrons (Eq. 8.1 only describes the T -dependence of the environment. The thermal excitations in the electron leads are not included.) Further confirmation of the applicability of the Einstein relations to our quantum dot system follows from the prediction:

$$\frac{I_{inel}(\varepsilon > 0) - I_{inel}(\varepsilon < 0)}{eA(|\varepsilon|)} = \frac{W_e - W_a}{A} = 1$$

which is valid independent of temperature. Figure 8.2c shows a plot of the normalized rates, W_a/A and W_e/A , versus $k_B T/|\varepsilon|$ for various ε and T up to 200 mK. The measured data closely follow the prediction $\frac{W_e - W_a}{A} = 1$; that is, the normalized rates, W_a/A and W_e/A , differ by one over the temperature range $T < 200$ mK without fitting any parameter.

The inelastic rate for a two-level system coupled to a bosonic environment at $T = 0$ is expected to have a T_c^2 dependence [14, 15]. Still without identifying the bosonic environment, we can test this dependence on the elastic tunnel coupling T_c between the two dots. Figure 8.3a shows that the inelastic current clearly increases with T_c . For the largest coupling we obtain a saturation where the elastic current peak can no longer be distinguished. By fitting the elastic current part to a lorentzian line shape [11] we can obtain rough estimates for T_c as long as the current is less than the saturation value. We find that with these fitted values, the inelastic current scales as T_c^α with an exponent $\alpha = 2.5 \sim 3$, may be somewhat larger than expected. Figure 8.3b shows the effect of the increased coupling on the symmetric part of the current at low temperature. For small tunnel coupling, we always obtain lorentzian line shapes. For increasing couplings, the data still fits to a lorentzian tail on the absorption side. However, we generally find significant deviations for small ε , implying that for large coupling the elastic and inelastic rates can become of the same order. This may form a significant limitation for the coherence time in coupled quantum devices [16].

The importance of fluctuations in the environment on electron tunneling

through quantum devices has been recognized for a long time. Environmental studies on Coulomb blockade devices have only discussed effects due to absorption [3, 17]. For emission it is required that electrons are first pumped to a higher energy state. This has recently been done in a superconducting Cooper pair transistor under microwave irradiation [18]. In the case of a double dot, pumping occurs when $E_L > E_R$ and an electron tunnels in from the left reservoir to E_L . A double dot thus offers a unique two-level system that is pumped by a dc voltage without inducing heating currents. It is therefore possible to reach an out-of-equilibrium situation so close to $T = 0$ that vacuum fluctuations become the main source for generating electron transport.

To identify whether photons, plasmons, or phonons form the bosonic environment [19], we measured spontaneous emission spectra while placing the double dot in different electromagnetic environments. In the regime 10-100 μeV , the typical wavelengths are 1-10 cm for photons and 0.3 to 30 cm for 2DEG plasmons. We have tested the coupling to the photonic environment by placing the sample in microwave cavities of different size [20]. To check the coupling to plasmons, we have measured different types of devices with largely different dimensions of the 2DEG leads, gate pads, and bonding wires. Both types of variation had no effect at all on the emission spectra; even the fine structure was reproduced.

The third option of acoustic phonons is the most likely possibility [?]. Phonon emission rates have been calculated for single dots [22]. For a double dot system, we can obtain the general energy dependence [15]. For a deformation potential we expect a rate dependence of ε^{D-2} (ε for 3D phonons and constant for 2D phonons) and for piezo-electric interaction of ε^{D-4} ($1/\varepsilon$ for 3D phonons and $1/\varepsilon^2$ for 2D surface acoustic waves) [23]. In Fig. 8.3c we compare traces measured on two different types of devices. Here, the emission current is plotted versus ε on a log-log scale. Ignoring the bumps, we find an energy dependence between $1/\varepsilon$ and $1/\varepsilon^2$. This implies that the dominant emission mechanism is the piezo-electric interaction with 2D or 3D acoustic phonons. Note that a $1/\varepsilon$ or $1/\varepsilon^2$ dependence should be avoided in coherent devices, since the inelastic rate becomes large near resonance ($\varepsilon \sim 0$) [16].

The bumps observed in both type of devices, suggest the existence of resonances, for instance, due to a finite size in the phonon environment. The bumps are particularly clear in the derivative of the current to energy (dotted curves in Fig. 8.3a). The large bump in Fig. 8.3a at $\varepsilon = 30 \mu\text{eV}$ corresponds to a frequency of $f = \varepsilon/h = 7.3 \text{ GHz}$. For 3D phonons this yields a wavelength $\lambda^{3D} = s^{3D}/f = 640 \text{ nm}$ ($s^{3D} = 4800 \text{ m/s}$ is the 3D sound velocity), whereas for 2D surface acoustic waves $\lambda^{2D} = s^{2D}/f = 380 \text{ nm}$ ($s^{2D} = 2800 \text{ m/s}$). These wavelengths both, more or less, fit with the dimensions of the two quantum dot devices. We have

not yet been able to control these resonance by studying devices with a variety of gate dimensions. However, we believe that it is possible to gain control over

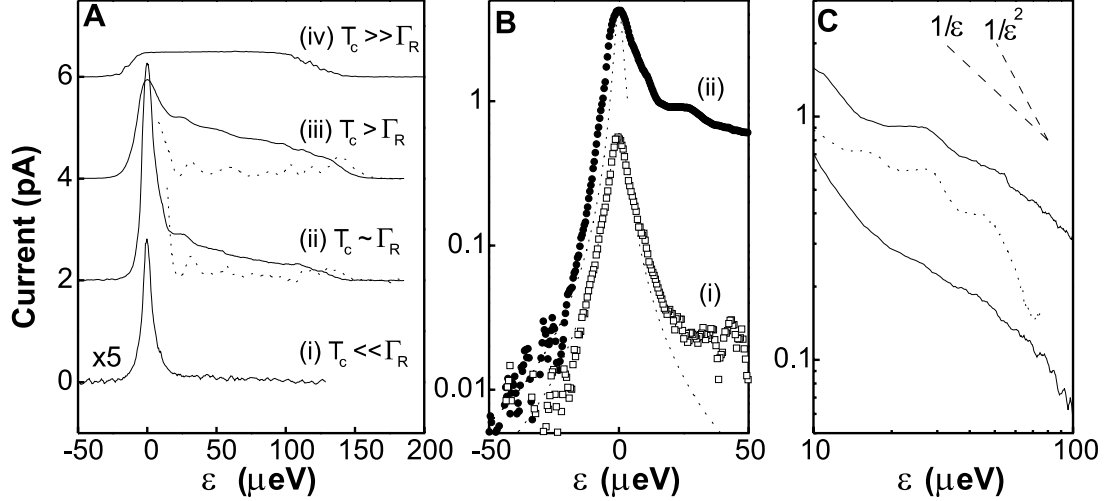


Figure 8.3: Current spectrum for different coupling energies at 23 mK. (a) The magnetic field is 1.6 T for (i) and 2.4 T for the other curves [10]. The curves have an offset, and curve (i) is multiplied by 5. Rough estimates for the coupling energies are: (i) hT_c ($\sim 0.1 \mu\text{eV}$) $\ll h\Gamma_R$ ($\sim 10 \mu\text{eV}$), (ii) hT_c ($\sim 1 \mu\text{eV}$) $\approx h\Gamma_R$ ($\sim 1 \mu\text{eV}$), (iii) $hT_c > h\Gamma_R$ ($\sim 0.1 \mu\text{eV}$), and (iv) $hT_c \gg h\Gamma_R$ ($\sim 0.01 \mu\text{eV}$) and $\Gamma_L \gtrsim \Gamma_R$ for all curves. The two dotted curves are the derivatives $-dI/d\varepsilon$ in arbitrary units for curves (i) and (ii) to enhance the bump-structure. (b) Logarithmic-linear plots for (i) and (ii). Dashed lines are lorentzian fits. For (ii) we chose parameters that fit the tail for negative ε . (c) Logarithmic-logarithmic plots of the emission spectrum for two different samples. The solid lines are taken on the FIB sample in Fig. 8.1a (upper trace is the same as (ii) in a; lower trace is for coupling energies between (i) and (ii) in a). The dotted line is taken on a surface gate sample with a distance between left and right barriers of 600 nm [12]. The dashed lines indicate a $1/\varepsilon$ and $1/\varepsilon^2$ dependence expected for piezo-electric interaction with 3D and 2D phonons, respectively.

the phonon environment by making 3D phonon cavities in hanging bridges [24] or by creating a 2D phonon band gap using a periodic gate geometry [25].

We thank M. Devoret, L. Glazman, S. Godijn, Y. Hirayama, J. Mooij, Yu. Nazarov, Y. Tohkura, N. Uesugi, M. Uilenreef and N. van der Vaart for help and discussions. Supported by the Dutch Foundation for Fundamental Research on Matter (FOM), L.P.K. by the Royal Netherlands Academy of Arts and Sciences.

References

- [1] H. Mizuta and T. Tanoue, *The Physics and Applications of Resonant Tunneling Diodes* (Cambridge Univ. Press, Cambridge, 1995).
- [2] *The New Superconducting Electronics, Proceedings of a NATO Advanced Study Institute*, H. Weinstock and R.W. Ralston Eds. (Kluwer, Dordrecht, 1992), ser. E, vol. 251.
- [3] H. Grabert and M.H. Devoret, Eds., *Single Charge Tunneling* (Plenum Press, New York, 1992), ser. B, vol. 294.
- [4] P.L. McEuen, *Nature*, **393**, 15 (1998); S.J. Tans, A.R.M. Verschueren and C. Dekker, *Nature* **393**, 49 (1998).
- [5] T. Fujisawa and S. Tarucha, *Superlattices and Microstructures* **21**, 247 (1997); *Jpn. J. Appl. Phys.* **36**, 4000 (1997).
- [6] For recent reviews, see R. Ashoori, *Nature* **379**, 413 (1996); L.P. Kouwenhoven and C.M. Marcus, *Physics World*, p. 35 (June 1998).
- [7] L.P. Kouwenhoven, C.M. Marcus, P.L. McEuen, S. Tarucha, R.M. Westervelt and N.S. Wingreen, *Electron transport in quantum dots*, in *Mesoscopic Electron Transport*, edited by L.L. Sohn, L.P. Kouwenhoven and G. Schön, (Kluwer, Series E **345**, 1997), p.105-214.
- [8] P.W. Milonni, *The Quantum Vacuum: An Introduction to quantum electrodynamics* (Academic Press, San Diego, CA, 1994).
- [9] The statistics of our inelastic emission should be regulated by the statistics of single-electron tunneling, see A. Imamoglu and Y. Yamamoto, *Phys. Rev. B* **46**, 15982 (1992).
- [10] The sample was cooled in a dilution refrigerator with a lowest temperature of 23 mK. Because of noise, the effective electron temperature is ~ 50 mK in the leads. In all measurements, we apply a perpendicular magnetic field between 1.6 and 2.4 T to maximize the single-particle spacing such that we can neglect transport through excited states.
- [11] The elastic current is given by the formula $I_{el}(\varepsilon) = eT_c^2\Gamma_R/[T_c^2(2 + \Gamma_R/\Gamma_L) + \Gamma_R^2/4 + (\varepsilon/h)^2]$, see Yu.V. Nazarov, *Physica B* **189**, 57 (1993); T.H. Stoof and Yu.V. Nazarov, *Phys. Rev. B* **53**, 1050 (1996).
- [12] N.C. van der Vaart, S.F. Godijn, Yu.V. Nazarov, C.J.P.M. Harmans and J.E. Mooij, *Phys. Rev. Lett.* **74**, 4702 (1995).
- [13] Also co-tunneling can give excess current for $\varepsilon \neq 0$. In our measurements, however, the co-tunneling current is less than 0.01 pA and can be neglected.

- For a review on co-tunneling see D.V. Averin and Yu. V. Nazarov, in Ref. [3], pp. 217-247.
- [14] A.J. Legget, S. Chakravarty, A.T. Dorsey, M.P.A. Fisher, A. Garg and W. Zwerger, *Rev. Mod. Phys.* **59**, 1 (1987).
 - [15] A T_c^2 -dependence can also be obtained from perturbation theory when $T_c \ll \varepsilon$, see L.I. Glazman and K.A. Matveev, *Sov. Phys. JETP* **67**, 1276 (1988).
 - [16] We have reported a coherent coupling effect in double quantum dots using photon-assisted tunneling experiments [T.H. Oosterkamp, T. Fujisawa, W.G. van der Wiel, K. Ishibashi, R.V. Hijman, S. Tarucha and L.P. Kouwenhoven, *Nature* **395**, 873 (1998)]. These observations are made when a small bias voltage is applied. In this case, emission processes do not give rise to current.
 - [17] Stimulated emission into the electromagnetic environment does play an important role for the presence of charging effects in single tunnel junctions [T. Holst *et al.*, *Phys. Rev. Lett.* **73**, 3455 (1994)].
 - [18] Y. Nakamura, C.D. Chen and J.S. Tsai, *Phys. Rev. Lett.* **79**, 2328 (1997).
 - [19] Bosonic excitations in a Fermi liquid (particle-hole excitations) can also be described as a bosonic bath with ohmic dissipation. For this case, the inelastic rate has a power-law dependence, $\Gamma(\varepsilon) \sim \varepsilon^\gamma$, where γ is related to the phase shift, δ , at the Fermi surface through $\gamma = 4/\pi^2 \delta^2 - 1$ [see [14] and F. Guinea *et al.*, *Phys. Rev. B* **32**, 4410 (1985)]. Because $\delta^2 > 0$, the power $\gamma > -1$. This does not agree with our observed energy dependence, which is between $1/\varepsilon$ and $1/\varepsilon^2$.
 - [20] We used a cylindrical cavity (diameter = 36 mm and height = 84 mm), which has a minimum resonance energy of about 20 μeV , and a rectangular cavity (22 mm by 19 mm by 8 mm) with a resonance frequency of about 40 μeV .
 - [21] Coupling to optical phonons is efficient only at much larger energies.
 - [22] U. Bockelmann, *Phys. Rev. B* **50**, 17271 (1994).
 - [23] For phonons the inelastic rate at $T = 0$ can be written as $\Gamma_i \sim (T_c/\varepsilon)^2 J(\varepsilon/\hbar)$ where $J(\varepsilon) \sim \frac{c^2(\varepsilon)}{\varepsilon} g(\varepsilon)$ is the spectral function [14]. The phonon density of states $g(\varepsilon) \sim \varepsilon^{D-1}$, such that $\Gamma_i \sim T_c^2 c^2(\varepsilon) \varepsilon^{D-4}$. When we neglect possible fine structure in $c(\varepsilon)$, we have for deformation potential $c \sim \varepsilon$ and thus $\Gamma_i \sim \varepsilon^{D-2}$, while for piezo-electric interaction $c \sim \text{constant}$ and thus $\Gamma_i \sim \varepsilon^{D-4}$.
 - [24] A.N. Cleland and M.L. Roukes, *Nature* **392**, 160 (1998).
 - [25] J.M. Shilton *et al.*, *J. Phys. Cond. matter* **8**, L531 (1997).

Chapter 9

Electro-magnetic Aharonov-Bohm effect in a 2D electron gas ring

W.G. van der Wiel, Yu.V. Nazarov, S. De Franceschi,
T. Fujisawa, J.M. Elzerman, E.W.G.M. Huizeling,
S. Tarucha and L.P. Kouwenhoven

We define a mesoscopic ring in a 2-dimensional electron gas (2DEG) interrupted by two tunnel barriers, enabling us to apply a well-defined potential difference between the two halves of the ring. The electron interference in the ring is modified using a perpendicular magnetic field and a bias voltage. We observe clear Aharonov-Bohm oscillations up to the quantum Hall regime as a function of both parameters. The electron travel time between the barriers is found to increase with the applied magnetic field. Introducing a scattering model, we develop a new method to measure the non-equilibrium electron dephasing time, which becomes very short at high voltages and magnetic fields. The relevance of electron-electron interactions is discussed.

This chapter has been submitted to Physical Review Letters.

Aharonov and Bohm predicted that the phase of an electron wave is affected by both magnetic and electric potentials, being observable in an interference experiment [1]. A magnetic flux, Φ , threading a loop leads to an oscillating contribution to the conductance with period $\Phi_0 = h/e$: the *magnetic* Aharonov-Bohm (AB) effect. In a solid state device, AB oscillations are observable at mesoscopic scale, where quantum coherence is preserved. The effect was first observed in a metal ring [2] and later in 2DEG rings [3].

In the case of the *electrostatic* AB effect, as originally suggested, the electron phase is affected by an electrostatic potential, although the electrons do not experience an electric field [1]. The required geometry is difficult to realize and so far only geometries have been investigated where an electric field changes the interference pattern [4-6]. In Ref. [7] a ring geometry interrupted by tunnel barriers was suggested, where a bias voltage leads to an electrostatically controlled AB effect with predictions very similar to the original proposal [1]. This effect was observed in a disordered metal ring with two tunnel junctions [8].

In this chapter, we report the observation of an electrostatic AB effect in a quasi-ballistic ring-shaped 2DEG system interrupted by tunnel barriers. There are two important distinctions from metal systems that play a key role in the present study. First, only a few electron modes are involved in transport, in contrast to tens of thousands in a typical metal wire. Second, in a 2DEG we can enter the quantum Hall regime using a perpendicular magnetic field, B .

We observe both a magnetic and electrostatic AB effect up to the edge channel regime (filling factor $\nu = 3$). The electron travel time between the barriers increases with B . We ascribe this to the bending effect of the Lorentz force on the electron trajectories. Importantly, the electrostatic oscillations form a new tool to determine the non-equilibrium electron dephasing time, τ_ϕ . The possibility to estimate the electron dephasing time at a controlled, finite energy and magnetic field distinguishes this method from weak localization experiments used to estimate the (equilibrium) electron dephasing time [9]. We find that τ_ϕ decreases as a function of B and V and reaches $\tau_\phi|\varepsilon| \simeq \hbar$ at the highest B , with ε the electron energy measured from the Fermi level. This demonstrates the increasing importance of many-body effects at quantizing magnetic fields where the Fermi-liquid picture and the quasi-particle concept are at the edge of applicability.

Our device (Fig. 9.1a) consists of an AB ring defined in a 2DEG [10]. The gate electrodes V_{gu} and V_{gl} define a barrier in each arm of the ring. The effective width of the arms supports $N_{tr} \simeq 10$ transport channels (i.e. the conductance of the ring without barriers is approximately $10e^2/h$ at $B = 0$ T). In addition to the dc bias voltage, V , we apply a relatively small ac voltage (3 to 10 μ V) between source and drain contacts. We measure the differential conductance, $G = dI/dV$,

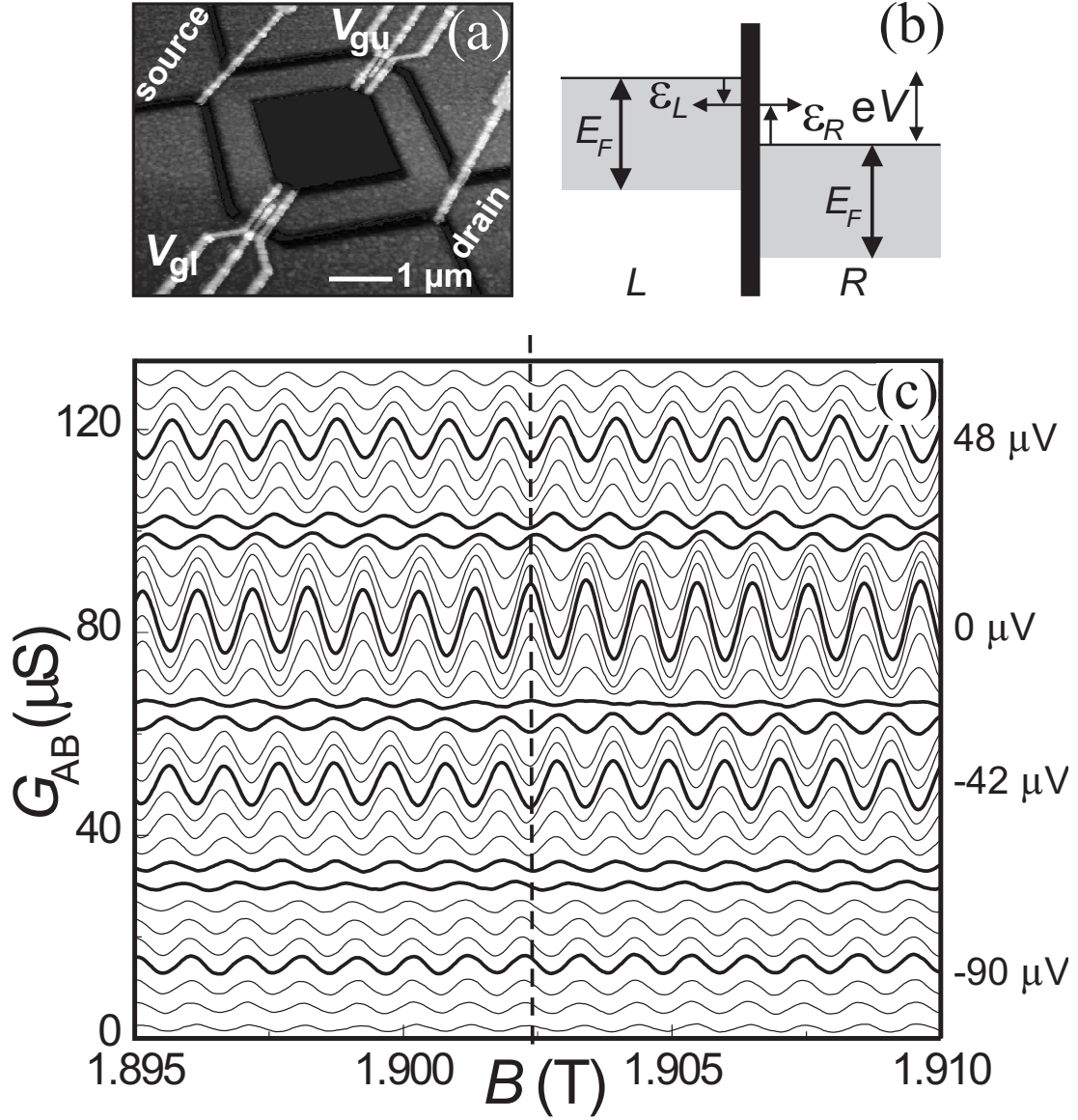


Figure 9.1: (a) Atomic force microscope image of the device. The AB ring is defined in a 2DEG by dry etching (dark regions, depth ~ 75 nm). The 2DEG with electron density $3.4 \times 10^{15} \text{ m}^{-2}$ is situated 100 nm below the surface of an AlGaAs/GaAs heterostructure. In both arms of the ring (lithographic width $0.5 \mu\text{m}$; perimeter $6.6 \mu\text{m}$) a barrier can be defined by applying negative voltages to the gate electrodes V_{gu} and V_{gl} . The other gates are not used. (b) Schematic energy picture at one of the barriers (see text). (c) Differential AB conductance, G_{AB} , as function of B at 15 mK for different source drain voltages, V , separated by $5.3 \mu\text{V}$. The traces have a vertical offset. Four values for V are indicated on the right. The dashed line highlights a phase change by a change in the amplitude and sign of the AB oscillations, indicating an electrostatic AB effect.

using a lock-in technique in a dilution refrigerator with a base temperature of 15 mK.

Figure 9.1c shows the differential AB conductance, G_{AB} , versus B and V , around 1.9 T. G_{AB} is extracted from the measured G , by fitting a polynomial to the smoothly varying background in G . Subtraction of this polynomial yields the oscillating part, G_{AB} . The barriers are tuned such that the conductance through one arm is $0.2 e^2/h$. G_{AB} as function of magnetic field exhibits AB oscillations

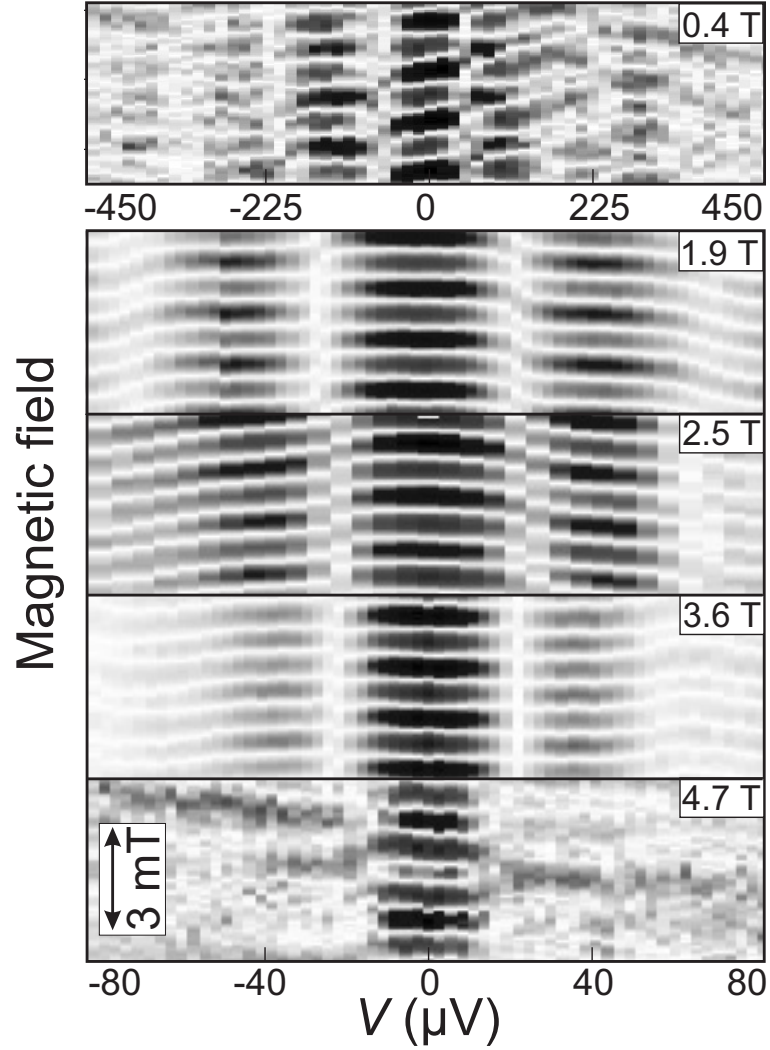


Figure 9.2: Gray-scale plots of the AB conductance in the plane of magnetic field (vertical axis) around different B values and voltage, V (horizontal axis). Light gray (dark gray) corresponds with maximum (minimum) AB conductance. White corresponds with zero AB conductance. The phase-changes indicate the electrostatic period which varies from $V_0 = 225 \mu\text{V}$ at $B = 0.4 \text{ T}$ to $V_0 = 60 \mu\text{V}$ at $B = 4.7 \text{ T}$.

with a period $B_0 = 1.0$ mT, in good agreement with $h/(eS)$, where S is the area enclosed by the ring. The effect of the dc bias voltage is schematically shown in Fig. 9.1b. The transmitted part of the electron wave has an energy ε_R , whereas the reflected part has an energy ε_L with respect to the Fermi level in each half of the ring (note $eV = \varepsilon_R - \varepsilon_L$ and $|\varepsilon_L|, |\varepsilon_R|, |eV| \ll E_F$). The energy difference leads to a phase difference $\Delta\Phi_V = 2\pi eV t_0/h$, where t_0 is the (B -dependent) time the reflected and transmitted electron waves spend in their respective parts of the ring before they interfere [7]. We thus expect electrostatic AB oscillations by changing V .

The dashed line in Fig. 9.1c highlights the effect of V . The bold curve at $V = 48$ μ V has a minimum when it crosses the dashed line. By decreasing V , the amplitude of the AB oscillations decreases. The two bold curves near $V = 24$ μ V show a case where the amplitudes are small and the sign of the amplitude changes. At $V = 0$ μ V, the amplitude is maximal. Comparing the 48 and 0 μ V traces, the AB oscillation has acquired a change in phase by π . This continues by another phase shift of π when V is decreased to -42 μ V. Thus, the electrostatic period, V_0 , is 90 μ V at this magnetic field. This corresponds to an electron travel time $t_0 = 45$ ps. We note that the Onsager-Büttiker symmetry relation $G(B) = G(-B)$ for a 2-terminal measurement [11] only holds at small bias voltages. Therefore, the phase of the oscillations at the field of the dashed line is not restricted to 0 or π .

Figure 9.2 shows a gray-scale plot of G_{AB} versus B and V for five different B ranges. The main features of the results are as follows. The amplitude of the AB oscillations is relatively small ranging from $\sim 0.01G$ to $\sim 0.1G$. The period of the oscillations in $G_{AB}(V)$ decreases with B , as is clearly seen by comparing the different panels in Fig. 9.2. For $B = 0.4$ T, 1.9 T, 3.6 T, and, less clearly, for $B = 4.7$ T, the phase of the magnetic oscillations exhibits sharp π -shifts at lower voltages. At higher voltages, the phase changes more smoothly. At $B = 2.5$ T, the phase changes smoothly over the entire voltage range. We return to the phase evolution at different B and V later, when we discuss our scattering model.

The AB amplitude decreases with V and, the higher B , the faster the decrease. The decreasing AB amplitude is clearly seen in Fig. 9.3 where we plot the normalized AB conductance, $G_{AB}(V)/G_{AB}(V=0)$, versus V at $B = 1.9$ T. We stress that Fig. 9.3 is obtained by taking a single horizontal cut, i.e. for a single B with no averaging [12], from the $B = 1.9$ T panel of Fig. 9.2 (but over a larger voltage range). Note that $G_{AB}(V)/G_{AB}(V=0)$ can be negative since it only represents the oscillating part of the total conductance. The curve is approximately symmetric in V ($G_{AB}(V) \approx G_{AB}(-V)$), indicating that within the range

of applied voltages the electron travel time, t_0 , hardly changes with V . Thus, the electrostatic period does not vary within the applied bias window and we cannot attribute the decrease with V in Fig. 9.3 to self-averaging of trajectories with different periods. We therefore believe that the only possible mechanism for the decrease is electron dephasing due to inelastic processes.

The small relative amplitude of the AB oscillations indicates strong elastic scattering in the arms, whereas the quickly decreasing AB amplitude with V indicates strong inelastic scattering. Since these scattering mechanisms were not included in the model of Ref. [7], we introduce a simple interference model including dephasing, proceeding along the lines of the general scattering formalism [13].

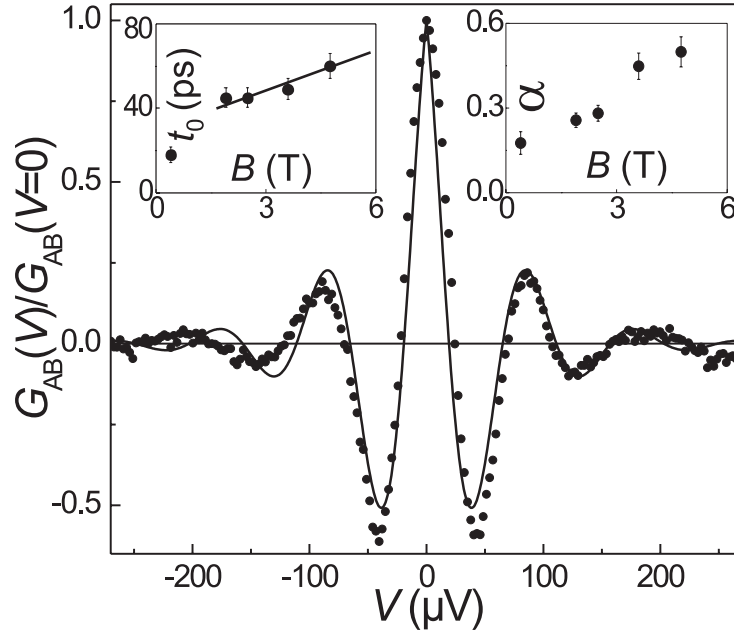


Figure 9.3: Normalized AB conductance $G_{AB}(V)/G_{AB}(V=0)$ versus V at $B = 1.9$ T. The amplitude decreases rapidly with V and, contrary to the magnetic AB effect, only a few oscillations can be observed. The solid curve is a fit with Eq. 9.4, $\alpha = 0.26$, $t_0 = 45$ ps. The left inset shows the values of the travel time t_0 versus B as extracted from fits with Eq. 9.4, varying from 18 ps at $B = 0.4$ T to 60 ps at $B = 4.7$ T ($L/v_F = 13$ ps, with L the distance between the barriers and v_F the Fermi velocity). The values of t_0 in the edge channel regime are fitted to a line with a slope of 6 ps/T. The right inset shows the extracted values for $\alpha = \hbar/2\varepsilon\tau_\phi(\varepsilon)$. The values of α increase with B , indicating an increasing importance of many-body effects at quantizing magnetic fields.

We assume single-channel tunnel junctions with transmission amplitudes t_1 and t_2 , respectively. A small AB amplitude implies that the amplitudes of propagating waves between the junctions, r_{12}^L or r_{21}^R (see Fig. 9.4), are small so that we only consider scattering processes of first order in r . The oscillating part of the transmission probability, T_{AB} , is built up from the pairwise interference of the electron trajectories shown in Fig. 9.4. Collecting the contributions at a given energy, we obtain

$$T_{AB} = 2\text{Re}(t_1 t_2^* e^{i\Phi_{AB}} (r_{12}^L + r_{21}^{*L})(r_{21}^R + r_{12}^{*R})) \quad (9.1)$$

We assume right-left symmetry [14] and specify the energy dependence of the propagation amplitudes as follows

$$r_{12(21)}^L = r_{-(+)} e^{i\varepsilon_L t_0/\hbar}, \quad r_{12(21)}^R = r_{+(-)} e^{i\varepsilon_R t_0/\hbar} \quad (9.2)$$

where $r_{+(-)}$ correspond to (counter)clockwise propagation of electrons along the ring (remind that $eV = \varepsilon_R - \varepsilon_L$). For the differential conductance this yields (assuming $t_1 = t_2$)

$$\begin{aligned} G_{AB}(V)/G = & |r_-|^2 \cos(eVt_0/\hbar) \cos(2\pi\Phi/\Phi_0 + \Phi_a) + \\ & |r_+|^2 \cos(eVt_0/\hbar) \cos(2\pi\Phi/\Phi_0 + \Phi_b) + \\ & 2|r_+ r_-| [\cos(eVt_0/\hbar + \Phi_c) + \\ & \sin(eVt_0/\hbar + \Phi_c) eVt_0/\hbar] \cos(2\pi\Phi/\Phi_0 + \Phi_d) \end{aligned} \quad (9.3)$$

where $\Phi_{a,b,c,d}$ are contributions to the phase that vary slowly with B in comparison to Φ/Φ_0 (e.g. due to bending of the electron trajectories). At small B time reversibility holds, implying $r_+ = r_-$ and $\Phi_{a,b,d} = 0$. Under these conditions, the phase of the magnetic oscillations only changes by π as a function of V . Interestingly, the same happens at high B . In this case Lorentz bending suppresses counterclockwise propagation, so that $r_+ \gg r_-$. The result is then dominated by the second term in Eq. 9.3. For a B -interval in which Φ_b can be considered constant, we find again that the phase of the magnetic oscillations only changes by π as a function of V . In the intermediate regime $r_+ \simeq r_-$, and $\Phi_{a,b,c,d}$ vary slowly with B . The phase of the magnetic oscillations in this case continuously shifts with voltage, saturating at $V \gg \hbar/t_0 e$.

To model electron dephasing due to inelastic processes, we assume that the electron amplitudes at a given energy are suppressed by a factor $\exp(-t/2\tau_\varphi)$, $\tau_\varphi(\varepsilon)$ being the energy-dependent dephasing time. In analogy with results found for a disordered electron gas in the quantum Hall regime [15], disordered metal-like systems [16], composite fermions [17] and a Luttinger liquid [18], we propose a

dephasing time proportional to energy, $\hbar/\tau_\varphi(\varepsilon) = 2\alpha\varepsilon$. Here α is a dimensionless factor of the order of the dimensionless 2DEG conductance, $G/(e^2/h)$. A small value for α ($\alpha \ll 1$) and large conductances ($G \gg e^2/h$) correspond to vanishing electron-electron interactions [16]. On the contrary, $\alpha \simeq 1$ and $G \simeq e^2/h$ signal the importance of many-body effects. In the limit of $r_+ \gg r_-$ our model for the dephasing gives

$$G_{AB}(V)/G = |r_+|^2 [\cos(eVt_0/\hbar) - \alpha \sin(e|V|t_0/\hbar)] e^{-\alpha e|V|/\hbar} \cos(2\pi\Phi/\Phi_0 + \Phi_b) \quad (9.4)$$

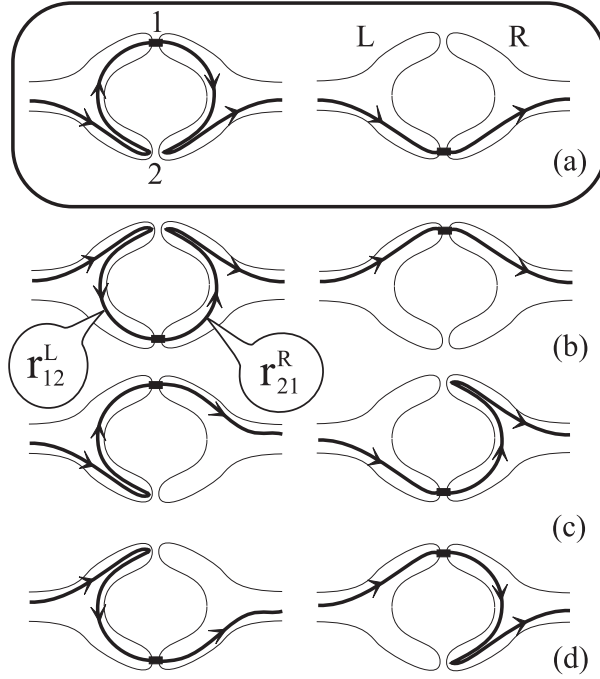


Figure 9.4: Schematic diagrams of interfering electron trajectories contributing (in first order) to the oscillating part of the transmission probability. At $B = 0$, the pairs of trajectories shown in (a)-(d) contribute equally, whereas at high magnetic field only the pair shown in (a) is relevant (\mathbf{B} points downwards).

Our scattering model provides an explanation for the observed experimental results. The model accounts for the abrupt π -phase changes observed in Fig. 9.2 at the lowest ($B = 0.4$ T and 1.9 T) and highest ($B = 3.6$ T and 4.7 T) magnetic fields (provided V is small). In the intermediate regime ($B = 2.5$ T) the model explains also why the phase varies more continuously. The well-defined period t_0 probably indicates the formation of an edge channel connecting the

junctions. However, the magnitude of the AB oscillations is small. This signals a strong scattering to and from the edge channel involving almost localized states at higher magnetic field. One can estimate $|r_+|^2$ as a classical probability, assuming uniform distribution over the transport channels in the ring and 1/3 suppression due to scattering near the openings to the source and drain leads. This gives $|r_+|^2 \simeq 1/3N_{tr} = 0.03$, which is in agreement with the experimental value of $G_{AB}(V=0)/G \simeq 0.02$ at low B .

We use Eq. 9.4 to fit the experimental V -dependence of the AB amplitude, as shown in Fig. 9.3 for the particular case $B = 1.9$ T. The reasonable quality of the fit supports our model for the dephasing time. From such fits we extract values for t_0 and α at various magnetic fields. The left inset to Fig. 9.3 shows our results for the B -dependence of t_0 . The values in the edge channel regime are fitted to a straight line with a slope of 6 ps/T. The increase of the travel time can be attributed to the decreasing drift velocity, $v_{drift} = |\mathbf{E}|/B$, $|\mathbf{E}|$ being the modulus of the confining electric field at the arm edges. An estimate based on parabolic confinement gives $|\mathbf{E}| \simeq 1 - 4 \cdot 10^5$ V/m. This implies a slope dt_0/dB between 5 and 20 ps/T, which is in reasonable agreement with the observed value.

In the right inset to Fig. 9.3 we show our results for $\alpha = \hbar/2\varepsilon\tau_\phi(\varepsilon)$. The α values are rather high and increase with B . At $\varepsilon = 10$ μ eV, we find $\tau_\phi = 180$ ps at $B = 0.4$ T and $\tau_\phi = 65$ ps at $B = 4.7$ T. The usual Fermi-liquid theory assumes well-defined quasi-particles, corresponding to $\alpha \ll 1$. The fact that we observe $\alpha \simeq 1$ signals the importance of many-body effects (electron-electron interactions). The Fermi-liquid theory here is on the edge of applicability. We attribute this to significant scattering in the arms of the ring. For a clean 2DEG one expects no significant many-body effects until $\nu < 1$ ($B_{\nu=1} = 14$ T in our 2DEG). One can consider α as an effective dissipative conductance in units of e^2/h [15, 16]. In our case, the relevant conductance is that of the arms of the AB ring, which is of the order of e^2/h at the highest magnetic fields. This is consistent with the observed α values.

In conclusion, using an electro-magnetic AB effect, we find a new method to determine the non-equilibrium electron dephasing time in a 2DEG, which becomes very short at high voltages and magnetic field.

We thank G. Seelig, M. Büttiker, T. Hayashi, A. van Oudenaarden and R. Schouten for their help. We acknowledge financial support from the Specially Promoted Research Grant-in-Aid for Scientific Research; the Ministry of Education, Science and Culture in Japan; the Dutch Organization for Fundamental Research on Matter; the New Energy and Industrial Technology Development Organization Joint Research Program (NTDP-98); and the European Union through a Training and Mobility of Researchers Program network.

References

- [1] Y. Aharonov and D. Bohm, Phys. Rev. **115**, 485 (1959).
- [2] R.A. Webb, S. Washburn, C.P. Umbach and R.B. Laibowitz, Phys. Rev. Lett. **54**, 2696 (1985).
- [3] G. Timp, A.M. Chang, J.E. Cunningham, T.Y. Chang, P. Mankiewich, R. Behringer and R.E. Howard, Phys. Rev. Lett. **58**, 2814 (1987).
- [4] S. Washburn, H. Schmid, D. Kern and R.A. Webb, Phys. Rev. Lett. **59**, 1791 (1987).
- [5] P.G.N. de Vegvar, G. Timp, P.M. Mankiewich, R. Behringer and J. Cunningham, Phys. Rev. B **40**, R3491 (1989).
- [6] B. Krafft, A. Förster, A. van der Hart and Th. Schäpers, Physica E **9**, 635 (2001).
- [7] Yu.V. Nazarov, Phys. Rev. B **47**, 2768 (1993); Yu.V. Nazarov, Physica B **189**, 57 (1993).
- [8] A. van Oudenaarden, M.H. Devoret, Yu. V. Nazarov, and J.E. Mooij, Nature **391**, 768 (1998).
- [9] P. Mohanty, E.M.Q. Jariwala and R.A. Webb, Phys. Rev. Lett. **78**, 3366 (1997).
- [10] W.G. van der Wiel, S. De Franceschi, T. Fujisawa, J.M. Elzerman, S. Tarucha and L.P. Kouwenhoven, Science **289**, 2105 (2000).
- [11] M. Büttiker, IBM J. Res. Dev. **32**, 317 (1988).
- [12] In Ref. [8] the correlation function $\langle G_{AB}(B, V)G_{AB}(B + \Delta B, V + \Delta V) \rangle$ is calculated, where the angle brackets denote an ensemble average. For a given ΔV , one averages over an ensemble of pairs of $G_{AB} - B$ traces, each pair having a ΔV voltage difference. This recipe causes that, if the potential landscape fluctuates on the scale of ΔV , and hence affects the (electrostatic) AB period, the correlation function decreases.
- [13] M. Büttiker, Phys. Rev. Lett. **57**, 1761 (1986).
- [14] This is a reasonable assumption, since in our experiment we tune the barriers to have equal transmission.
- [15] D.G. Polyakov and K.V. Samokhin, Phys. Rev. Lett. **80**, 1509 (1998).
- [16] B.L. Altshuler and A.G. Aronov in Electron-Electron Interactions in Disordered Systems, edited by A.L. Efros and M. Pollak (North-Holland, Amsterdam, 1985).

-
- [17] P.A. Lee, E.R. Mucciolo and H. Smith, Phys. Rev. B **54**, 8782 (1996).
 - [18] M.P.A. Fisher and L.I. Glazman in Mesoscopic Electron Transport, edited by L.L. Sohn, L.P. Kouwenhoven and G. Schön, NATO ASI, Ser. E, Vol. 345 (Kluwer, Dordrecht, 1997) pp. 331-373.

Appendix A

Electrostatic energy of quantum dots

In this appendix we derive the electrostatic energy of a single and double quantum dot system. Before addressing these specific systems, we briefly discuss the method followed [1].

A.1 Electrostatics of a system of N conductors

Consider a system consisting of N conductors. A capacitance can be defined between each conductor and every other conductor as well as a capacitance from each of the N conductors to ground. This results in a total of $N(N + 1)/2$ capacitors. The capacitor between node j and node k has a capacitance c_{jk} and stores a charge q_{jk} . The total charge on node j is the sum of the charges on all of the capacitors connected to node j

$$Q_j = \sum_{k=0}^N q_{jk} = \sum_{k=0}^N c_{jk}(V_j - V_k) \quad (\text{A.1})$$

Here V_j is the electrostatic potential of node j and ground is defined to be at zero potential, $V_0 = 0$. The charges on the nodes are linear functions of the potentials of the nodes so this can be expressed more compactly in matrix form

$$\vec{Q} = \mathbf{C}\vec{V} \quad (\text{A.2})$$

where \mathbf{C} is called the capacitance matrix. A diagonal element of the capacitance matrix, C_{jj} , is the total capacitance of node j

$$C_{jj} = \sum_{k=0, k \neq j}^N c_{jk} \quad (\text{A.3})$$

An off-diagonal element of the capacitance matrix is minus the capacitance between node j and node k , $C_{jk} = C_{kj} = -c_{jk}$. The electrostatic energy of this system of conductors is the sum of the electrostatic energy stored on the $N(N+1)/2$ capacitors and can be conveniently expressed using the capacitance matrix

$$U = \frac{1}{2} \vec{V} \cdot \mathbf{C} \vec{V} = \frac{1}{2} \vec{V} \cdot \vec{Q} = \frac{1}{2} \vec{Q} \cdot \mathbf{C}^{-1} \vec{Q} \quad (\text{A.4})$$

Voltage sources can be included in the network by treating them as nodes with large capacitances to ground and large charges on them such that $V = Q/C$. In this case, it is numerically difficult to compute the inverse of the capacitance matrix since it contains large elements. However, it is not necessary to invert the entire capacitance matrix since the voltages on the voltage sources are already known. Only the voltages on the other nodes need to be determined. These voltages can be determined by writing the relation between the charges and the voltages as

$$\begin{pmatrix} \vec{Q}_c \\ \vec{Q}_v \end{pmatrix} = \begin{pmatrix} \mathbf{C}_{cc} & \mathbf{C}_{cv} \\ \mathbf{C}_{vc} & \mathbf{C}_{vv} \end{pmatrix} \begin{pmatrix} \vec{V}_c \\ \vec{V}_v \end{pmatrix} \quad (\text{A.5})$$

Here \vec{Q}_c and \vec{V}_c are the charges and the voltages on the charge nodes, \vec{Q}_v and \vec{V}_v are the charges and the voltages on the voltage sources, and the capacitance matrix has been expressed in terms of four sub-matrices. The voltages on the charge nodes are then

$$\vec{V}_c = \mathbf{C}_{cc}^{-1} (\vec{Q}_c - \mathbf{C}_{cv} \vec{V}_v) \quad (\text{A.6})$$

and the electrostatic energy can be calculated with Eq. A.4.

A.2 Single quantum dot

We write the total charge Q_1 on the dot as the sum of the charges on all the capacitors connected to the dot (see Fig. A.1)

$$\begin{aligned} Q_1 &= C_L(V_1 - V_L) + C_g(V_1 - V_g) + C_R(V_1 - V_R) \Rightarrow \\ Q_1 + C_L V_L + C_g V_g + C_R V_R &= C_1 V_1 \end{aligned} \quad (\text{A.7})$$

where C_1 is the total capacitance coupled to the dot, $C_1 = C_L + C_g + C_R$. The capacitance matrix \mathbf{C}_{cc} only has one element. Using Eq. A.4 and substituting $Q_1 = -(N_1 - N_0)|e|$, we find

$$U(N_1) = \frac{[-(N_1 - N_0)|e| + C_L V_L + C_g V_g + C_R V_R]^2}{2C_1} \quad (\text{A.8})$$

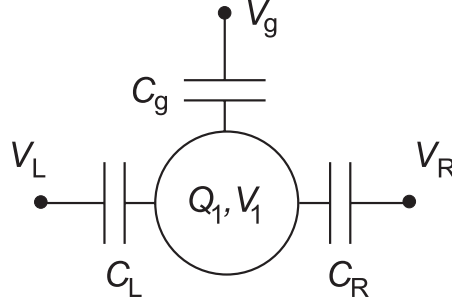


Figure A.1: Network of capacitors and voltage nodes used to calculate the electrostatic energy of a single quantum dot.

where N_0 is the number of electrons on the dot when all voltage sources are zero, which compensates the positive background charge originating from donors in the heterostructure.

A.3 Double quantum dot

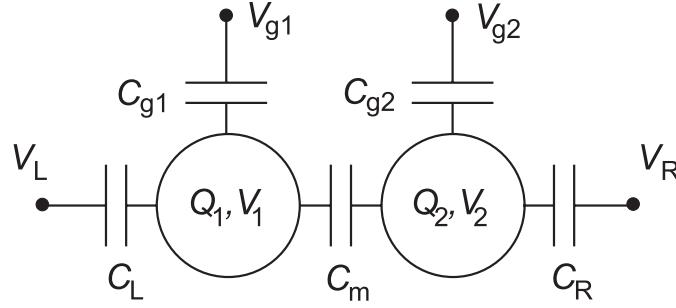


Figure A.2: Network of capacitors and voltage nodes used to calculate the electrostatic energy of a double quantum dot.

We write the total charge $Q_{1(2)}$ on dot 1(2) as the sum of the charges on all the capacitors connected to dot 1(2) (see Fig. A.2)

$$\begin{aligned} Q_1 &= C_L(V_1 - V_L) + C_{g1}(V_1 - V_{g1}) + C_m(V_1 - V_2) \\ Q_2 &= C_R(V_2 - V_R) + C_{g2}(V_2 - V_{g2}) + C_m(V_2 - V_1) \end{aligned} \quad (\text{A.9})$$

We can write this as

$$\begin{pmatrix} Q_1 + C_L V_L + C_{g1} V_{g1} \\ Q_2 + C_R V_R + C_{g2} V_{g2} \end{pmatrix} = \begin{pmatrix} C_1 & -C_m \\ -C_m & C_2 \end{pmatrix} \begin{pmatrix} V_1 \\ V_2 \end{pmatrix} \quad (\text{A.10})$$

where $C_2 = C_R + C_{g2} + C_m$. The above expression in the form of Eq. A.6 reads

$$\begin{pmatrix} V_1 \\ V_2 \end{pmatrix} = \frac{1}{C_1 C_2 - C_m^2} \begin{pmatrix} C_2 & C_m \\ C_m & C_1 \end{pmatrix} \begin{pmatrix} Q_1 + C_L V_L + C_{g1} V_{g1} \\ Q_2 + C_R V_R + C_{g2} V_{g2} \end{pmatrix} \quad (\text{A.11})$$

The electrostatic energy of the double dot system can now be calculated using Eq. A.4. For the case $V_L = V_R = 0$ and $Q_{1(2)} = -N_{1(2)}|e|$ this becomes

$$\begin{aligned} U(N_1, N_2) &= \frac{1}{2} N_1^2 E_{C1} + \frac{1}{2} N_2^2 E_{C2} + N_1 N_2 E_{Cm} + f(V_{g1}, V_{g2}) \quad (\text{A.12}) \\ f(V_{g1}, V_{g2}) &= \frac{1}{-|e|} \{ C_{g1} V_{g1} (N_1 E_{C1} + N_2 E_{Cm}) + C_{g2} V_{g2} (N_1 E_{Cm} + N_2 E_{C2}) \} \\ &\quad + \frac{1}{e^2} \{ \frac{1}{2} C_{g1}^2 V_{g1}^2 E_{C1} + \frac{1}{2} C_{g2}^2 V_{g2}^2 E_{C2} + C_{g1} V_{g1} C_{g2} V_{g2} E_{Cm} \} \end{aligned}$$

with

$$E_{C1} = e^2 \frac{C_2}{C_1 C_2 - C_m^2}; \quad E_{C2} = e^2 \frac{C_1}{C_1 C_2 - C_m^2}; \quad E_{Cm} = e^2 \frac{C_m}{C_1 C_2 - C_m^2} \quad (\text{A.13})$$

References

- [1] For a discussion of the electrostatics of a charging network see <http://qt.tn.tudelft.nl/~hadley/set/electrostatics.html>.

Summary

Electron transport and coherence in semiconductor quantum dots and rings

This thesis describes a number of experiments on electron transport and coherence in semiconductor vertical and lateral quantum dots and semiconductor rings. The vertical quantum dots are sub-micron pillars fabricated in an In/Al/GaAs double-barrier heterostructure. A metal gate electrode is deposited around them. The lateral quantum dot and ring devices are defined in the two-dimensional electron gas (2DEG) of a GaAs/AlGaAs heterostructure by means of etched trenches and metal gate electrodes fabricated on top of the heterostructure.

The quantum dots are weakly coupled to source and drain contacts by tunnel barriers. The addition of a single electron to the dot changes the charge on the dot by the elementary charge $-|e|$. The charging energy is given by e^2/C , where C is the total capacitance between the dot and its environment. At low temperature, this charging energy can block electron transport through the quantum dot, known as ‘Coulomb blockade’. By varying the voltage applied to one or more of the gate electrodes, the electrostatic potential of the dot can be changed. For certain gate voltages, two charge states are degenerate and single-electron tunneling is possible. The alternation of Coulomb blockade and single-electron tunneling as the gate voltage is varied, leads to so-called ‘Coulomb oscillations’ in the conductance through the dot.

The confinement in all three directions of electrons in a quantum dot leads to the formation of a discrete energy spectrum, resembling that of atoms. This and other similarities have therefore led to the name ‘artificial atoms’ for quantum dots.

An example of this atom-like behavior are the spin-singlet – spin-triplet transitions observed in quantum dots. These transitions can be explained by taking into account exchange interaction and a magnetic field dependent direct Coulomb interaction. The contribution from the direct Coulomb and exchange interactions is determined and can be measured as a function of the number of confined elec-

trons. Electrons tend to have parallel spins when they occupy nearly degenerate single-particle states, in line with Hund's first rule from atomic physics.

Another spin-related phenomenon that is discussed in this thesis, is the Kondo effect. The Kondo effect is a many-body phenomenon arising from the interaction between a localized spin and free electrons. It was originally discovered in metals containing small amounts of magnetic impurities. Quantum dots connected to source and drain leads can mimic that system and offer the possibility to measure and tune the Kondo effect in the case of a single spin impurity. If the dot has spin-degenerate single-particle levels, which are pairwise filled with 'spin-up' and 'spin-down' electrons, the dot only has a non-zero spin, $S = 1/2$, for an *odd* electron number. In this case, the Kondo effect is expected to be present for odd and absent for even electron numbers.

A strong Kondo effect at small magnetic field is observed in a lateral quantum dot. The Coulomb blockade is overcome completely by the Kondo effect and the conductance reaches the unitary-limit value at $2e^2/h$. The experimental Kondo temperature shows very good agreement with the spin-1/2 Anderson impurity model throughout the Kondo regime. It is shown that phase-coherent transport through a Kondo quantum dot is possible, by measuring electron interference in an Aharonov-Bohm ring with the dot embedded in one of its arms.

In general, the problem of electron transport through a quantum dot exhibiting the Kondo effect does not map onto the problem of the resistivity in a bulk metal, as described by the Anderson impurity model. An experiment is presented in which an unexpected Kondo effect is realized in a vertical few-electron quantum dot. The energy difference between spin-singlet and spin-triplet states is tuned by a magnetic field. A Kondo effect occurs for an *even* number of electrons at the degeneracy of a singlet and triplet state. The characteristic energy scale is found to be much larger than for the ordinary spin-1/2 case in this system. This type of Kondo effect has not been considered before, probably because a singlet-triplet degeneracy does not occur in magnetic elements.

Another Kondo phenomenon without analog in bulk-metal systems is the multi-level Kondo effect at high magnetic field that has been studied in a selective area growth lateral quantum dot. This unusually strong Kondo effect is also ascribed to a singlet-triplet transition in the ground state of the dot. In contrast to the singlet-triplet Kondo effect observed in the vertical dot, away from the transition, for low bias voltages and temperatures, the conductance is sharply reduced. The observed behavior is compared to predictions for a two-stage Kondo effect in quantum dots coupled to *single*-channel leads. The different behavior of this singlet-triplet Kondo effect in a lateral quantum dot in comparison to the results in a vertical dot is ascribed to a different number of conductance channels

in the leads coupled to the dot.

The next logical step after studying individual quantum dots is to study systems of more than one dot. By coupling two quantum dots in series, a system is obtained with fundamentally different behavior and possibilities in comparison to a single quantum dot. Where single quantum dots are regarded as ‘artificial atoms’, two quantum dots can be coupled to form an ‘artificial molecule’. Motivated by their relevance for realizing solid state quantum bits, electron transport experiments on two lateral quantum dots coupled in series are reviewed. An introduction to the charge stability diagram is given. Resonant tunneling experiments show that the double dot geometry allows for an accurate determination of the intrinsic lifetime of discrete energy states in quantum dots. The evolution of discrete energy levels in magnetic field is studied. The resolution allows to resolve avoided crossings in the spectrum of a quantum dot. With microwave spectroscopy it is possible to probe the transition from ionic bonding (for weak inter-dot tunnel coupling) to covalent bonding (for strong inter-dot tunnel coupling) in a double dot artificial molecule.

The rates for elastic and inelastic transitions in the two-level system formed by a double quantum dot are measured by the dc current through the system. The inelastic transition rates are well described by the Einstein coefficients, relating absorption with stimulated and spontaneous emission. For these inelastic processes, energy is exchanged most effectively with acoustic phonons. The results demonstrate the importance of vacuum fluctuations in the environment for little circuits of coherent quantum devices.

Finally, an electro-magnetic Aharonov-Bohm effect in a 2D electron gas ring is studied. The mesoscopic 2DEG ring is interrupted by two tunnel barriers, enabling to apply a well-defined potential difference between the two halves of the ring. The electron interference in the ring is modified using a perpendicular magnetic field and a bias voltage, resulting in clear Aharonov-Bohm oscillations up to the quantum Hall regime as a function of both parameters. Introducing a scattering model, a new method is developed to measure the non-equilibrium electron dephasing time, which becomes very short at high voltages and magnetic fields, with a focus on the role of electron-electron interactions.

Wilfred G. van der Wiel
November 2001

Samenvatting

Transport en coherentie van elektronen in halfgeleider quantum dots en ringen

Dit proefschrift beschrijft een aantal experimenten met als onderwerp transport en coherentie van elektronen in verticale en laterale halfgeleider quantum dots en ringen. De verticale quantum dots zijn sub-mikron pilaartjes gefabriceerd in een In/Al/GaAs dubbele-barrière heterostruktuur. Rondom een pilaartje wordt er een metalen ‘gate’-elektrode aangebracht. De laterale quantum-dot- en ringstructuren zijn gedefinieerd in het 2D elektronengas (2DEG) van een GaAs/AlGaAs heterostruktuur door middel van geëtste geultjes en metalen elektrodes gefabriceerd op het oppervlak van de heterostruktuur.

De quantum dots zijn zwak gekoppeld aan ‘source’- en ‘drain’-kontakten door middel van tunnelbarrières. De toevoeging van een enkel elektron aan de dot verandert de lading op de dot met de elementaire lading $-|e|$. De ladingsenergie bedraagt e^2/C , waar C de totale capaciteit is tussen de dot en zijn omgeving. Bij lage temperatuur kan deze ladingsenergie het elektrontransport door de quantum dot blokkeren. Dit fenomeen wordt ‘Coulomb-blokkade’ genoemd. Door het voltage op één of meer van de gate-elektrodes te variëren kan de elektrostatische potentiaal van de dot veranderd worden. Voor bepaalde gate-voltages zijn twee ladingstoestanden ontaard en is het één voor één tunnelen van elektronen mogelijk. De afwisseling van Coulomb-blokkade en de mogelijkheid tot het tunnelen van elektronen door de dot wanneer de spanning op de gate-elektrode wordt veranderd, leidt tot zogenoemde ‘Coulomb-oscillaties’ in de geleiding door de dot.

De opsluiting van de elektronen in alle drie de richtingen in een quantum dot leidt tot het ontstaan van een diskreet energiespektrum, gelijkend op dat van atomen. Deze en andere overeenkomsten hebben daarom geleid tot de bijnaam ‘kunstmatige atomen’ voor quantum dots.

Een voorbeeld van dit atoom-achtige gedrag zijn de spin-singlet – spin-triplet-overgangen waargenomen in quantum dots. Deze overgangen kunnen verklaard worden als ‘exchange’-interactie en een magneetveld-afhankelijke directe Cou-

lomb-interactie meegenomen worden in de beschouwing. De bijdrage van directe Coulomb- en exchange-interakties is bepaald en kan kan gemeten worden als functie van het aantal elektronen in de dot. Elektronen hebben de neiging parallelle spins te hebben, wanneer zij bijna-ontaarde enkele-deeltjestoestanden bezetten, in overeenkomst met de eerste regel van Hund uit de atomaire fysica.

Een ander spin-gerelateerd fenomeen dat behandeld wordt in dit proefschrift, is het Kondo-effekt. Het Kondo-effekt is een veel-deeltjes-verschijnsel, voortkomend uit de interactie tussen een gelokaliseerde spin en vrije elektronen. Het is oorspronkelijk ontdekt in metalen met een lichte verontreiniging van magnetische atomen. Quantum dots, verbonden met source- en drain-kontakten kunnen zo'n systeem nabootsen en bieden de mogelijkheid het Kondo-effekt te meten en te manipuleren op de schaal van een enkele spin-onzuiverheid. Als de dot spin-ontaarde enkele-deeltjestoestanden heeft, die paarsgewijs gevuld worden met 'spin-omhoog'- en 'spin-omlaag'-elektronen, heeft de dot alleen een totale spin ongelijk aan nul voor een *oneven* aantal elektronen. In dit geval wordt het Kondo-effekt verwacht op te treden voor een oneven, maar niet voor een even aantal elektronen.

Een sterk Kondo-effekt is waargenomen bij laag magneetveld in een laterale quantum dot. De Coulomb-blokkade wordt volledig overwonnen door het Kondo-effekt en de geleiding bereikt de unitaire limiet van $2e^2/h$. De experimentele Kondo-temperatuur vertoont zeer goede overeenkomst met het spin-1/2 Anderson-model voor een magnetische onzuiverheid in het gehele Kondo-regime. Door middel van het meten van elektroninterferentie in een Aharonov-Bohm-ring, met de dot opgenomen in een van de armen, wordt aangetoond dat fase-coherent transport door een Kondo-quantum-dot mogelijk is.

In het algemeen kan het probleem van elektrontransport door een Kondo-quantum-dot niet één op één vertaald worden in het probleem van de weerstand in een bulk metaal als beschreven door het Anderson-model voor een magnetische onzuiverheid. Een experiment wordt beschreven waarin een onverwacht Kondo-effekt optreedt in een verticale dot met een klein aantal elektronen. Het energieverval tussen spin-singlet- en spin-triplet-toestanden wordt ingesteld door een magneetveld. Een Kondo-effekt treedt op voor een *even* aantal elektronen, wanneer de singlet- en triplet-toestand ontaard zijn. De karakteristieke energieschaal blijkt veel groter te zijn dan voor het gebruikelijke spin-1/2 geval in dit systeem. Dit type Kondo-effekt is niet eerder beschouwd, waarschijnlijk omdat singlet-triplet-ontarding niet optreedt in magnetische elementen.

Een ander Kondo-verschijnsel zonder tegenhanger in metalen systemen is het multi-niveau-Kondo-effekt bij een hoog magneetveld, bestudeerd in een quantum dot gefabriceerd met een selectieve groei methode. Dit ongebruikelijk sterke

Kondo-effekt wordt eveneens toegeschreven aan een singlet-triplet-overgang in de grondtoestand van de dot. In tegenstelling tot het singlet-triplet-Kondo-effekt waargenomen in een verticale dot, is de geleiding nabij de overgang sterk gereduceerd voor lage spanningen en temperaturen. Dit gedrag wordt vergeleken met voorspellingen voor een twee-fase Kondo-effekt in quantum dots gekoppeld aan kontakten met één geleidingskanaal. Het verschillende gedrag van het singlet-triplet-Kondo-effekt in een laterale dot in vergelijking met een verticale dot wordt toegeschreven aan een verschillend aantal geleidingskanalen in de kontakten gekoppeld aan de dot.

De volgende logische stap na het bestuderen van individuele quantum dots is het onderzoeken van systemen bestaande uit meer dan één dot. Door twee quantum dots te koppelen in serie, wordt een systeem verkregen met fundamenteel verschillende eigenschappen en mogelijkheden in vergelijking met een enkele quantum dot. Waar enkele quantum dots beschouwd worden als ‘kunstmatige atomen’, kunnen twee dots gekoppeld worden om een ‘kunstmatig molecuul’ te vormen. Gemotiveerd door de relevantie voor het realiseren van vastestof-quantum-bits, wordt elektrontransport door twee laterale quantum dots gekoppeld in serie in ogenschouw genomen. Een introductie in het ladingsstabiliteitsdiagram wordt gepresenteerd. Resonante-tunneling-experimenten laten zien dat de dubbele-dot-geometrie de nauwkeurige bepaling van de intrinsieke levensduur van diskrete energieniveaus in quantum dots mogelijk maakt. De evolutie van diskrete energieniveaus in een magneetveld wordt bestudeerd. De resolutie maakt het mogelijk afstoting tussen energieniveaus in het spektrum van een quantum dot te meten. Met mikrogolf-spektroskopie is het mogelijk de overgang van een ionische binding (voor zwakke inter-dot-tunnelkoppeling) naar een covalente binding (voor sterke inter-dot-tunnelkoppeling) zichtbaar te maken in een dubbele dot.

De frequenties waarmee elastische en inelastische overgangen plaatsvinden in een twee-niveau-systeem gevormd door een dubbele quantum dot, worden gemeten door middel van een dc stroom door het systeem. De frequentie van de inelastische overgangen wordt goed beschreven door de Einstein-coëfficiënten, die absorptie relateren aan gestimuleerde en spontane emissie. Voor deze inelastische processen wordt energie het meest efficiënt uitgewisseld met akoestische fononen. De resultaten tonen het belang aan van vacuümfluctuaties in de omgeving van circuits bestaande uit coherente quantum-strukturen.

Tenslotte wordt een elektro-magnetisch Aharonov-Bohm-effekt in een 2D elektronengas-ring bestudeerd. De mesoskopische 2DEG-ring is onderbroken door twee tunnelbarrières die het mogelijk maken een goed gedefinieerd potentiaalverschil over de twee helften van de ring aan te leggen. De elektroninterferentie in de ring

wordt gemanipuleerd door een loodrecht magneetveld en een spanning, resulterend in duidelijke Aharonov-Bohm-oscillaties, tot in het quantum-Hall-regime, als een functie van beide parameters. Met behulp van een verstrooiingsmodel wordt een nieuwe methode ontwikkeld voor het meten van de defaseringsstijd van de elektronen met een focus op de rol van elektron-elektron-interakties. De defaseringsstijd wordt zeer kort bij hoge voltages en magneetvelden.

Wilfred G. van der Wiel
november 2001

概要

半導体量子ドットおよびリングにおける電子輸送とコヒーレンス

本博士論文では縦型・平面型半導体量子ドットおよび半導体リングにおける電子輸送とコヒーレンスに関するいくつかの実験について述べる．縦型量子ドットはIn/Al/GaAs 二重障壁ヘテロ構造を加工して作製したサブミクロンサイズの柱状構造であり，周囲を金属ゲート電極が取り囲んでいる．平面型量子ドットおよびリング素子は，GaAs/AlGaAs ヘテロ構造中の2次元電子ガス（2DEG）をベースに，エッチングによる溝加工やヘテロ構造上の金属ゲート電極を用いることにより構成される．

量子ドットはトンネル障壁を介してソースおよびドレイン電極と弱く結合している．1電子をドット上加えるとドット上の電荷が素電荷 $-|e|$ 変化する．それに伴う帯電エネルギーは，ドットと周囲の環境の間の全静電容量 C を用いて， e^2/C で与えられる．低温においてはこの帯電エネルギーがドットを介した電子輸送を妨げる．これが「クーロンブロッケイド」である．一方，1つあるいは複数のゲート電極上の電圧を変えることにより，ドット上の静電ポテンシャルを制御することができる．ある特定のゲート電圧においては2つの電荷状態が縮退し，単一電子トンネリングが可能となる．ゲート電圧の変化に伴ってクーロンブロッケイドと単一電子トンネリングが交互に実現することにより，ドットを介したコンダクタンスにいわゆる「クーロン振動」が現れる．

量子ドット中では3次元すべての方向において電子が空間的に閉じ込められているので，原子内のように，不連続なエネルギー準位が形成される．これおよび以下に述べるような類似性により，量子ドットは「人工原子」とも呼ばれる．

原子物理によく似た現象の一例が，量子ドットで観測されるスピン1重項 - スピン3重項遷移である．この遷移は交換相互作用および磁場依存する直接クーロン相互作用により説明される．これらの相互作用の寄与はドット内に閉じ込められた電子の数の関数として決定され，また実験的に測定することができる．原子物理におけるフントの第一則と同様に，電子がほぼ縮退した一電子状態を占めているときには，それらのスピンの平行になるように相互作用が働く．

本論文で議論するスピンに関連したもうひとつの現象は近藤効果である。近藤効果は局在スピンと自由電子の間の相互作用により生じる多体効果である。この効果は少量の磁性不純物を含んだ金属において初めに発見された。ソースおよびドレイン電極と結合した量子ドットを用いると、1スピン不純物による近藤効果を実際に制御し測定することが可能になる。ドットが、「上向きスピン」と「下向きスピン」の2つの電子で占められるような、スピン縮退した1電子準位を持っているとき、電子数が奇数の場合のみドット中にゼロでないスピン $S = 1/2$ が存在する。その結果電子数が奇数のときのみ近藤効果が起こり、偶数のときは起こらないと予想される。

弱磁場における強い近藤効果が平面型量子ドットにおいて観測される。クーロンブロッケイドは近藤効果により完全に抑制され、コンダクタンスはユニタリー極限に相当する値 $2e^2/h$ に達する。実験で得られた近藤温度は近藤領域全体に渡ってスピン $1/2$ のアンダーソン不純物モデルでよく説明される。量子ドットを一方の径路にはめ込んだアハラノフ・ボームリングでの電子干渉を測定することにより、量子ドットを介した位相コヒーレントな電子輸送が近藤状態下で可能であることが示される。

近藤効果を示す量子ドットを介した電子輸送の問題は、一般的には、アンダーソン不純物モデルで記述されるバルク金属中の抵抗異常の問題に帰着することができない。少数電子を閉じ込めた縦型量子ドットにおいて、予想されていなかった近藤効果を観測した結果を示す。スピン1重項状態とスピン3重項状態のエネルギー差を磁場で制御すると、2つの状態の縮退する点において、偶数電子数状態の近藤効果が観測される。この効果の特徴的なエネルギースケールは同じ系における通常のスピン $1/2$ の場合のものよりずっと大きい。おそらく磁性元素では1重項 - 3重項状態間の縮退が起こらないためであろうが、この種の近藤効果はこれまで考察されていなかった。

バルク金属では見られないもうひとつの近藤効果—複数量子ドット系—を選択成長で形成した平面型量子ドットを用いて研究した。この異常に強い近藤効果の起源もまたドットの基底状態における1重項 - 3重項遷移に帰着できる。縦型ドットで観測された1重項 - 3重項近藤効果と異なり、遷移が起きる条件から外れたところでは、低バイアス電圧および低温のもとでのコンダクタンスが強く抑制される。観測された振舞いを、単一チャンネルを持つリードと結合した量子ドットにおける2段階近藤効果に関する理論的予言と比較した。縦型量子ドットと平面型量子ドットにおける1重項 - 3重項近藤効果の相違はリードにおける伝導チャンネル数の違いに帰着される。

単一量子ドット研究の次に来るものは当然ながら複数量子ドット系の研究である。2つの量子ドットを直列に結合することにより、単一量子ドットと比べて本質的に異なる振舞いと可能性を示す系を構成することができる。単一量子ドット

を「人工原子」と呼んだのに対応して、結合量子ドットは「人工分子」とみなすことができる。これらが固体素子量子ビットの実現と結びついていることに触発されて、直列の平面型結合量子ドットの電子輸送に関する実験をレビューする。はじめに結合量子ドットの電荷状態の安定性を示す図を紹介する。結合量子ドットにおける共鳴トンネリングの実験により量子ドット中の量子化準位の本質的な寿命が正確に評価できる。一方、量子化準位の磁場依存性も測定されている。その測定の高い分解能により、量子ドットのエネルギースペクトル中の準位非交差を観測することが可能である。またマイクロ波スペクトロスコピーにより結合量子ドット人工分子におけるイオン結合（弱いドット間結合に対して）から共有結合（強いドット間結合に対して）への遷移が観測される。

直流電流測定により結合量子ドットにおける2準位間の弾性および非弾性遷移確率が測定される。非弾性遷移確率は、誘導および自発放出と吸収とを関係付けるアインシュタイン係数によりよく記述される。非弾性過程においては、散逸されるエネルギーは音響フォノンモードへ最も効率よく放出される。この結果はコヒーレント量子素子の小規模回路において環境の量子揺らぎの影響が重要であることを示している。

最後に、2次元電子ガスを用いて構成されたリングにおける電氣的 - 磁氣的アハラノフ - ボーム効果に関する研究成果を示す。この微小リングには2つのトンネル障壁が挿入されており、左半分と右半分の間にきちんと定まったポテンシャル差を与えることができる。リング内の電子干渉は垂直磁場およびバイアス電圧により変調され、零磁場から量子ホール効果領域に至るまで磁場・電圧双方に対して明確なアハラノフ - ボーム振動が観測された。電子 - 電子相互作用に注目した散乱モデルを導入することにより、非平衡状態における電子の位相緩和時間を測定する新しい方法を記述する。この位相緩和時間は高バイアス電圧、高磁場下において非常に短くなる。

ウィルフレッド G. ファンデルヴィール

2001 年 11 月

Curriculum Vitae

Wilfred Gerard van der Wiel

- 28-05-1975 Born in Gouda, the Netherlands.
- 1987-1993 Grammar school at the Coornhert Gymnasium in Gouda.
- 1992 Prize awarded by the Federal Republic of Germany:
Premium Program of the Pedagogical Exchange Service.
- 1993 Awarded participation of the Summer Science Institute of
the Weizmann Institute of Science, Rehovot, Israel.
- 1993-1997 M.Sc. Applied Physics, cum laude
Delft University of Technology.
Graduate research in the Quantum Transport group of
prof.dr.ir. J.E. Mooij.
Subject: Magnetoresistance Oscillations of a 2D Electron
Gas Ring in contact with a Superconductor.
- 1996, 1997 Shell International Traineeships at Thai Shell Exploration
and Production Company, Ltd., Bangkok, Thailand.
- 1998-2002 Ph.D research at Delft University of Technology
and NTT Basic Research Laboratories, Atsugi, Japan,
under supervision of prof.dr.ir. L.P. Kouwenhoven
Subject: Electron transport and coherence in semiconductor
quantum dots and rings.

List of publications

1. *Microwave spectroscopy on a quantum-dot molecule*
T.H. Oosterkamp, T. Fujisawa, W.G. van der Wiel, K. Ishibashi, R.V. Hijman, S. Tarucha and L.P. Kouwenhoven, Nature **395**, 873-876 (1998).
2. *Spontaneous emission spectrum in double quantum dot devices*
T. Fujisawa, T.H. Oosterkamp, W.G. van der Wiel, B.W. Broer, R. Aguado, S. Tarucha and L.P. Kouwenhoven, Science **282**, 932-935 (1998).
3. *Singlet-triplet transitions in a few-electron quantum dot*
W.G. van der Wiel, T.H. Oosterkamp, J.W. Janssen, L.P. Kouwenhoven, D.G. Austing, T. Honda and S. Tarucha, Physica B **256-258**, 173-177 (1998).
4. *Electron ground states in a few-electron quantum dot*
T.H. Oosterkamp, W.G. van der Wiel, L.P. Kouwenhoven, D.G. Austing, T. Honda and S. Tarucha, Festkörper Probleme/Advances in Solid State Physics **38**, 139-152 (1999).
5. *Photon assisted tunneling spectroscopy on a double quantum dot*
T. Fujisawa, T.H. Oosterkamp, W.G. van der Wiel, S. Tarucha and L.P. Kouwenhoven, Compound Semiconductors 1998, IOP Conf. Ser. **162**, 493 (1999).
6. *Microwave spectroscopy on a double quantum dot*
W.G. van der Wiel, T. Fujisawa, S. Tarucha, T.H. Oosterkamp, R. Aguado, R.M Schouten and L.P. Kouwenhoven, Proceedings of the 24th International Conference on the Physics of Semiconductors, p. 149-154.
7. *Elastic and inelastic single electron tunneling in coupled two dot system*
S. Tarucha, T. Fujisawa, K. Ono, D.G. Austing, T.H. Oosterkamp, W.G. van der Wiel and L.P. Kouwenhoven, Microelectronic Engineering **47**, 101-105 (1999).
8. *Photon assisted tunneling in quantum dots*
T.H. Oosterkamp, W.G. van der Wiel, S. de Franceschi, C.J.P.M. Harmans and L.P. Kouwenhoven, cond-mat/9904359 (1999).
9. *Inelastic tunneling in a double quantum dot coupled to a bosonic environment*
Toshimasa Fujisawa, Wilfred G. van der Wiel and Leo P. Kouwenhoven, Physica E **7**, 413 (2000).

10. *Microwave spectroscopy of a double quantum dot in the low and high power regime*
W.G. van der Wiel, T. Fujisawa, T.H. Oosterkamp and L.P. Kouwenhoven, *Physica B* **272/1-4**, 31, (1999).
11. *Suppression of the Kondo Effect in a Quantum Dot by Microwave Radiation*
J.M. Elzerman, S. De Franceschi, D. Goldhaber-Gordon, W.G. van der Wiel and L.P. Kouwenhoven, *Jrnl. of Low Temp. Phys.* **118**, 375 (2000).
12. *Direct Coulomb and Exchange Interaction in Artificial Atoms*
S. Tarucha, D.G. Austing, Y. Tokura, W.G. van der Wiel and L.P. Kouwenhoven, *Phys. Rev. Lett.* **84**, 2485 (2000).
13. *Kondo effect in an integer-spin quantum dot*
S. Sasaki, S. De Franceschi, J.M. Elzerman, W.G. van der Wiel, M. Eto, S. Tarucha and L.P. Kouwenhoven, *Nature* **405**, 764 (2000).
14. *Effects of Coulomb interactions on spin states in vertical semiconductor quantum dots*
S. Tarucha, D.G. Austing, S. Sasaki, Y. Tokura, W.G. van der Wiel and L.P. Kouwenhoven, *Appl. Phys. A* **71**, 367-378 (2000).
15. *The Kondo Effect in the Unitary Limit*
W.G. van der Wiel, S. De Franceschi, T. Fujisawa, J.M. Elzerman, S. Tarucha and L.P. Kouwenhoven, *Science* **289**, 2105 (2000).
16. *Electron Cotunneling in a Semiconductor Quantum Dot*
S. de Franceschi, S. Sasaki, J.M. Elzerman, W.G. van der Wiel, S. Tarucha and L.P. Kouwenhoven, *Phys. Rev. Lett.* **86**, 878-881 (2001).
17. *A Double Quantum Dot as an Artificial Two-level System*
W.G. van der Wiel, T. Fujisawa, S. Tarucha and L.P. Kouwenhoven, *Japanese Journal of Applied Physics* **40**, 2100 (2001).
18. *Electron transport through quantum dots: an unusual Kondo effect*
S. De Franceschi, S. Sasaki, J.M. Elzerman, W.G. van der Wiel, M. Eto, S. Tarucha and L.P. Kouwenhoven, to be published in the Proceedings of the Nato workshop in Pecs (June 2000) by Kluvert Academic Plenum Publishers.
19. *Transport through artificial Kondo impurities*
S. De Franceschi, S. Sasaki, J.M. Elzerman, W.G. van der Wiel, M. Eto, S. Tarucha and L.P. Kouwenhoven, to be published in *Macroscopic Quantum Coherence and Quantum Computing*, eds. D. Averin and P. Silvestrini, pp.317-324 (2001), Kluwer Academic Plenum Publishers.

-
20. *Spin effects in semiconductor quantum dot structures*
S. Tarucha, D.G. Austing, S. Sasaki, Y. Tokura, W.G. van der Wiel, S. De Franceschi and L.P. Kouwenhoven, *Physica E* **10**, 45-51 (2001).
 21. *Kondo-effect in kwantumdots*
Wilfred van der Wiel, Jeroen Elzerman en Leo Kouwenhoven, *Natuur & Techniek*, februari 2001, p. 44-49 (2001).
 22. *Novel Kondo Anomaly in Quantum Dots*
S. Tarucha, D.G. Austing, S. Sasaki, Y. Tokura, J.M. Elzerman, W.G. van der Wiel, S. De Franceschi and L.P. Kouwenhoven, *Materials Science and Engineering B* **84**, 10-16 (2001).
 23. *Multi-level Kondo regimes in a quantum dot*
S. De Franceschi, W.G. van der Wiel, T. Fujisawa, J.M. Elzerman, W. Izumida, S. Tarucha and L.P. Kouwenhoven, to be published in the proceedings of the Moriond conference (January 2001).
 24. *Low-temperature transport in dual-gated SETs fabricated by selective area metalorganic vapor phase epitaxy*
J. Motohisa, W.G. van der Wiel, J.M. Elzerman, S. De Franceschi, F. Nakajima, Y. Ogasawara, T. Fukui and L.P. Kouwenhoven, to be published in *Physica E*.
 25. *Electro-magnetic Aharonov-Bohm effect in a 2-D electron gas ring*
W.G. van der Wiel, Yu.V. Nazarov, S. De Franceschi, T. Fujisawa, J.M. Elzerman, E.W.G.M. Huizeling, S. Tarucha and L.P. Kouwenhoven, submitted to *Physical Review Letters*.
 26. *Two-stage Kondo effect in a quantum dot at high magnetic field*
W.G. van der Wiel, S. De Franceschi, J.M. Elzerman, S. Tarucha, L.P. Kouwenhoven, J. Motohisa, F. Nakajima and T. Fukui, submitted to *Physical Review Letters*.
 27. *Double Quantum Dots in Series*
W.G. van der Wiel, S. De Franceschi, J.M. Elzerman, T. Fujisawa, S. Tarucha and L.P. Kouwenhoven, review (2001).
 28. *Fabrication and low-temperature transport properties of selectively grown dual-gated single-electron transistors*
J. Motohisa, W.G. van der Wiel, J.M. Elzerman, S. De Franceschi, F. Nakajima, T. Fukui and L.P. Kouwenhoven, submitted to *Applied Physics Letters*.

